General Disclaimer

One or more of the Following Statements may affect this Document

- This document has been reproduced from the best copy furnished by the organizational source. It is being released in the interest of making available as much information as possible.

- This document may contain data, which exceeds the sheet parameters. It was furnished in this condition by the organizational source and is the best copy available.

- This document may contain tone-on-tone or color graphs, charts and/or pictures, which have been reproduced in black and white.

- This document is paginated as submitted by the original source.

- Portions of this document are not fully legible due to the historical nature of some of the material. However, it is the best reproduction available from the original submission.

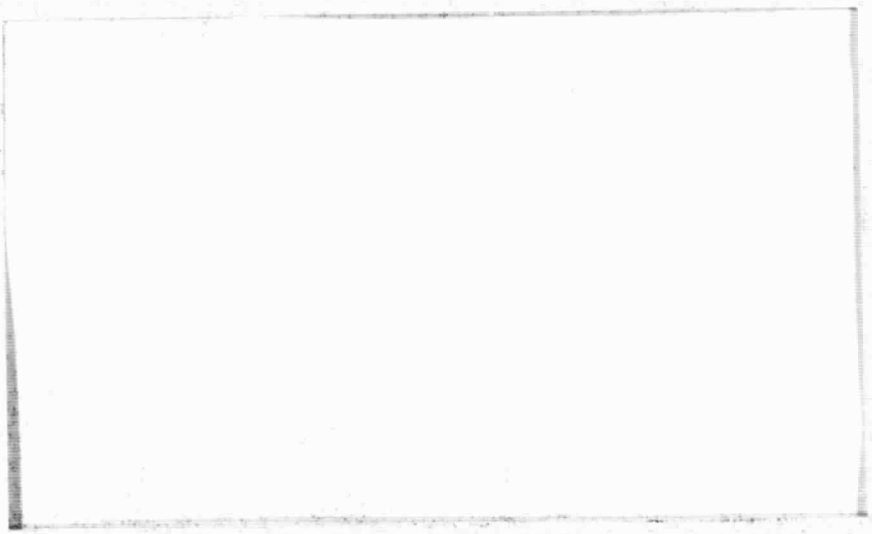

Research Laboratories for the Engineering Sciences

University of Virginia

Charlottesville

Report No. EME-4029-109-69U

September 1969

A FORCE BALANCE SYSTEM FOR THE MEASUREMENT OF SKIN FRICTION DRAG FORCE IN THE PRESENCE OF LARGE VIBRATIONS AND TEMPERATURES

Interim Technical Report

on

NASA Grant NGR 47-005-026

Submitted by Co-Principal Investigators:

Dr. Eugene S. McVey

Professor of Electrical Engineering and
Co-Chairman of The Automatic Control Area

Dr. James W. Moore

Professor of Mechanical Engineering and
Co-Chairman of The Automatic Control Area

Divisions of Electrical and Mechanical Engineering

RESEARCH LABORATORIES FOR THE ENGINEERING SCIENCES

SCHOOL OF ENGINEERING AND APPLIED SCIENCE

UNIVERSITY OF VIRGINIA

CHARLOTTESVILLE, VIRGINIA

Report No. EME-4029-109-69U
September 1969

Copy No. __

TABLE OF CONTENTS

LIST OF FIGURES

LIST OF FIGURES (continued)

FOREWORD

This is an interim technical report for research on force balance instrumentation to measure the skin friction of hypersonic vehicles at extreme temperatures, high altitudes and in a vibration field. This serves as a final report on one phase of the work, a motor-sensor system which uses cobalt magnetic material. In addition, comprehensive information is also presented concerning counterbalancing of acceleration and a gas bearing to support motor-sensor armatures. A later report or addendum to this report will be published on the ceramic electrical-sensor type system.

This report serves as a status report too because current research effort is reported.

CHAPTER I

INTRODUCTION

The purpose of the research reported in this report on NASA Grant NGR 47-005-026 is to develop a system to aid in the measurement of skin friction. It is a primary goal to develop instrumentation which will work over a temperature range from near absolute zero to 2000°F at altitudes to 100,000 feet and in a vibration field. Instruments developed which do not meet the specification end points are useful for measurements in more benign environments. In addition, it is anticipated that the motors and sensors developed will find use in other systems which must work in very hostile environments because, judging by the literature and availability of hardware, little work has been done on components which meet the specifications being used.

Three basic approaches have been worked on and all are of a force balance type which employ feedback to minimize parameter variation: 1) an electrical system which uses a motor-sensor assembly which employs cobalt magnetic material - cobalt was chosen because of its relatively high Curie temperature; 2) a system similar to the cobalt system except that the electrical coils are wound on ceramic, i.e., it is an "air core" configuration; 3) a fluidic system. The electrical system requires an "electronic package" which must be placed in a temperature environment compatible with transistors. The fluidic system is completely self-contained except for the readout equipment which will probably contain transistors.

The cobalt motor-sensor approach is being reported on in final form because it is to be discontinued. The reasons for discontinuing this approach

are mostly pragmatic in nature rather than due to known technical limitations. This work was started one year after the other electrical approach and it has remained approximately one year behind. The "air core" approach justifies continued work based on actual high temperature data. Resources of research personnel and funds are not adequate to finalize more than two approaches. Thus, the cobalt approach is to be discontinued even though the possibility of useful results to approximately 1750°F may be possible.

The report on the "air core" system is to be presented as a masters thesis. The chapters on gas bearings and on counterbalancing have already been accepted as masters theses. This material is presented in thesis form for completeness and to effect a significant saving in publication cost. This accounts for the manner in which the material is presented. Final operational data on the prototype systems will be in a more concise form.

The work on the fluidic system is only a summary. A doctoral dissertation will be available in the near future which will contain the details of this work. The fluidic amplifier work is expected to lead to a masters thesis.

Present plans are to complete all effort to make the fluidic and "air core" system prototypes operational within the next three years. The third year will be devoted primarily to reports and assisting in operational problems. If future work indicates that one of the two approaches will not be useful only the most promising system will be pursued.

CHAPTER II

COBALT MOTOR-SENSOR

Introduction

The cobalt skin friction sensor is composed of a motor-sensor assembly and an electronics package. The motor-sensor assembly is mounted within the test structure, and the test section is attached to the motor-sensor by a short rod (sting). This places the motor-sensor in approximately the same environment as the test section whereas the electronics package can be remotely located in a less severe environment. Because of the extreme temperature range (≈ 0°K to 2000°F), the motor-sensor assembly is the most critical component of the measurement system.

The motor-sensor combination that employs cobalt as a magnetic core material basically consists of two identical sets of opposing cobalt E laminations around which nichrome wire is wound and a core of cobalt I laminations. The core is free to rotate, and the test section of the skin is attached to this core. The motor-sensor combination is shown schematically in Figure 1.

The operation of this motor-sensor combination can be briefly explained as follows: a force applied to the test section causes a rotation of the core about the flexure. This rotation is converted into a proportional voltage by the sensor, and the polarity of the voltage is determined by the direction of rotation. This voltage is applied to two power amplifiers which increase the current in one side of the motor and decrease the current in the other side. This results in a change in the magnetic fields of the two coils which exerts a force on the core. This force nulls the position error (within a specified

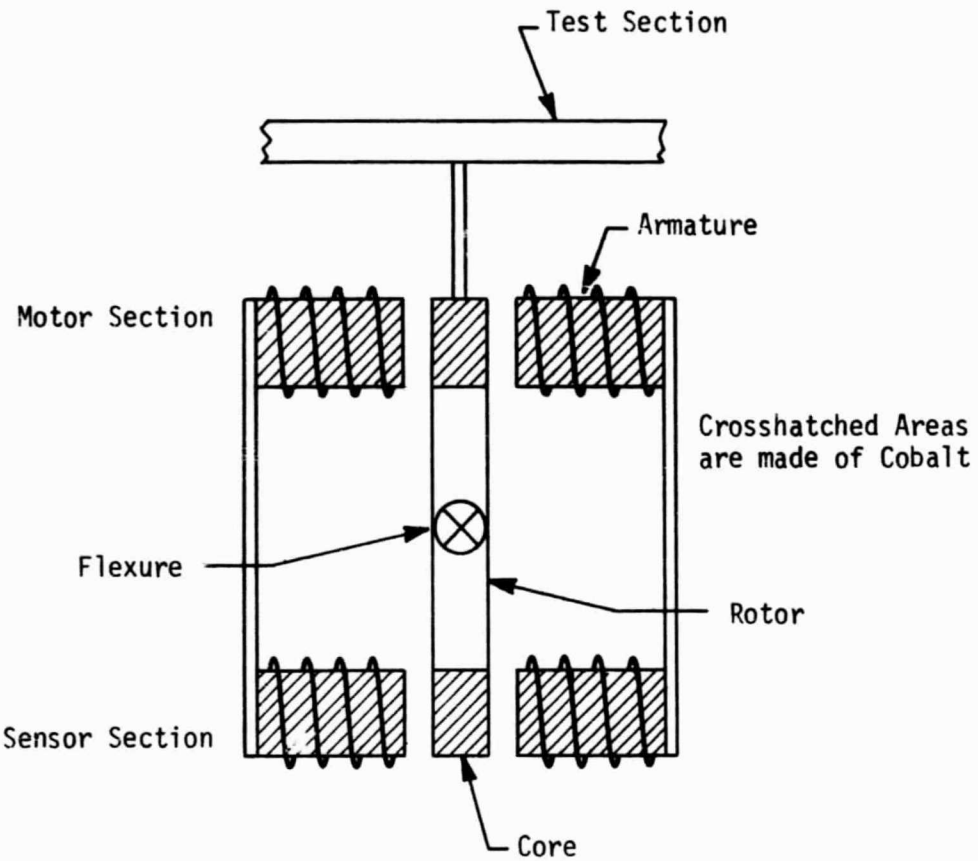

Figure 1. Schematic of Cobalt Motor-Sensor

nonzero tolerance), and the applied force is determined by measuring the difference between the two coil currents.

There are two obvious advantages of this general method of measuring skin friction. First, the position of the test section can be maintained within close tolerances, and second, the force is measured by reading the differential current. This second advantage facilitates remote readout of the force.

Of the three approaches that have been considered, the cobalt motor-sensor has the advantage of being potentially the most compact structure. This is possible because the incremental permeability of pure cobalt is greater than that of air thus requiring fewer turns on the coils to produce the required force constant. Furthermore, because the rotating element of the motor-sensor is made of a magnetic material, there is no requirement to furnish current to the rotor through the flexures. This simplifies the flexure design problem considerably.

The primary disadvantage of this approach is the requirement that the incremental permeability of the cobalt remain above a minimum value throughout the specified temperature range. (This requirement is developed later.) Thus the maximum operating temperature of this device is limited by the permeability versus temperature performance of magnetic material.

Cobalt Motor-Sensor System Equations

In order to specify the components of a system, an overall description of the proposed system is almost essential. In the skin-friction measurement system the motor-sensor is the key component, and therefore, it serves as a

good staring point for the description.

For a rigid body in rotation,

$$\sum M = J\alpha \tag{1}$$

where M = vector moments acting on the body,

J = moment of inertia of the body,

α = angular acceleration of the body.

Referring to Fig. 1, the following equation can be written for the rotor (assuming that the rotor is balanced)

$$d_2F_a + d_1\Delta F = J\ddot{\theta} + k\theta \tag{2}$$

where d_2 = distance from the flexure to the applied force (test section)

F_a = applied force

d_1 = distance from the flexure to the position on the rotor opposite the center of the pole face

ΔF = force developed by the motor

θ = angular displacement

k = rotational spring constant of the flexure.

Taking the Laplace transform (assuming zero initial conditions) of Eq. (2) and solving for $\theta(s)$ yields:

$$\theta(s) = \frac{1}{J}\left[\frac{d_2F_a(s) + d_1\Delta F(s)}{s^2 + \frac{k}{J}}\right] \tag{3}$$

In deriving Eq. (3) friction (both static and viscous) has been assumed negligible.

The motor current is given by (assuming negligible armature inductance)

$$\Delta I(s) = \frac{e_a(s) - sK_v d_1 \theta(s)}{R_a} \tag{4}$$

where $e_a(s)$ = motor armature voltage,

K_v = back emf constant of motor,

R_a = armature winding resistance,

and the motor force is given by:

$$\Delta F(s) = K_m \Delta I(s) \tag{5}$$

where K_m = motor constant relating current to force.

If the power amplifiers and sensor electronics do not limit the system response, the armature voltage is given by:

$$e_a(s) = - K_a d_1 K_s \theta(s) \tag{6}$$

where K_a = amplifier transconductance

K_s = sensor constant relating displacement of the core to voltage.

Equations (3), (4), (5) and (6) can be used to draw the system block diagram shown in Fig.2. This block diagram relates the input applied force to the output differential armature current in terms of the system parameters.

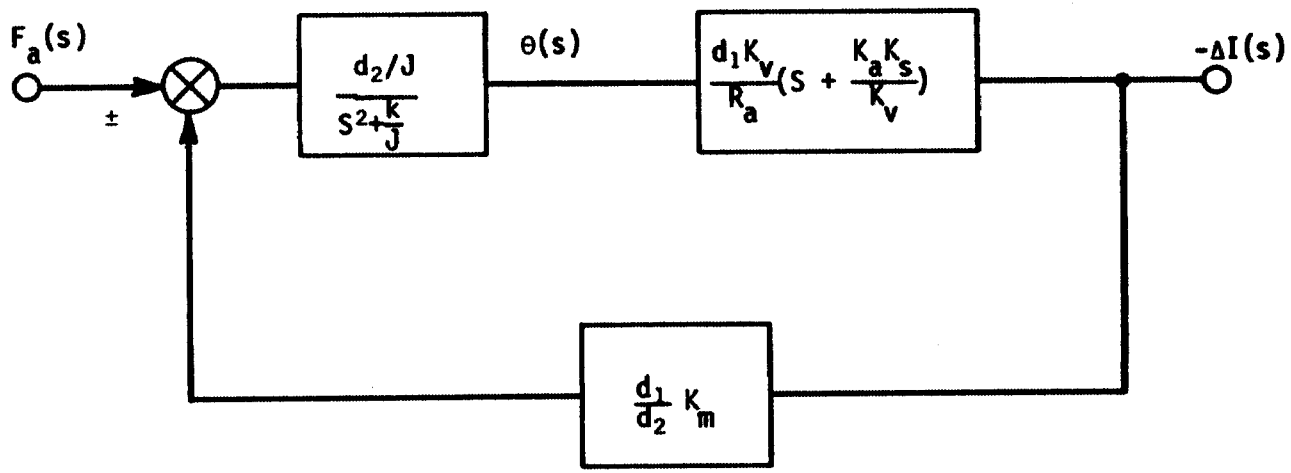

Figure 2. Cobalt Motor-Sensor Block Diagram

The loop gain and the closed-loop transfer function are:

$$GH = -\frac{K_m K_v d_1^2}{R_a J}\left(\frac{s + \frac{K_a K_s}{K_v}}{s^2 + \frac{k}{J}}\right) \tag{7}$$

and

$$\frac{\Delta I(s)}{F_a(s)} = -\frac{d_1 d_2 K_v}{R_a J}\left[\frac{s + \frac{K_a K_s}{K_v}}{s^2 + \frac{d_1^2 K_m K_v}{R_a J}\, s + R_a k + \frac{d_1^2 K_m K_a K_s}{R_a J}}\right] \tag{8}$$

Applying the final value theorem to Eq. (8) yields:

$$\left.\frac{\Delta I}{F_a}\right|_{\text{steady-state}} = -\frac{d_2}{d_1 K_m} \tag{9}$$

where the applied force has been assumed to be a step of amplitude F_a, and it has been assumed that $R_a k << \frac{d_1^2 K_m K_a K_s}{R_a J}$.

Equation (9) shows that the readout quantity, ΔI, is proportional to a constant (the ratio of the moment arm of the applied force to the moment arm of the motor force) times the reciprocal of the motor force constant.

Another system specification that enters into the design is the steady-state error or displacement. In order to prevent significant rotation of the test section from introducing errors in the measurement, the steady-state rotation must be kept below a specified value. In this case the design

specification was one half thousandths of an inch at the end of a one inch support or 0.5 milliradian of rotation.

An explicit expression for the rotation as a function of the applied force and the system parameters can be derived from Eqs. (3) through (6). This expression is

$$\frac{\theta(s)}{F_a(s)} = \frac{d_2/J}{s^2 + \frac{d_1^2 K_m K_v}{R_a J} s + \left(\frac{k}{J} + \frac{d_1^2 K_a K_m K_s}{R_a J}\right)} \tag{10}$$

If the applied force is considered to be a step of amplitude F_a,

$$\left.\frac{\theta}{F_a}\right|_{\text{steady-state}} = \frac{R_a d_2}{d_1^2 K_a K_m K_s} \tag{11}$$

where it has been assumed that $\frac{k}{J} << \frac{d_1^2 K_a K_m K_s}{R_a J}$. The block diagram of the system with angle considered to be the output is shown in Fig. 3.

Cobalt Motor Design

The constant relating force to input current for the cobalt motor can be derived by considering the configuration shown in Fig. 4. and considering first only one side and the core. The force acting on the core due to current in the coils of one side is given by:

$$F = \frac{dE}{dx_o} \tag{12}$$

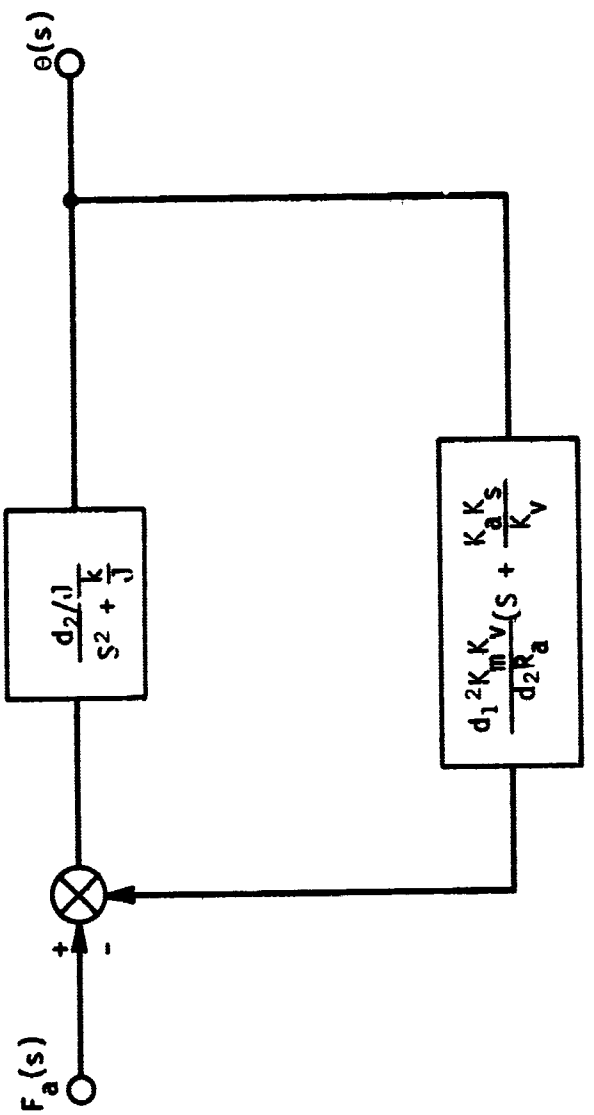

Figure 3. Cobalt Motor-Sensor Block Diagram

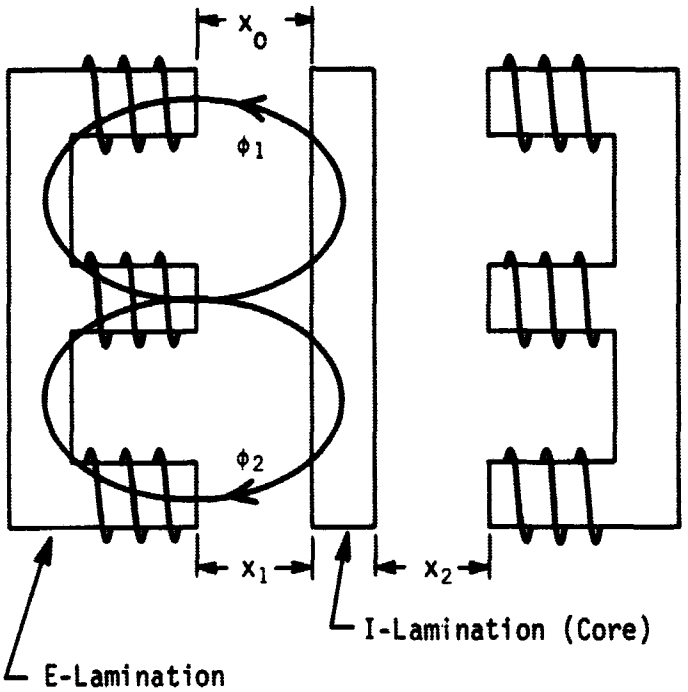

Note: x_0 is the air gap for the single magnet motor derivation and x_1 and x_2 are the air gaps for the two magnet derivation.

Figure 4. Cobalt Motor-Sensor: Schematic of Top View

where

E = stored energy in the magnet

x_o = length of the air gap.

For a magnet with inductance L, the stored energy is

$$E = \frac{1}{2} LI^2 \tag{13}$$

Substitution of Eq. (13) into Eq. (12) yields

$$F = \frac{\partial E}{\partial L} \frac{dL}{dx_o} + \frac{\partial E}{\partial I} \frac{dI}{dx_o} \tag{14}$$

or

$$F = \frac{1}{2} I^2 \frac{dL}{dx_o} + LI \frac{dI}{dx_o} \tag{15}$$

The second term on the right of Eq. (15) is negligible if the amplifier driving the motor is a good current source. Therefore

$$F = \frac{1}{2} I^2 \frac{dL}{dx_o} \tag{16}$$

The reluctance of the total magnetic path (assuming that the center pole face has twice the cross-sectional area of the other two faces) is

$$R_T = \frac{2\ell_1}{\mu A} + \frac{4x_o}{\mu_o A} \tag{17}$$

where

ℓ_1 = mean length of the path in the magnetic material encountered by flux ϕ_1

A = cross-sectional area of the magnetic material

u = permeability of the magnetic material

μ_o = permeability of free space.

Therefore, the inductance is given by

$$L = \frac{N\phi}{I} = \frac{N^2\phi}{NI} = \frac{N^2\phi}{\phi R_T} = \frac{N^2}{R_T} \tag{18}$$

or

$$L = \frac{\mu_o A N^2}{\frac{2\ell_1}{\mu_r} + 4x_o} \tag{19}$$

where μ_r = relative permeability of the magnetic material.

Substitution of Eqs. (19) and (13) into Eq. (12) gives the expression for the force developed by one side of the motor.

$$F = \frac{-2\mu_o A(NI)^2}{\left(\frac{2\ell_1}{\mu_r} + 4x_o\right)^2} \tag{20}$$

Equation (20) shows that the force of a single magnet motor is a nonlinear function of the current. This is an undesirable feature because it unnecessarily complicates system stability and force readout. The motor constant can be linearized by adding a second magnet which acts in opposition to the force of the other magnet. The sum of the two forces is

$$\Delta F = F_1 - F_2 = \mu_o AN^2 \left[\frac{(I_o + \Delta I)^2}{(\frac{2\ell_1}{\mu_r} + 2x_3 + 4x)^2} - \frac{(I_o - \Delta I)^2}{(\frac{2\ell_1}{\mu_r} + 2x_3 - 4x)^2} \right] \tag{21}$$

where

$I_1 = I_o + \Delta I$ = current in one side of motor = quiescent plus differential current

$I_2 = I_o - \Delta I$ = current in other side of motor = quiescent current minus the differential current

$x_3 = x_1 + x_2$ = total air gap

x = relative position of the armature

$x_1 = \frac{x_3}{2} + x$ = air gap of one side

$x_2 = \frac{x_3}{2} - x$ = air gap of the other side

If the system gain is high (resulting in a small steady-state displacement), the change of the core position is small compared to the air gap, and Eq. (21) simplifies to

$$F = \frac{4\mu_o AN^2}{\sqrt{2}} \left[\frac{I_o \Delta I}{(\frac{\ell_1}{\mu_r} + x_3)^2} \right] \tag{22}$$

From Eq. (22) it is apparent that the force developed by the two magnet motor is linear with respect to the differential current.

Equation (22) also makes apparent one of the most important motor design considerations - the relative permeability of the core material. If the cobalt

motor sensor is to satisfactorily operate over the specified temperature range, then the inequality

$$\frac{\ell_1}{\mu_r} << x_3 \tag{23}$$

must hold over the entire range. If this inequality is not true over the range, then the force reading will be affected by the temperature because the permeability of any magnetic material is a function of temperature - particularly in the vicinity of the Curie temperature. The above inequality therefore provides a specification for the minimum relative permeability for the core material at the upper end of the temperature range. Assuming a magnetic path length of 1.9 inches and an air gap of 0.025 inches, a relative permeability of 380 will satisfy the inequality by a factor of ten.

A literature search for properties of high temperature magnetic materials resulted in the choice of pure cobalt (at least 99% cobalt) as the only known magnetic material which would operate in the vicinity of 2000°F (1093°C). The Curie temperature (the temperature at which the relative permeability becomes unity) of pure cobalt is 2050°F (1121°C) according to Young [R. S. Young, COBALT, Its Chemistry, Metallurgy, and Uses, Reinhold Publishing Corp., New York (1960).] Unfortunately this literature search failed to provide a reliable profile of permeability as a function of temperature. Therefore the exact maximum operating temperature of the cobalt motor cannot be predicted, but extrapolation of available data indicates that this maximum should occur at 1600 - 1800°F (871 - 982°C).

In order to test the feasibility of this type of motor for the skin friction application, a low temperature model was constructed utilizing brass for the housing, 14% vanadium supermendur for the magnetic material, 12 turns of #22, B & S 80-20 nichrome wire with Hi-Temp Wire Company woven quartz insulation on each magnet and two Bendix free-flex cantilever pivots type 5006-600 for the flexure. Furthermore, the model incorporated Teflon insulators which determine the model temperature limit of approximately 500°F (260°C).

Static data at room temperature was taken using the experimental apparatus shown partially assembled in Fig. 5. This apparatus with its precise adjustments for positioning the balance and centering the LVDT body with respect to the core was necessitated by the problems encountered in taking data with a less sophisticated balance. All of the motor data was taken by loading the balance and then increasing the motor current until the motor force equaled the applied force. This null was detected by reading the LVDT output voltage.

Figure 6 shows the force curves obtained when only a single electromagnet is energized. Curve I is the force curve for an air gap of 0.050 inch and curve II for an air gap of 0.025 inch. These curves clearly show the nonlinearity predicted by Eq. (20), and they corroborate the inverse square dependence on the size of the air gap.

Figure 7 shows the force curves when two opposing electromagnets were energized. Again curve I is for 0.050 inch air gap and curve II for a 0.025 inch air gap. These curves clearly show the linear relationship predicted by Eq. (22), and they corroborate the inverse square dependence on the size of the air gap.

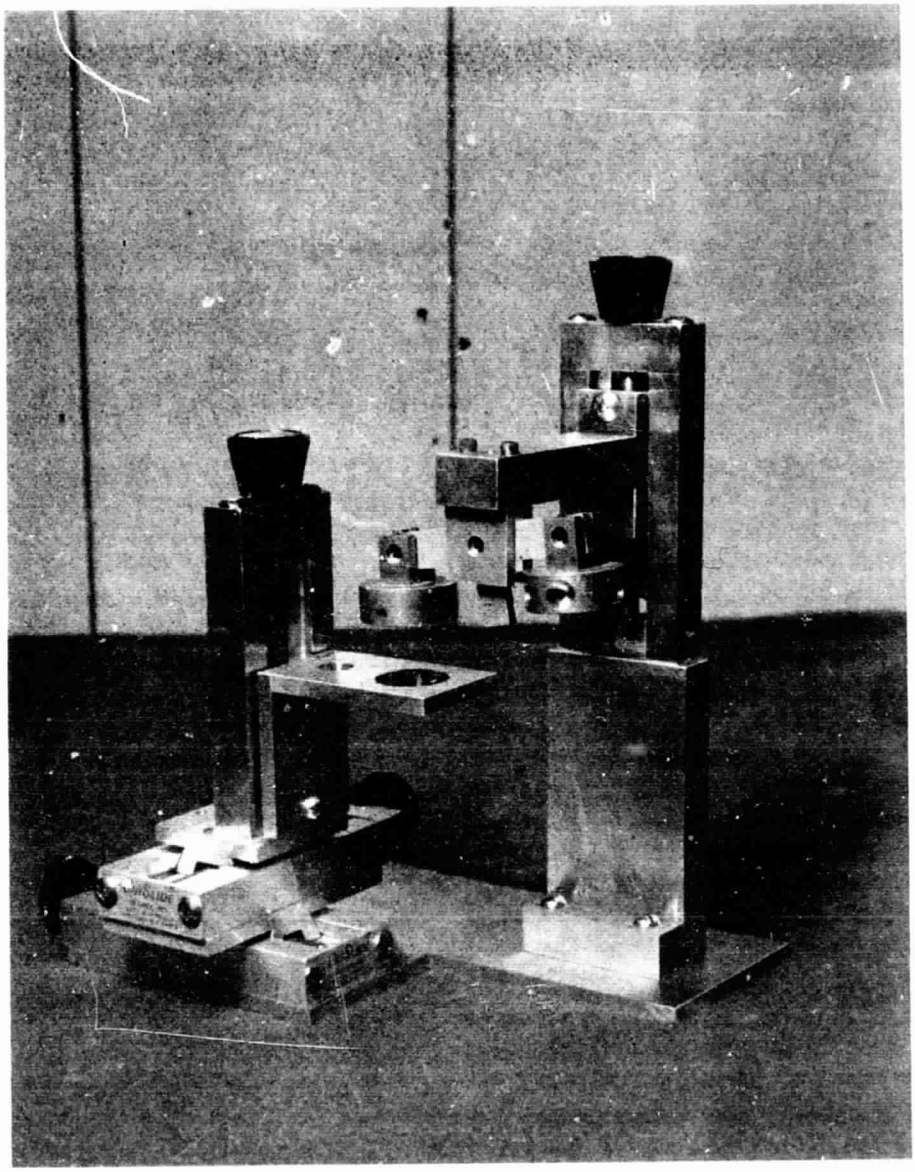

Figure 5. Cobalt Motor-Sensor: Photographs of Partially Assembled Balance

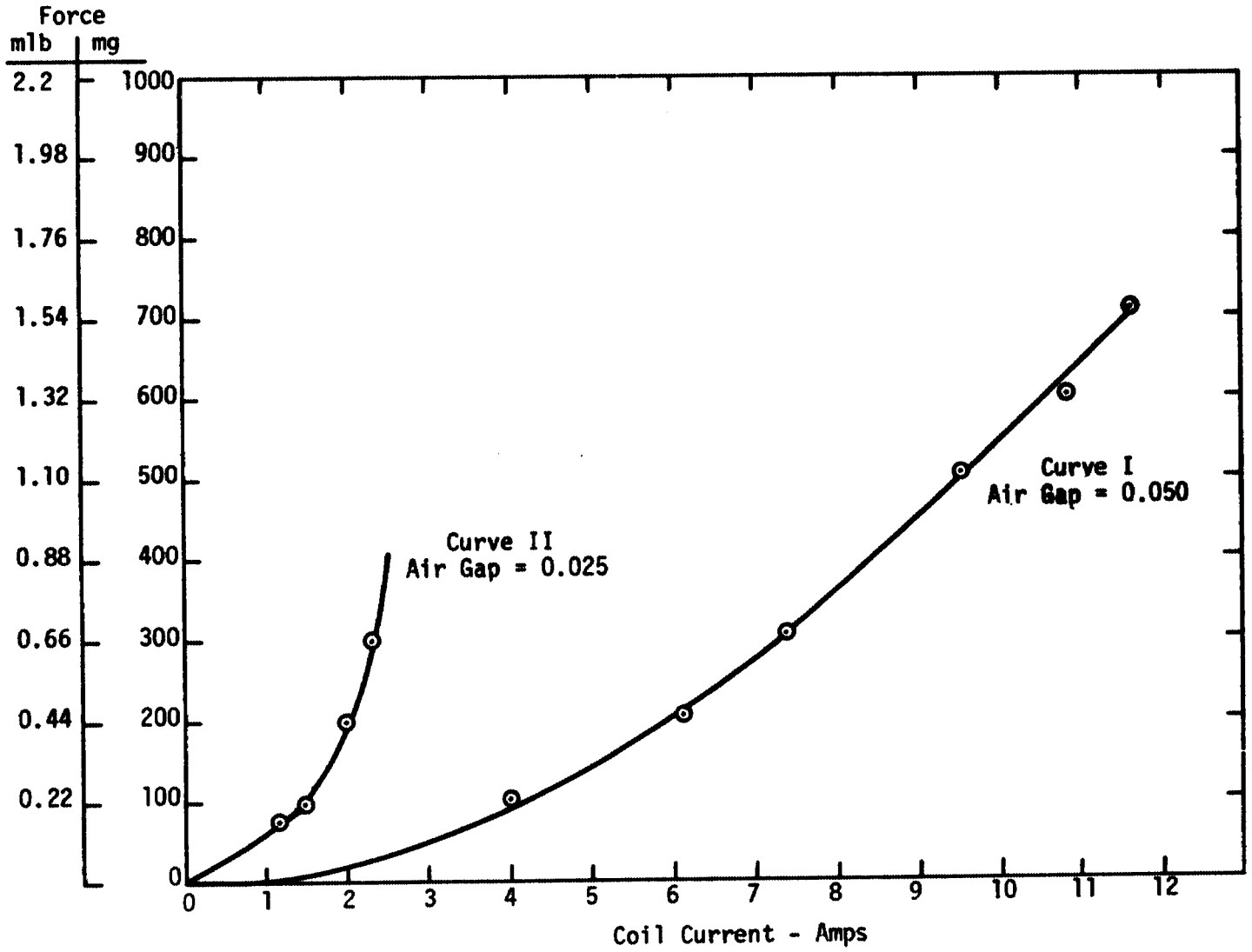

Figure 6. Cobalt Motor-Sensor: Force Curves for Single Electromagnet

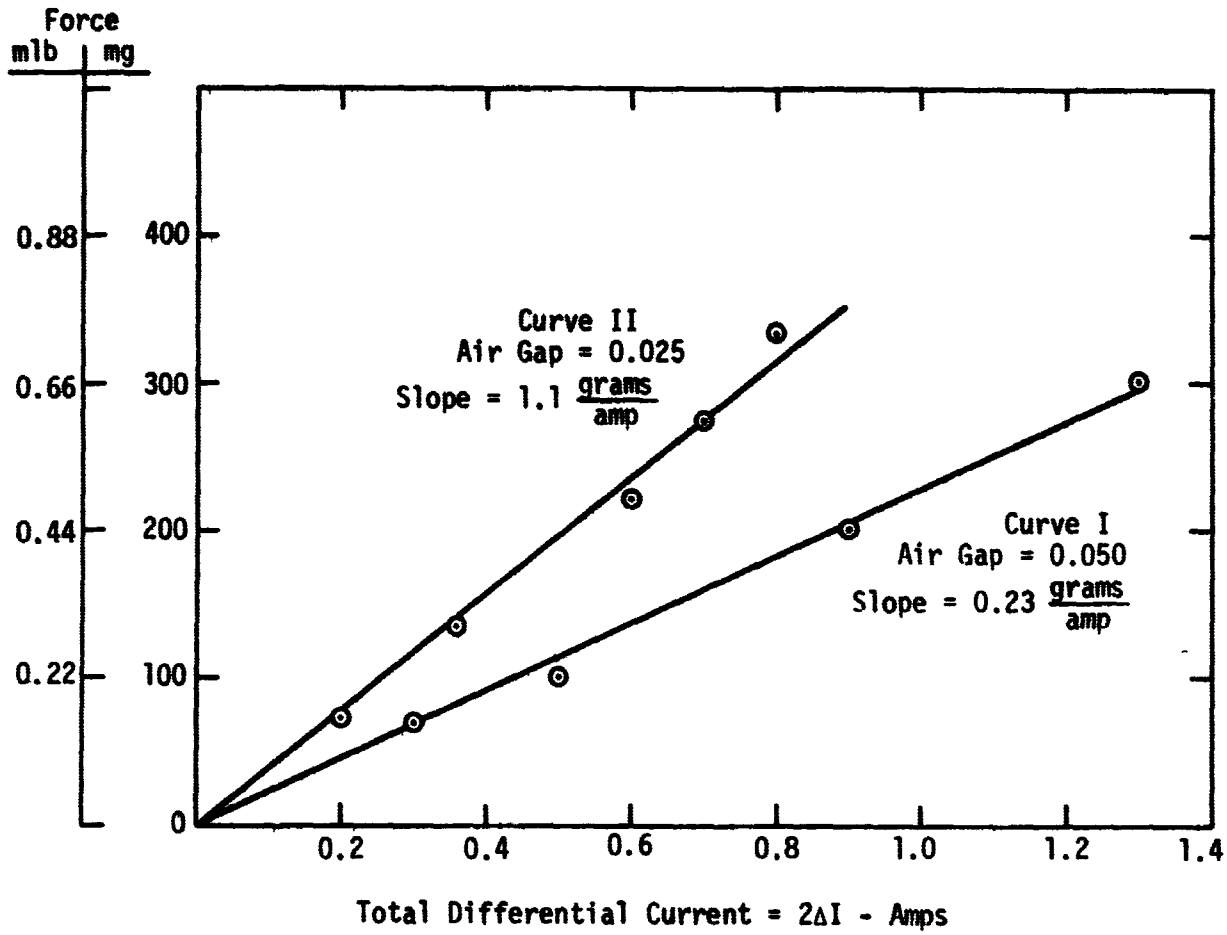

Figure 7. Cobalt Motor-Sensor: Force Curves for Double Electromagnet

Cobalt Sensor

The type of motor-sensor structure that has been described can be realized in several configurations. For example, one configuration uses the lower coil pair and core as two elements in a bridge. The signal from the bridge can be amplitude or phase detected. This configuration is shown schematically in Fig. 8.

The bridge is balanced when the core is centered between the two electromagnets (null position). A movement of the core in either direction from the null position will result in a bridge unbalance, and the voltage on the output will increase from the null value. This output voltage can be amplitude detected to give a dc voltage that is proportional to the distance of the core from the null position; however, this does not provide information that indicates the direction of displacement. If mechanical stops are provided to limit motion to only one direction, the directional information is not necessary.

Alternatively, the output of the bridge can be phase detected. This provides directional information because the sign of the phase reverses as the null is traversed. Therefore in order to provide a more generally useful instrument which could balance forces in either direction, phase detection was chosen.

In order to minimize adverse temperature effects, the two added bridge elements should be identical electrically and mechanically to the sensor elements except that the core of the added elements will be fixed in position. The added bridge elements then become a part of the motor-sensor structure and are subjected to the same environment. In the prototype that has been built, the external bridge elements have been simulated by slug tuned inductors and variable resistors in order to obtain preliminary closed loop data.

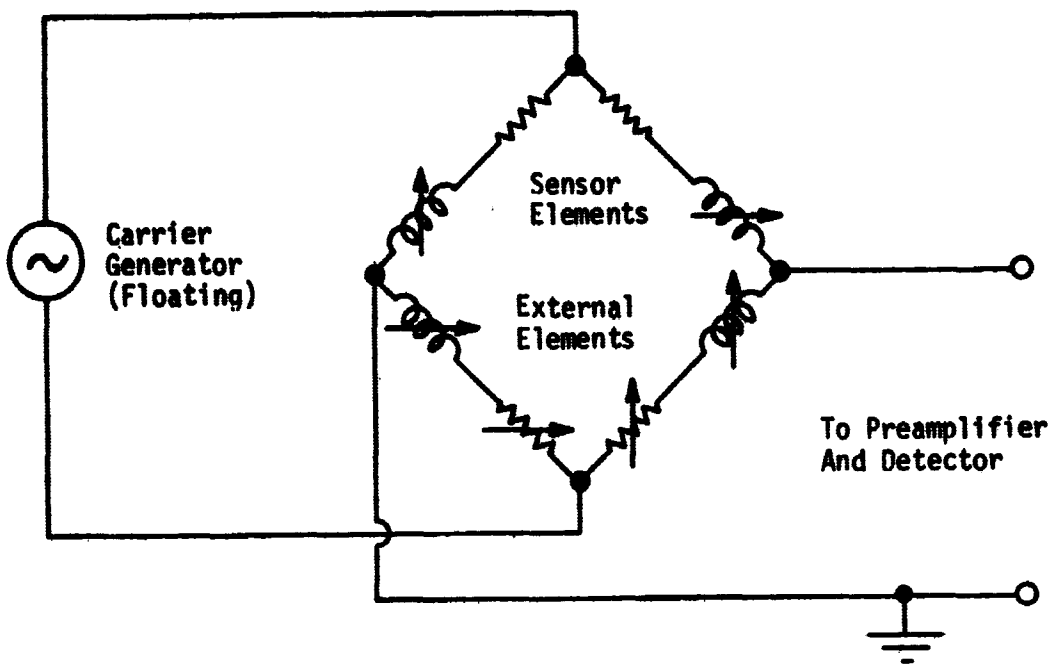

Figure 8. Cobalt Motor-Sensor: Sensor With External Bridge Elements

The schematic diagram of the electronics package given in the next section shows the associated sensor driving and detection circuits. The sensor bridge is driven by the output of a differential amplifier. This allows one side of the output of the bridge to be grounded. The output signal is amplified by a preamplifier with a gain of 1000 and passed through an adjustable phase shifter to the signal input of the phase detector. The reference input of the phase detector is driven by the output of one side of the differential amplifier through a gain 20 preamplifier. By deriving the reference from the signal that is actually driving the bridge (as opposed to using the output of the 20 kHz generator), the effects of phase and amplitude distortion by the bridge and driving amplifier are minimized.

The transfer characteristic of the sensor is given in Fig. 9 for two amplitudes of carrier generator voltage. This is the voltage measured at the output of the carrier generator as shown in the schematic. The dashed lines indicate the specified maximum steady-state angular displacement and the resultant output.

Control and Sensing Electronics

The electronics package for the sensor basically consists of four sections: carrier section, demodulator section, gain and compensation section, and the power amplifiers. The complete schematic is shown in Fig. 10 with the major sections outlined.

The carrier section consists of the 20 kHz sine wave generator (hp 651A), emitter follower buffer stage, and current source stabilized differential amplifier. The differential amplifier is provided with balance and bias level controls.

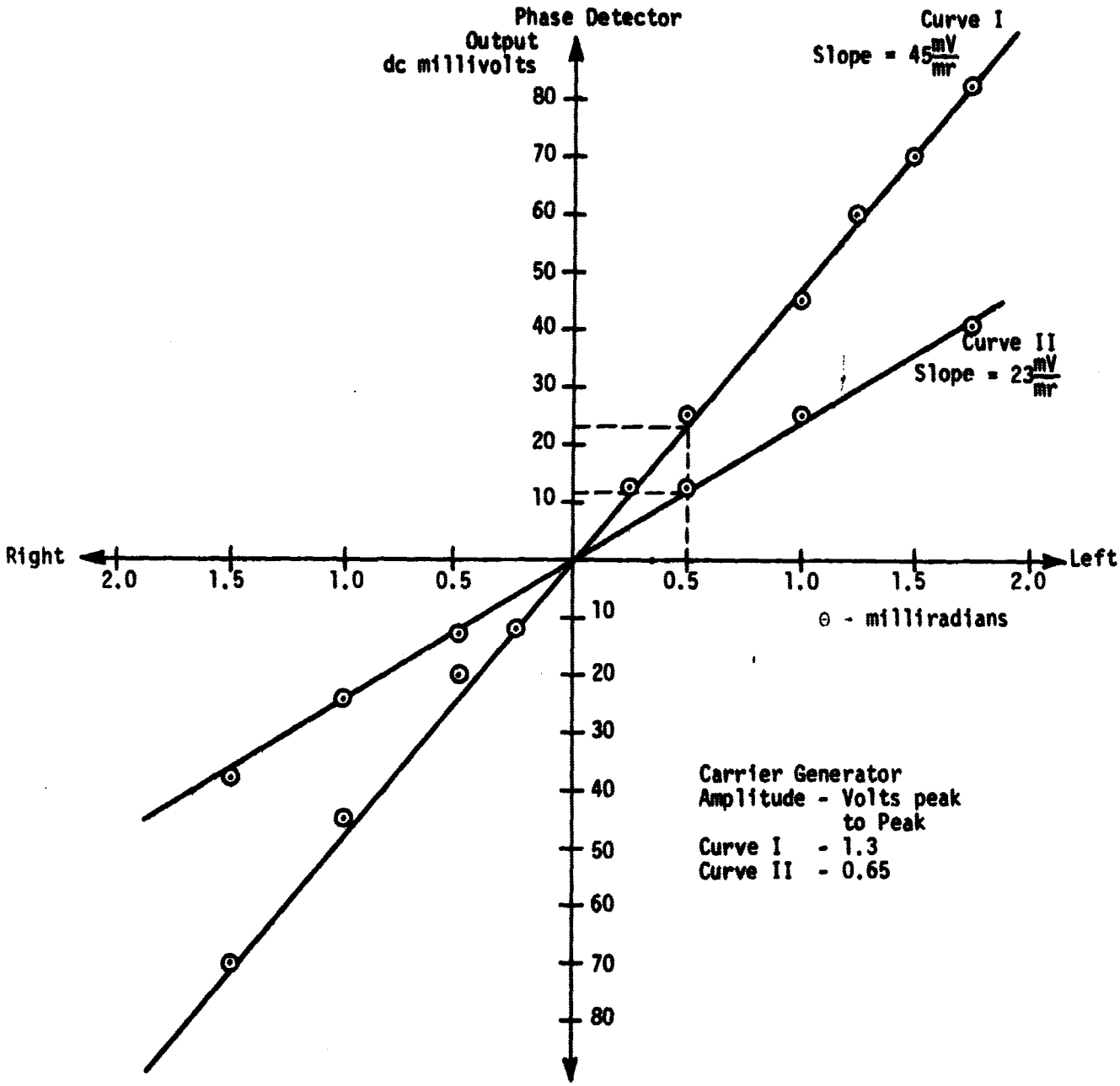

Figure 9. Cobalt Motor-Sensor: Sensor Transfer Characteristic

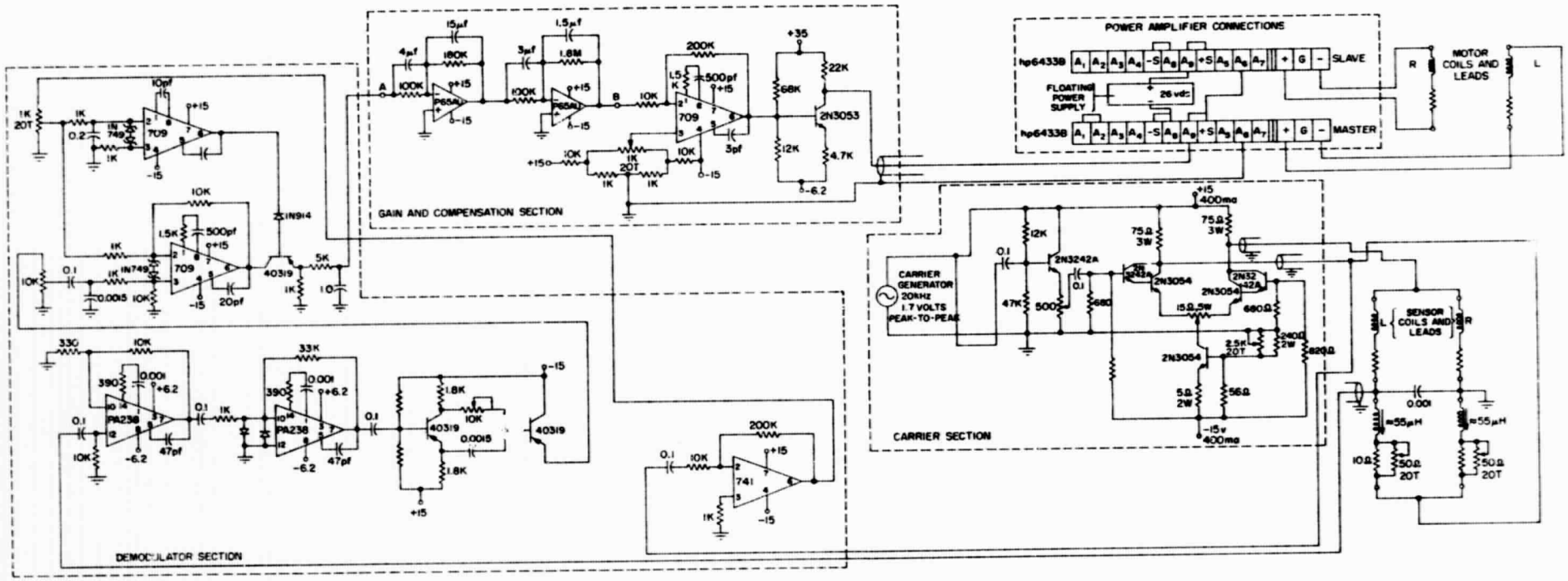

Figure 10. Cobalt Motor-Sensor: Electronic Schematic Diagram

The demodulator consists of a preamplifier with a gain of 1000, an adjustable unity gain phase shifter, an untuned phase detector, and a reference preamplifier. Adjustments are provided for signal level, phase and reference level.

The type of phase detector shown in the schematic was chosen for expediency and did not exhibit amplitude rejection as good as can be obtained. This caused a problem because changes in the carrier generator amplitude vary the null of the system. This phase detector should be replaced by a tuned phase detector.

The power amplifiers that have been used in all testing to date have been hp-Harrison 6433B dc power supplies connected in a master-slave configuration with the master remotely programmed by the amplified error signal. The programming connections are shown on the schematic. These power supplies are suitable as power amplifiers as long as relatively fast response is not necessary. The bias necessary to establish the quiescent motor current is provided by the single transistor output stage of the gain and compensation section.

The gain and compensation section embodies two stages of combined gain and frequency response shaping, a third stage of gain, and finally a stage providing gain and bias to set the quiescent current level. The total required voltage gain is dictated by the steady-state displacement specification and the sensor sensitivity of Fig. 9. The power amplifiers have unity voltage gain.

A plot of the uncompensated open-loop frequency response is shown in Fig. 11. This data was obtained with the power amplifiers described above, and it is believed that they primarily establish the frequency response although no data was taken to confirm this. The asymptotic approximation to a frequency

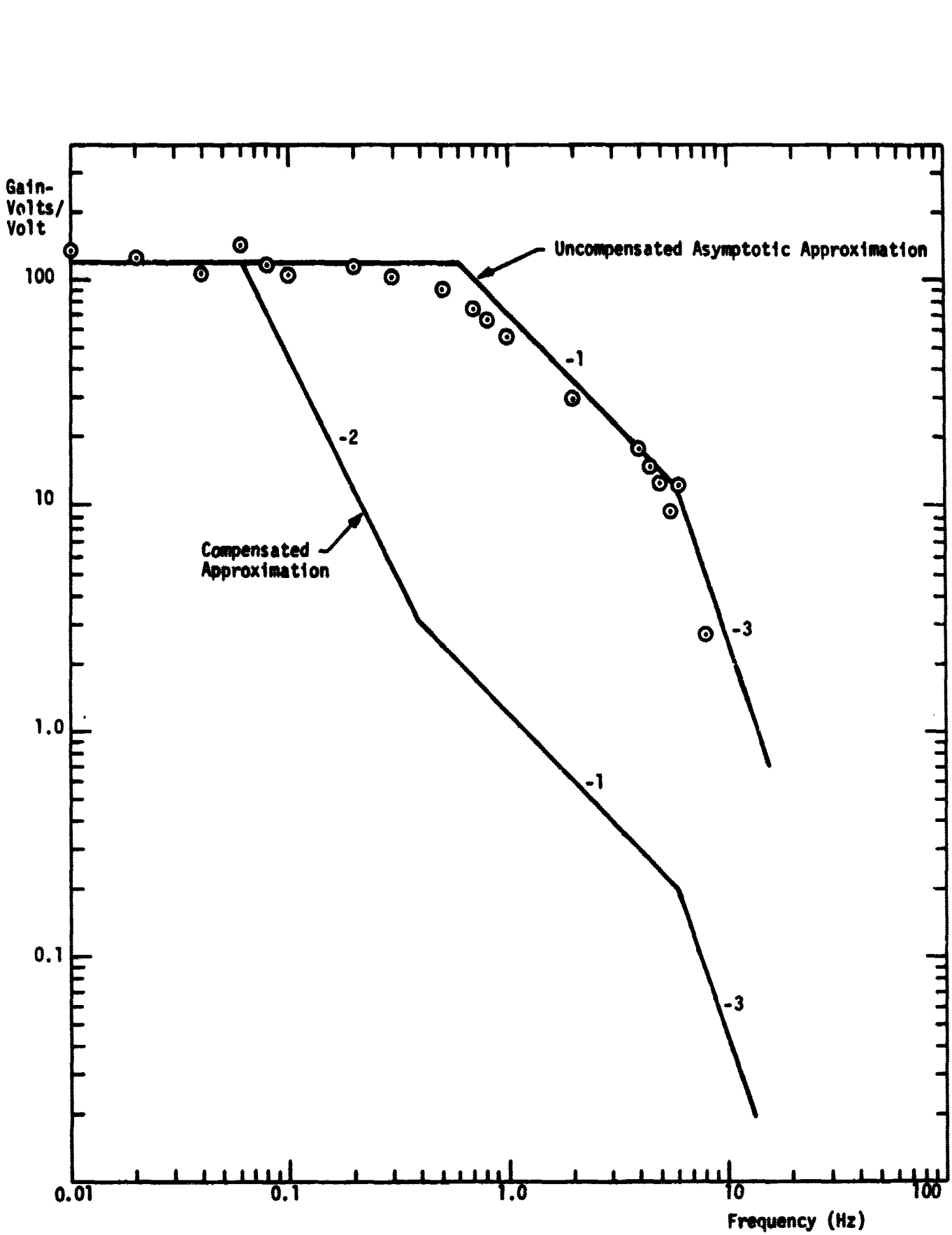

Figure 11. Cobalt Motor-Sensor: Frequency Response

response that will be stable is also shown in Fig. 11. This requires a compensator with a double pole at 0.06Hz, a zero at 0.4 Hz, and another zero at 0.6 Hz. The compensation shown in the schematic was inserted and stabilized the system.

Closed Loop Data

The cobalt skin friction sensor was operated closed loop with the prototype motor-sensor and electronics package. The results of the room temperature tests were encouraging, but extensive high temperature tests were not conducted for reasons to be discussed.

Calibration curves for two different values of quiescent motor current are shown in Fig. 12, and the corresponding values of steady-state deflection are shown in Fig. 13. The calibration curves exhibit good linearity and a maximum experimental deviation of less than 5%.

The experiments were conducted with a maximum applied force of 1400 milligrams (3.08) millipounds) which is slightly less than half the specified maximum force because of power amplifier limitations. This can be overcome by decreasing the motor air gap by a factor of $\sqrt{2}$ and retaining a quiescent current of 2.0 amperes. This would double the system gain and further decrease the steady-state displacement. Even with the 0.025 inch air gap and 2.0 ampere quiescent current, the steady-state displacement is within the specifications.

It has been previously mentioned that minimization of adverse temperature effects requires that all of the bridge elements of the sensor should be identically constructed and subjected to the same temperature environment.

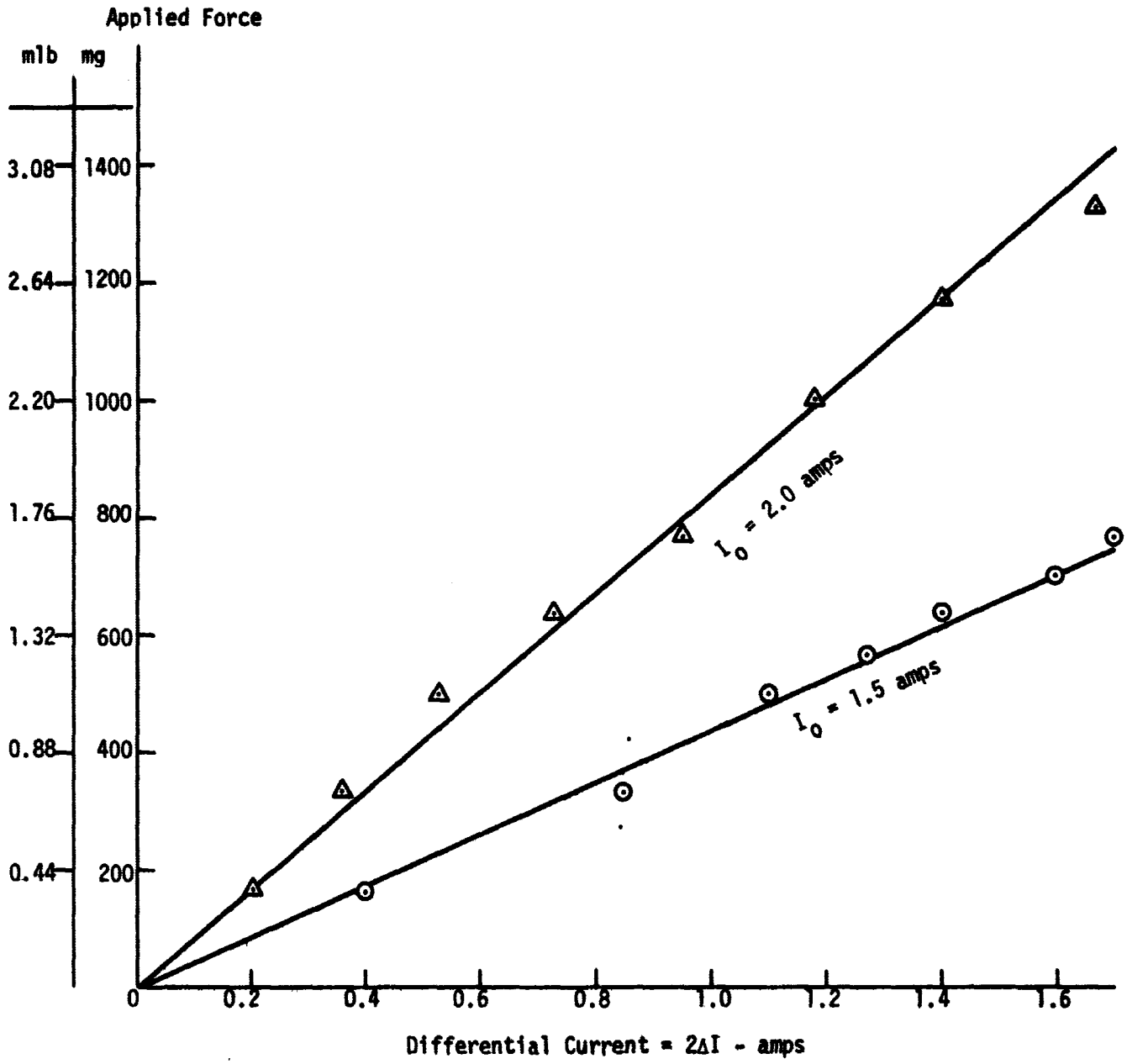

Figure 12. Cobalt Motor-Sensor: Room Temperature Calibration Data (Air Gap = 0.025 inch)

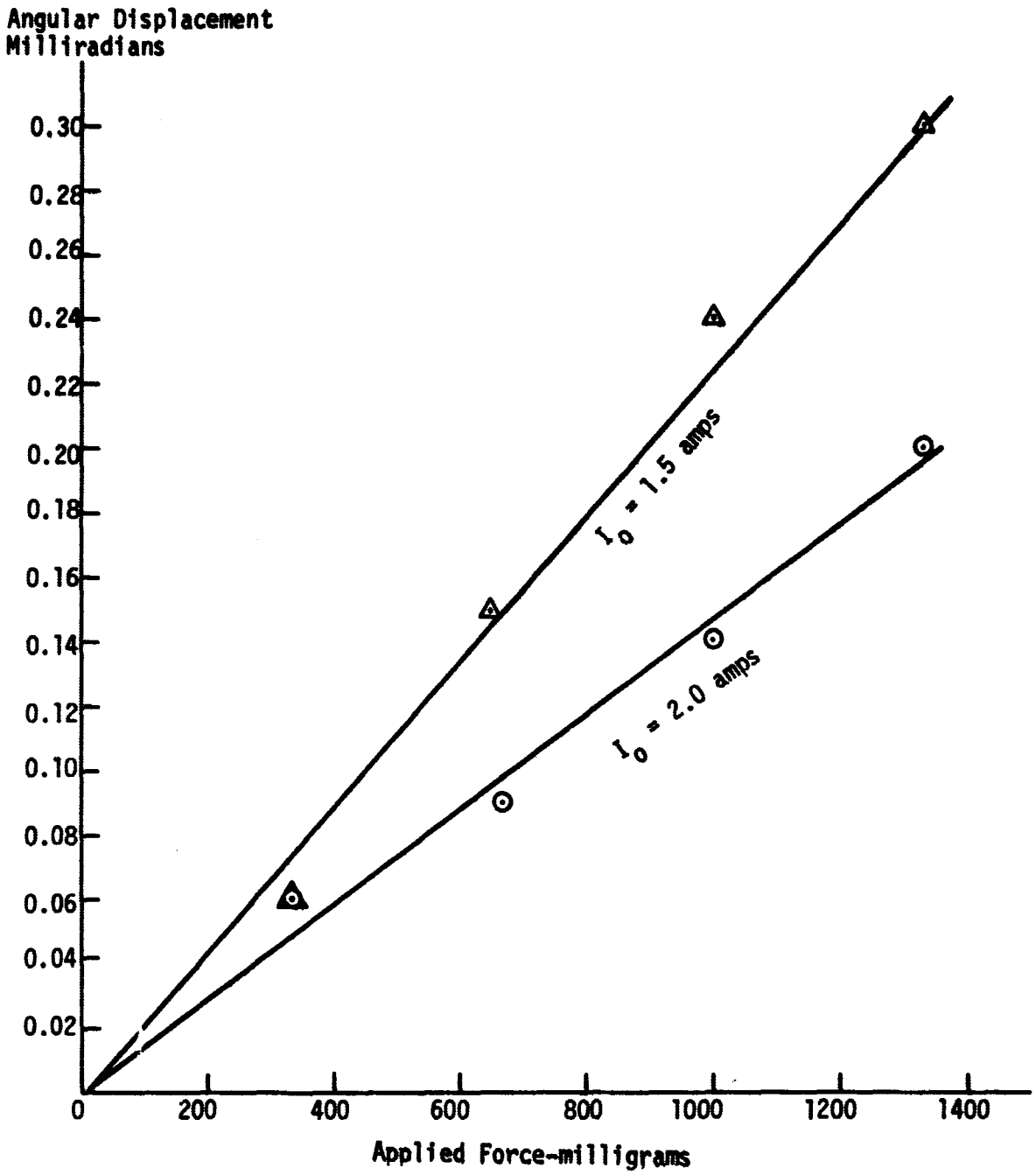

Figure 13. Cobalt Motor-Sensor: Steady-State Displacement Data at Room Temperature (Air Gap = 0.025 inch)

In the prototype this was not done in order to expedite obtaining closed-loop data. Therefore, when the motor-sensor structure was heated, the null shift was too large to obtain meaningful high temperature data.

Temperature Effects

The extreme temperature environment in which the skin friction sensor must operate creates several problems. In addition to the error caused by permeability change in the magnetic material of the stator and rotor, the following areas should be examined for the effects produced by the wide temperature variation:

1. Flexure spring constant and null position variation
2. Coil winding resistance variation
3. Structural dimensional variation.

Flexure spring constant and null position variations are still a subject of study and are considered in the flexure section of this report. It can be said, however, that the spring constant variations will have little effect on the operation of the cobalt motor-sensor as long as the inequalities given below Eqs. (9) and (11) continue to be satisfied.

The effects of changes in the coil winding resistances can be held within acceptable limits with proper electronic package design. The motor force constant is proportional to differential current, and the calibration of the instrument can be maintained if the power amplifiers are good voltage to current transducers rather than just power amplifiers. Furthermore resistance change effects on the sensor can be minimized by using the configuration proposed in the next section.

Structural dimensional changes probably produce the most significant errors except those introduced by permeability changes. Linear and volumetric expansion of the core and pole material will produce changes in the gap and area of the motor and sensor. Operation of the motor-sensor in the configuration of the next section will tend to minimize the sensor errors, but the motor force constant will be changed. Furthermore, there is a discontinuity in the magnitude of the error when the structure of the metal changes from hexagonal close-packed to face centered cubic at a temperature in the range of 752 to 842°F (400-450°C). The coefficient of linear expansion for temperatures below the transition is 12.6×10^{-6}/°C and for the higher temperatures is 14.2×10^{-6}/°C [R. S. Young, COBALT, Its Chemistry, Metallurgy, and Uses, Reinhold Publishing Corp., New York (1960).] Even within the two ranges (below and above the transition), the coefficients are weak functions of temperature.

Some idea of the change in the motor constant can be obtained by assuming a "worst case" in which all of the expansion of the poles is in the direction of decreasing gap. Over the range of room temperature to 2000°F (1092°C), each gap will change by almost 0.009 inch or from 0.025 to 0.016 inch. The motor force constant is inversely proportional to the square of the gap, and for this temperature range, the motor constant increases by a factor of 2.75. The force readout can be calibrated to read the correct force despite this change if the motor temperature is monitored.

This discussion points out the necessity for very careful design of the high temperature version. It should be possible to mount and constrain the pole pieces within the structure such that their expansion will be fully or partially offset by expansion of the structure. The expansion of the core itself would remain, but for the previous range, this amounts to only a 0.002 inch change in each gap.

Suggested Improvements for the Cobalt Motor-Sensor

The motor force constant for a given cobalt skin friction sensor can be doubled and the temperature characteristics and sensitivity of the sensor can be significantly improved by operating the same motor-sensor assembly in a somewhat different configuration. This configuration is shown schematically in Fig. 14. In this figure L_1 & R_1, L_2 & R_2, L_3 & R_3, and L_4 & R_4 represent the four coils of the motor-sensor, and L_5 through L_{10} are external chokes added to decouple the high frequency carrier path from the low frequency motor path. The capacitors are for dc blocking.

The motor force constant is doubled in this configuration because the torque on the rotor is produced by an opposing coil pair on the top and an opposing coil pair on the bottom. In order to accomplish this, diagonally opposite coils are driven in series or parallel by the same amplifier while the other diagonal pair is driven in series or parallel by the other amplifier.

In this configuration the sensor consists of a bridge formed by the four coils with appropriate decoupling elements to prevent the power amplifiers from affecting the bridge. If the force on the test section moves the section to the right, the inductances of the top right and bottom left coils increase, and the inductances of the top left and bottom right coils decrease. This change will unbalance the bridge, and the signal can be phase or amplitude detected as before. However, in this case, the sensitivity should double because all four elements of the bridge are changing. Furthermore, changes of inductance caused by temperature variations should be minimized by the self-compensating nature of the bridge because all four coils are identical and are subjected to the same temperature environment.

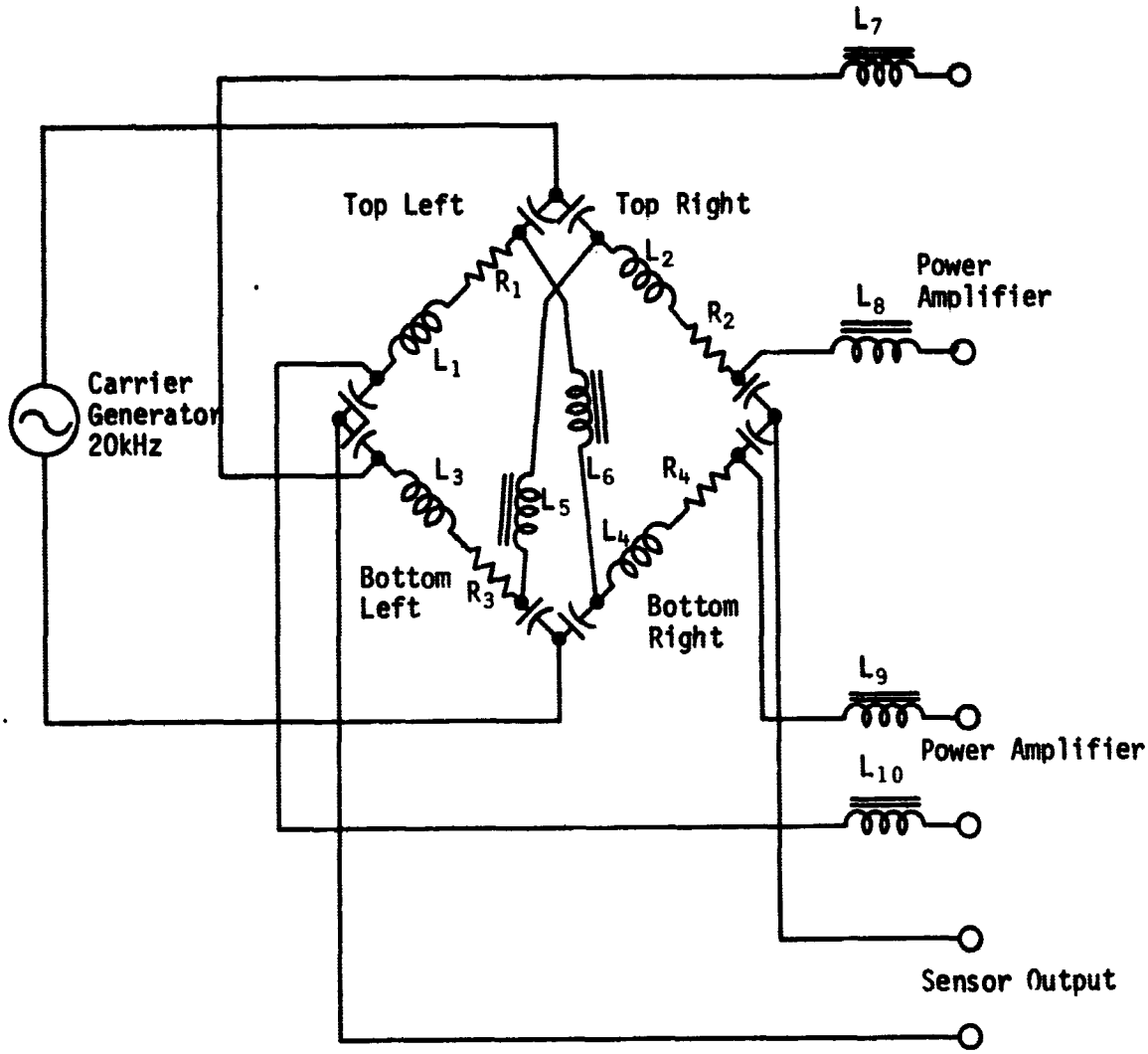

Figure 14. Cobalt Motor-Sensor: Proposed Improved Method of Operation

This method of operation of the skin friction sensor requires the addition of the chokes and they must be rated to carry the full motor current of a few amps. This makes the external electronics package significantly heavier, and this might limit the applicability of this configuration in some cases.

Conclusions

The data and developments that have been presented in this chapter indicate that the cobalt motor-sensor approach could be developed to produce an instrument which would be useful over the temperature range from near absolute zero to approximately 1750°F (954°C). In order to extend its operation to cover this range, the motor-sensor structure and the electronics package would have to be modified as discussed in the previous section.

It was stated in Chapter I that the cobalt motor-sensor approach to the skin friction measurement problem was started one year behind the other electrical approach and that it has remained approximately one year behind. This is the primary reason for discontinuing this approach.

CHAPTER III

PNEUMATIC SYSTEM

A high temperature breadboard model has been built and tested to 2000°F. Figure 15 contains a picture of the breadboard model. The picture was taken after the high temperature test. Figures 16 and 17 show the schematic and block diagrams of the system respectively.

The complete experimental setup is shown in Figs.18 and 19. A Bendix 5/8 inch diameter flexure is used as the frictionless pivot for the force applicator. The sting is made from lava and a metal spear head is attached to the end of the lava sting by a high temperature ceramic adhesive Ceramabond 503. In order to reduce the stiction between the sting and the flapper arm, sonic vibrations were applied to the force applicator by a speaker. Reduction of the stiction to a negligible amount was possible.

Data were taken at seven temperatures (75,400,800,1200,1500,1800, and 2000°F). For each temperature three sets of open loop data (data on pneumatic damper alone) for different damper supply pressures (P_o = 5, 8, and 12 psig) were obtained. Three sets of closed loop data were obtained by changing the flapper-nozzle valves supply pressures ($P_1 = P_1' = 5$, 10, and 15 psig). The damper supply pressure P_o for the closed loop test was a constant of 8 Psig.

Data on Pneumatic Damper

Taking the applied torque, τ, as the input and the angular deflection of the flexure flapper, θ, as the output, the experimental results can be plotted as a family of curves with respect to temperature for a constant supply

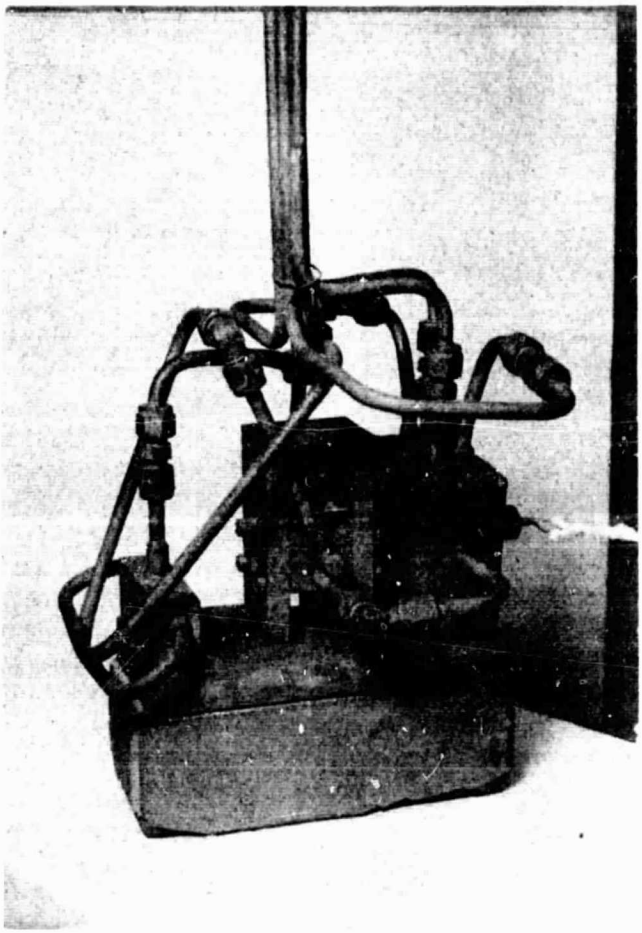

Figure 15. Pneumatic System: Breadboard Model of The Skin-Friction Meter After High Temperature Testing

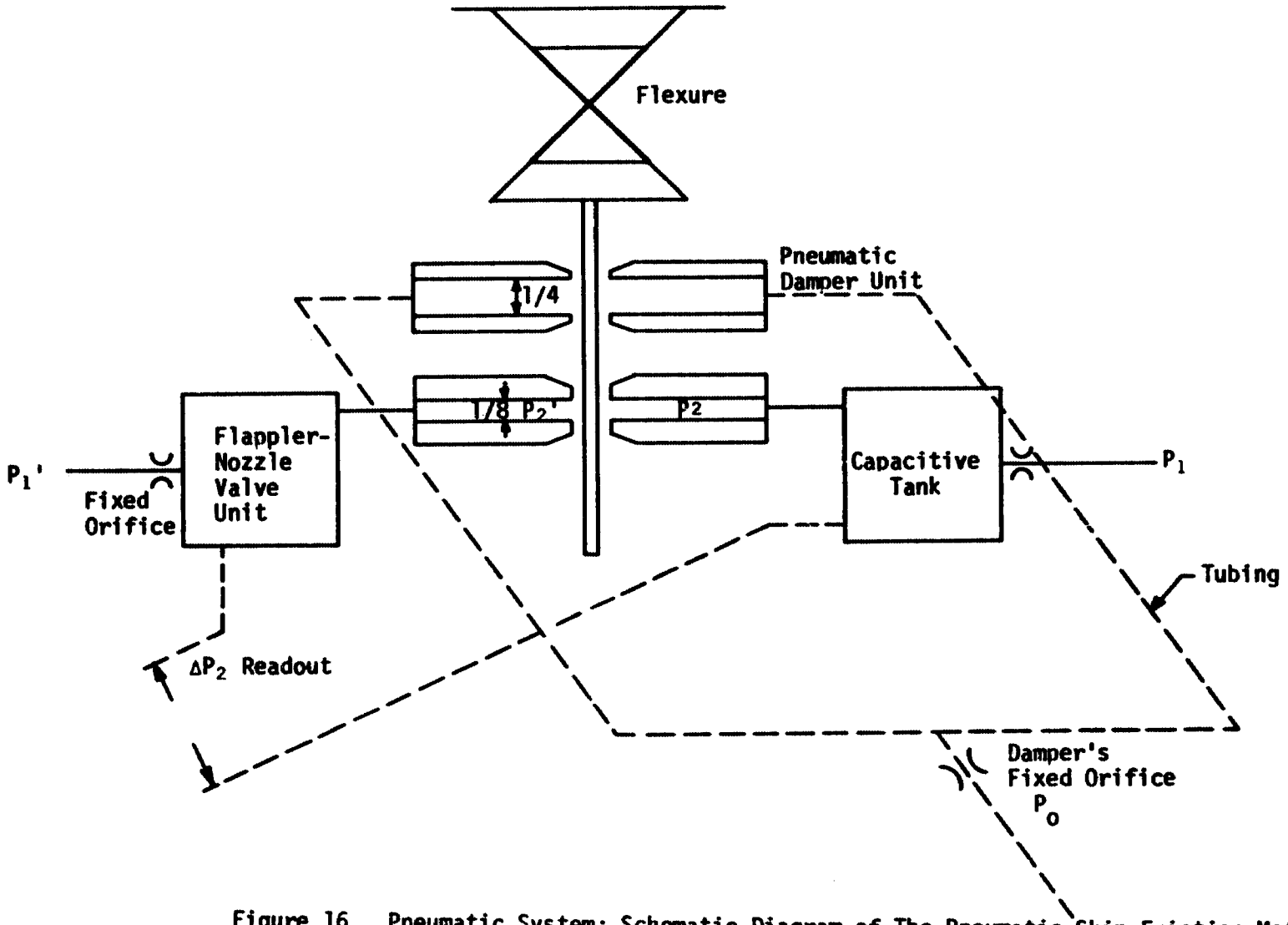

Figure 16. Pneumatic System: Schematic Diagram of The Pneumatic Skin-Friction Meter

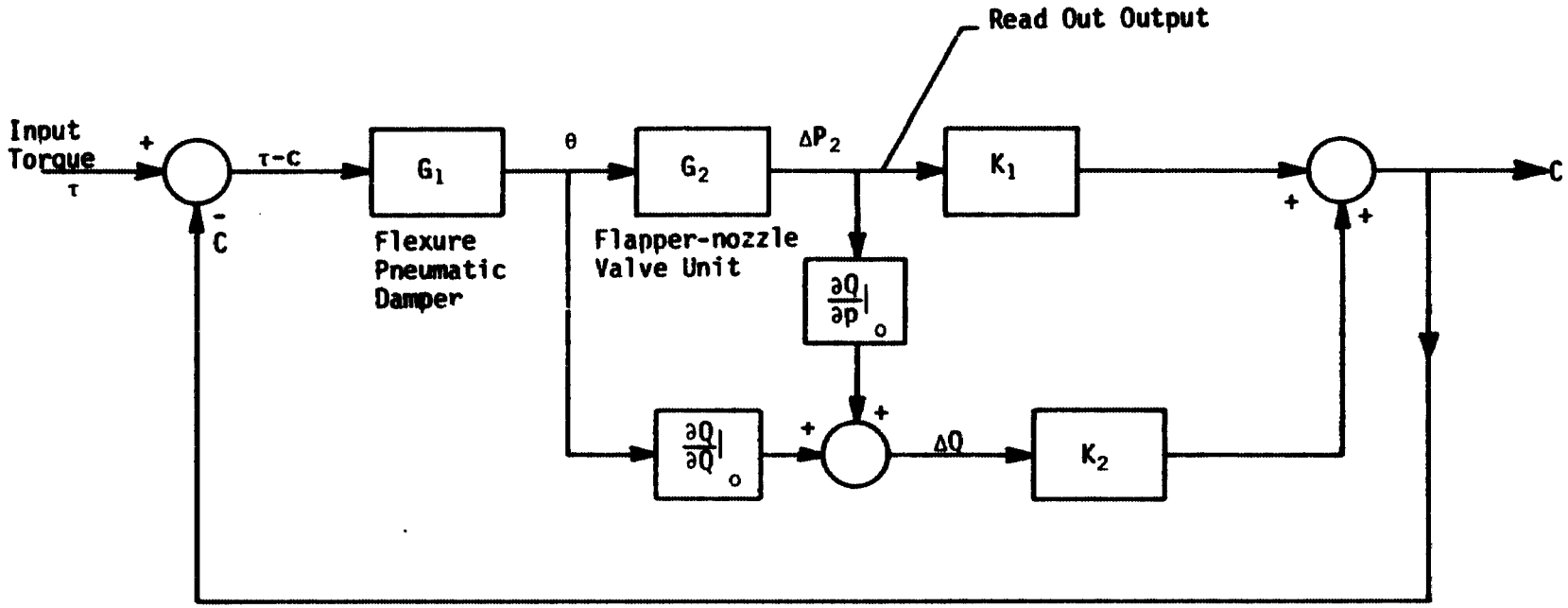

Figure 17. Pneumatic System: Block Diagram

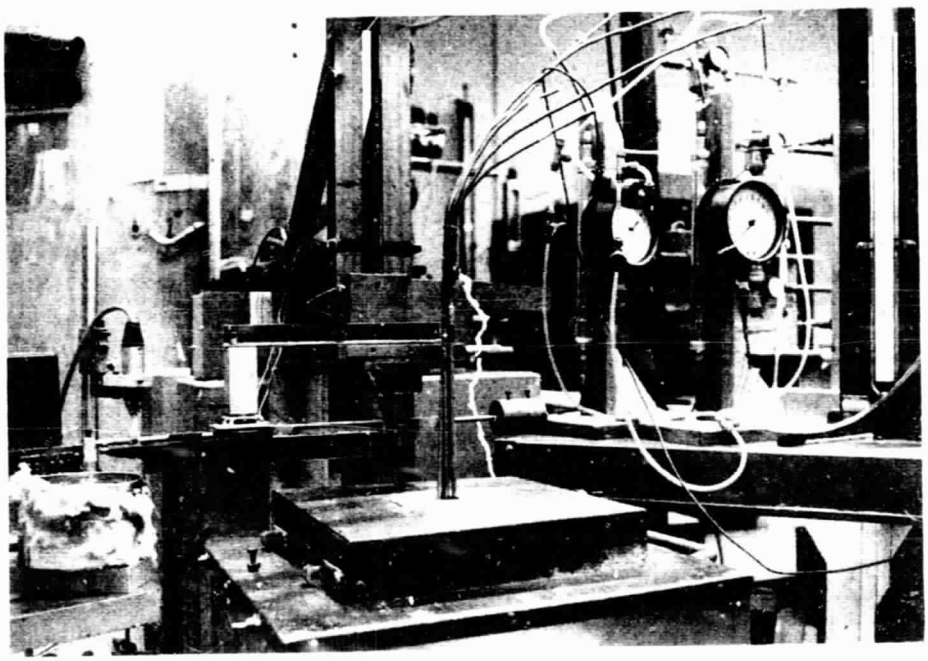

Figure 18. Pneumatic System: High Temperature Experiment Setup

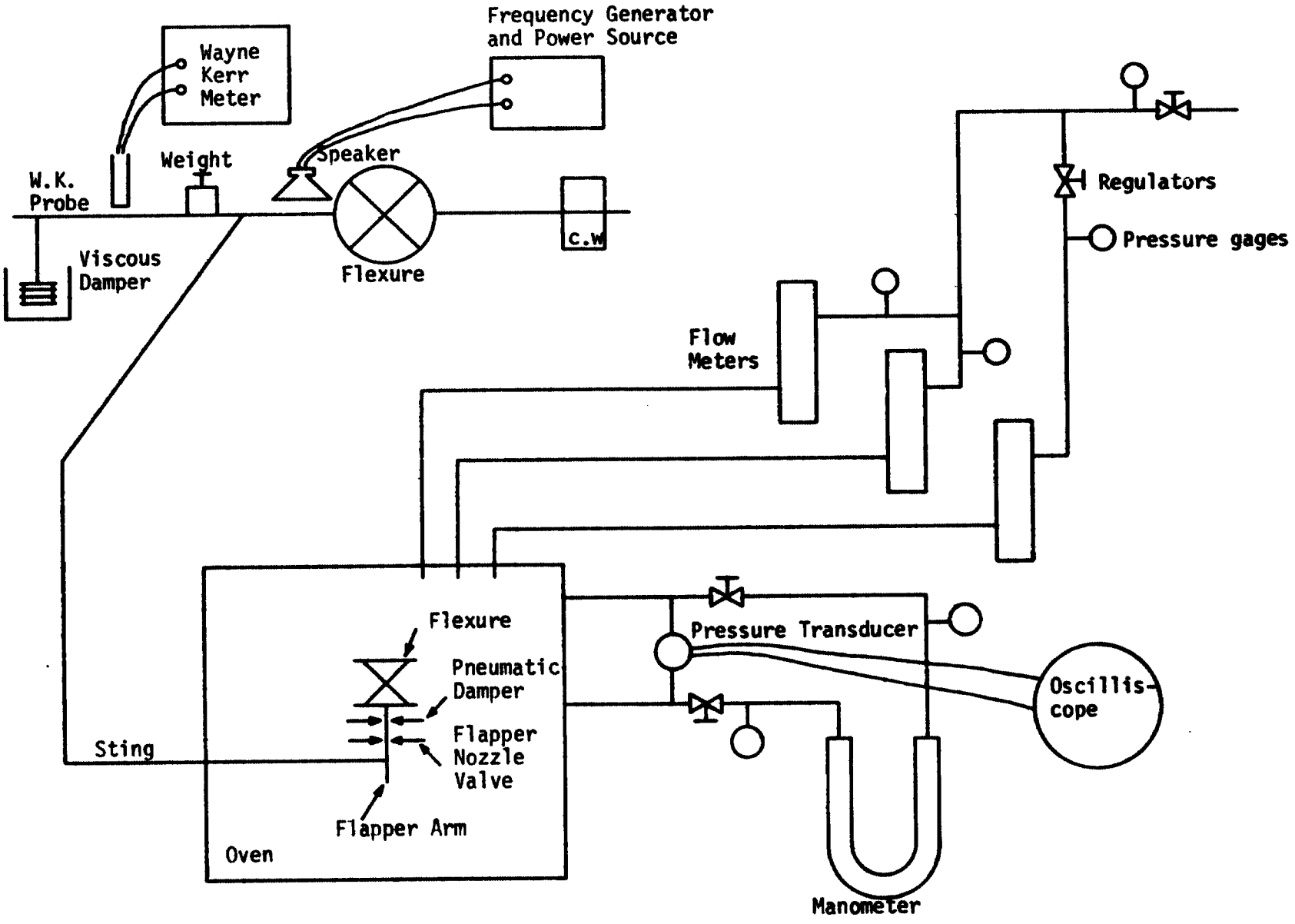

Figure 19. Pneumatic System: Schematic Diagram of the High Temperature Experiment Setup

pressure P_o. Figure 20 shows the load versus deflection relation for a damper supply pressure of 8 psig. It is interesting to note that the relation between input and output is nearly linear. A least square straight line fit is used, which shows that all the data points are within 6% error* of the straight line. The value τ/θ decreases with temperature. This is predicted by the theory. Table I summarizes the straight line load and deflection relations for all the tested data.

Closed Loop Data

Three different supply pressures for the two identical flapper-nozzle valves were used: 5, 10, and 15 psig. As mentioned before, the damper supply pressure is 8 psig for all the closed loop experiments. Figures 21 and 22 show the relation between input torque and angular deflection, θ, for room temperature and 2000°F respectively. Three important points should be noted. First, if the test element is mounted on an arm having an effective radius of one inch (from the surface of the floating element to the rotation center) and a one inch square surface area is assumed, the angular displacement is limited to 0.5×10^{-3} rad for the full load of 7×10^{-3} in-lb. It is shown in Figs.21 and 22 that all the closed loop data meet this specification. Second, temperature has a definite effect on the system gain. This is partially due to the gain increase of the air damper for higher temperatures and partially due to the static characteristic of the flapper-nozzle valve unit. The temperature effects will be discussed further in the following section. Third, with only a few exceptions the data can be considered to be linear. The straight line representations were

*error is defined as $\left|\frac{\text{actual value - desired value}}{\text{desired value}}\right|$

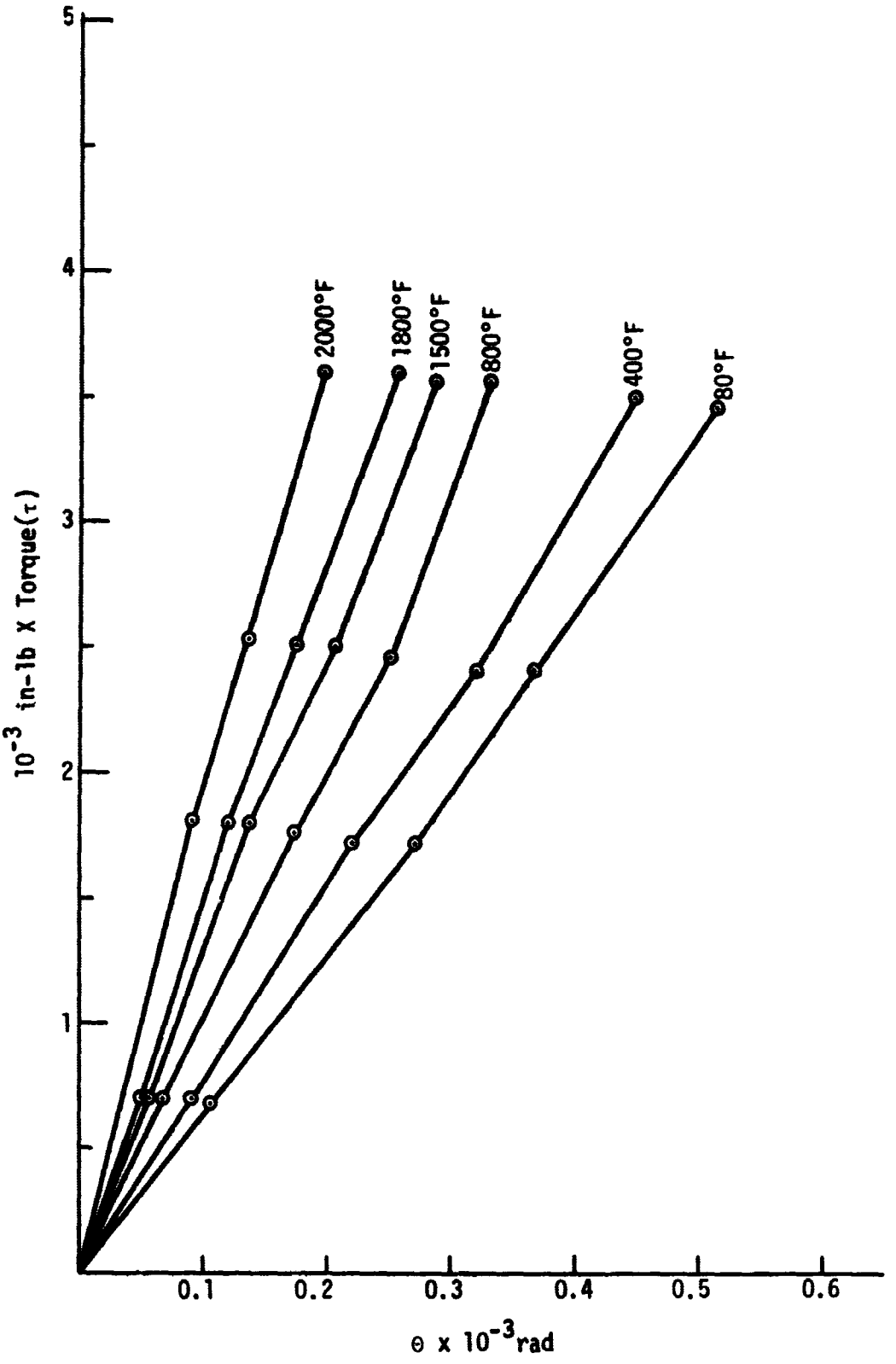

Figure 20. Pneumatic System: Load Versus Deflection Relation for a Pneumatic Damper With P_0 = 8 psig

P_o / Temperature	5 psig	8 psig	12 psig
75°F	$\frac{\tau}{\theta}$ = 4.603 $\frac{\text{in-lb}}{\text{rad.}}$	6.614	9.522
400°F	5.896	7.959	11.148
800°F	6.765	10.454	13.478
1200°F	8.612	10.823	13.929
1500°F	9.239	12.313	15.776
1800°F	10.983	14.266	19.432
2000°F	13.461	19.251	23.545

TABLE I

Pneumatic System: Slopes of the Load and Deflection Relation for Different Supply Pressure P_o and Temperatures

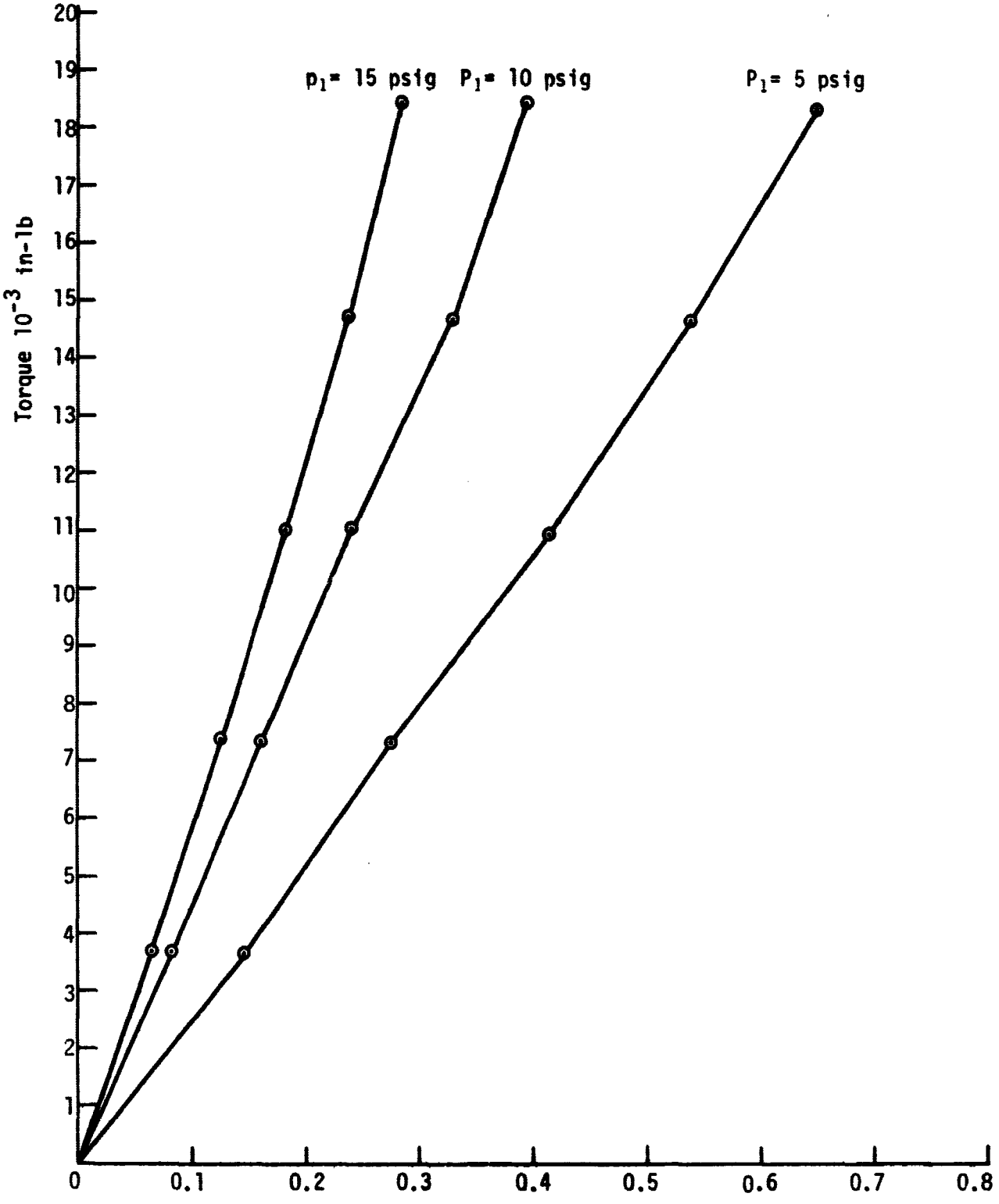

Figure 21. Pneumatic System: Load Versus Deflection Relation for the Closed Loop System at Room Temperature

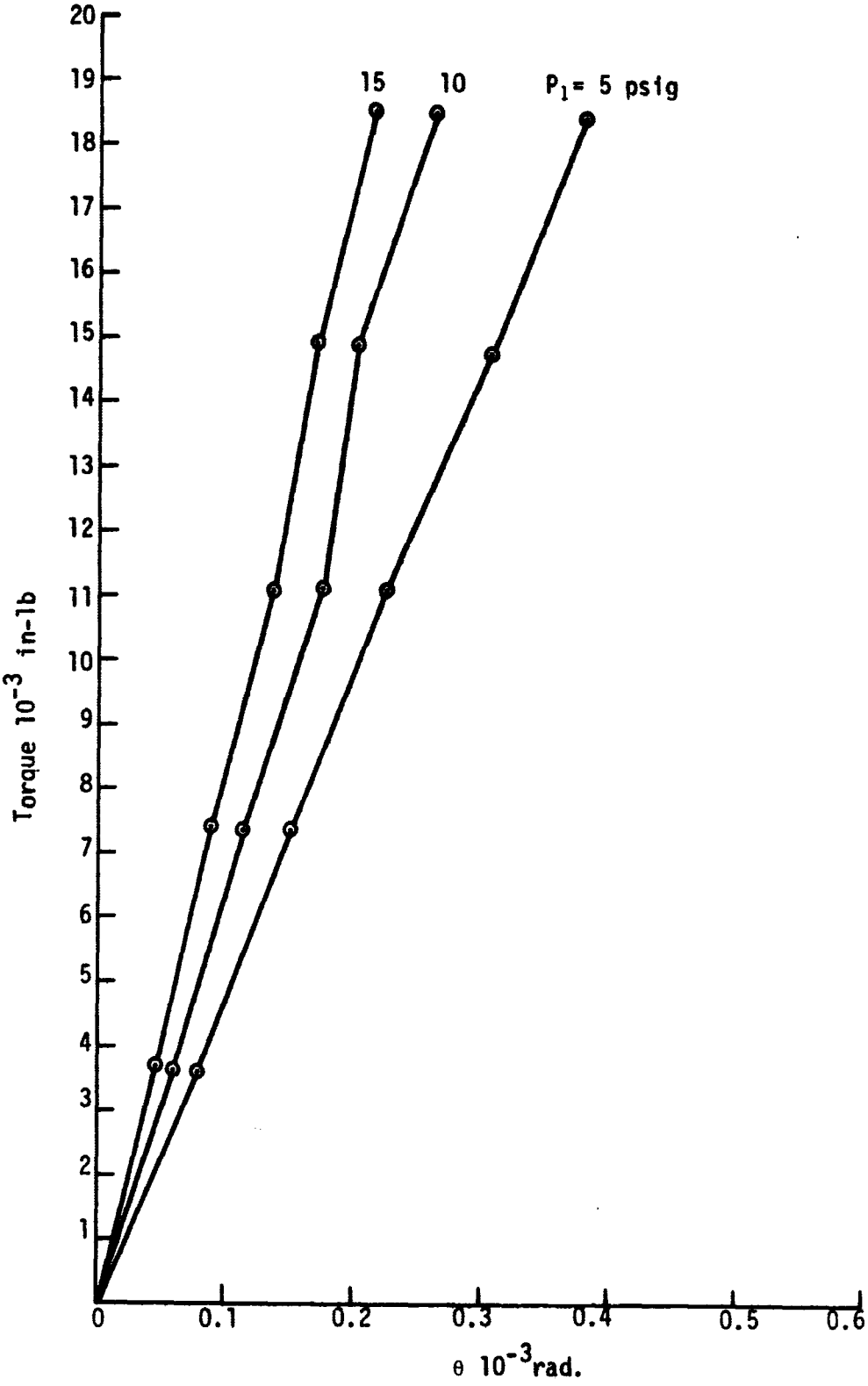

Figure 22. Pneumatic System: Load Versus Deflection Relation for the Closed Loop System at 2000°F

obtained by a least squares fit. The slopes of the lines are shown in Table II.

The output of this breadboard model is the differential pressure ΔP_2 from the flapper-nozzle valve unit. Figures 23 and 24 show the relation between input torque and differential pressure for room temperature and 2000°F respectively. Since applied torque is the actual input and differential pressure from the flapper-nozzle valves is the actual output, the relations shown in Figs. 23 and 24 serve as calibration curves for the system. Again, linear least square curve fitting is employed. The slopes are shown in Table III.

Temperature Effects

Temperature effects can be emphasized by plotting the straight line slopes of the torque versus ΔP_2 relation as shown in Fig. 25 and torque versus θ relation as shown in Fig. 26 , in which both open loop and closed loop data are included.

Conclusions

All the vital parts of the breadboard model system are made of RA 330 stainless steel while all the tubing and fittings are made of 316 stainless steel. The breadboard model system has been tested to 2000°F. After the system cooled little oxidation showed on the RA 330 stainless steel but some oxidation was on the tubing. It was not possible to take data from 2000°F back to room temperature because some oxide clogged the jets. It is believed that the oxide was from the 316 stainless steel tubing.

$P_1 = P_1'$ / Temperature	5 psig	10 psig	15 psig
75°F	$\frac{T}{\theta} = 28.10 \frac{\text{in-lb}}{\text{rad.}}$	46.42	63.80
400°F	30.47	44.80	64.05
800°F	35.35	53.18	74.58
1200°F	38.45	50.33	71.99
1500°F	38.45	55.35	78.35
1800°F	43.92	64.95	80.50
2000°F	48.52	69.52	85.20

TABLE II

Pneumatic System: Slopes of the Load and Deflection Relation of the Closed Loop System for Different Supply Pressures P_1 and Temperatures

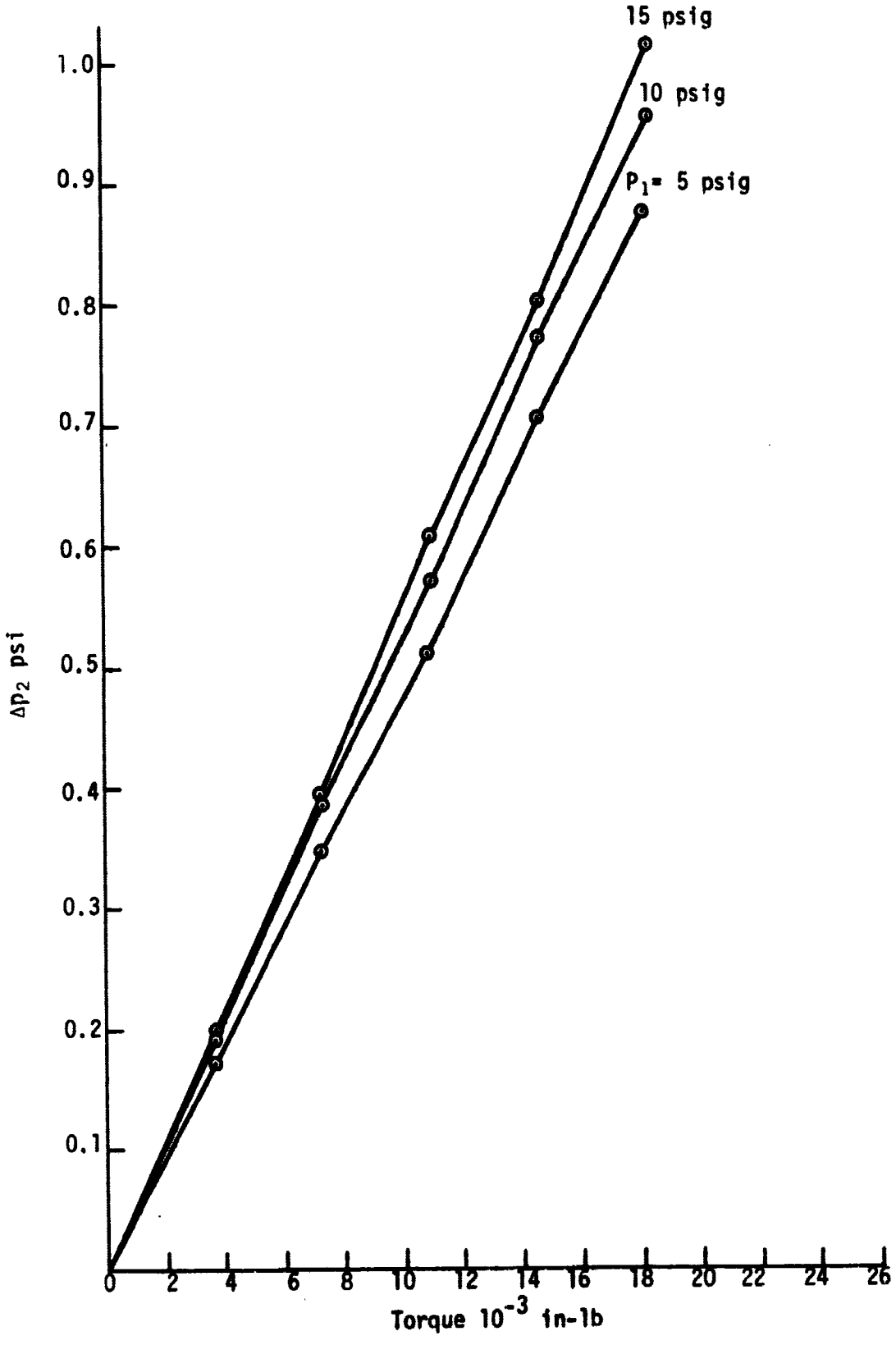

Figure 23. Pneumatic System: P_o Load Versus Differential Pressure ΔP_2 for the Closed Loop System at Room Temperature

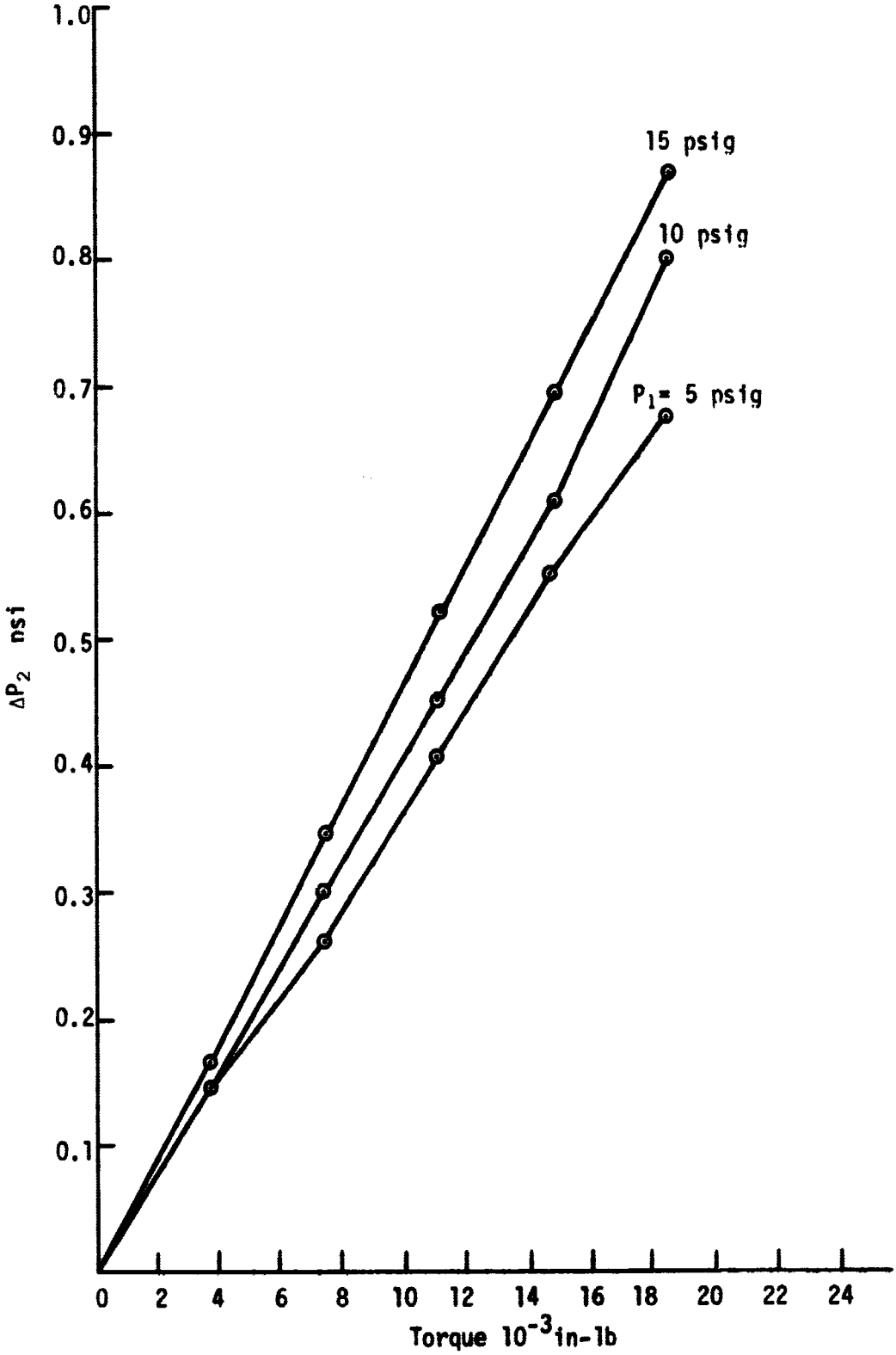

Figure 24. Pneumatic System: Load Versus Differential Pressure ΔP_2 for the Closed Loop System at 2000°F

$P_1=P_1'$ / Temperature	5 psig	10 psig	15 psig
75°F	$\frac{\Delta P_2}{\tau} = 48.18 \frac{psi}{in\text{-}lb}$	52.19	54.52
400°F	45.88	51.51	52.76
800°F	43.12	49.07	52.45
1200°F	42.09	49.47	51.31
1500°F	41.15	48.33	49.39
1800°F	39.17	45.07	47.22
2000°F	36.56	42.06	46.19

TABLE III

Pneumatic System: Slopes of the ΔP_2 and Load Relation of the Closed Loop System for Different Supply Pressures P_1 and Temperatures

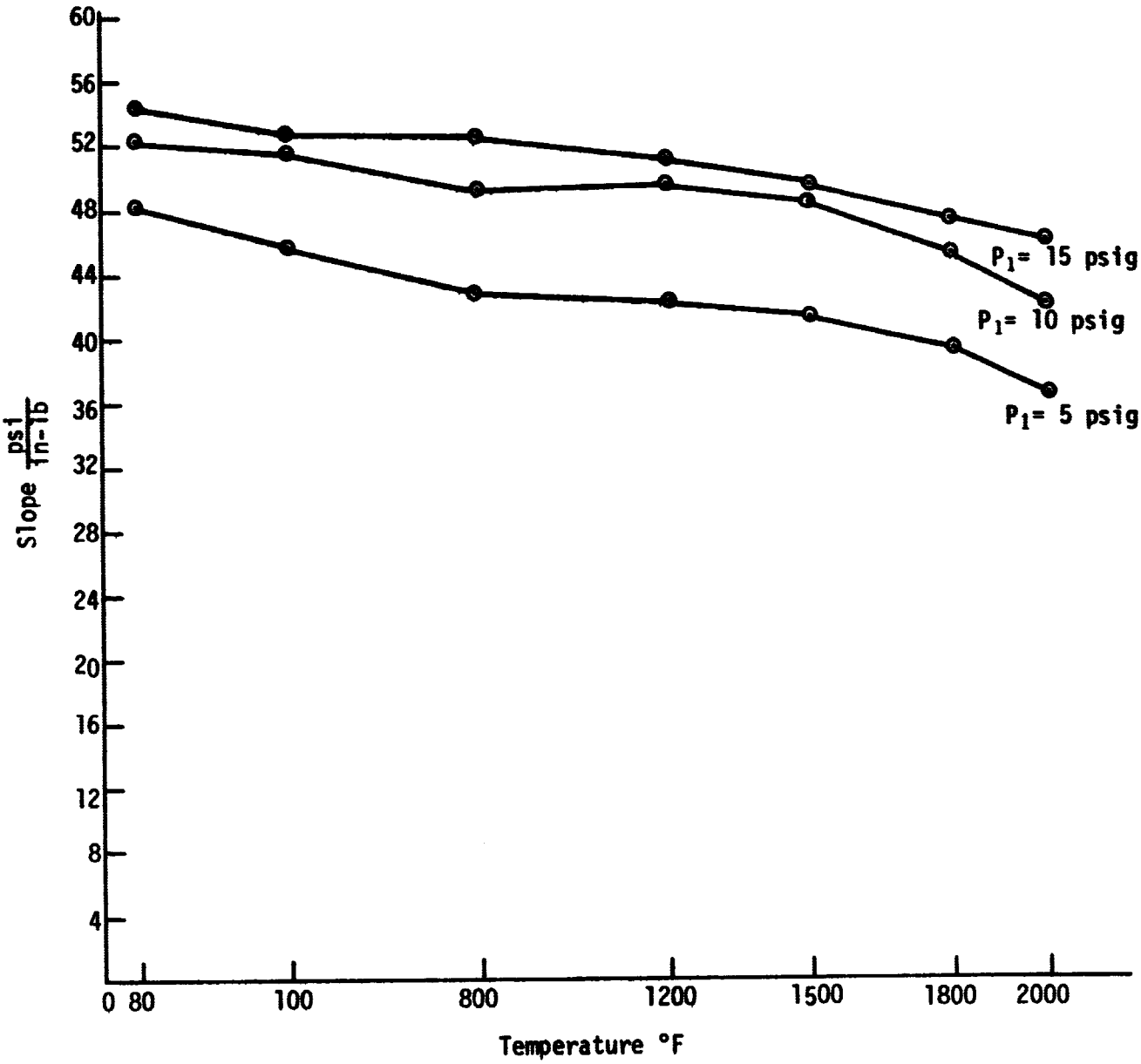

Figure 25. Pneumatic System: Input-Output Variation Due to Temperature

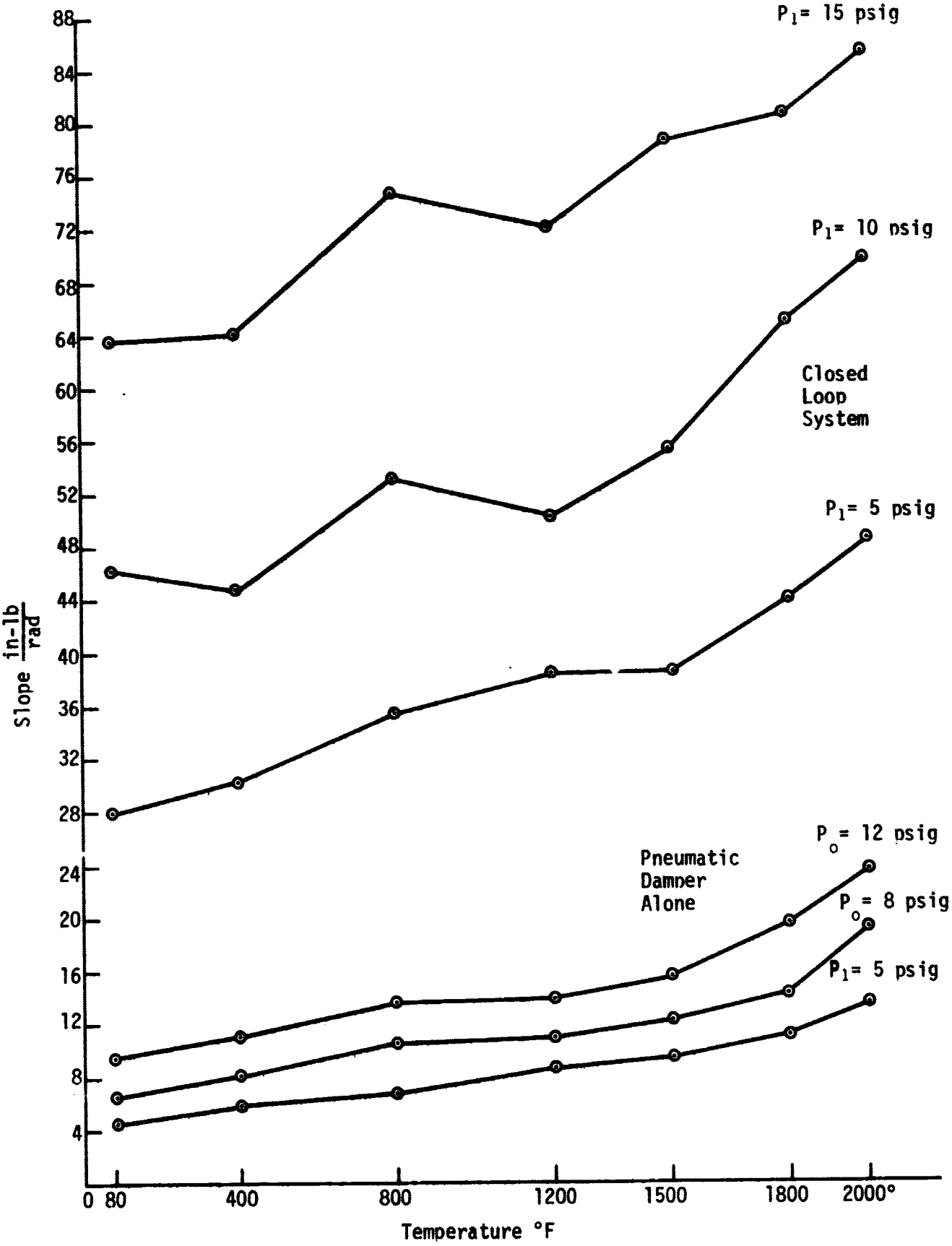

Figure 26. Pneumatic System: Input-Displacement Due to Temperature

Based on the high temperature experimental results and previous research, development of a skin-friction meter which will work in temperatures to 2000°F appears to be practical.

CHAPTER IV

HIGH TEMPERATURE PROPORTIONAL FLUIDIC AMPLIFIER

The vented jet proportional amplifier shown in Fig.27 is being developed to use in the fluidic system. It has been tested at 2000°F. It is made of RA 330 stainless steel (AMS 5592) produced by Rolley Alloy, Inc. Tests performed after cooling indicated that groove dimensions were not affected by corrosion. Most of the corrosion was found in the 316 stainless steel pipes and unions.

Dimensions of channels and the angle between the two output ports were limited by the facilities available for machining. For the same reason it was necessary to make the center dump. In order to avoid any internal or external leakage, both plates were lapped and brazed together. A vacuum oven at NASA Langley Field was used for this purpose.

Supply flow was measured at different temperatures and Fig. 28 shows its variation.

Static response normalized data is presented in Figs. 29 to 34 . From these data it is not possible to predict accurately the output characteristics for other temperatures than those given. Input characteristics are much more predictable.

From the amplifier gain, Figs. 35 to 39 , it is apparent that the gain was affected by temperature, varying from 5.18 at 70°F down to 2.90 at 2000°F. An explanation for this decrease in gain is available from Fig. 40 . It shows how the output load decreases as temperature increases.

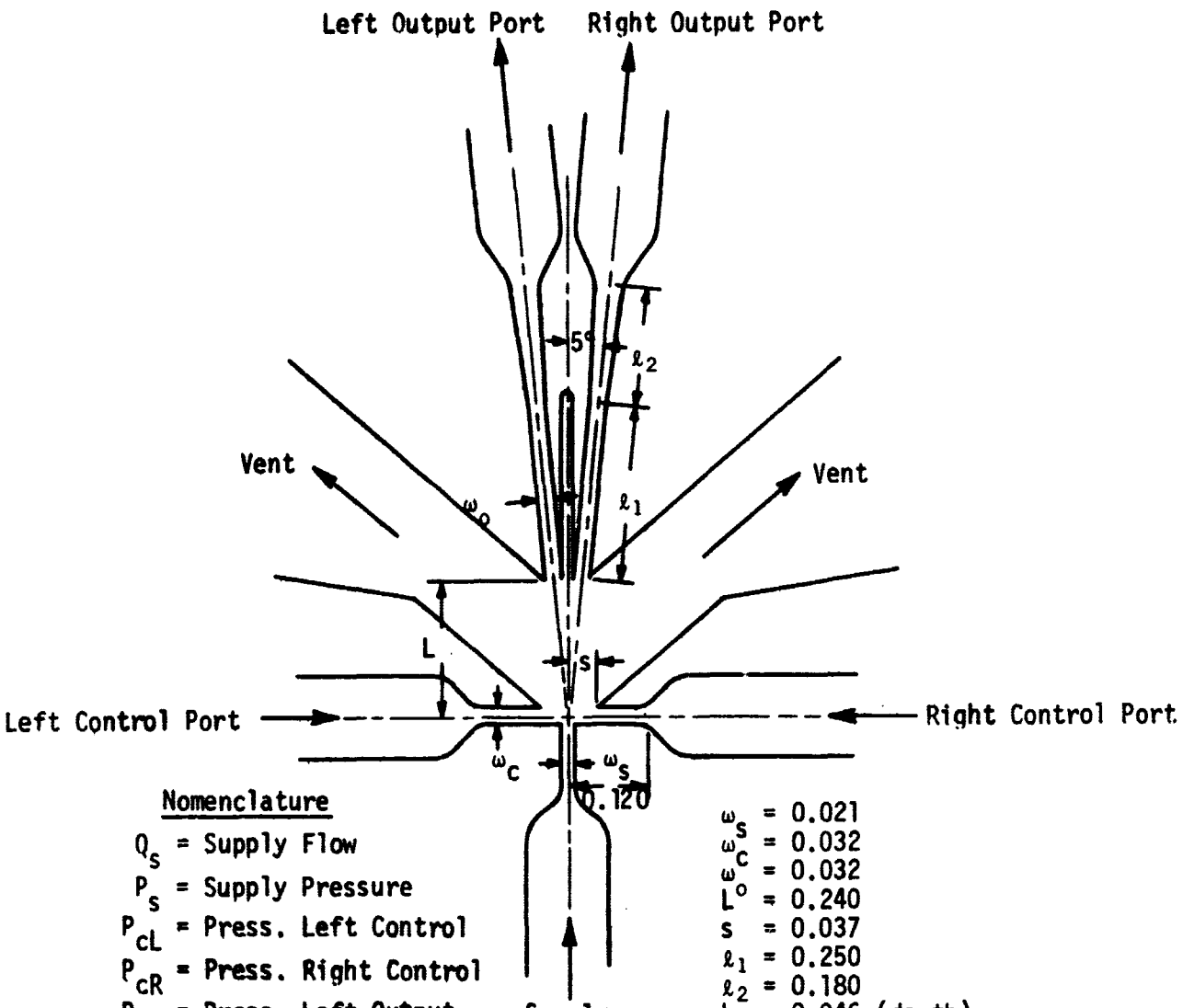

Nomenclature

Q_s = Supply Flow
P_s = Supply Pressure
P_{cL} = Press. Left Control
P_{cR} = Press. Right Control
P_{oL} = Press. Left Output
P_{oR} = Press. Right Output
Q_{cL} = Flow Left Control
Q_{cR} = Flow Right Control
Q_{oL} = Flow Left Output
Q_{oR} = Flow Right Output
$\Delta P_c = P_{cL} - P_{cR}$

ω_s = 0.021
ω_c = 0.032
ω_o = 0.032
L^o = 0.240
s = 0.037
ℓ_1 = 0.250
ℓ_2 = 0.180
h = 0.046 (depth)

Aspect ratio = $\frac{h}{\omega_s}$ = 2.19

Figure 27. Fluidic Amplifier: Schematic

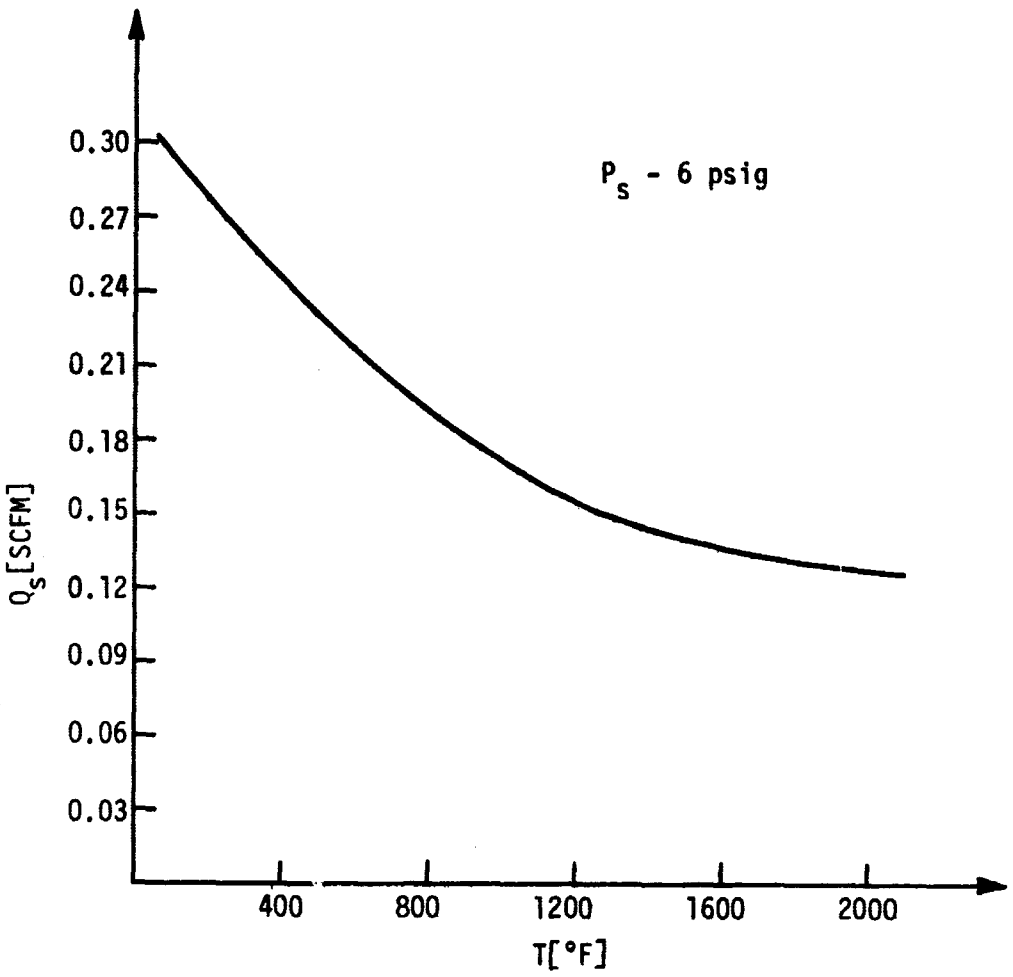

Figure 28. Fluidic Amplifier: Supply Flow vs. Temperature

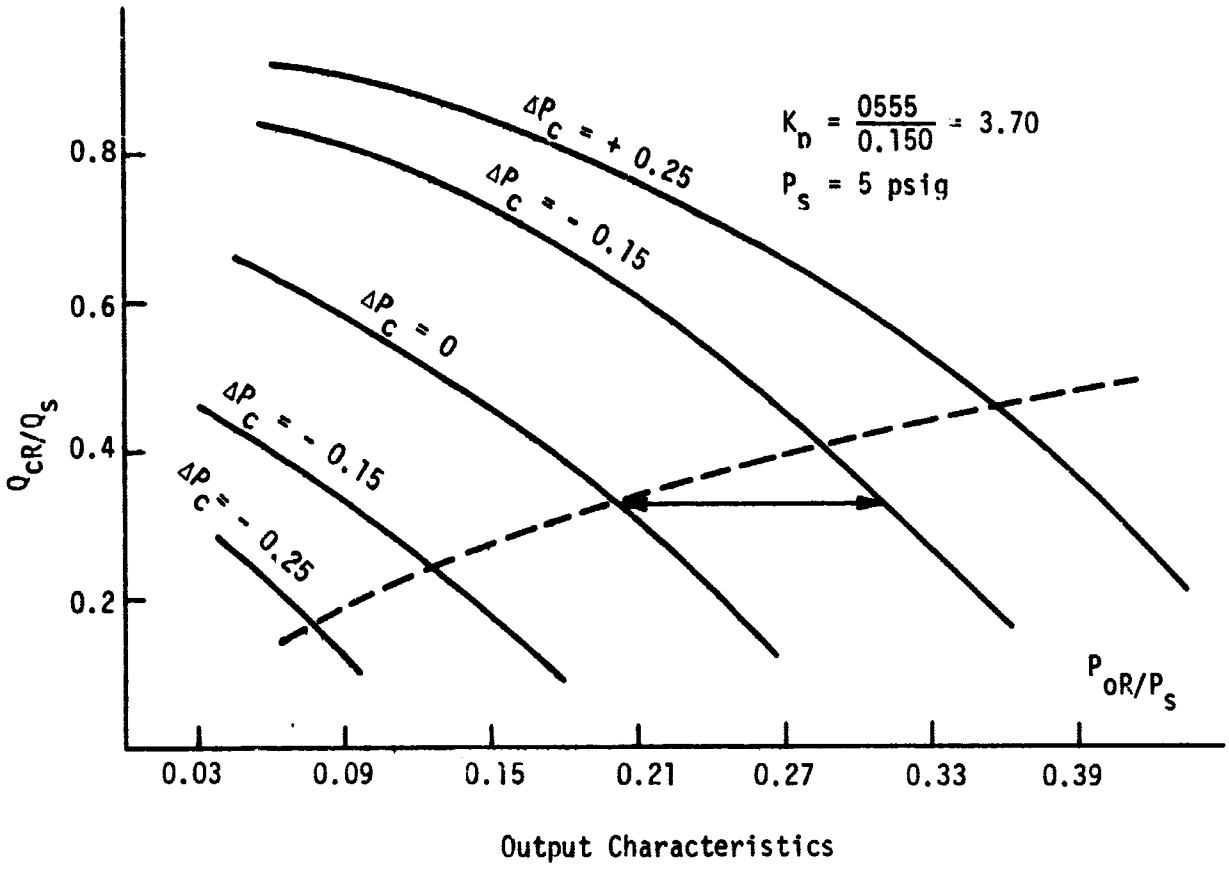

Output Characteristics

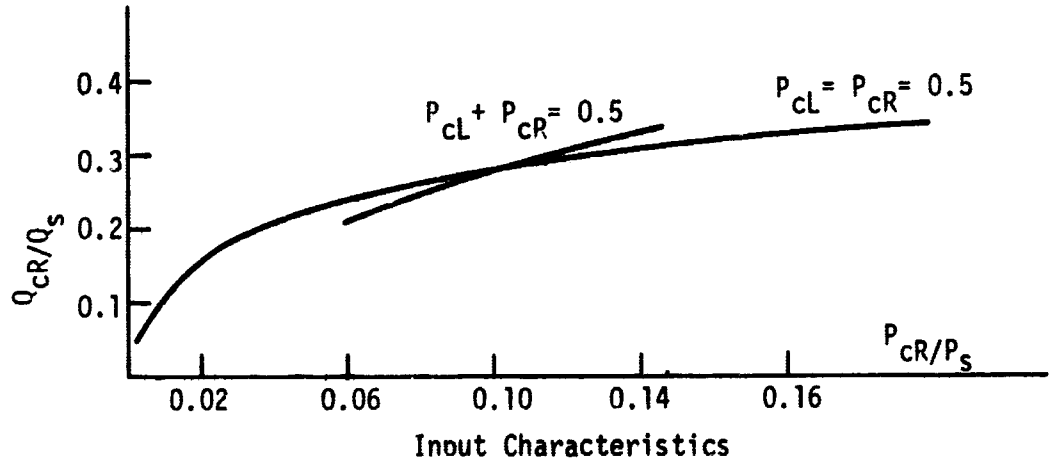

Inout Characteristics

Figure 29: Fluidic Amplifier: Normalized Characteristics - 70°F

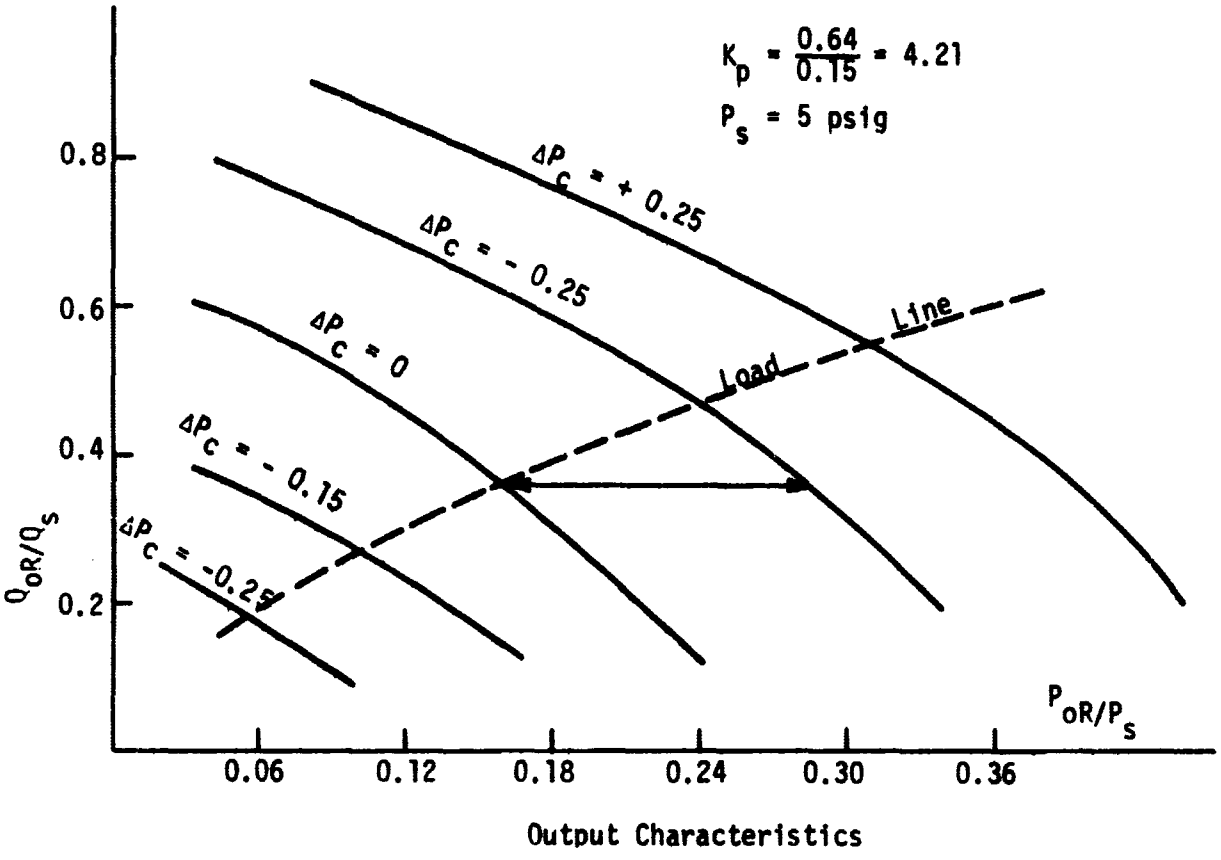

Output Characteristics

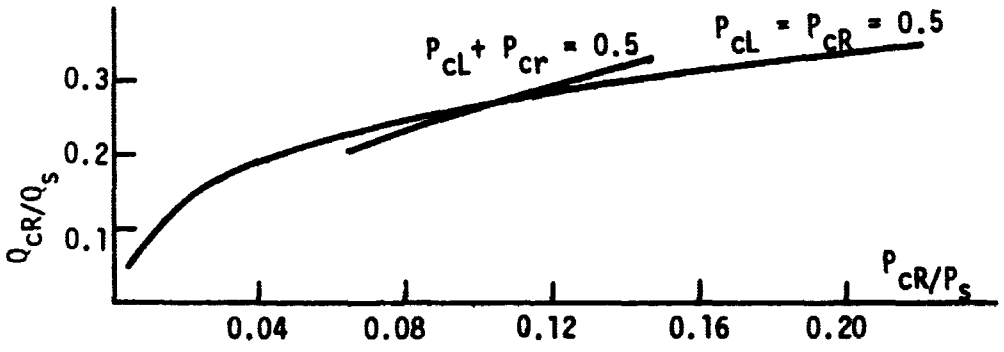

Input Characteristics

Figure 30. Fluidic Amplifier: Normalized Characteristics - 500°F

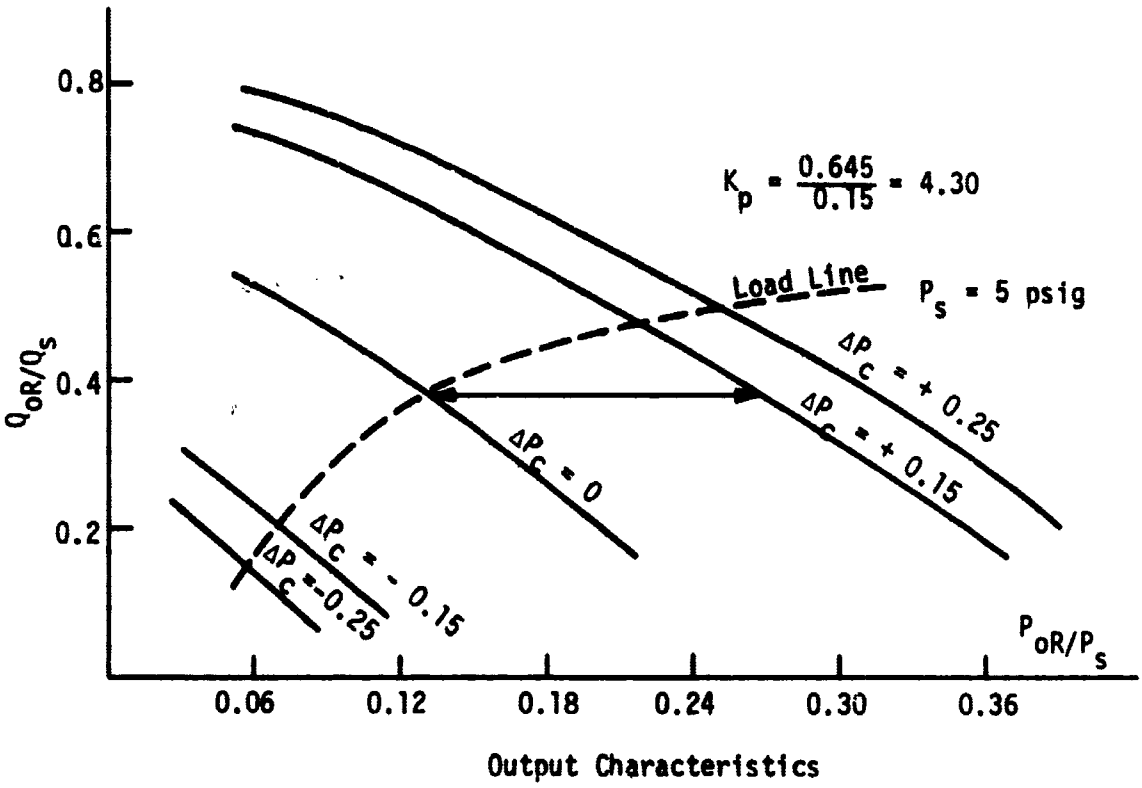

Output Characteristics

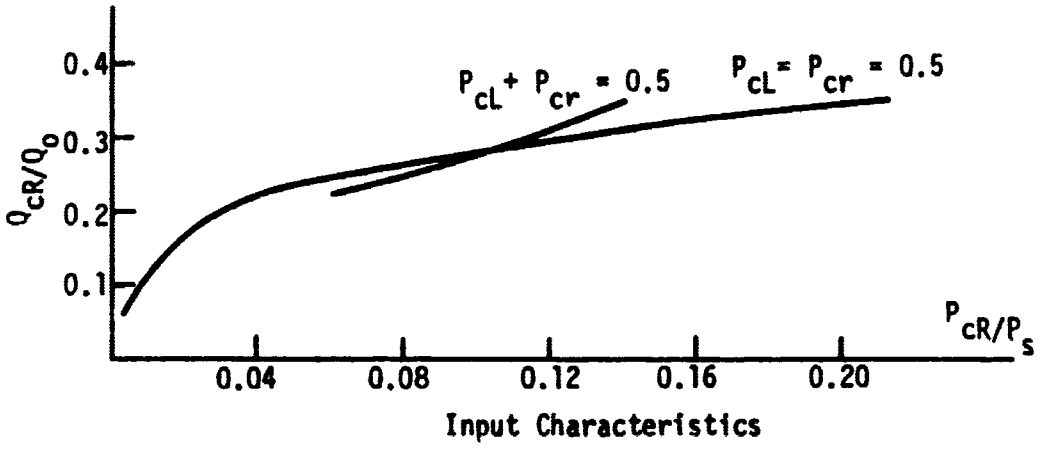

Input Characteristics

Figure 31. Fluidic Amplifier: Normalized Characteristics - 1000°F

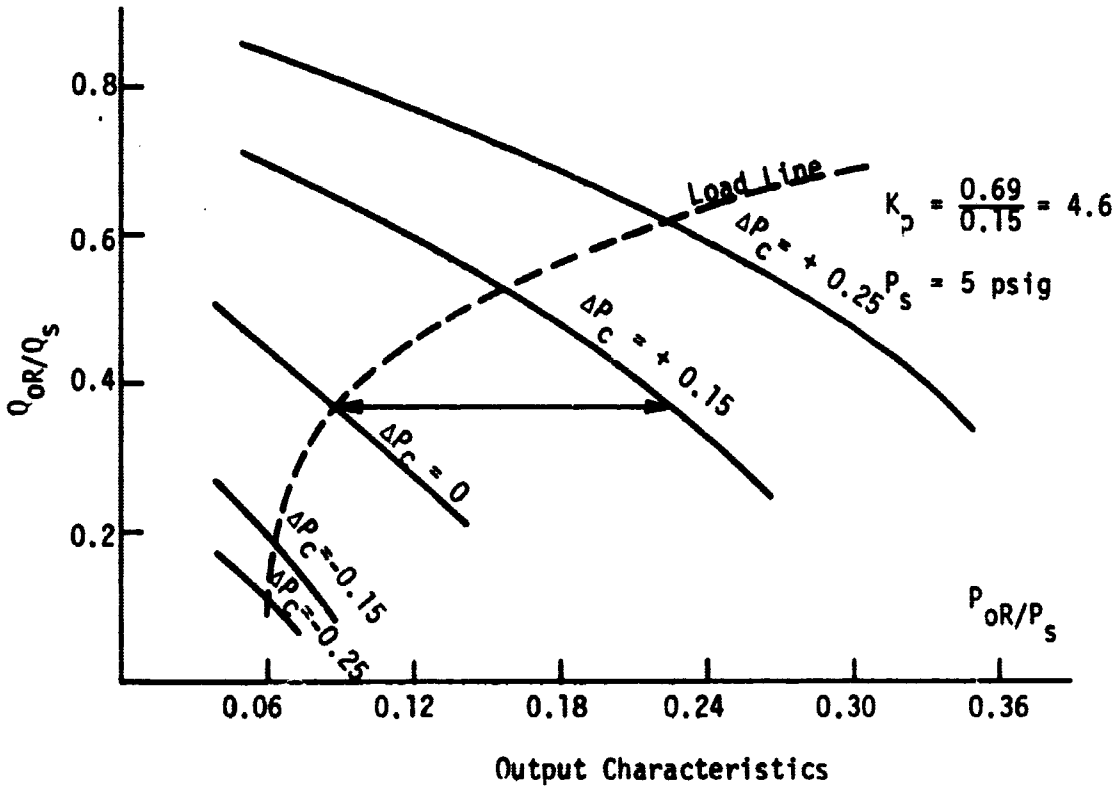

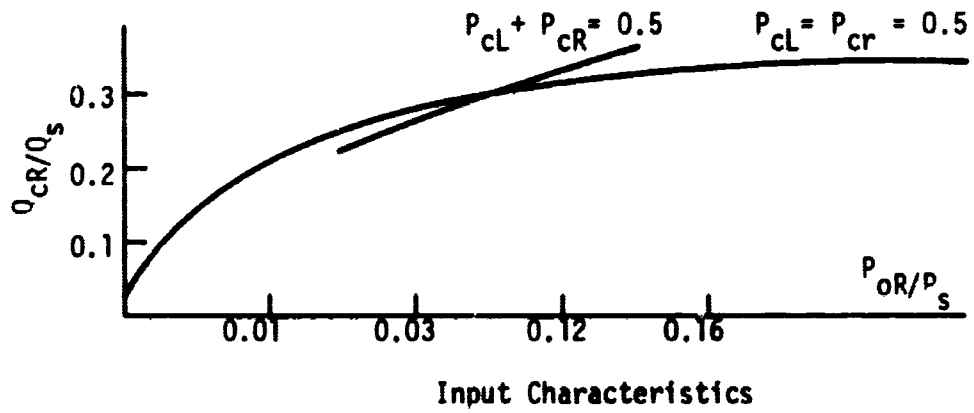

Figure 32. Fluidic Amplifier: Normalized Characteristics - 1500°F

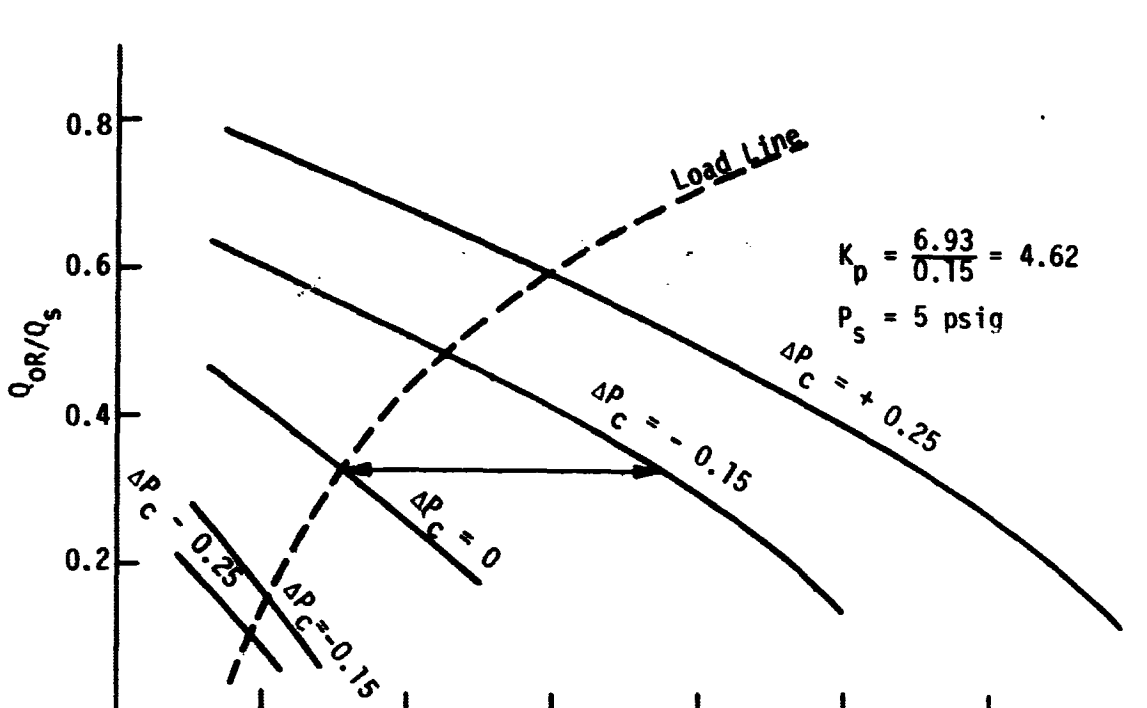

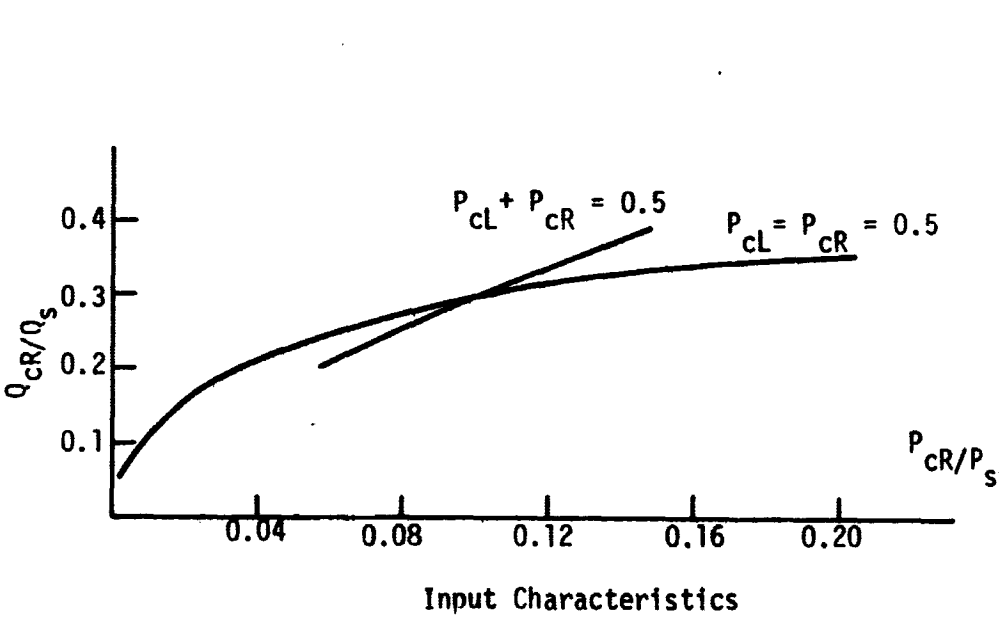

Figure 33. Fluidic Amplifier: Normalized Characteristics - 1800°F

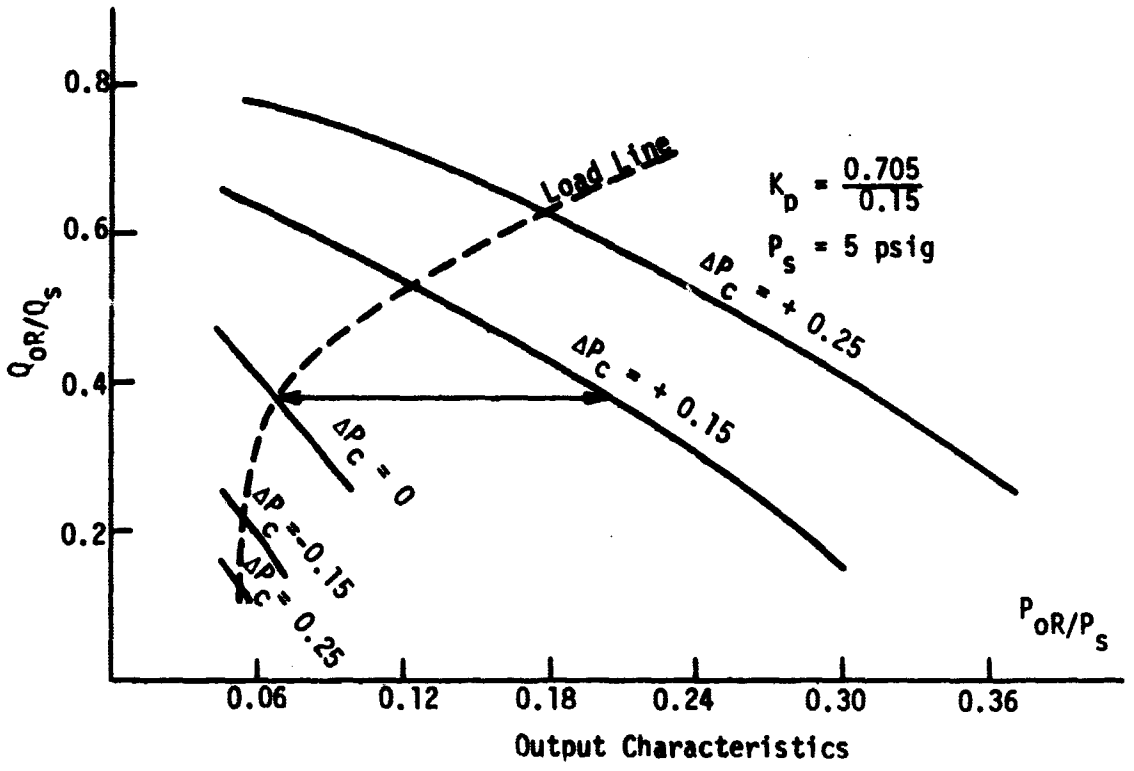

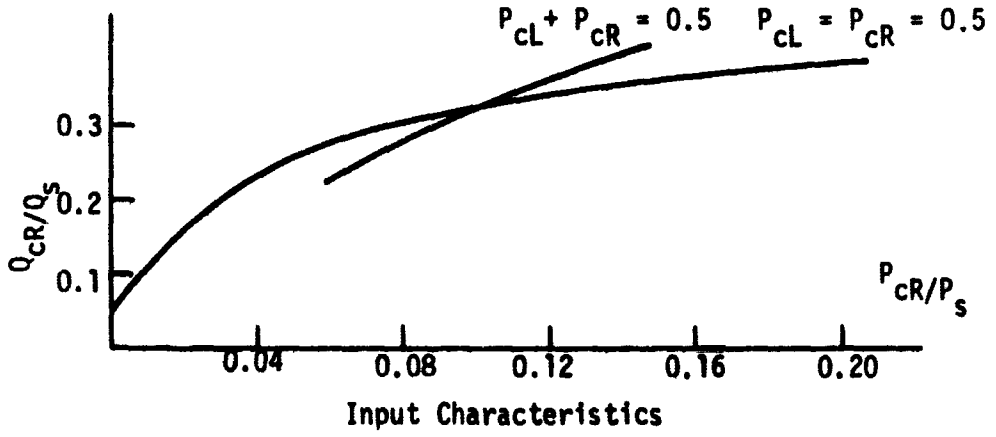

Figure 34. Fluidic Amplifier: Normalized Characteristics - 2000°F

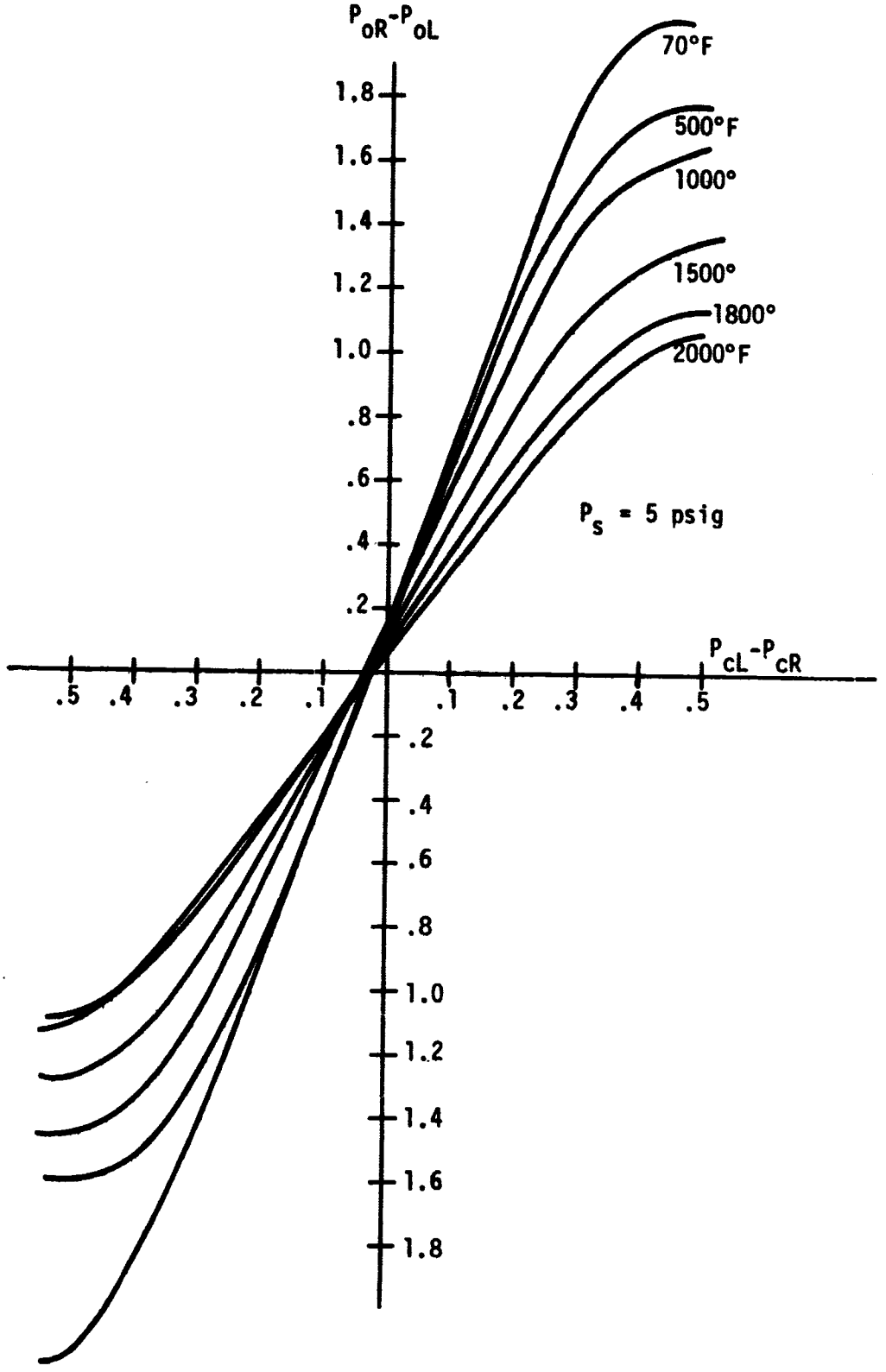

Figure 35. Fluidic Amplifier: Transfer Characteristics for Different Temperatures

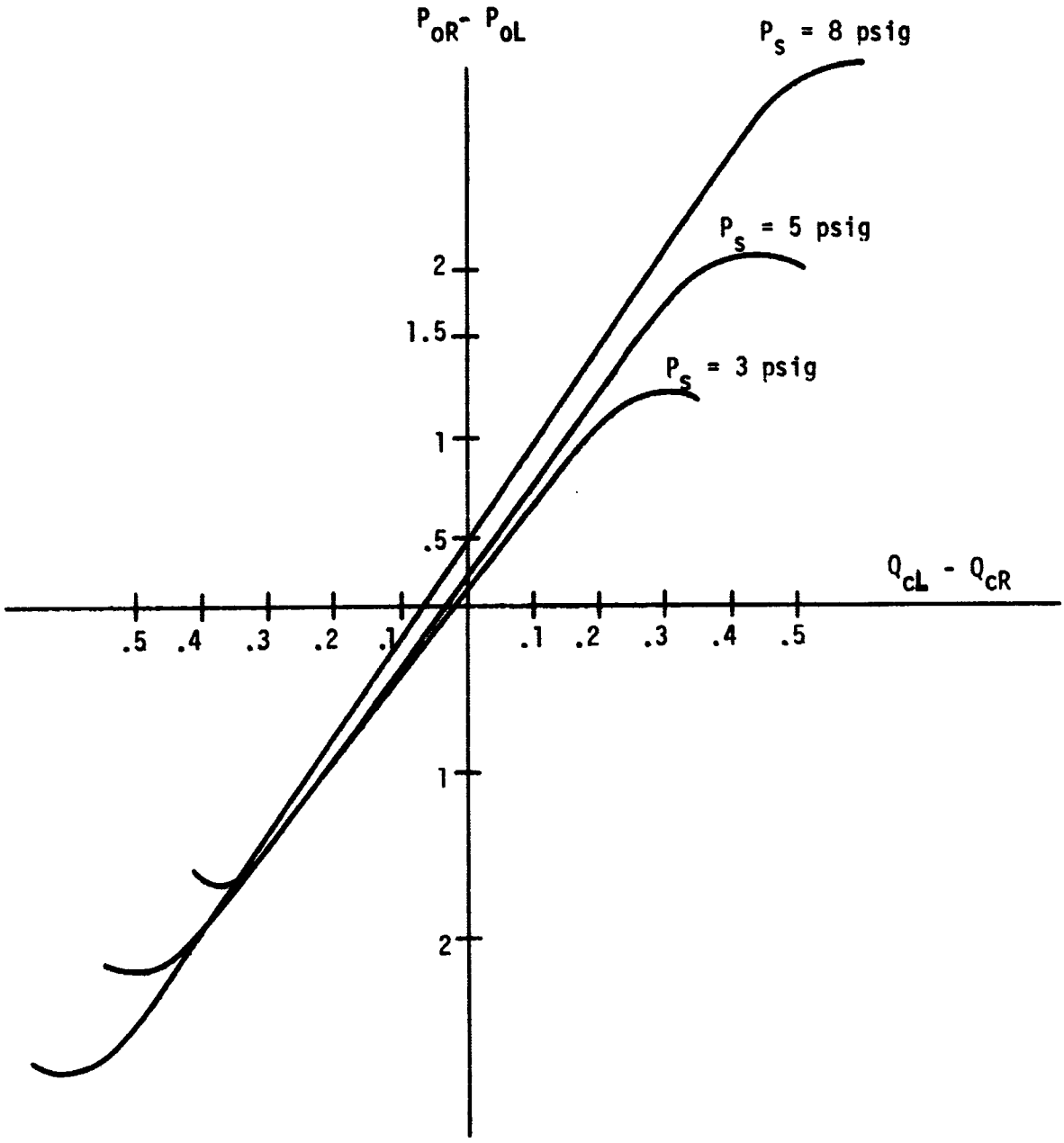

Figure 36. Fluidic Amplifier: Transfer Characteristics - 70°F

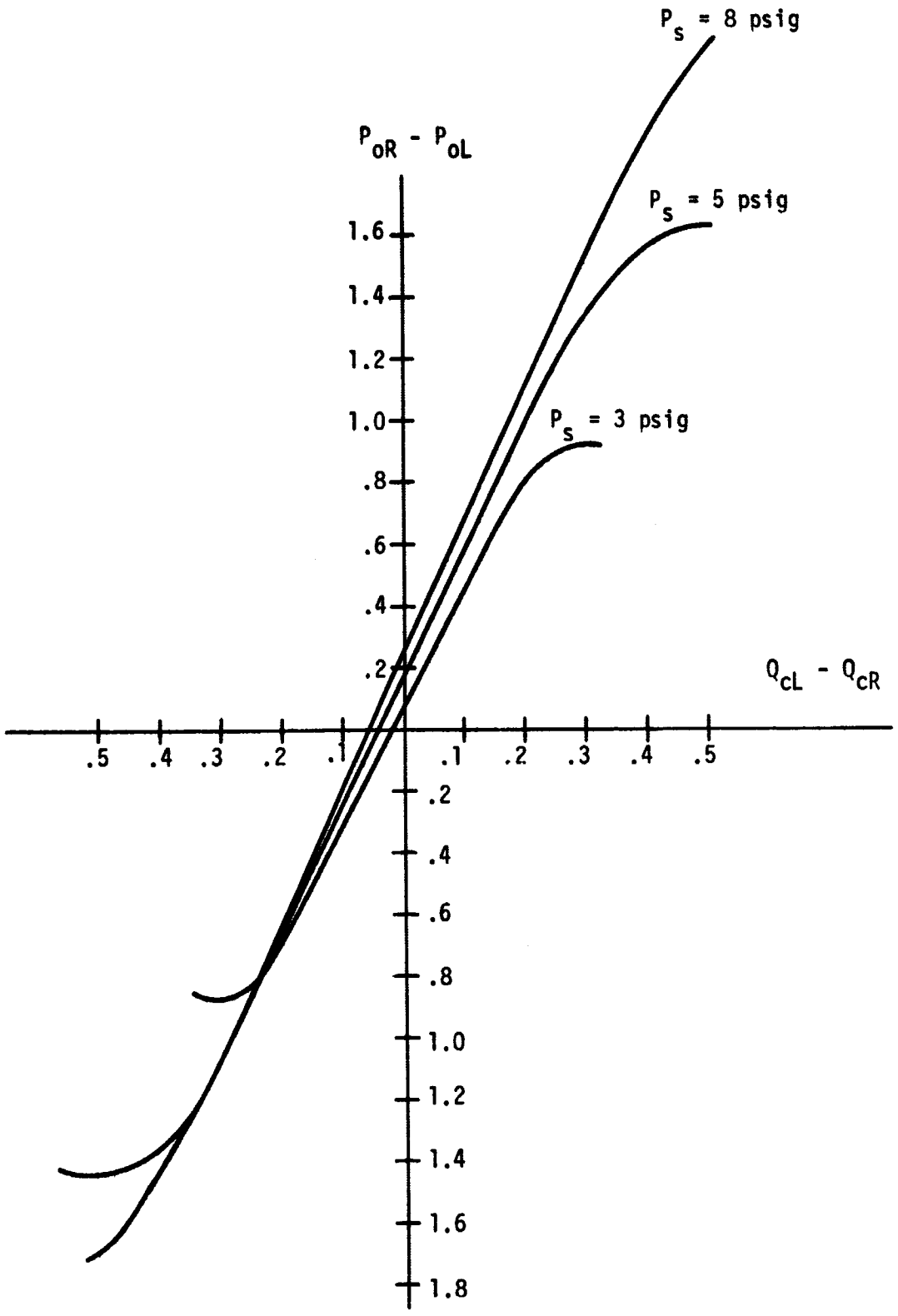

Figure 37. Fluidic Amplifier: Transfer Characteristics - 1000°F

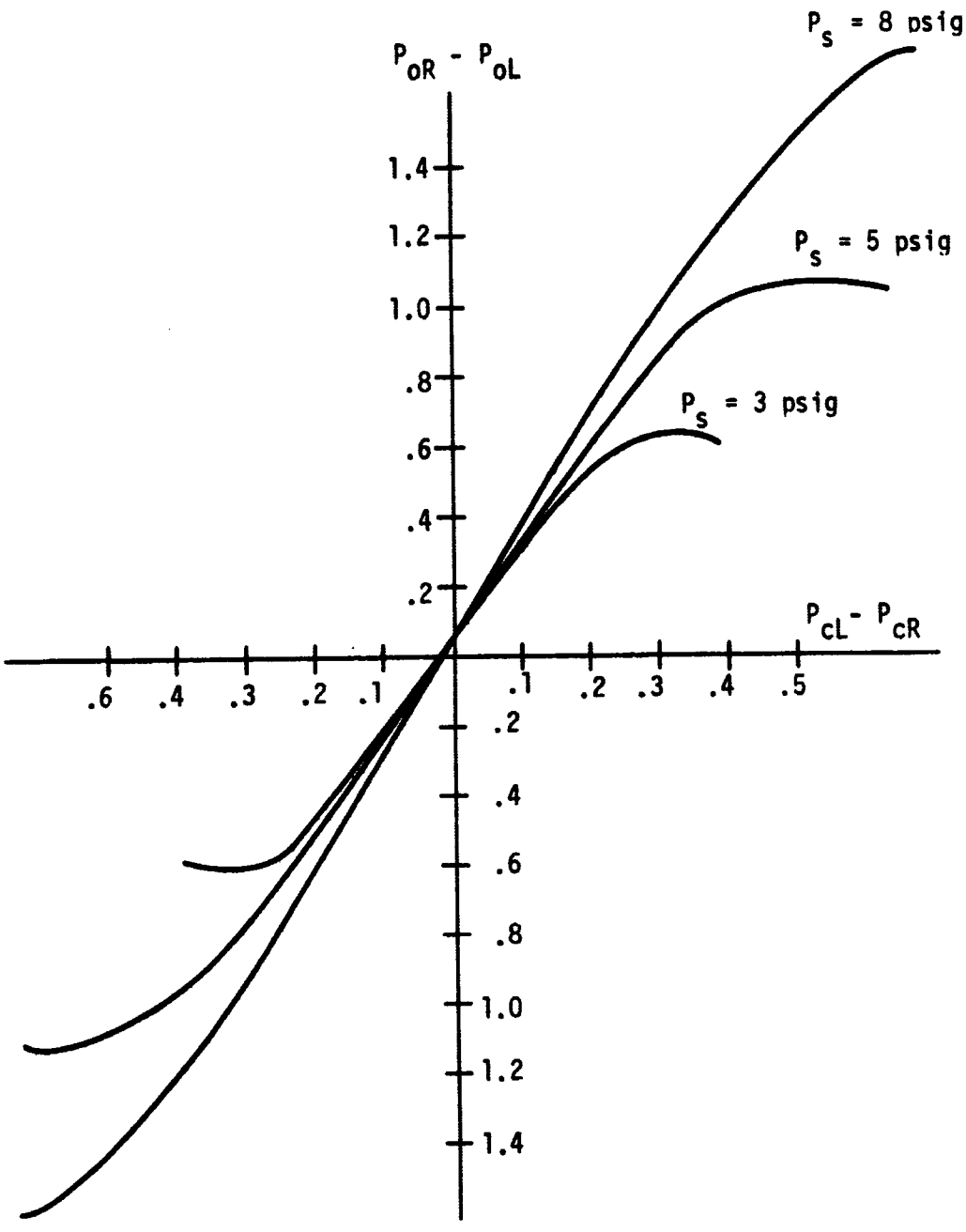

Figure 38. Fluidic Amplifier: Transfer Characteristics - 2000°F

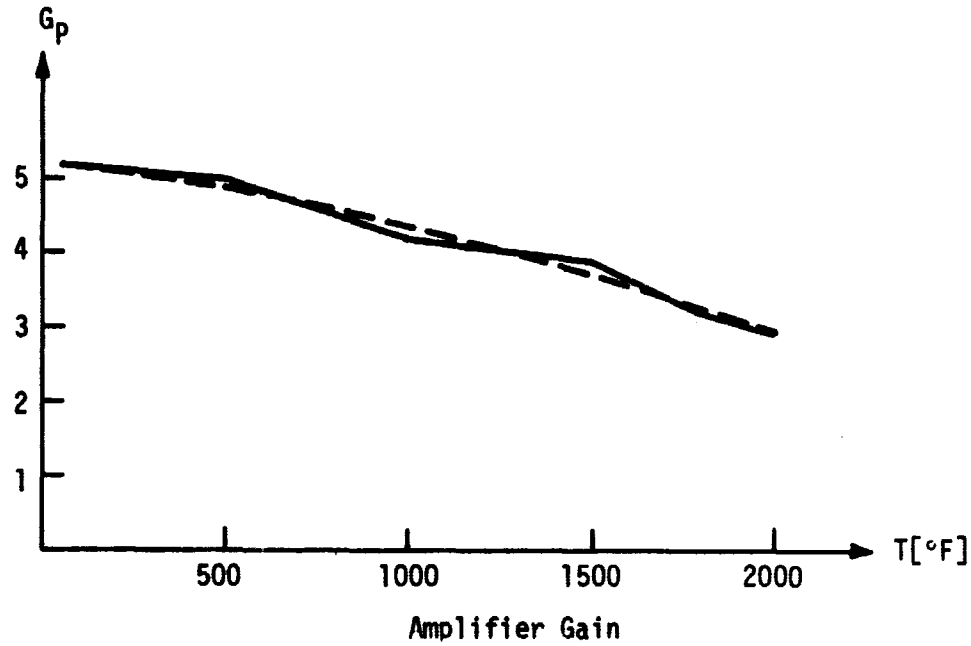

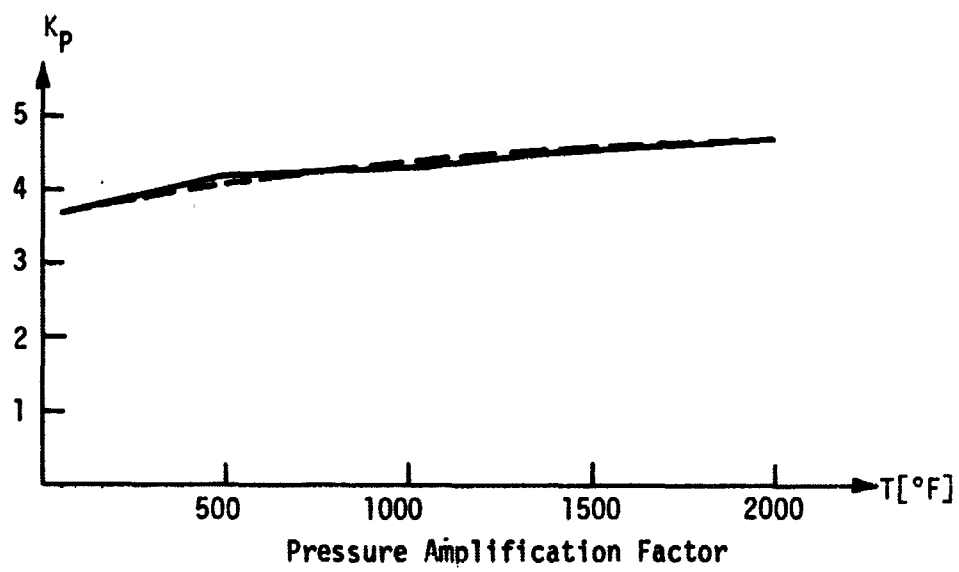

Figure 39. Fluidic Amplifier: Effect of Temperature on Amplifier Gain and Pressure Amplification Factor

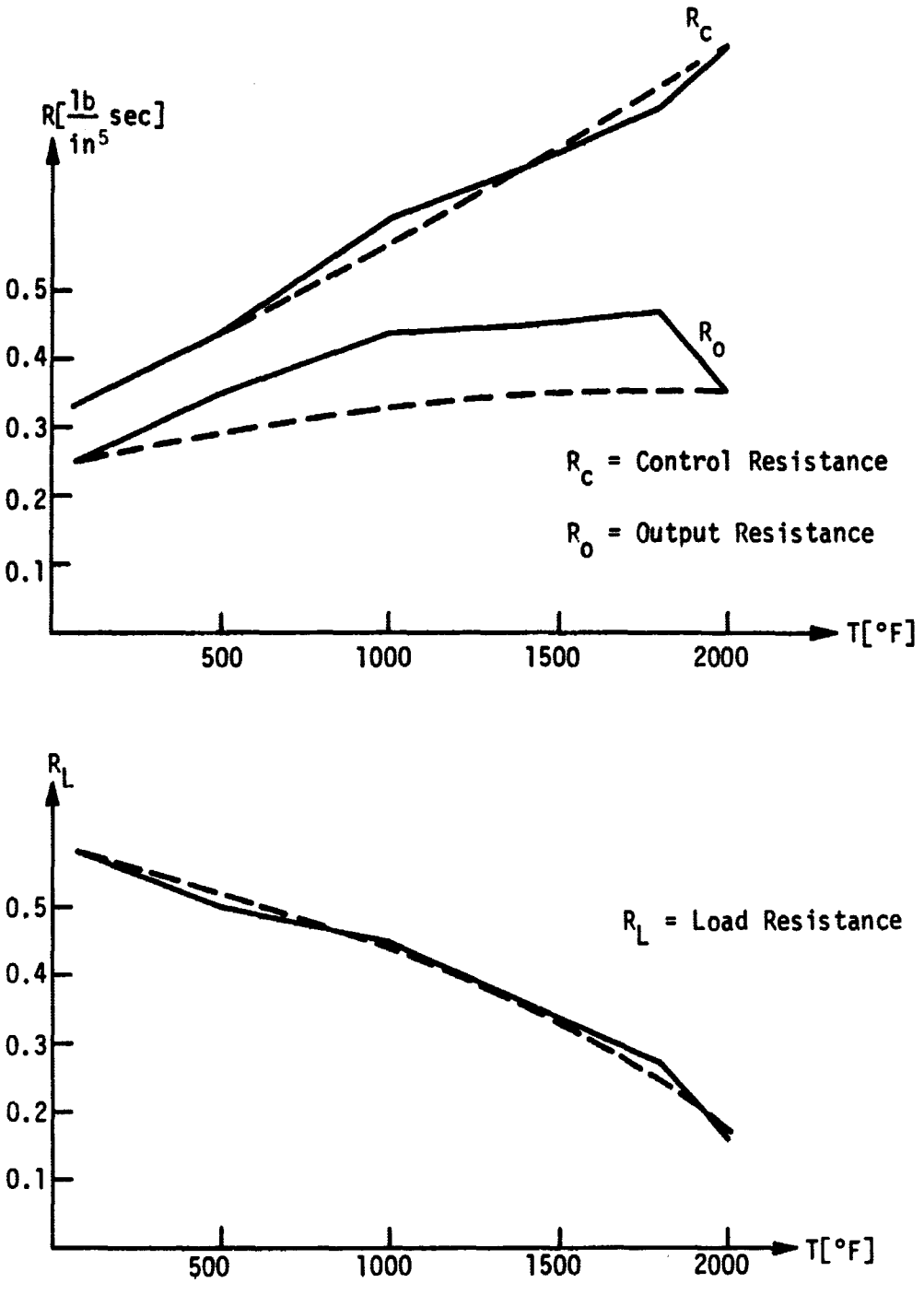

Figure 40: Fluidic Amplifier: Amplifier Resistances vs. Temperature

Tests were also performed for different supply pressures at room temperature, 1000°F and 2000°F. Increasing the supply pressure increases both the gain and the linear range. The pressure amplification factor K_p, defined as the ratio of the change in output pressure to the change in control pressure when the output flow is constant, increased from 3.70 at 70°F to 4.70 at 2000°F as shown in Fig. 39.

Null shift, is defined as either the differential output pressure required for zero control differential pressure or as the differential control pressure for zero differential output pressure. Null shift is shown in Fig. 41 as a function of temperature.

The amplifier linear range is nearly constant over a realtively large temperature range. Its largest change is in the range from room temperature to 500°F. These data are in Fig. 42.

Test results show that control resistance increased with increasing temperature. Output resistance behaved in the same way for temperatures to 1800°F; beyond 1800°F, output resistance decreased at a large rate.

The frequency response has been calculated from theoretical considerations of the system. Work is in progress on a pneumatic sinusoidal signal generator which will be used to obtain experimental frequency response data.

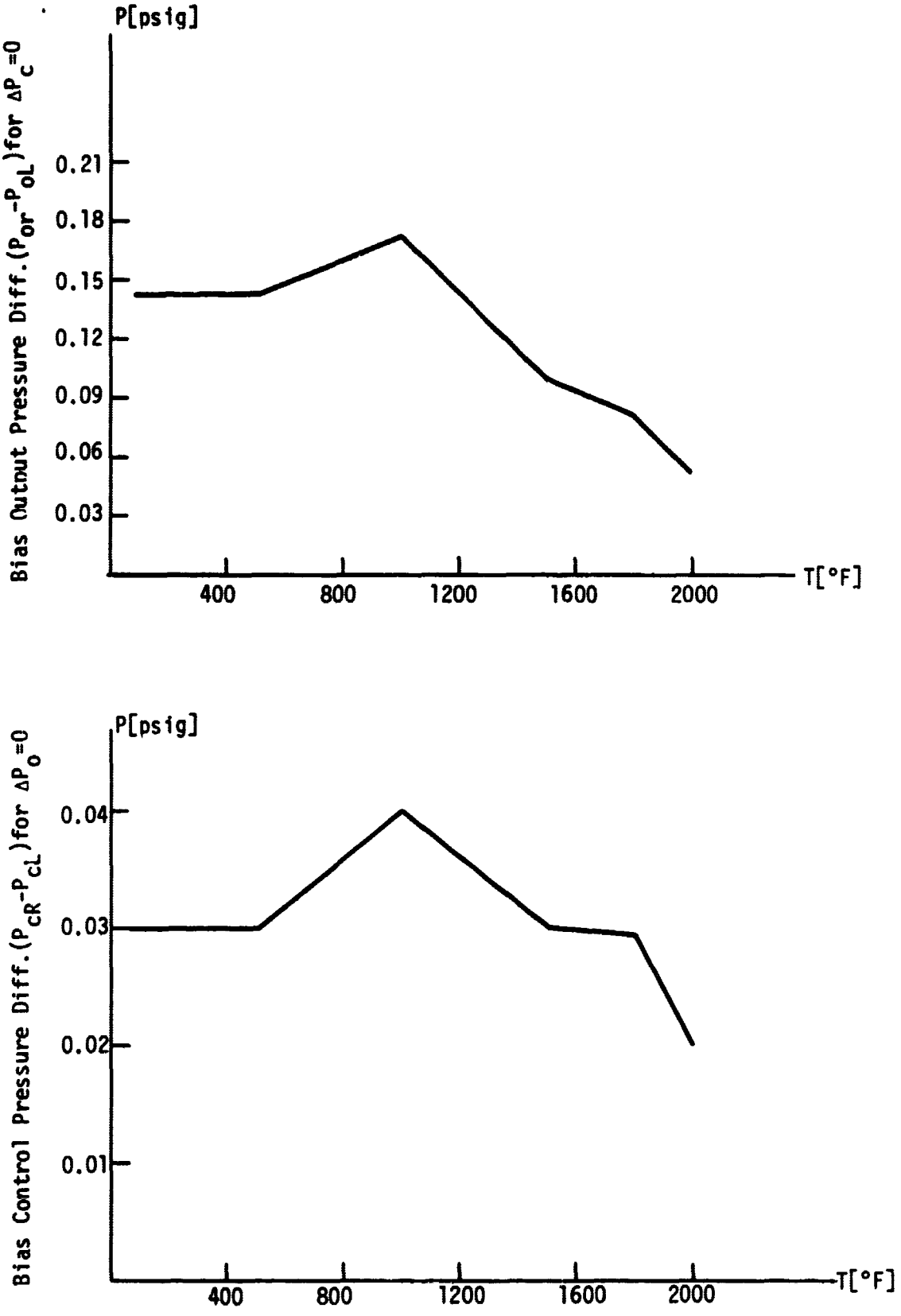

Figure 41. Fluidic Amplifier: Effect of Temperature on Null Shift

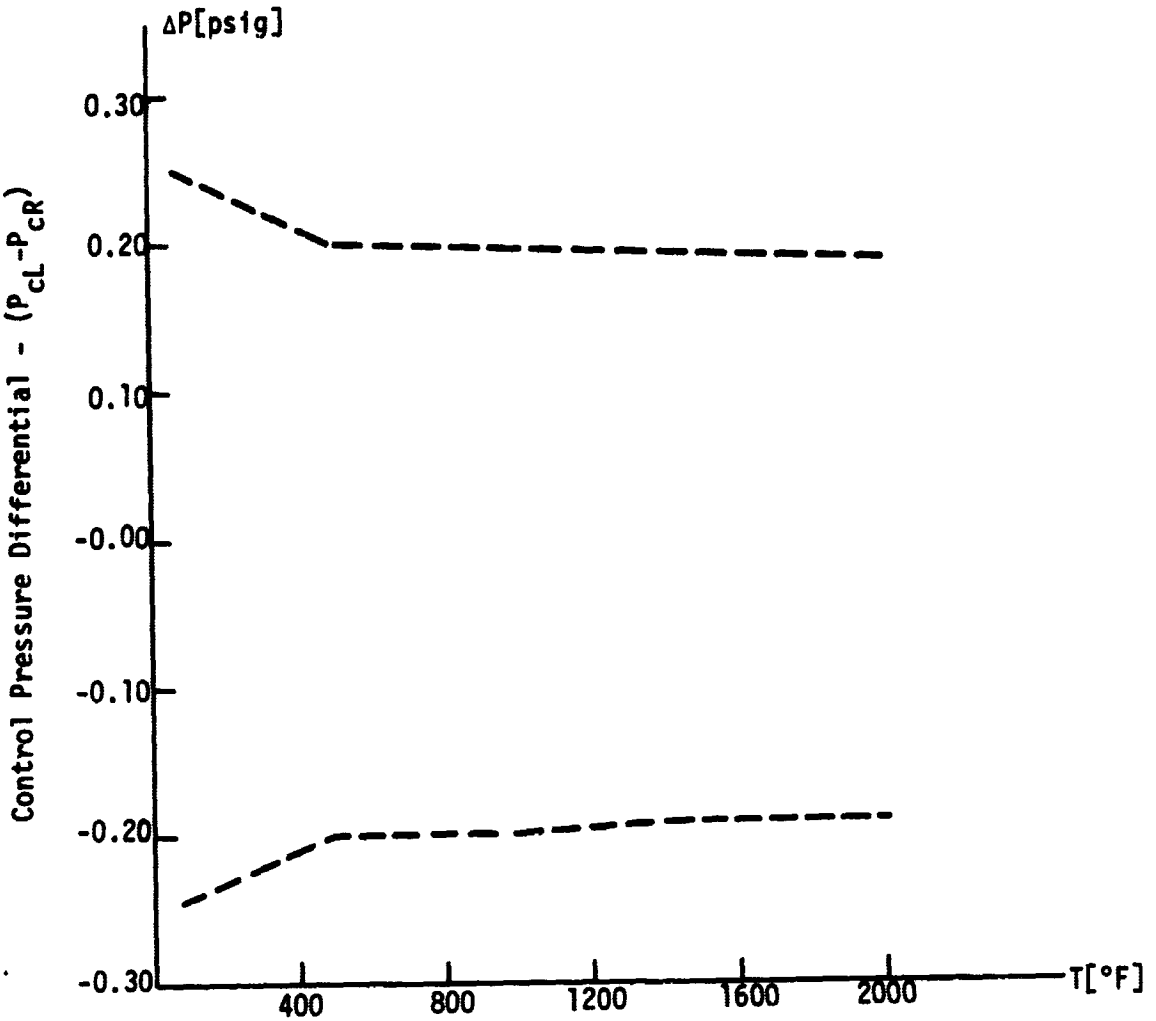

Figure 42. Fluidic Amplifier: Linear Range Variation With Temperature

CHAPTER V

GAS BEARING SUPPORT

This chapter contains a complete reproduction of a Masters Thesis presented to the School of Engineering and Applied Science by Andrew Ludwig Schilbe, June 1969.

DESIGN AND EVALUATION OF A GAS BEARING SUPPORT FOR A SKIN FRICTION METER

A Thesis

Presented To

the Faculty of the School of Engineering and Applied Science

University of Virginia

In Partial Fulfillment

of the Requirements for the Degree

Master of Mechanical Engineering

by

Andrew Ludwig Schilbe, Jr.

June 1969

APPROVAL SHEET

This thesis is submitted in partial fulfillment of

the requirements for the degree of

Master of Mechanical Engineering

_____

Author

Approved:

_____

Faculty Adviser

_____

Dean, School of Engineering and
Applied Science

June 1969

ABSTRACT

A gas bearing support system for a skin friction meter to operate in an extreme temperature environment is presented. Restrictor fed hemispherical bearings with three symmetrically located pads are employed for support of the moving elements of the meter.

An experimental investigation was performed to determine the static stiffness of the gas bearing system. The influence of temperature on the stiffness and load carrying capacity of the bearing was determined experimentally. The entire system was successfully tested at ambient temperatures up to 2000°F.

Finally, recommended design changes to increase the stiffness, based on the experimental analysis, are suggested.

ACKNOWLEDGMENT

The author expresses sincere appreciation to Dr. J. W. Moore for his advice during the preparation of this thesis.

He also wishes to thank his fellow students for their encouragement and helpful criticisms in the design of the experimental apparatus. Recognition is due Mr. Frederick Schenkel for his performance of the tedious task of lapping the spherical bearing surfaces.

The author's wife deserves special thanks for her encouragement and understanding during the entire project.

Graduate study was made possible by a teaching assistantship provided by the Mechancial Engineering Department. Financial support for the research was provided by NASA Grant NGR 47-005-026. This financial assistance is greatly appreciated.

TABLE OF CONTENTS

LIST OF TABLES

LIST OF FIGURES

FIGURE PAGE

LIST OF SYMBOLS

a	Acceleration, ft/sec^2
A	Area, in^2
b	Land width, inches
c	Clearance, inches
C_D	Orifice discharge coefficient, dimensionless
d	Differential operator
F	Force, pounds
k	Ratio of specific heats C_p/c_v, dimensionless
K	Static stiffness, lb/in
L	Land length, inches
$\mathcal{L}$	Lift, pounds or grams
m	Mass, lb_m
M	Mass flow rate, $lb_{m/sec}$
	or Moment, in-lb
p	Pivot center
P	Prsssure, lb/in^2 absolute
r	Radius, inches
R	N_2 gas constant, 55.16 $\frac{ft\text{-}lb}{lb_m\text{-}°R}$
s	Arc length, inches
T	Temperature, °F or °R
W	Weight, pounds or grams
x	Coordinate axis
y	Coordinate axis

α Angular displacement, radians

Δ Linear displacement, inches

θ Angular displacement, radians

μ Viscosity, $lb_m/sec\text{-}ft$

ρ Density, lb_m/in^3

Σ Summation

ω Frequency

Subscripts

a Atmosphere

A Balance arm position

B Balance arm position

C Balance arm position

c Choked

ℓ Lower

L Land

n Polytropic exponent

N Natural

o Orifice or oven

p Pad

s Supply

t Total

u Upper

1 Exit of tube, Land entrance, or balance arm position

CHAPTER I

INTRODUCTION

This thesis concerns the development and evaluation of an externally pressurized gas bearing support for a skin friction meter. The support system must be able to operate in a hostile enviornment consisting of extreme temperatures and large vibration and acceleration fields.

Background

In the development of a high speed rocket or jet engine, the direct measurement of aerodynamic skin friction drag is necessary in order to determine the in-flight thrust. During the past year, a joint research effort by the Electrical and Mechanical Engineering Departments at the University of Virginia has been undertaken to develop an instrument to measure skin friction drag at high Mach numbers. Sponsorship of this research is by the Force Measurements Group of NASA at Langley Research Center, Hampton, Virginia. The purpose of the skin friction meter will be to measure the thrust of a hypersonic ramjet engine that will be mounted below a high speed aircraft. These measurements will be made at altitudes up to 123,000 feet and Mach numbers up to 8.0 (1). The meter will also be generally useful for wind tunnel experimentation at high temperatures.

Guidelines for the development of the meter are as follows (1), (2):

1) The meter must operate at temperatures up to 2000°F.

2) Forces due to acceleration, g units:

$^{+ 4.5}_{- 3.0}$ g longitudinal

$^{+ 1.0}_{- 1.0}$ g transverse

$^{+ 6.8}_{- 1.0}$ g normal

3) Accelerations: The maximum acceleration in the direction of flight in 3.5 g.

4) Space requirements: The height is to be no greater than 2 inches. The other two dimensions could be somewhat larger.

5) Vibration: Environmental levels of 0.06 inch double amplitude from 10 to 55 H_Z and 10 g vibration from 55 to 2000 H_Z are possible.

6) Force measurement range: The instrument is to be capable of measuring a force of 0.7 to 7 millipounds.

7) The maximum deflection of the target shall not exceed 0.0005 inch. The target is a small area of the aircraft skin which is free to move when acted upon by a friction drag force.

Three approaches to the development of the meter are being investigated. Two are primarily electrical and the other is a pneumatic system. A schematic of the pnematic system is shown in Figure 1 since that is the approach that will best accommodate the gas bearing support. The flapper valves sense the deflection of the arm by a differential pressure output. The pressure difference will be fed through a fluidic amplifier to the air motor thus applying a restoring force to the arm to make a

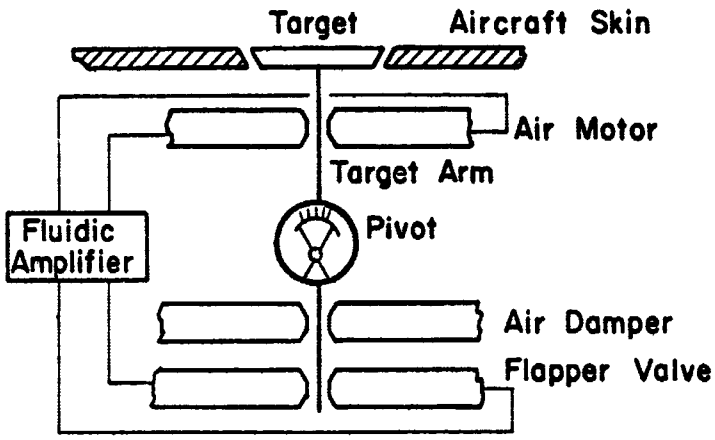

FIGURE 1

Schematic Diagram of Pneumatic Skin Friction Meter

closed loop position control system. The skin friction force readout will be proportional to the pressure difference sensed by the valves.

Since the flexure pivot used in Figure 1 adds a constraining force to the system, a pivot of zero starting friction (stiction) with no constraining force would be desirable. This can be realized by replacing the pivot with a gas bearing.

The entire system is subjected to large accelerations. Ashby (2) had developed a means to counterbalance the skin friction meter against the effects of the accelerations. These accelerations cause high inertia loading on the flexure or the gas bearing which will replace it. Therefore, a high stiffness in the direction of loading is necessary to insure minimum displacement of target. The stiffness of the bearing is therefore of particular interest in this work.

Scope

This thesis covers the development of a set of two hemispherical gas bearings and the mating target carrier or rotor. A brief survey of the pertinent literature on externally pressurized gas bearings is presented. A simplified analysis of the bearing lift and its dependence on various system parameters is included. Other factors which influence the design of the bearing system are considered. The experimental investigation, including the design and construction of the apparatus is presented with special emphasis on the bearing system stiffness results. The lift results are compared with the simplified analysis. Recommendations are given for possible improvement of the overall system performance.

Conclusions are stated as to the feasibility of applying the described bearings in the hostile environment.

Literature Survey

The literature available on externally pressurized gas bearings is much too great to list here. Only those of particular interest or of notable use in preparation of this thesis are cited.

A book by Gross (3) deals entirely with gas lubrication, both self-acting and externally pressurized. However, the treatment of the externally pressurized bearings is limited. Relationships for pressure distribution and load for a hemispherical bearing are presented. Application of these equations will not hold for the present design, since coincident centers or symmetrical eccentricity about the line joining the center of the sphere and source are assumed.

A paper by Laub and Norton (4) deals with the analytical and experimental study of externally pressurized spherical gas bearings. Corey, et al. (5) presented experimental work on spherical bearings from which some empirical equations are derived. Both of the systems mentioned above support loads along a limited number of axes (i.e., a sphere in a single mating bearing).

The load carrying and operational properties of a multiple pad sperical bearing support system are dealt with by Speen and Grant (6). Six circular concave spherical pads support a sphere in all directions by orienting pairs of opposed pads at 90° to each other in three mutually perpendicular directions.

An extremely informative survey on the design, construction and use of fluid film bearings has been compiled by Geary (7). Many design suggestions are cited along with an extensive bibliography.

Boyd, Kaufman, and Raimondi (8) have presented design and reference data for simple as well as opposed pad bearings. A design manual by Rippel (9) is available which lists many bearing configurations and related design factors.

Gas lubricated bearings as applied to instruments are dealt with in a paper by Denhard and Pan (10). A thorough list of references that covers three types of lubrication (Self-Acting, Externally Pressurized, and Squeeze Film) is given.

Finally a survey on gas bearing technology since 1959 is given by Gross (11). A discussion of the major changes in gas bearing technology is presented along with numerous references.

No reference was found that considered the particular geometric configuration that is dealt with in this thesis.

CHAPTER II

BEARING SUPPORT SYSTEM

General Considerations

In developing a support for the target area, the following objectives are considered.

1. Sufficient load carrying capacity
2. Maximum stiffness
3. Minimum flow (gas consumption)
4. Maximum clearance between surfaces
5. Zero stiction
6. Freedom from instabilities
7. Zero turbine torque
8. Materials to withstand 2000°F
9. Minimum alignment problems

The above objectives are liable to conflict, so that design compromises must be made in order to obtain a practical design.

Gas bearings are classified as self-acting, if the lubricating film exists because of relative tangential motion, squeeze, if due to relative normal motion, and externally pressurized, if due to an external pressure source (3). In instrument design, externally pressurized gas bearings have proved particularly useful when applied as supports for null devices, as is the case in this study. This is due to the very low frictional resistance to rotation and zero starting friction (stiction) (6). Other advantages include no wear, relatively large film thicknesses

(on the order of 5 to 20 x 10^{-4} inches), and a viscosity increase with increasing temperature.

To minimize gas flow and increase stiffness of an externally pressurized bearing, a restriction such as an orifice or a capillary can be added between the supply and the bearing surface. Increased load capacity and alignment capabilities are consequences of providing pads or pressure zones separated by grooves on the bearing surface. The grooves are fed from the aforementioned restrictors. In this way the load capacity is provided without large volumes of gas as would be present in recesses. Recesses are commonly used in liquid lubricated bearings to maximize the load carrying efficiency and to avoid pressure peaks by more evenly distributing the pressure over the bearing area. Instabilities in the gas film are less likely to occur with grooved pads since the smaller volumes of gas indicate increased stability. To insure proper gas flow, exhaust grooves can be placed between each pad. This essentially isolates the effects of each pad, thereby eliminating any cross feeding between the pressure zones.

Support Configuration

The support system consists of two hemispherical bearings, a mating target carrier (rotor), and bearing holder structure. The bearing holder was used for stationary fastening of the bearings and for positioning the bearings relative to one another in the experimental set-up. Accurate positioning was accomplished by employing a differential screw mechanism on one bearing while fixing the other. The hemispherical

bearing mounted in the holder structure is shown in Figure 2.

The pad orientation and hemispherical bearing geometry are shown in Figure 3. Detail sections for the exhaust and pad (grid) grooves are also given. There are three pads located symmetrically with respect to the line of centers of the bearings and separated by exhaust grooves. The pads are fed from 0.0135 inch diameter capillary tubes of length 0.375 inch.

The rotor was made cylindrical in shape with hemispherical cavities in each end. Many trials were necessary to achieve a rotor configuration that was free from any instabilities. The most successful is shown in Figure 4.

The hemispherical bearings and cavities are lapped to 1.0015 inch and 0.9980 inch diameters, respectively. Bearing diameter was measured by a micrometer which would read to the nearest 0.0001 inch. After assembly, the rotor cavity diameter was measured with a 0.0001 inch dial indicator by determining the total clearance between the bearing and cavity.

Selection of the bearing dimensions was dictated by the maximum height specification of 2 inches and also the availability of 1 inch diameter spheres. The rotor was constructed so as to mate with the bearings. Its' length was chosen from the standpoint of ease of manufacture and consideration of existing experimental apparatus.

Material Selection

Since one of the objectives of this study was the operation of

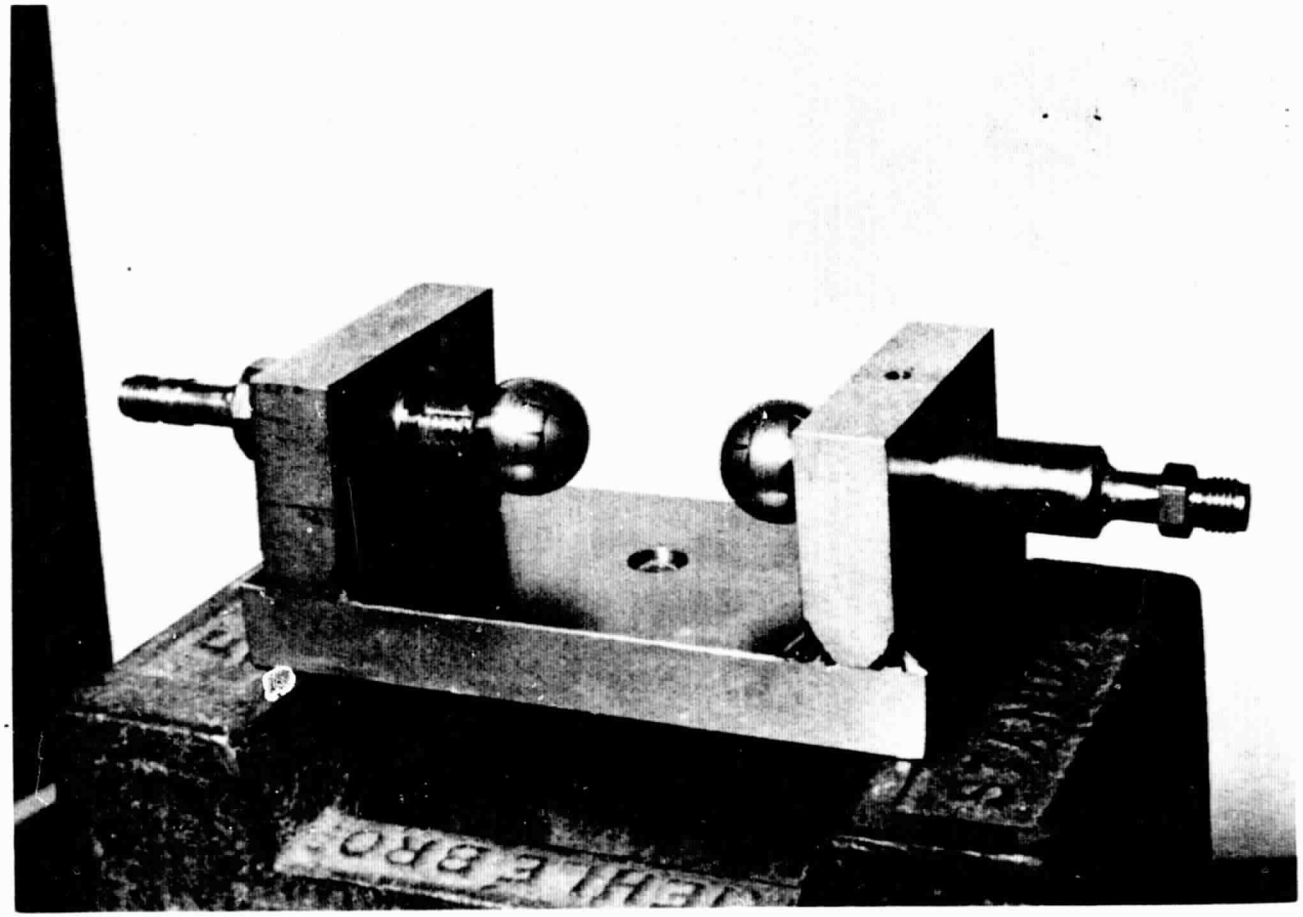

FIGURE 2

Hemispherical Bearings and Holder Structure

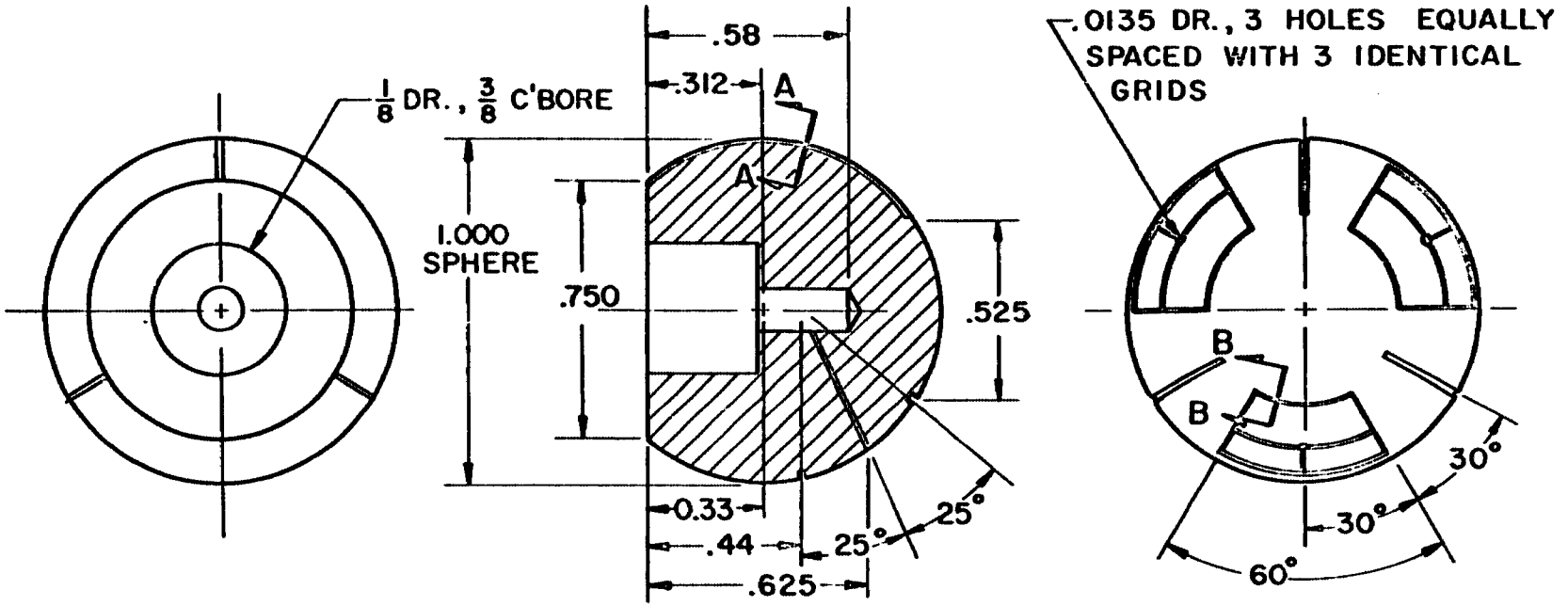

SCALE: DOUBLE SIZE

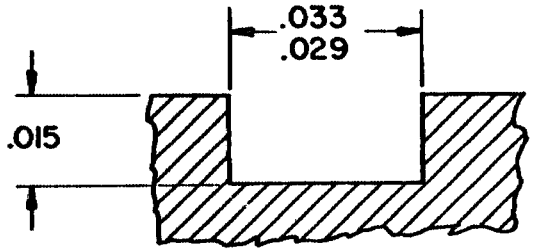

SEC. A–A

EXHAUST GROOVE
SCALE: 1" = .03"

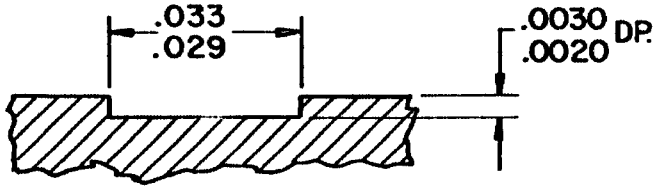

SEC. B–B

GRID GROOVE
SCALE: 1" = .03"

FIGURE 3

Hemispherical Bearing Geometry

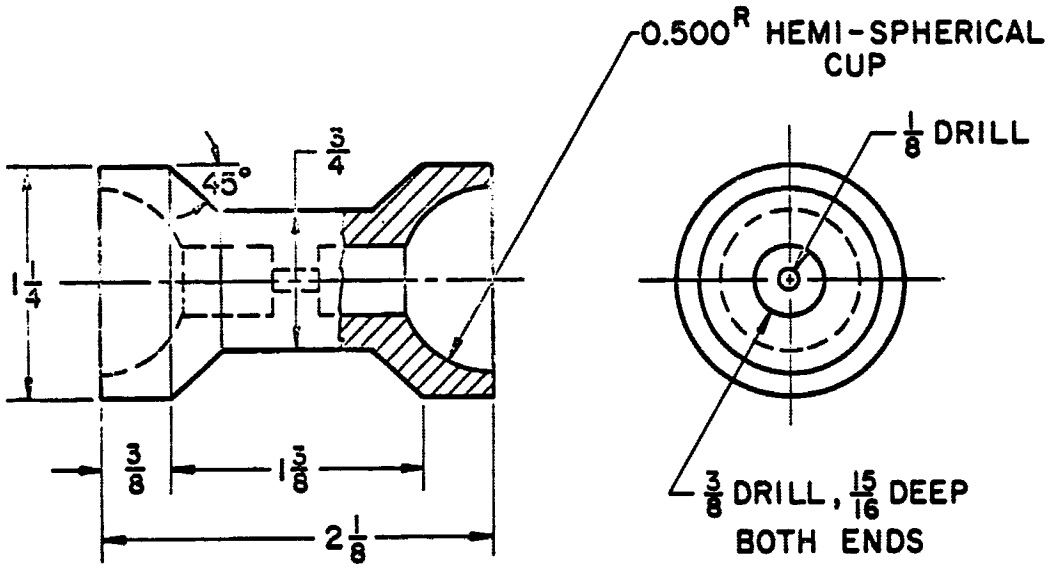

FIGURE 4

Rotor Configuration

the system at temperatures up to 2000°F, materials that would withstand this environment must be employed. Some of the criteria that was followed in selection of the materials are listed below.

1) Oxidation or scaling resistance at extreme temperatures
2) High melting point
3) Sufficient strength at temperature and resistance to creep
4) Resistance to thermal shock
5) Resistance to furnace atmospheres containing nitrogen
6) Thermal expansion rates of differing materials should be similar
7) Weldability
8) Ease of fabrication

The hemispherical bearings were made from AlSl 613 bearing steel. This is a Martensitic secondary hardening steel that is commonly referred to as M-50. This choice was dictated due to the ready availability of 1 inch diameter M-50 spheres.

The rotor and bearing holder was made from AMS 5592 stainless steel (RA 330). Selection of this material was made after careful consideration of the aforementioned criteria. Data available on RA 330 confirm service temperatures up to and including 2300°F with good oxidation resistance up to 2100°F.

The nominal percent compositions for M-50 and RA 330 are listed below for comparison.

RA 330

C	Mn	Si	P	S	Fe	Cr	Ni
0.05	1.5	1.25	0.015	0.015	42	19	36

M-50

C	Mn	Si	Cr	Mo	V
7.6	2.8	1.9	38.3	40	9.4

TABLE 1

CHEMICAL COMPOSITION BY PERCENT

OF RA 330 AND M-50

In Table 2 some selected properties of RA 330 and M-50 that proved useful in preparation of the bearing system and experimental apparatus are listed (12), (13).

Gas supply lines and tube fittings that were to be subjected to extreme temperatures were type 316 stainless steel. Type 316 was used since a local supplier could provide quick delivery and also the application was less critical than for the bearing and rotor.

To insure that the system could be dismantled easily after the experimentation, an anti-seize and lubricating compound ("Never-Seez") was used on all screw threads. This was also used on the structure, excepting bearing surfaces, to help decrease any corrosion or oxidation.

MATERIAL	COEFFICIENT OF THERMAL EXPANSION (in./in./°F)		TENSILE STRENGTH (1000 psi)	YIELD STRENGTH (2%) (1000 psi)	MODULUS OF ELASTICITY (10^6 psi)	MELTING RANGE °F	DENSITY LB./in.^{3}	HARDNESS ROCKWELL
		x10^6						
RA 330	70 to 1500°F	9.9	RM. TEMP.-85	RM. TEMP.-42	RM. TEMP.-85	2550/2600	0.289	75-85B
	70 to 1600°F	10.0	1600°F-20	1600°F-13	400°F-27.0			
	70 to 1700°F	10.1	2000°F-7	2000°F-5	800°F-25.0			
	70 to 1800°F	10.2			1200°F-22.3			
					1600°F-19.5			
					1800°F-18.0			
M-50	-100 to + 70°F	5.59	RM. TEMP-410	RM. TEMP-335	RM. TEMP.-29.5	2550/2800	0.283	64C
	70 to 1000°F	7.38	800°F-345	800°F-260				
			1000°F-309	1000°F-250				

TABLE 2
SELECTED PROPERTIES OF M-50 AND RA 330

CHAPTER III

FLOW AND LIFT ANALYSIS

General Discussion

Flow through the bearing can be separated into three distinct regions. The first region being the gas flow from the source to the pad through a restrictor. This can be thought of as orifice flow since experiments on short tubes show that the orifice pressure-flow law applies (14). Then the gas flows from the exit of the restrictor to extremities of the bearing pad. Radial and longitudinal flow occur in this region simultaneously. Finally, the flow from the bearing pad to the exhaust over lands will be primarily longitudinal. No attempt will be made to determine the distributed pressure distribution over the spherical pad since this is beyond the scope of this thesis. This pressure will be assumed to be uniform over the entire pad area.

Restrictor Flow

The mass flow rate through the restrictor can be written as follows, if subsonic adiabatic gas flow is assumed (15).

$$M_o = C_D A P_s \left[\frac{2k}{(k-1) RT} \left[\left(\frac{P_1}{P_s} \right)^{2/k} - \left(\frac{P_1}{P_s} \right)^{\frac{k+1}{k}} \right] \right]^{1/2} \qquad (3\text{-}1)$$

where T is the absolute temperature of the inlet gas at pressure P_s.

Sonic velocity at the orifice occures when P_1/P_s is less than the critical pressure ratio, $(2/1+k)^{\frac{k}{k-1}}$. The flow is then said to be choked

and the mass flow rate becomes

$$M_{oc} = C_D A P_s \left[\frac{2k}{(k-1) RT} \left[\left(\frac{2}{1+k} \right)^{\frac{2}{k-1}} - \left(\frac{2}{1+k} \right)^{\frac{k+1}{k-1}} \right] \right]^{1/2} \qquad (3\text{-}2)$$

The above equation holds for $P_1/P_s \leq \left(\frac{2}{1+k} \right)^{\frac{k}{k-1}}$ and is independent of downstream pressure, P_1.

Bearing Land Flow

If the bearing land flow is considered to be longitudinal and the following assumptions made:

1) The flowing gas film obeys a polytropic relation
2) Fully developed laminar flow
3) Viscosity is independent of pressure
4) Steady flow
5) No body or inertia forces
6) Isothermal flow

then the mass flow rate can be written as (16),

$$M_L = \frac{bh^3}{24\mu LRT_i} (P_i^2 - P_a^2) \quad . \qquad (3\text{-}3)$$

In addition to the above analysis, the flow through the lands could be considered as orifice flow. In this case, Eqs. (3-1) and (3-2) could be used. The only problem would be the determination or choice of a discharge coefficient.

The choice of equations is dictated by the flow regime. If the Mach number is less than 0.3, the laminar longitudal flow equation can

be used with an error of less than 15% (16). For Mach number greater than 0.3, Eq. (3-1) would be applicable. When the flow velocity reaches sonic velocity, (Mach number = 1), the use of Eq. (3-2) is necessary.

Both Eq. (3-2) and Eq. (3-3) will be compared with the experimental data. A rough velocity computation has shown that choked flow could exist, thus Eq. (3-2) will be compared with experimental results.

Lift

Neglecting the land area, the load carrying capacity or lift of the opposed pad bearing system is given by

$$\mathcal{L} = |P_\ell - P_u| A_p \tag{3-4}$$

where P_ℓ is the assumed uniform pressure over the lower pads and P_u is the pressure over the upper pad. Since the pads are located symmetrically, the projected area, A_p, in any plane parallel to the line of centers of the bearings is the same. Determination of each pressure and the projected area will then yield the total lift provided by the bearing system.

Assuming constant and equally distributed mass flow through the tubes, the pressure in each pad can be found from Eq. (3-3) as a function of h.

$$P_1 = \sqrt{\frac{24\mu LRTM_L}{bh^3} + P_a^2} \tag{3-5}$$

Using subscripts ℓ and u, the pressure difference becomes

$$P_{1\ell} - P_{1u} = \sqrt{\frac{A\mu LRTM_L}{bh_\ell^3} + P_a^2} - \sqrt{\frac{24\mu LRTM_L}{bh_u^3} + P_a^2} \qquad (3\text{-}6)$$

If one of the gap heights and the total clearance are known, then the other gap height can be calculated from

$$h_\ell + h_u = C \quad . \qquad (3\text{-}7)$$

This assumes that the curvature of the bearing can be neglected in comparison with the gap heights as is true in the laminar flow analysis. However some radial flow may take place and the gap height will then be a function of the spherical shape.

An alternative method of calculating the pad pressures is to use the orifice equation as stated before. Then the appropriate values can be substituted into Eq. (3-4) to yield the total lift.

CHAPTER IV

EXPERIMENTAL INVESTIGATION

In order to ascertain the bearing system lift and stiffness as a function of temperature, a model of the system was constructed and tested. Supply pressure, gas flow, applied load, rotor displacement and oven temperature were monitored. A related task was to observe for any instability of the system. High temperature experimentation required means external to the oven for gathering data and special consideration of the materials used to build the bearing system.

Apparatus

In Figure 5, a schematic of the gas flow and pressure measuring set-up is shown. The gas used was untra-high purity (UHP) nitrogen so as to eliminate the need for filtering the working medium. Also, the nitrogen will help prevent oxidation on the surfaces and may nitride the materials. Each bearing received the gas from separate sources. Supply pressures to each bearing were regulated with KGM single stage nitrogen flow regulators. These pressures were measured with Bourdon tube pressure gages having 2 psi graduations. Both gages measure from 4 - 400 psi. Manostat Predictability Flowmeters were used to measure the volume flow rates to each bearing. With the Predictibility Flowmeter, a calibration curve can be calculated directly eliminating the need for experimental calibration. The calibration curves for the flowmeter and pressure gages are presented in Appendix A.

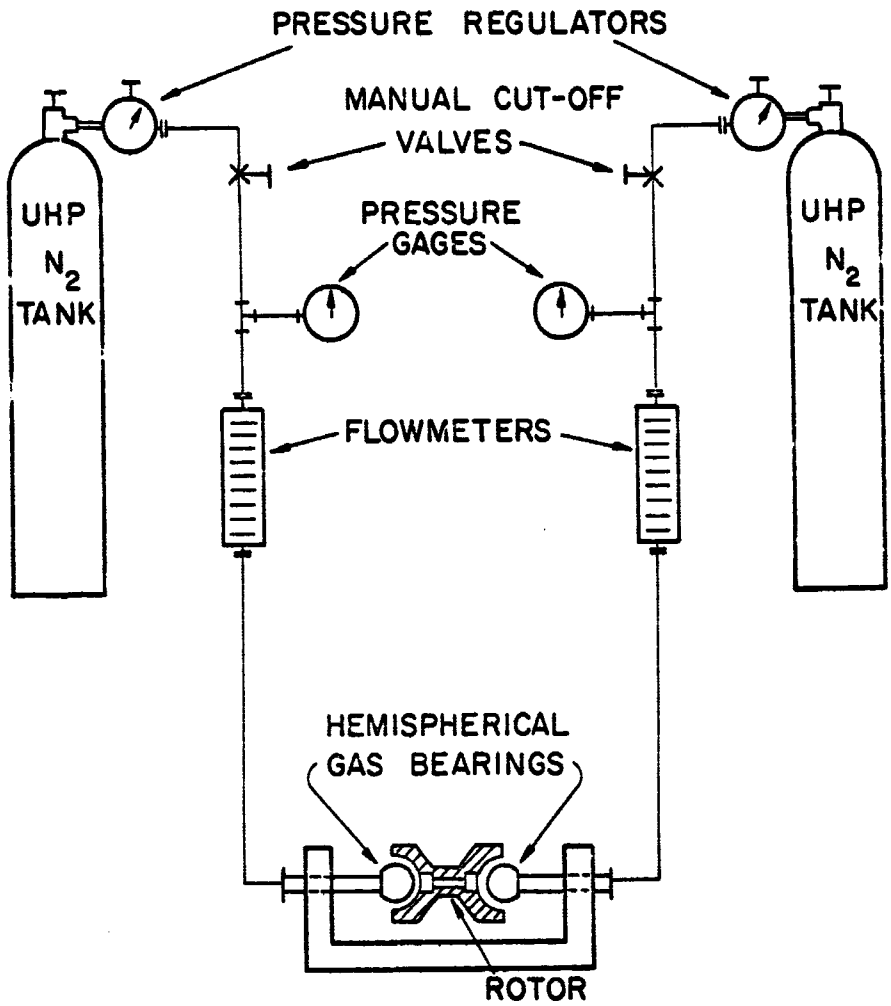

FIGURE 5

Schematic of Gas Flow and Pressure Measurement System

The bearing lift and vertical gap height measurements were made using the balance system shown schematically in Figure 6. A balance arm was mounted on a Bendix 'Free Flex' Pivot which was in turn mounted to a rigid base that could be accurately positioned in three mutually perpendicular directions. On one end of the balance, a viscous damper was used to damp out the oscillations that occur due to the application and removal of the applied loads. To compensate for the unbalanced arm and the damper force, an adjustable counterweight was added to the balance arm opposing the damper. The bearing rotor and lava sting were connected to the balance arm with a short length of nichrome wire at a distant of 1 inch from the flexure pivot. The wire was used to allow the applied force to remain in a constant direction and thereby eliminate the possibility of cocking the rotor. Weights were applied to the balance arm at a distance of 10 inches from the flexure pivot. Therefore, the effective force on the rotor would be magnified by 10. This will be explained in the next section.

Displacement measurements were obtained using a Wayne Kerr vibration and distance meter. Maximum rotor displacements of the order of 0.001 to 0.002 inches were to be measured; thus, an amplification of this displacement was necessary. To accomplish this, the Wayne Kerr probe was positioned over a smoothly ground surface on the balance arm at a distance of 9 inches from the pivot. The displacement of the rotor was sensed at a 1 inch moment arm from the pivot; therefore, the Wayne Kerr measured 9 times the actual displacement, assuming small angular displacement for the balance arm.

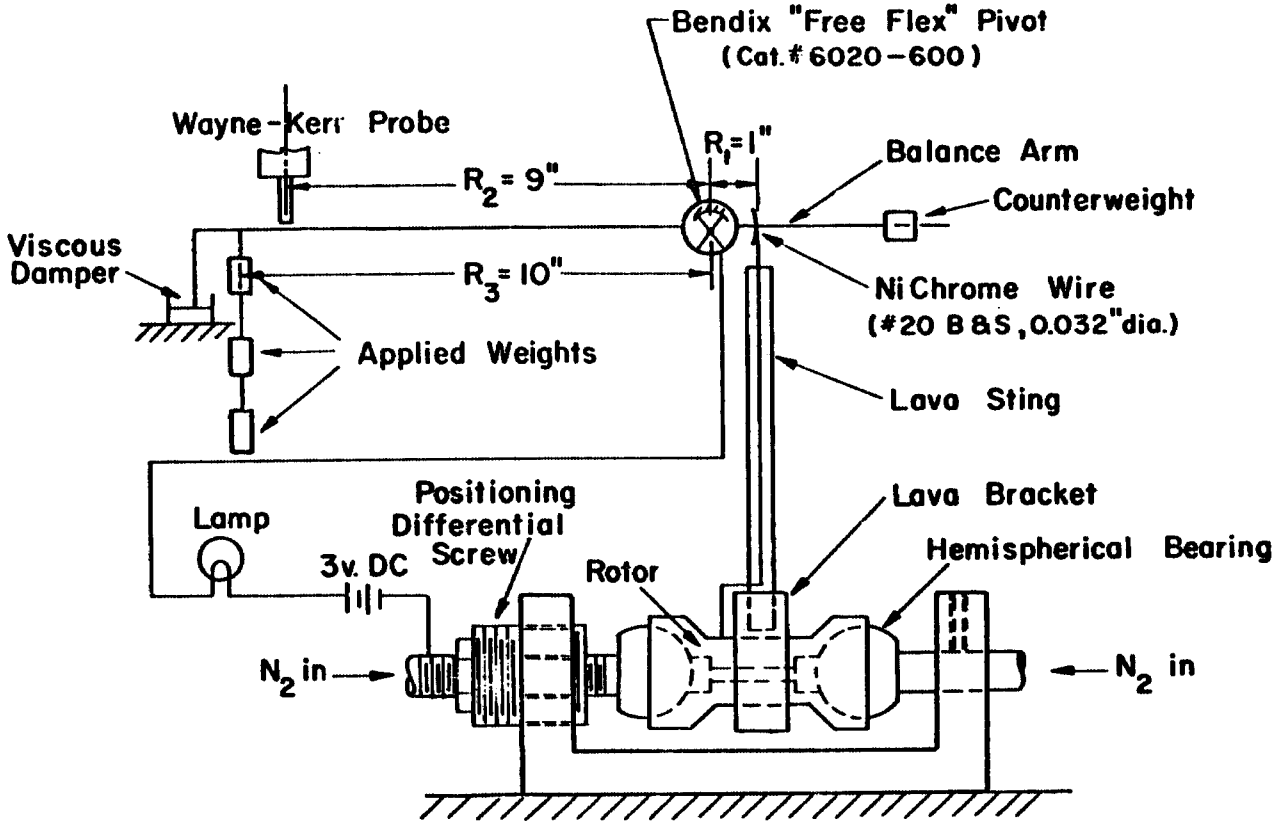

FIGURE 6

Schematic of Balance System

Wayne-Kerr Probe C was used. The calibration curve for Probe C is given in Appendix A. The full scale range for this probe is 0.010 inches. A requirement for distance measurement is that the two surfaces that form the capacitor be parallel. However, if the angle between them is less than 5° the distance measurement will be in error by 0.4 percent. If the angle is as great as 8°, the error will be 1 percent. By visual inspection alone, the angle can be kept less than 8°, thus insuring an error of no more than 1 percent (17).

To determine contact between the rotor and bearings, an electrical circuit across the gap was formed using a 3 volt D.C. source and a pen-light lamp. When contact occured, the circuit would be completed and the lamp would light. Sensitivity of this set-up was improved by placing a voltmeter across the lamp terminals. When the surfaces were barely contacting, the lamp would not light; however, the voltmeter would indicate a slight voltage drop. A zero voltage reading meant complete separation of the surfaces.

A photograph of the entire test apparatus is shown in Figure 7.

The bearing system (rotor and hemispherical bearings) along with the sting, bearing housing and gas supply lines were placed in the oven. At temperatures above the ambient room temperature, insulation was placed on the oven in an attempt to decrease thermal effects on the balance.

Analysis of Balance Arm

1. Rotor Displacement

Displacement of the rotor was to be measured. The rotor and sting

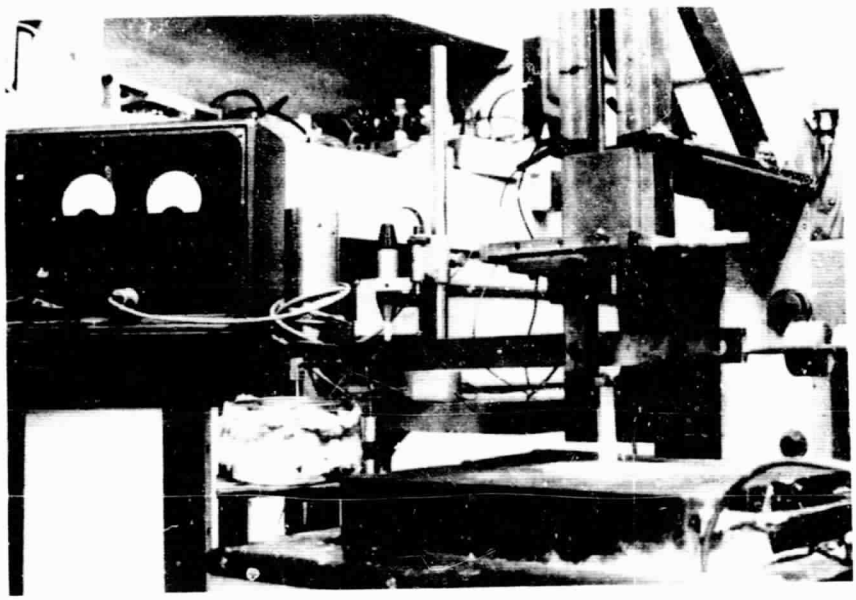

FIGURE 7

Experimental Apparatus

were connected to the balance arm by a flexible wire which was able to wrap around a machined radius on the arm. The deflection of the rotor was then the arc length, s_B, as shown in Figure 8. This arc length can be expressed as follows:

$$S_B = r_B \theta_1 \tag{4-1}$$

Assuming no bending of the balance arm, the angle α_1 is then equal to θ_1. The deflection indicated by the Wayne Kerr meter is $\Delta_1 - \Delta_0$. As long as α_1 is less than 5°, S_A will be $\Delta_1 - \Delta_0$ within 0.4 percent (17). Let $\Delta_1 - \Delta_0$ equal Δ. Therefore the deflection S_B becomes:

$$S_B = r_B \alpha_1 \tag{4-2a}$$

since,

$$\alpha_1 = \theta_1$$

and,

$$\alpha_1 = \frac{S_A}{r_A} = \frac{\Delta}{r_A} \tag{4-2b}$$

then,

$$S_B = \left(\frac{r_B}{r_A}\right)\Delta \ . \tag{4-2c}$$

The ratio of the radii, r_B/r_A, were made 1:9. Thus, S_B was one-ninth of the measured deflection.

Using the values of S_B maximum and r_B, the angle α_1 can be calculated according to Eq. (4-2a) as,

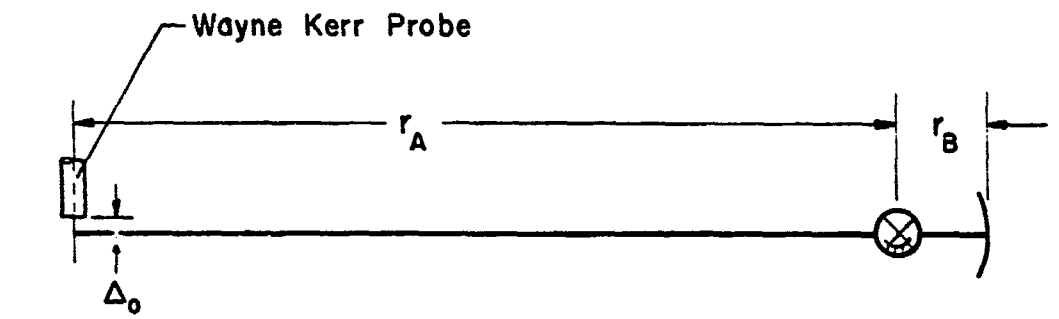

ZERO POSITION

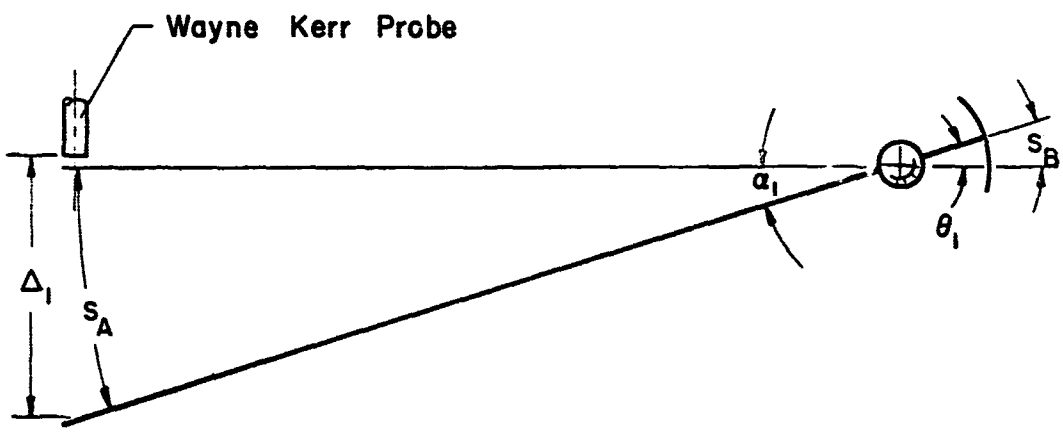

DEFLECTED POSITION

FIGURE 8

Space Diagram of Balance Arm

$S_{B_{max}}$ = 0.002 inches

r_B = 1.00 inches

$\alpha_1 = \frac{0.002}{1.00}$ = 0.002 radians or 0.115°.

Therefore, S_A will equal Δ with an error less than 0.4 percent.

2. Bearing System Lift

Consider the free-body diagram shown in Figure 9 . F_B is the load transmitted from the balance due to the applied load. The weight of the rotor, sting, and associated fasteners are designated as W. The lift provided by each hemispherical bearing is $L/2$. For equilibrium the summation of forces in the y-direction must be zero, assuming all members are rigid, e.g.:

$$\sum F_y = 0$$

therefore,

$$F_B - \frac{L}{2} - \frac{L}{2} - W = 0 \qquad (4\text{-}3a)$$

or,

$$L = F_B - W \; . \qquad (4\text{-}3b)$$

Next consider the free-body diagram of the loaded balance arm as shown in Figure 10. The arm was originally balanced with respect to the damper force and balance arm weight. Therefore, these forces will not be considered in the analysis of the loaded arm. This assumption will

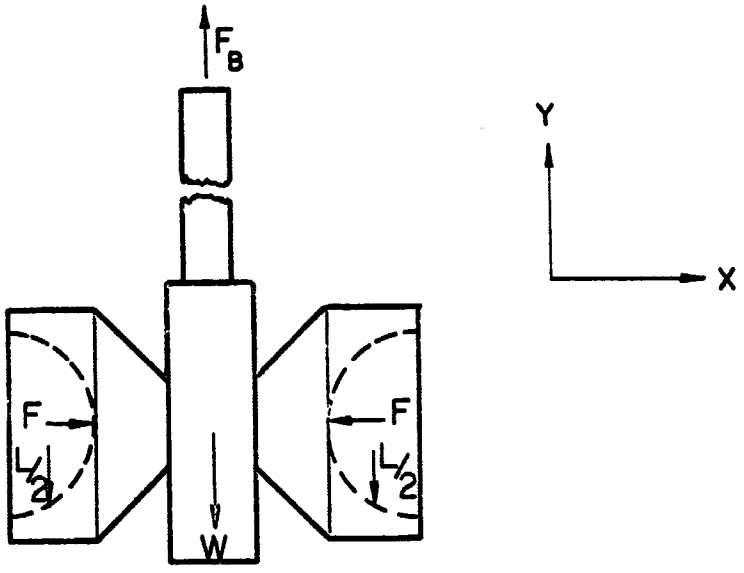

FIGURE 9

Free-Body Diagram of Rotor and Sting

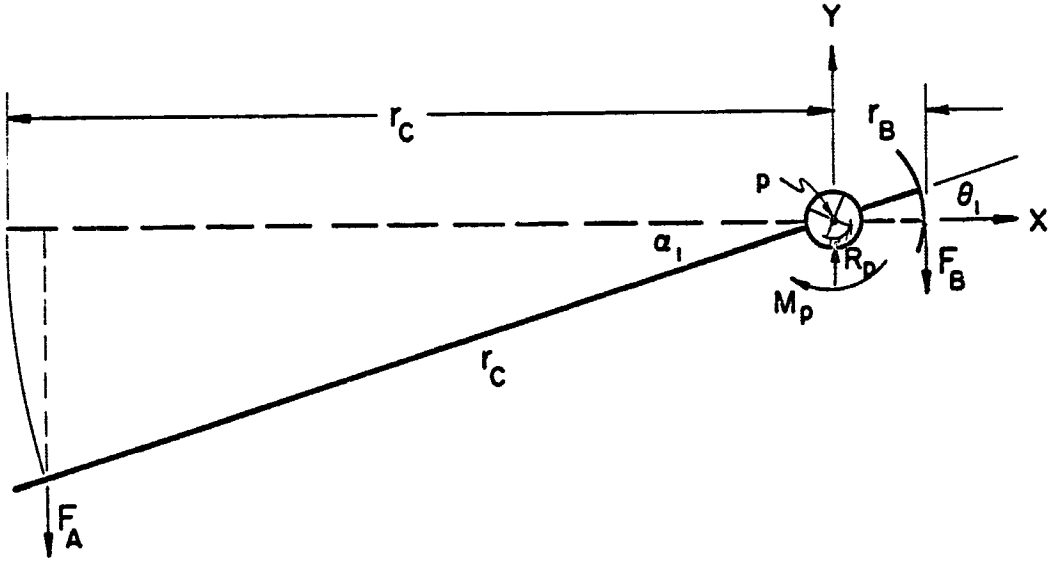

FIGURE 10

Free-Body Diagram of Loaded Balance Arm

hold since angular displacements are very small as stated in the discussion of the balance arm.

The load, F_A, is applied at a distance, r_c, from the flexure pivot center, p. The load transmitted from the sting is F_B. The flexure pivot produces a restoring moment, M_p, when the arm is deflected. The summation of moments about point p, set equal to zero, yields the equilibrium condition, e.g.,

$$\sum M_p = 0, \text{ assume clockwise positive}$$

$$M_p + F_B r_B - F_A r_c \cos \alpha_1 = 0 \qquad (4\text{-}4a)$$

then,

$$F_A = \frac{M_p + F_B r_B}{r_c \cos \alpha_1} \quad . \qquad (4\text{-}4b)$$

In the previous section, the maximum value for α_1 was 0.115°. The cosine of 0.115° is 1.0000. Therefore Eq. (4-4b) becomes:

$$F_A = \frac{M_p}{r_c} + F_B\left(\frac{r_B}{r_c}\right) \quad . \qquad (4\text{-}5)$$

The moment produced by the flexure pivot, M_p, can be calculated knowing the torsional spring constant and the angular deflection. The torsional spring constant is 13.3 lb.-in./radian (18). Angular deflection reaches a maximum of 0.002 radians. Therefore, the flexural pivot moment is a maximum of 0.026 lb-in. The magnitude of r_c in the experimental apparatus is 10 inches. Then the force, M_p/r_c, in Eq. (4-5) is approximately 0.003 pounds. This force is negligible in comparison with

the term $F_B(r_B/r_c)$. Rearranging Eq. (4-5), neglecting the term, M_p/r_c, yields:

$$F_B = F_A\left(\frac{r_c}{r_B}\right) \quad . \tag{4-6}$$

Subsituting Eq. (4-6) into Eq. (4-5), the lift becomes,

$$L = F_A\left(\frac{r_c}{r_B}\right) - W \quad . \tag{4-7}$$

The balance arm was constructed with the ratio of the radii $r_c:r_B$ equal to 10:1. Therefore Eq. (4-7) becomes,

$$L = 10\ F_A - W \quad . \tag{4-8}$$

Results

Prior to the high temperature stiffness tests, the tube flow at room temperature was investigated. The supply pressure and mass flow rate were monitored. The mass flow rate dependence on supply pressure is shown in Figure 11. This is the mass flow through each restricting tube exhausting to the atmosphere. For comparison, Eq. (3-2) is also plotted on the figure. Values of the various constants used are listed below.

$k = 1.40$

$R = 55.16\ \frac{ft\text{-}lb}{lb_m\text{-}^\circ R}$

$T = 535^\circ R$

$A = 1.431 \times 10^{-4}\ in^2$

$C_D = 0.68$

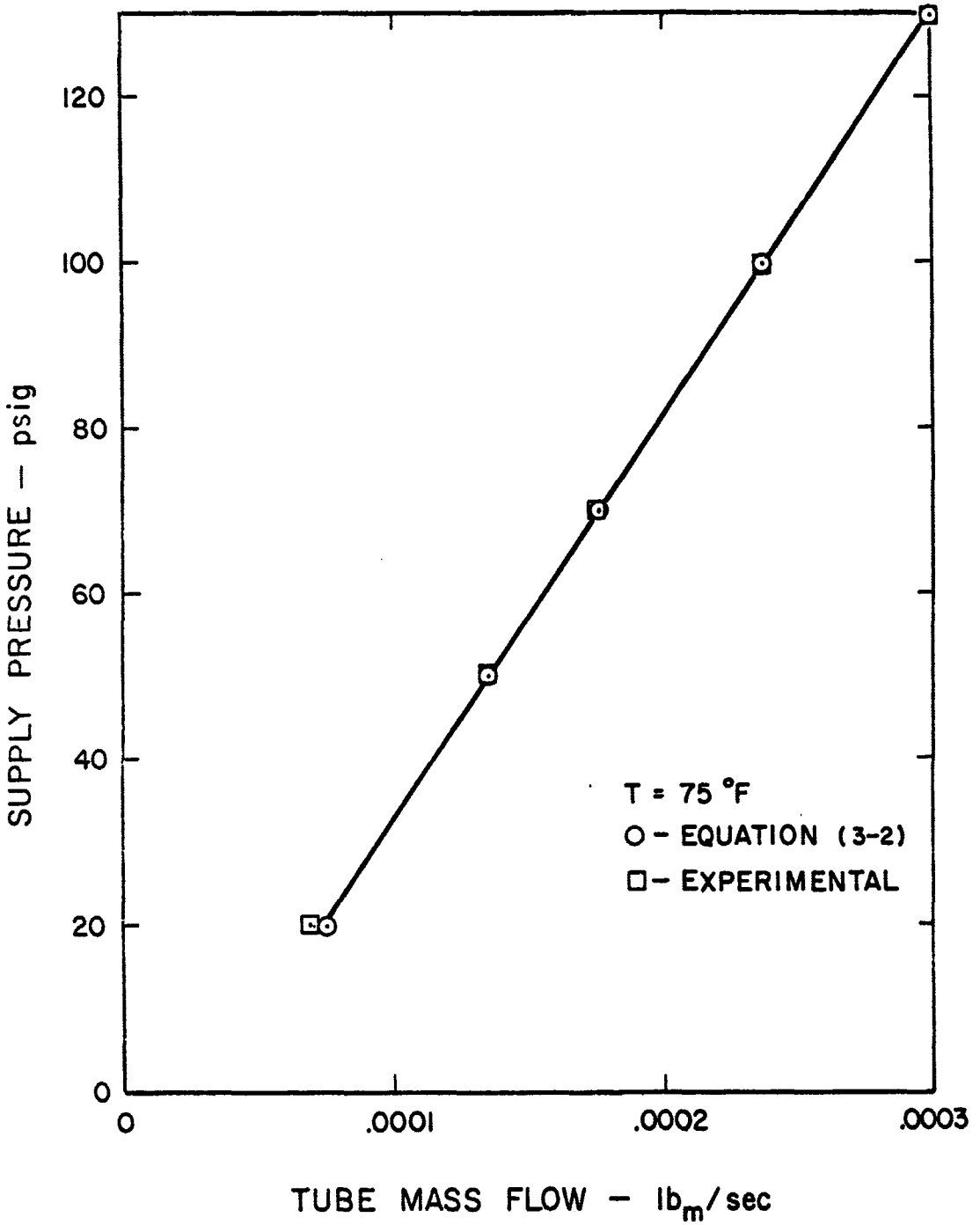

FIGURE 11

Supply Pressure versus Mass Flow Rate for Tubes

At supply pressures above approximately 50 psig, agreement between the orifice equation and the results is very good. As long as the pressure at the exhaust remains less than 0.53 (critical pressure ratio) times the supply pressure, the equation for choked orifice flow is applicable.

The bearing system was assembled and placed in the oven for the next phase of the investigation.

The balance arm was loaded until contact was established between the lower surfaces of the bearing and rotor. Then, the load was removed in increments and the corresponding deflection was measured. The plots of reduced lift versus rotor displacement (vertical gap height) for various ambient temperatures up to 2000°F are presented in Figures 12, 13, 14, 15, 16, 17, 18, and 19.

All of the aforementioned plots are for a supply pressure of 100 psig. At room temperature, 1000°F, and 2000°F pressures of 80 and 120 psig were used in addition to 100 psig. The 80 psig supply pressure provided only approximately 1.65 pounds maximum lift at 75°F. At 120 psig, the lift was approximately 10% greater than that for 100 psig, however the mass flow rate was also greater. A value of load carrying capacity of about 2 pounds and minimum flow rate were desired. A compromise was made in selection of the supply pressure and 100 psig was selected.

The maximum load carrying capacity was approximately 2.5 pounds at 75°F and 100 psig. At 2000°F and 100 psig, the load carrying capacity was reduced to approximately 1.8 pounds. This was due to the decrease

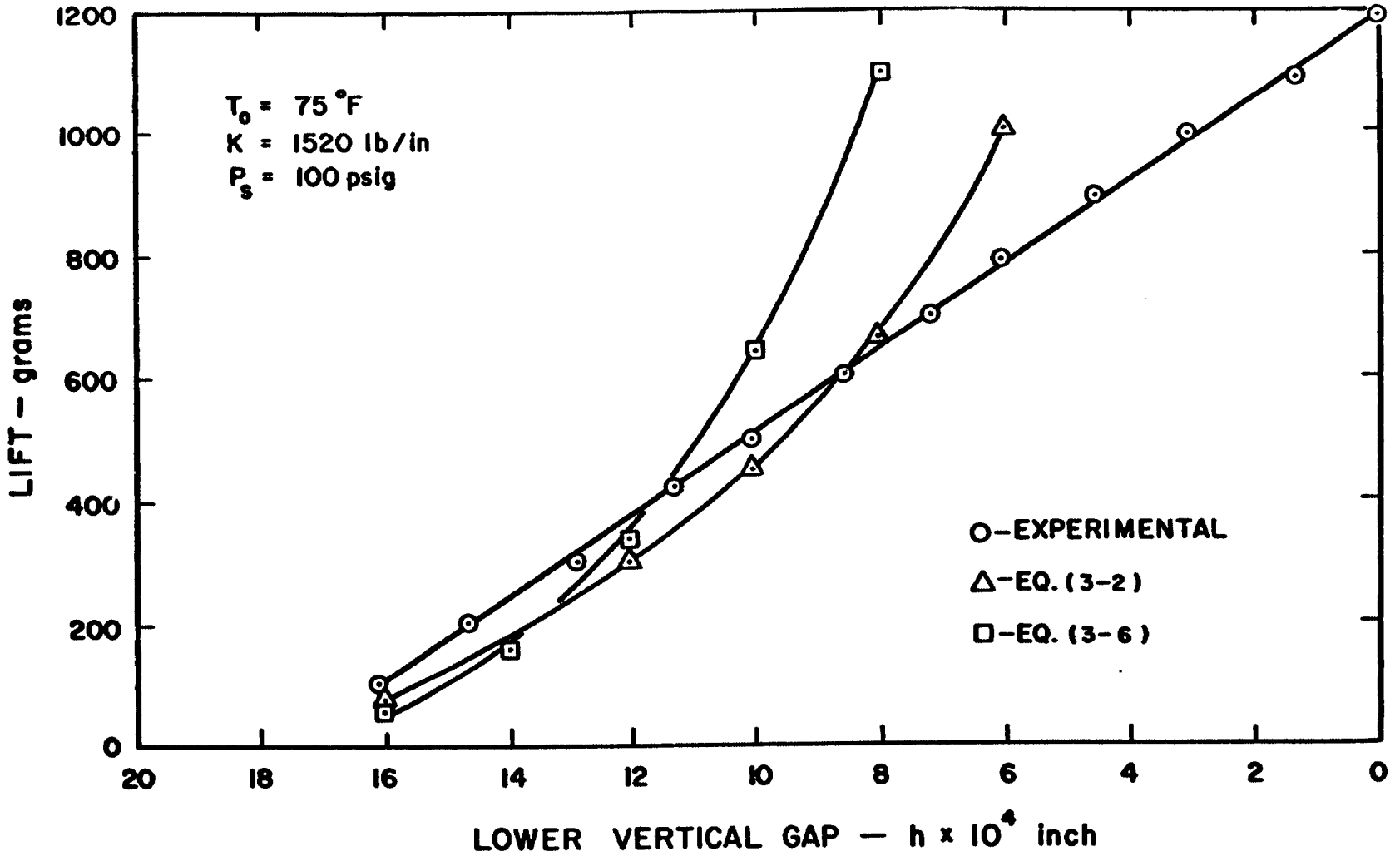

FIGURE 12

Lift versus Vertical Gap Height at T_0 = 75°F

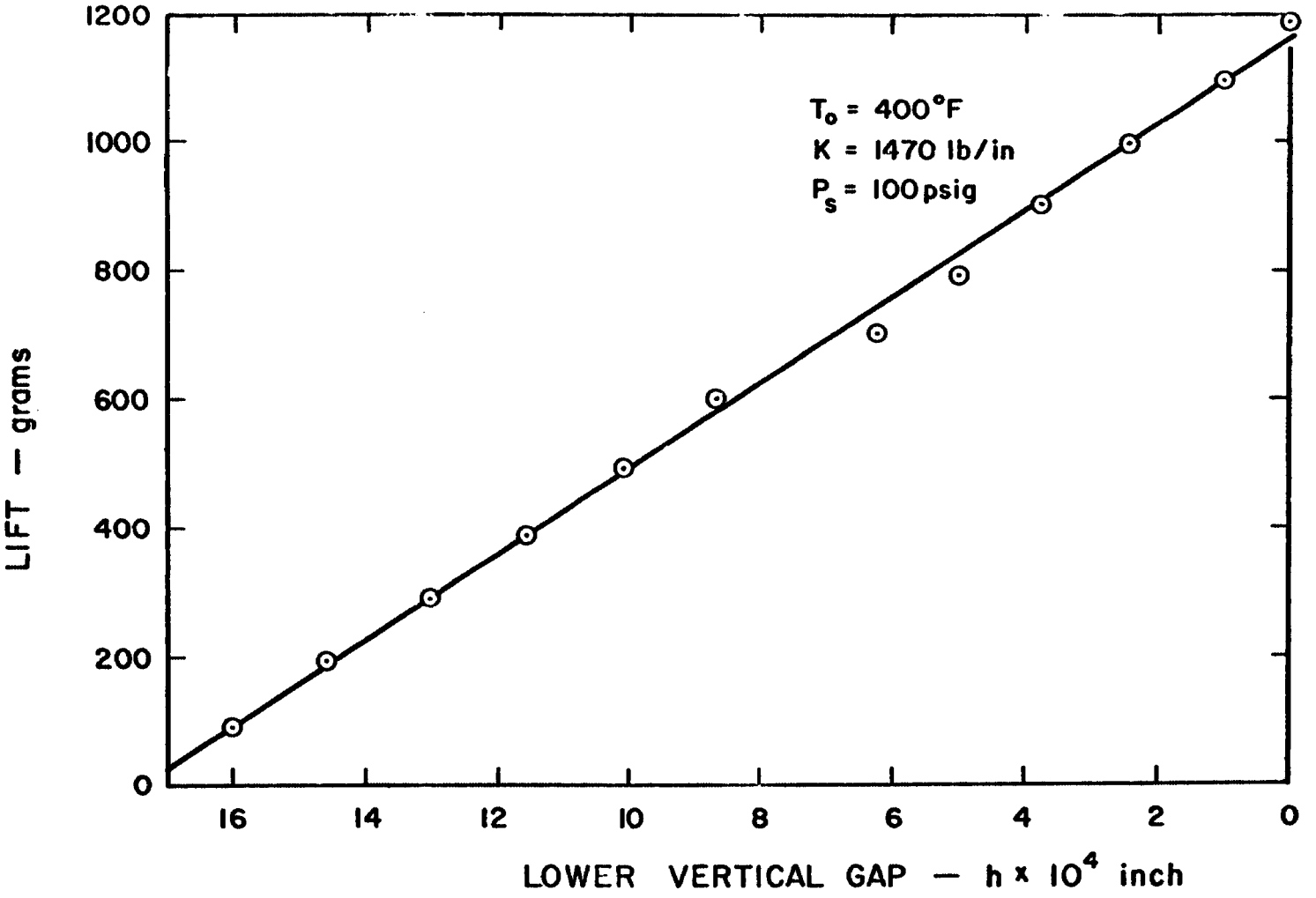

FIGURE 13

Lift versus Vertical Gap Height at T_0 = 400°F

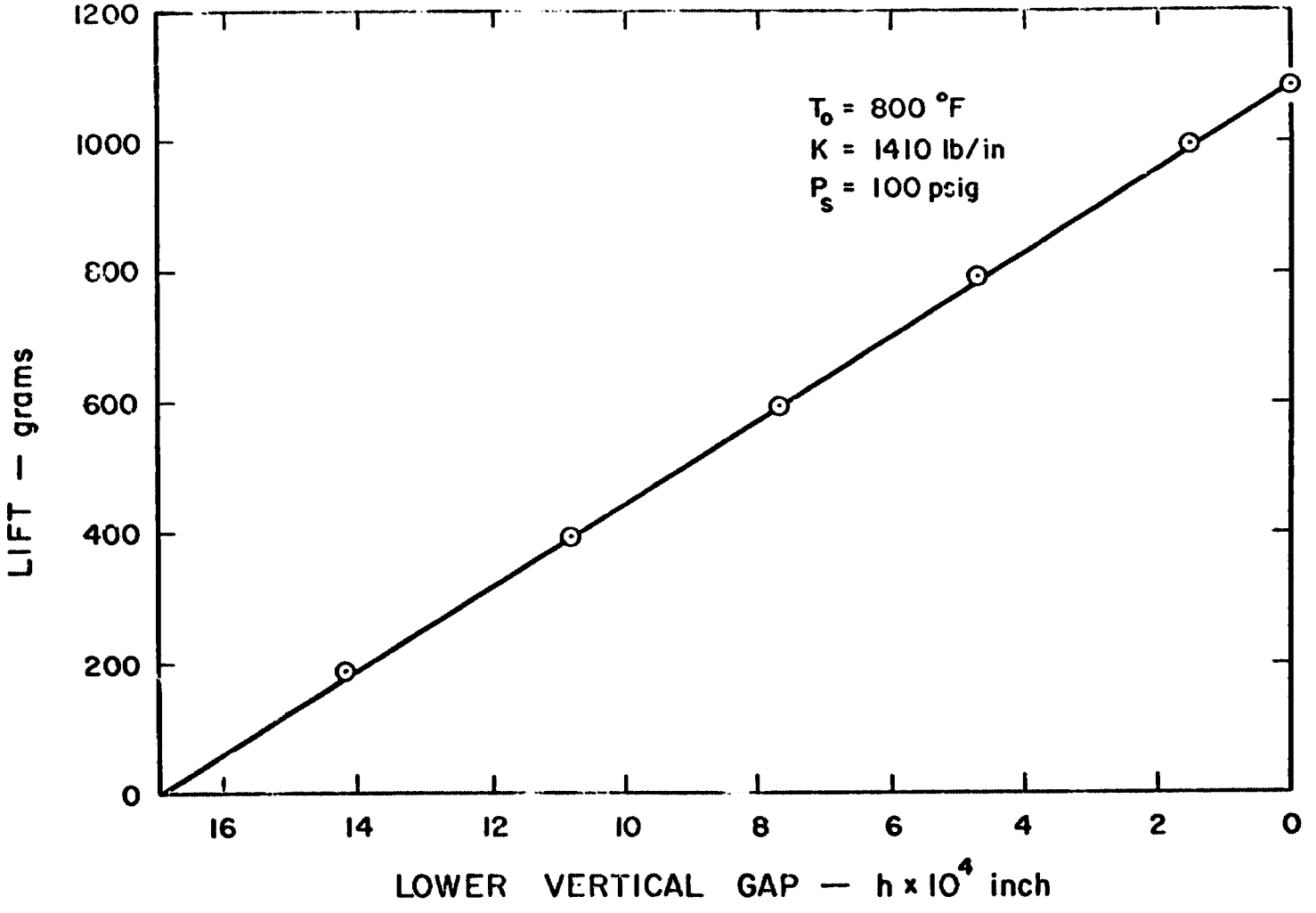

FIGURE 14

Lift versus Vertical Gap Height at T_0 = 800°F

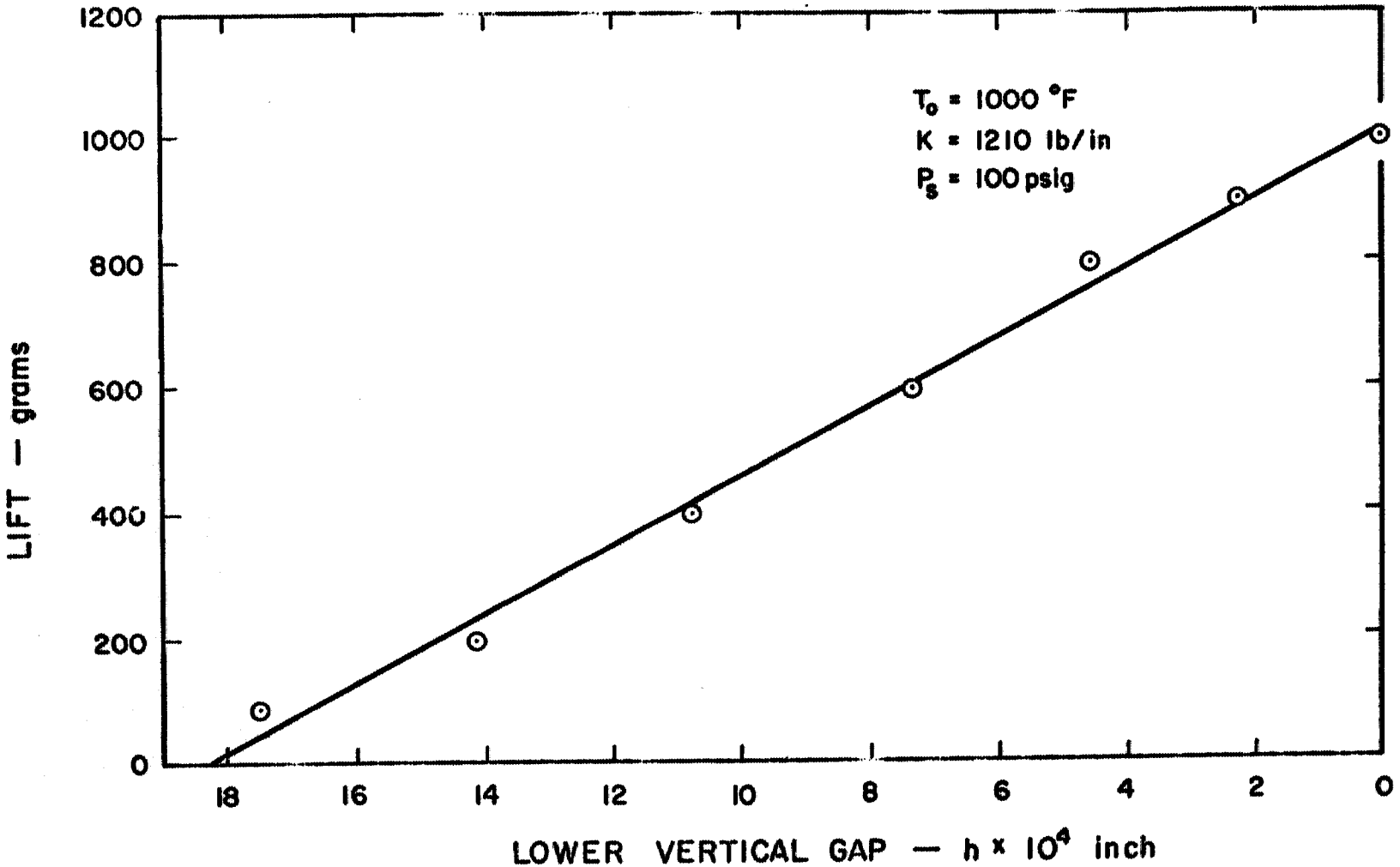

FIGURE 15

Lift versus Vertical Gap Height at T_0 = 1000°F

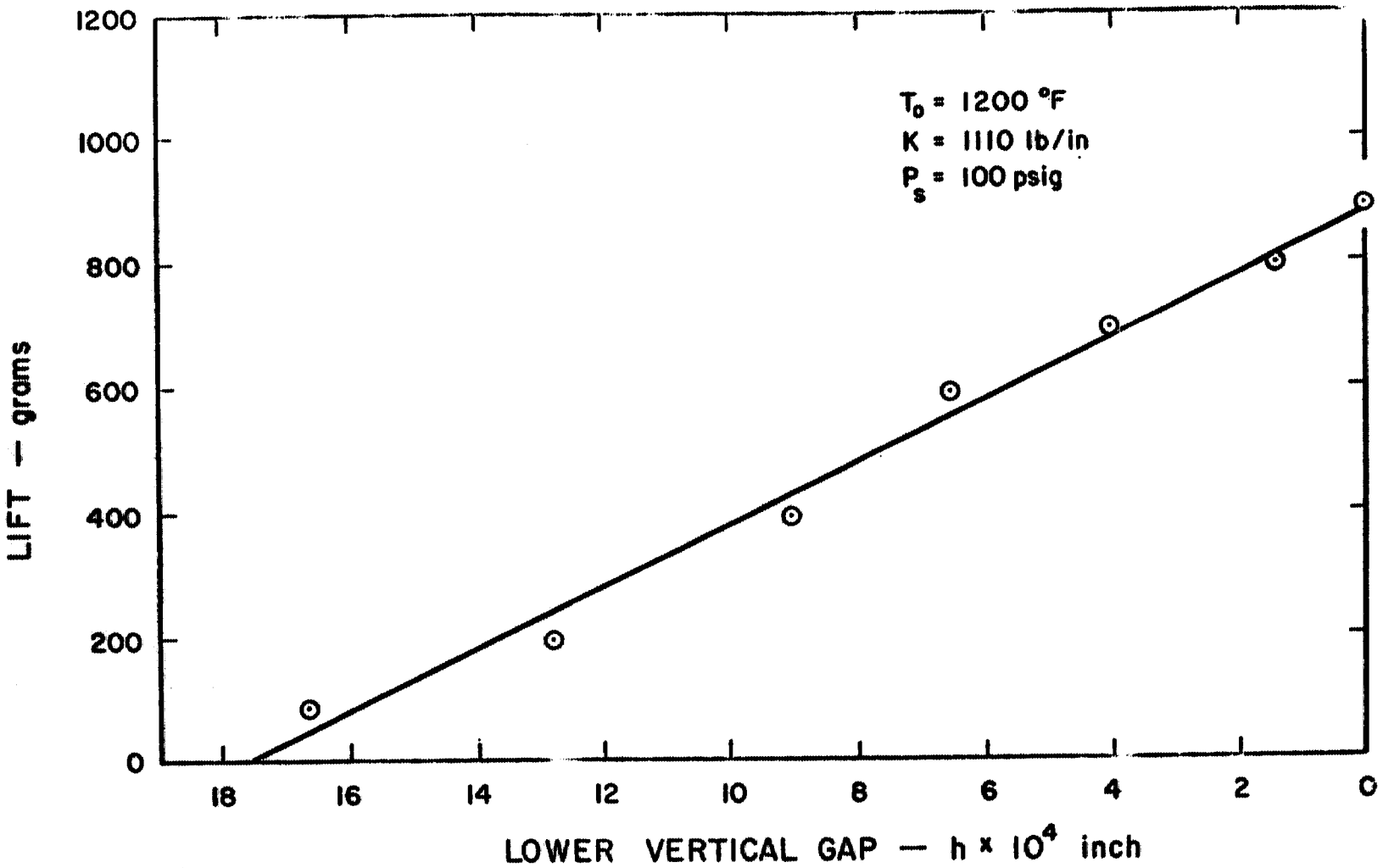

FIGURE 16

Lift versus Vertical Gap Height at T_0 = 1200°F

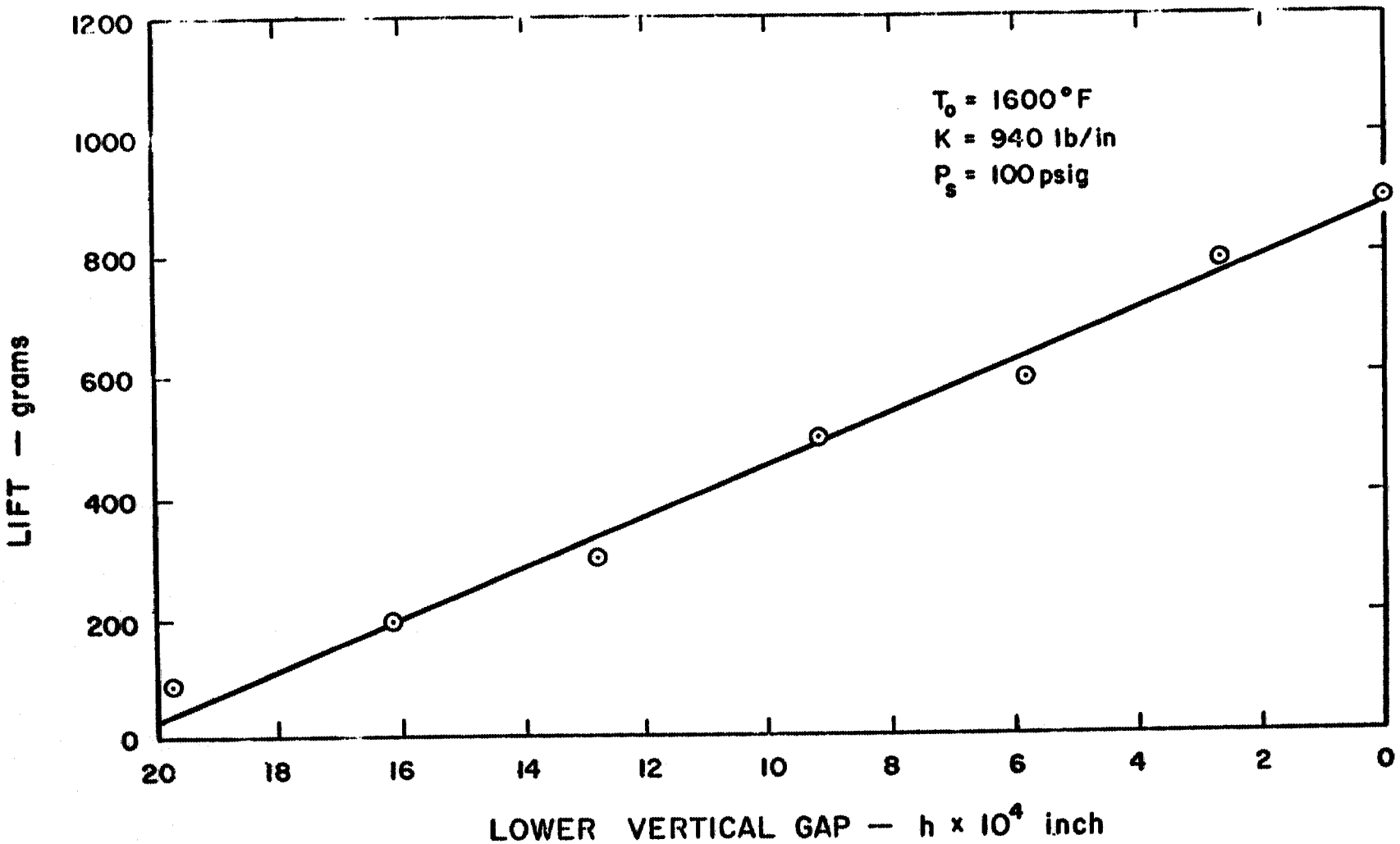

FIGURE 17

Lift versus Vertical Gap Height at T_0 = 1600°F

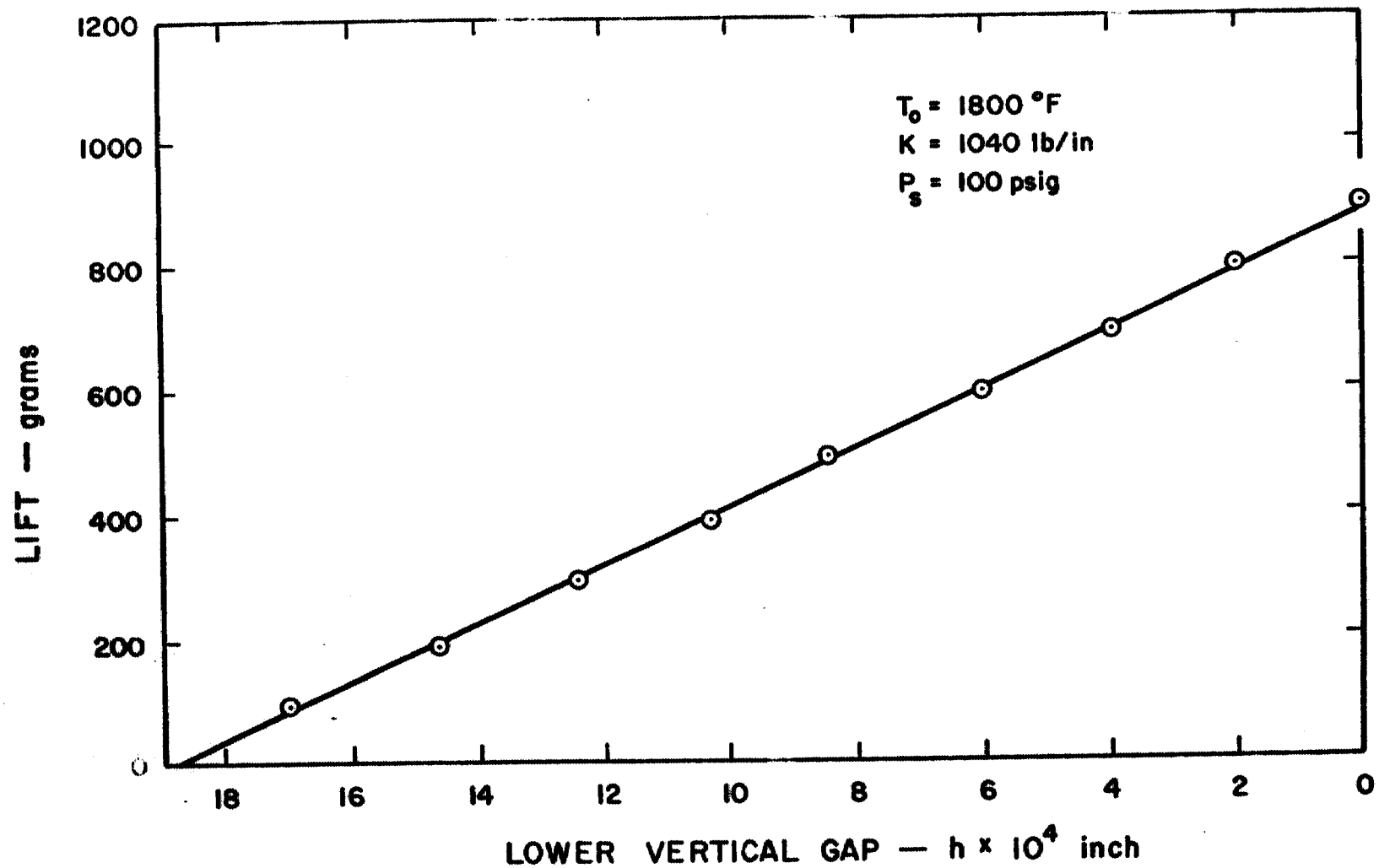

FIGURE 18

Lift versus Vertical Gap Height at T_0 = 1800°F

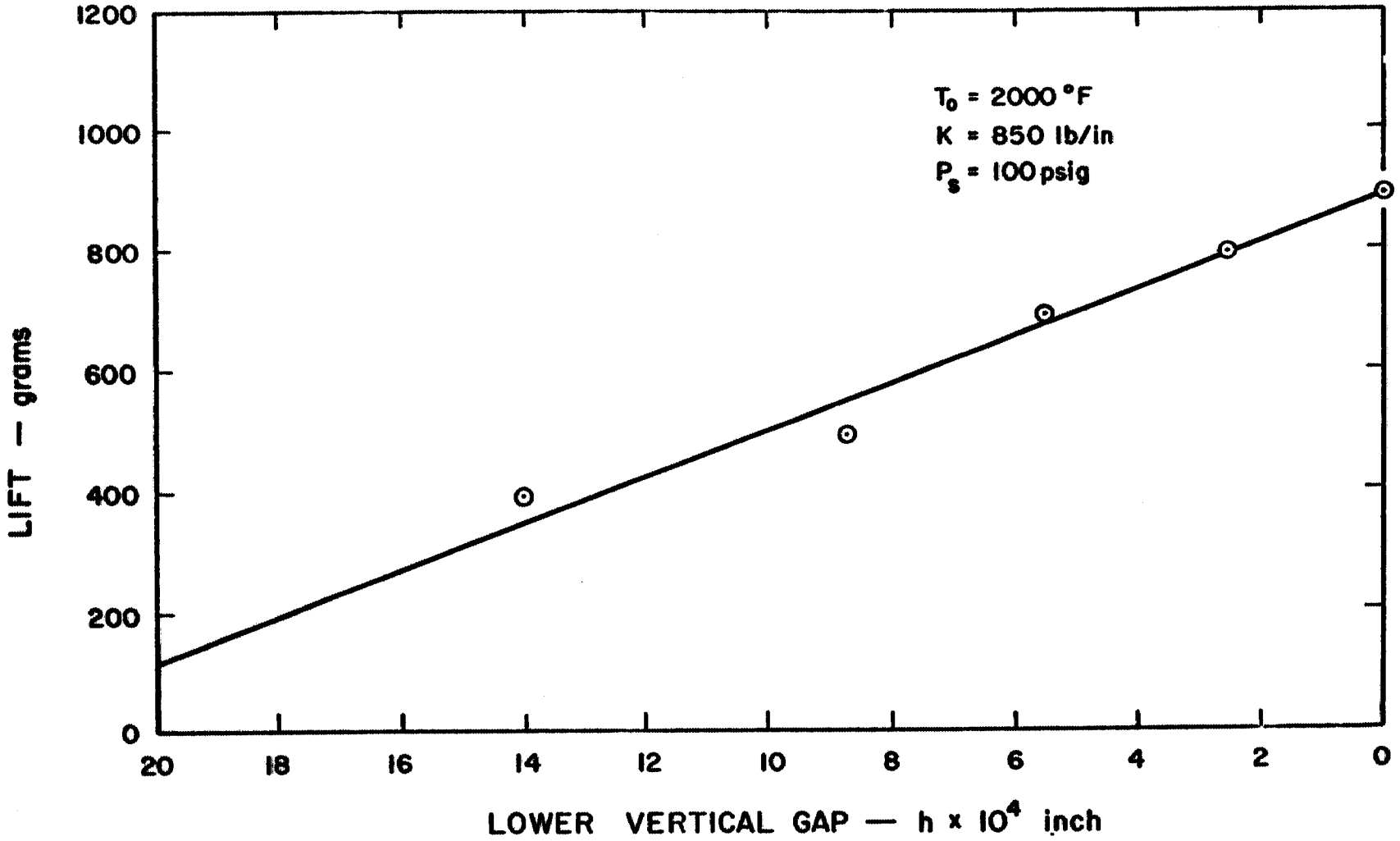

FIGURE 19

Lift versus Vertical Gap Height at T_0 = 2000°F

in mass flow rate and the increase in clearance as the temperature increased. A plot of mass flow rate versus oven temperature is shown in Figure 20. This is the total mass flow rate supplied to one bearing. Thus, the flow through each restrictor will be one-third of this total.

For comparison purposes, the lift as a function of gap height at 75°F was calculated from the laminar longitudinal flow analysis and also from the choked orifice pressure-flow law. The following values were used.

$\mu = 1.04 \times 10^{-5}$ $lbm/sec\text{-}ft$
N_2 @ 446°R

$R_{N_2} = 55.16 \ \frac{ft - lb_f}{lb_m - {}^\circ R}$

$T = 446^\circ R$

$M_L = 203.7 \times 10^{-6}$ $lb_{m/sec.}$

$b = 2$ inches

$L = 0.125$ inches

$k = 1.40$

$A_p = 0.125$ in^2 per bearing, normal to applied load direction

$C_D = 0.61$

The results are shown plotted in Figure 12. Agreement between the choked pressure-flow law theory is within 15% for values of upper and lower gap heights that are within 0.001 inch of one another. When the lower gap height is 0.0008 inches or less the theory does not agree. Better agreement between theory and results in the range, $0.0008 \leq h_\ell \leq 0.0017$ inch, could be achieved by modifying the discharge coefficient. The laminar longitudal flow analysis yields results which are in poor agreement with

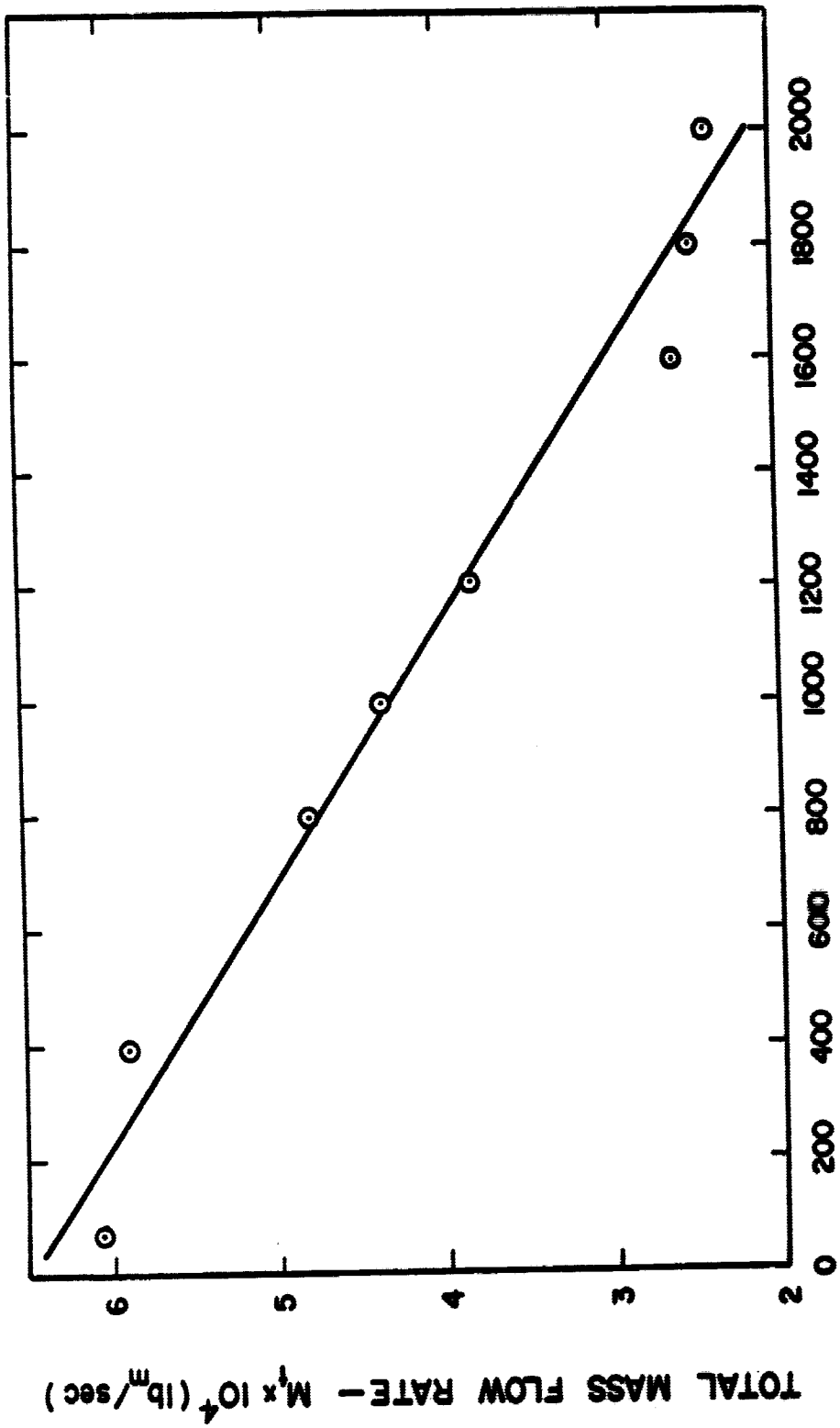

FIGURE 20

Mass Flow Rate versus Oven Temperature

with the experimental results.

As the temperature increased, the clearance between the bearing and rotor also increased. This was due to different coefficients of thermal expansion for the rotor and bearing materials. These coefficients are listed in Table 2. No attempt will be made to calculated the change in clearance, since the exact temperature gradient across the bearing and rotor materials in unknown, and insufficient thermal expansion coefficient data is available.

A least squares curve fit was made on each of the lift versus deflection curves. The slope is therefore the static stiffness of the bearing system. This stiffness is plotted versus oven temperature in Figure 21. The stiffness ranged from 1520 to 850 pounds per inch over the temperature range of 75°F to 2000°F.

No instabilies were observed throughout the entire test. However, there could have been some turbine torques developed in the film which would not have been detected by this apparatus. The determination of any turbine torques will be left for further study.

After the tests were completed, the bearing system was disassembled and the bearing and rotor surfaces were inspected. These surfaces were found to be in excellent condition except for discolored spots that were due to the hot gas. In Figures 22 and 23, the rotor and bearing condition after being heated to 2000°F are shown. All other surfaces had a slight scale due to the oxidation.

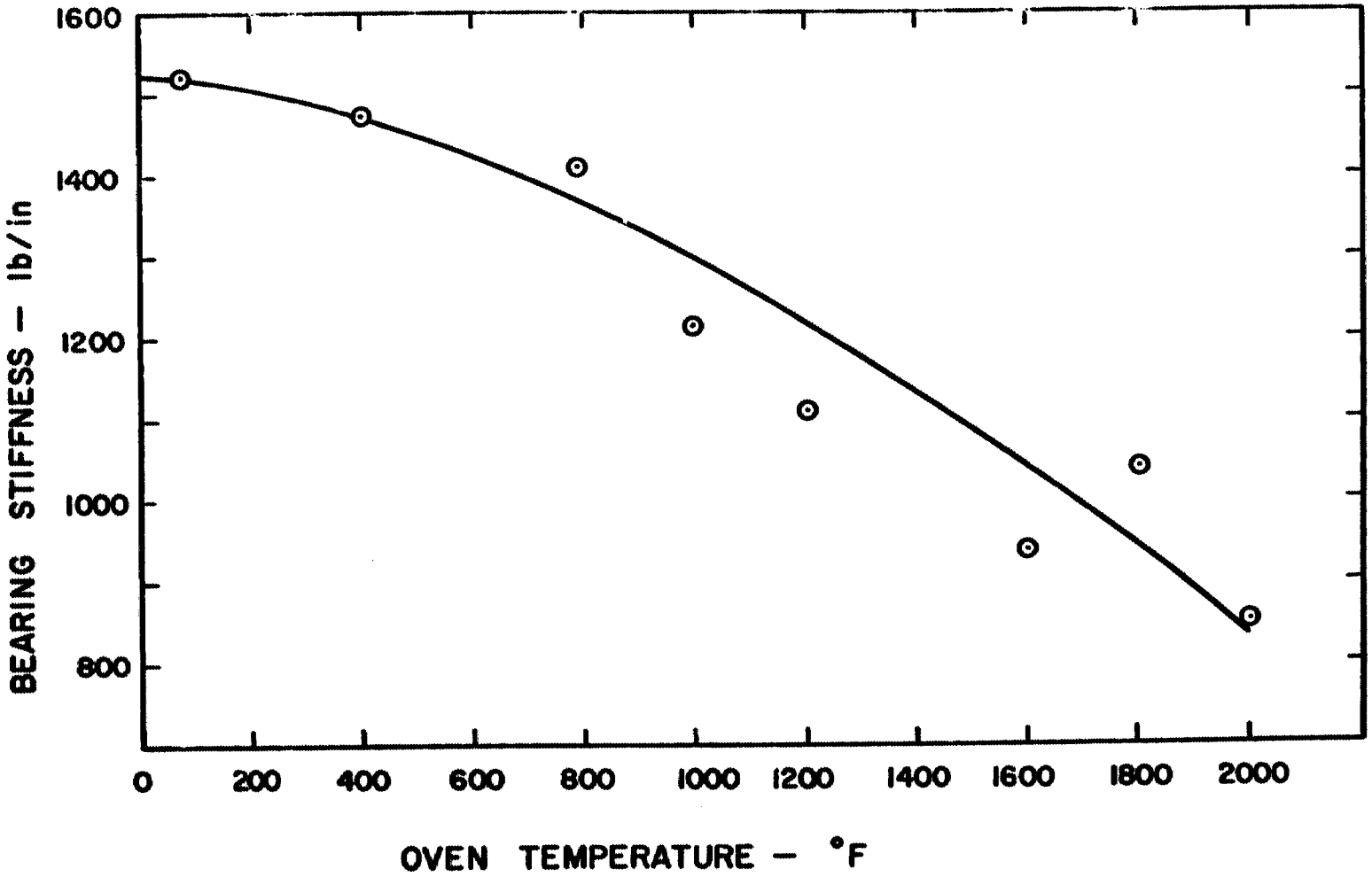

FIGURE 21

Bearing Stiffness versus Oven Temperature

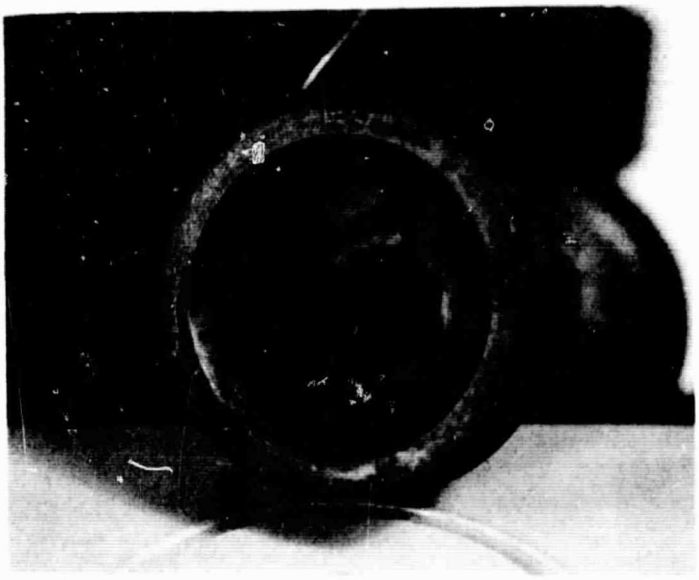

FIGURE 22

Rotor Condition After 2000°F Test

FIGURE 23

Bearing Condition After 2000°F Test

Discussion of Results

As has been stated previously, the system stiffness is of considerable importance. The stiffness decreased as the clearance or gap between the bearing and rotor increased. This clearance increase was caused by the larger coefficient of thermal expansion of the rotor in comparison to the bearing. The static stiffness is defined as dL/dh. Using the choked orifice equation, the lift, $\mathcal{L}$, is inversely proportional to h. Therefore, the stiffness is inversely proportional to h^2. For an increase in the clearance, a corresponding decrease of stiffness occurs. The exact value of this decrease can not be calculated since the properties of the film are also changing with increases in film temperature. The film temperature was not measured in this experiment.

The maximum percent deviation from linearity is 8% and occurs at low lift values. At 1600°F and 2000°F the deviations are the greatest. A noticable drift was present in the Wayne Kerr meter at 1600°F and could have been the major cause of the deviation. Drift was so excessive at 2000°F that a limited amount of data was taken. The standard error in the slope was calculated for each plot of lift versus deflection and was found to be less that 1% in all cases.

The gap height at zero lift shifts a small amount. This is due to the controller on the oven which allows the temperature to range from + 10°F to - 50°F about the preset desired value.

The maximum load carrying capacity required can be estimated from an analysis of the applied forces. These forces are due to the large accelerations to which the skin friction meter is subjected. The maximum

value for the acceleration is 10 g as specified in the design guidelines listed in Chapter I. If the mass of the supported members (target, counterweights, and rotor) is constructed to be 0.18 lb_m, then the load carrying capacity must be at least 1.8 lb_f. This can be shown from an analysis of Newton's second law.

$$F = \frac{m\ a}{g_c} \tag{4-9}$$

where,

F = force, lb_f
m = mass, lb_m
a = acceleration, ft/sec^2
$g_c = 32.2\ \frac{lbm - ft}{lb_f - sec^2}$

Substituting m = 0.18 lbm and a = 10g ft/sec^2 yields F = 1.8 lb_f.

The undamped natural frequency of the bearing system can be calculated from the following equation.

$$\omega_N = \sqrt{K/m} \tag{4-10}$$

where K equals the system stiffness. For a mass of 0.18 lb_m and a stiffness of 1520 lb/in, ω_N becomes 1805 radians/sec or 288 Hz. At 2000°F the stiffness is 850 lb/in and ω_N becomes 1350 radians/sec or 215 Hz.

The deviation between the experimental and calculated curves in Figure 12 was excessive at values of small gap height. One of the assumptions made in order to calculate the bearing system lift was that

the mass flow was equally distributed through each of the restrictors. As the gap height becomes smaller the pressure will increase at the exit of the restrictor, thus allowing the flow regime to change from choked to unchoked. This will cause an unequal distribution of the mass flow; therefore, the analysis used in this thesis will not be applicable for small gap heights. The matching of flow through the tube, Eq. (3-1), with the flow through the lands would be necessary; however, this was beyond the scope of this thesis.

CHAPTER V

CONCLUSIONS AND RECOMMENDATIONS

Based on the experimental investigation presented in Chapter IV, the following conclusions are made.

1) The bearing system design is adequate, with respect to the load capacity, temperature, and space limitation specifications, for support of the skin friction target area and counterbalancing components.
2) With use of the proper materials, extreme environmental conditions can be tolerated.
3) Stiffness of the bearing system is not optimal and could be improved. Maximum stiffness is obtained with minimum clearance. The limiting factor in decreasing the clearance is the degree of lapping accuracy obtainable. Stiffnesses ranged from 1520 lb/in to 850 lb/in over the entire temperature range considered.
4) The mass flow was within 6×10^{-4} lb_m/sec with a supply pressure of 100 psig.
5) The lift of the bearing system ranged from 2.5 lb to 1.8 lb. To increase the lift, a higher supply pressure could be used. But this would also increase the flow rate which was kept to a minimum because of the amount of gas needed over the entire test period. A compromise was made concerning these factors. Another alternative would be to in-

crease the effective pad area.

6) Theoretical analysis of the lift proved to be inaccurate for certain ranges of the gap.

Modifications of the design are recommended as follows:

1) Separate the pad areas more effectively by enlarging the exhaust grooves and making a circular exhaust groove to connect the three existing ones.
2) Construct bearing and rotor from the same material; thus eliminating the differing expansion rates.
3) Coat all surfaces except the lubricating surfaces with an oxidation resisting material such as a ceramic.
4) Increase the supply pressure up to the value that yields the maximum allowable flow. This will increase the lift and stiffness.

Recommendations for further study include:

1) Theoretical determination of the pressure distribution over the entire surface of the bearing will lead to a more accurate determination of the lift and stiffness.
2) A means for direct measurement of the pressure at various points over the pad would be extremely valuable.
3) Measure the film terperature as function of ambient temperature.
4) Theoretical and experimental determination of the optimum tube and bearing land dimensions for maximum stiffness will provide much needed design information.

5) Develop a means to accurately lap spherical surfaces.

LIST OF REFERENCES

1. "Conceptual and Preliminary Design of the Hypersonic Ramjet," Statement of Work, Exhibit AL-4947, April 15, 1965, Langley Research Center, Langley Station, Hampton, Virginia.

2. Ashby, Richard G., "The Counterbalancing of Accelerations in a Skin Friction Meter," Master's Thesis, The University of Virginia, Charlottesville, August 1968, pp. 1-2.

3. Gross, W. A., Gas Film Lubrication, New York, John Wiley and Sons, 1962.

4. Laub, John H. and Norton, Robert H., Jr., "Externally Pressurized Spherical Gas Bearings," ASLE Transactions, Vol. 4, 1961, pp. 172-180.

5. Corey, T. L., Tyler, C. M., Rowand, H. H., and Kipp, E. M., "Behavior of Air in the Hydrostatic Lubrication of Loads Spherical Bearings," Transaction of the ASME, July 1956, pp. 893-898.

6. Speen, G. B., and Grant, J. M., "Omni-Directional Support of Spheres Using Externally Pressurized Gas Lubricated Bearing Pads," ASLE Transactions, Vol. 5, 1962, pp. 375-384.

7. Geary, P. J., Fluid Film Bearings, South Hill, British Scientific Instrument Research Association, 1962.

8. Boyd, J., Kaufman, H. N., and Raimondi, A. A., "Basic Hydrostatic Pad Design," Lubrication Engineering, 1965, pp. 391-394 and pp. 439-442.

9. Rippel, H. C., Cast Bronze Hydrostatic Bearing Design Manual, Cleveland, Cast Bronze Bearing Institute, 1963.

10. Denhard, W. G., and Pan, C. H. T., "Application of Gas-Lubricated Bearings to Instrument," Presented at the ASME Lubrication Symposium, Las Vegas, 1968.

11. Gross, W. A., "A Review of Development in Externally Pressurized Gas Bearing Technology Since 1959," Presented at the ASME Lubrication Symposium, Las Vegas, 1968.

12. Rolled Alloys, Inc., Technical Data Book, Rolled Alloys, Inc., Detroit, Michigan.

13. Johnson, Alan R., "High-Temperature High-Strength Iron-Base Alloys," Machine Design, September 9, 1965, pp. 44-48.

14. Letham, Daryl L., "Fluidic System Design," reprinted from Machine Design, February 17, March 3, 7, 31, 1966, pp. 15-16.

15. Bisson, E. E., and Anderson, W. J., Advanced Bearing Technology (NASA SP-38), Washington, D. C., U. S. Government Printing Office, 1964, p. 128.

16. Blockburn, J. F., Reethof, G., and Shearer, J. L., Fluid Power Control, Cambridge, The M. I. T. Press, 1960, pp. 78-80.

17. The Wayne Kerr Laboratories, Ltd., Vibration Meter B731A, Distance Meter DM 100, Instruction Manual, The Wayne Kerr Laboratories, Ltd., Chessington, England.

18. The Bendix Corporation, Technical Information for Bendix 'Free Flex' Pivots, Pub. No. 19U-6-6411A, The Bendix Corporation, Utica, New York.

19. Monostat Corporation, Predictability Flowmeters, Monostat Corporation, New York.

APPENDIX A

Flowmeter

Calibration of the Monostat Predictability Flowmeters was obtained using predictability charts (19). A calibration curve for the conditions of flow (T = 75°F, P = 100 psig) is given in Figure 24. The accuracy of these meters is within 2% full scale.

Pressure Gages

The pressure gages were calibrated using a standard dead weight tester. Calibration curves are given in Figures 25 and 26 for the two gages used. Note that there is some hysteresis present, which is due to the internal friction and slack motion of the pressure gage components.

Wayne Kerr Meter

The "C" probe was calibrated using grade B gage blocks. For this grade gage block, the tolerance is 8×10^{-6} inches. The calibration curve is shown in Figure 27.

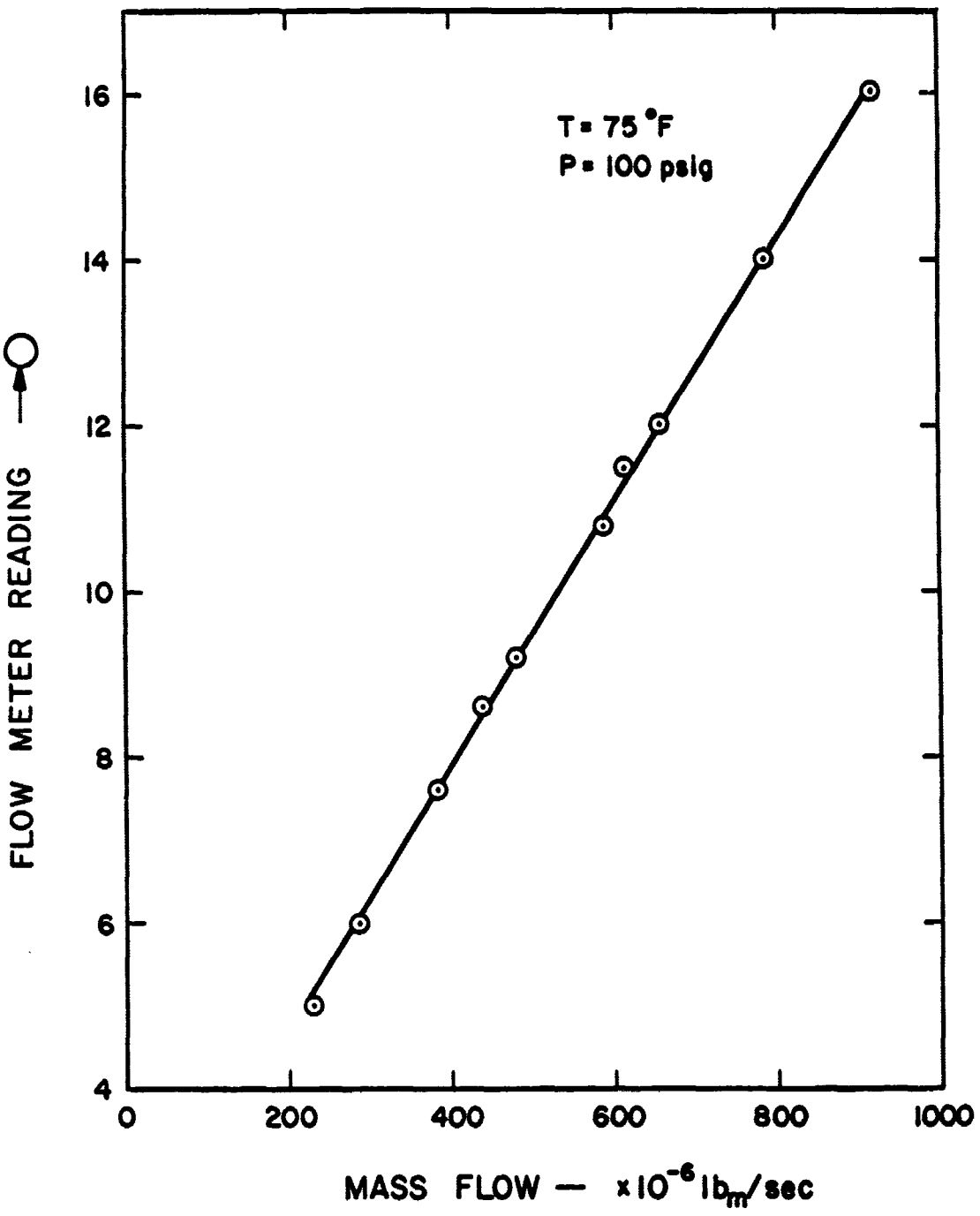

FIGURE 24

Predictability Flowmeter Calibration Curve

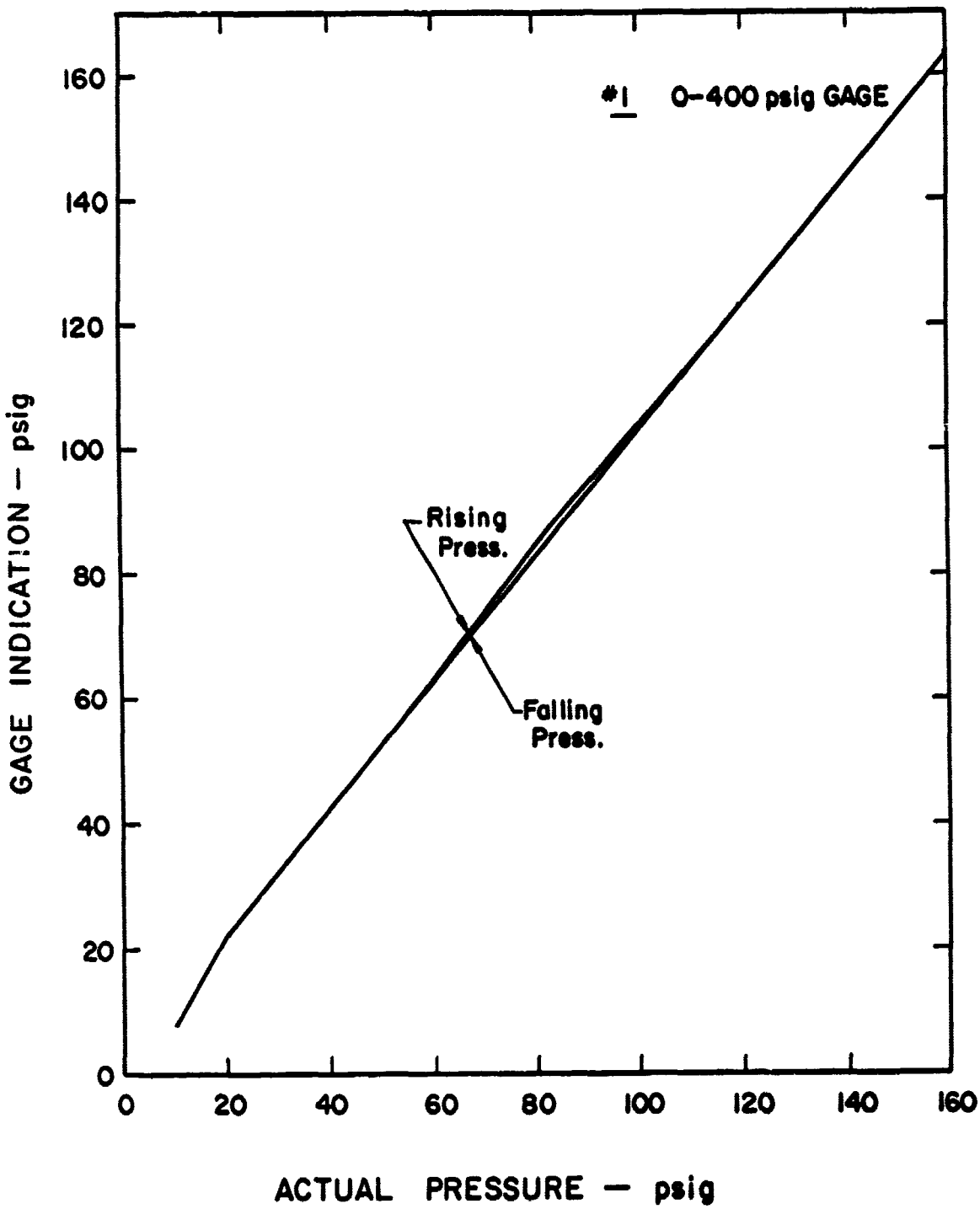

FIGURE 25

Pressure Gage #1 Calibration Curve

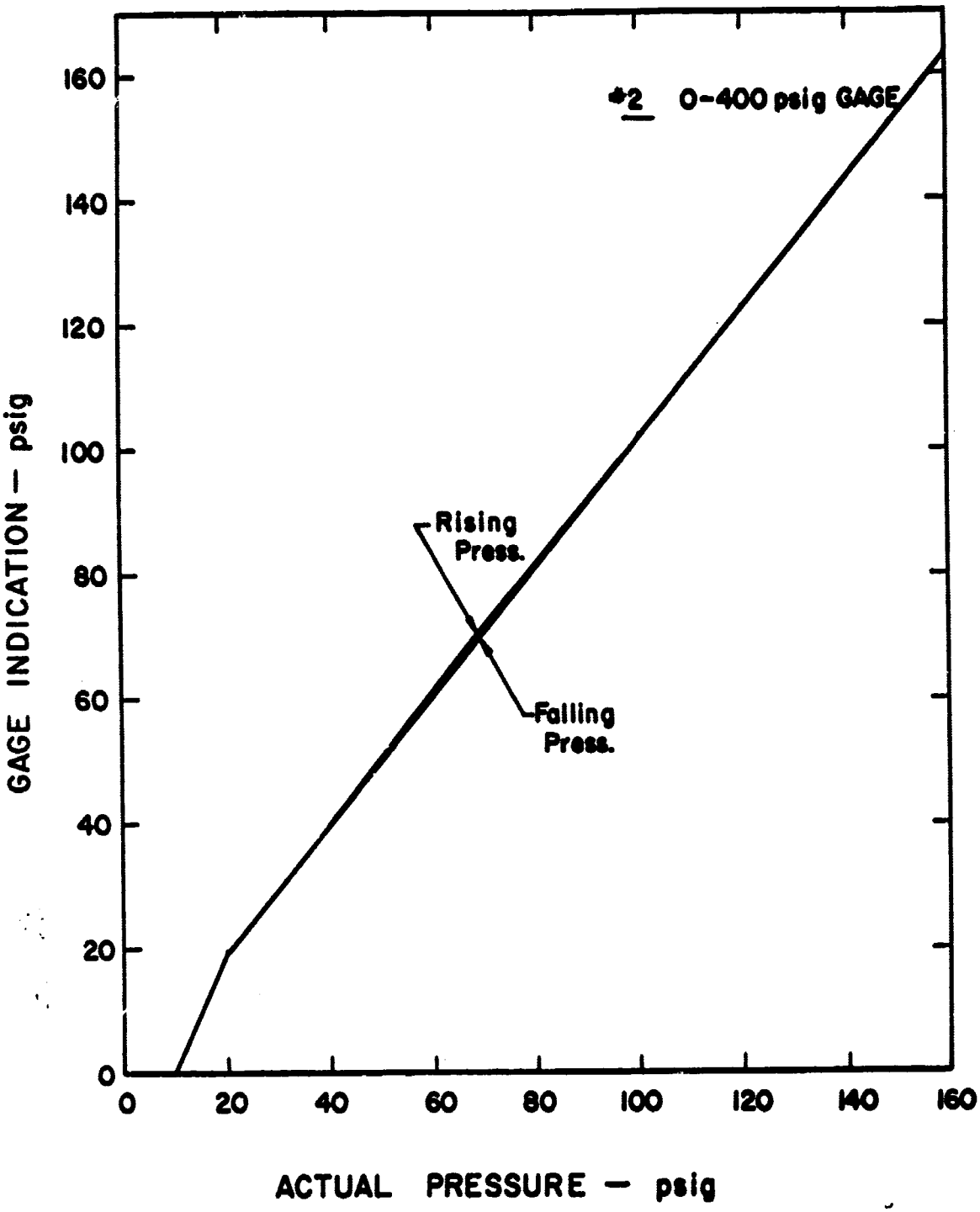

FIGURE 26

Pressure Gage #2 Calibration Curve

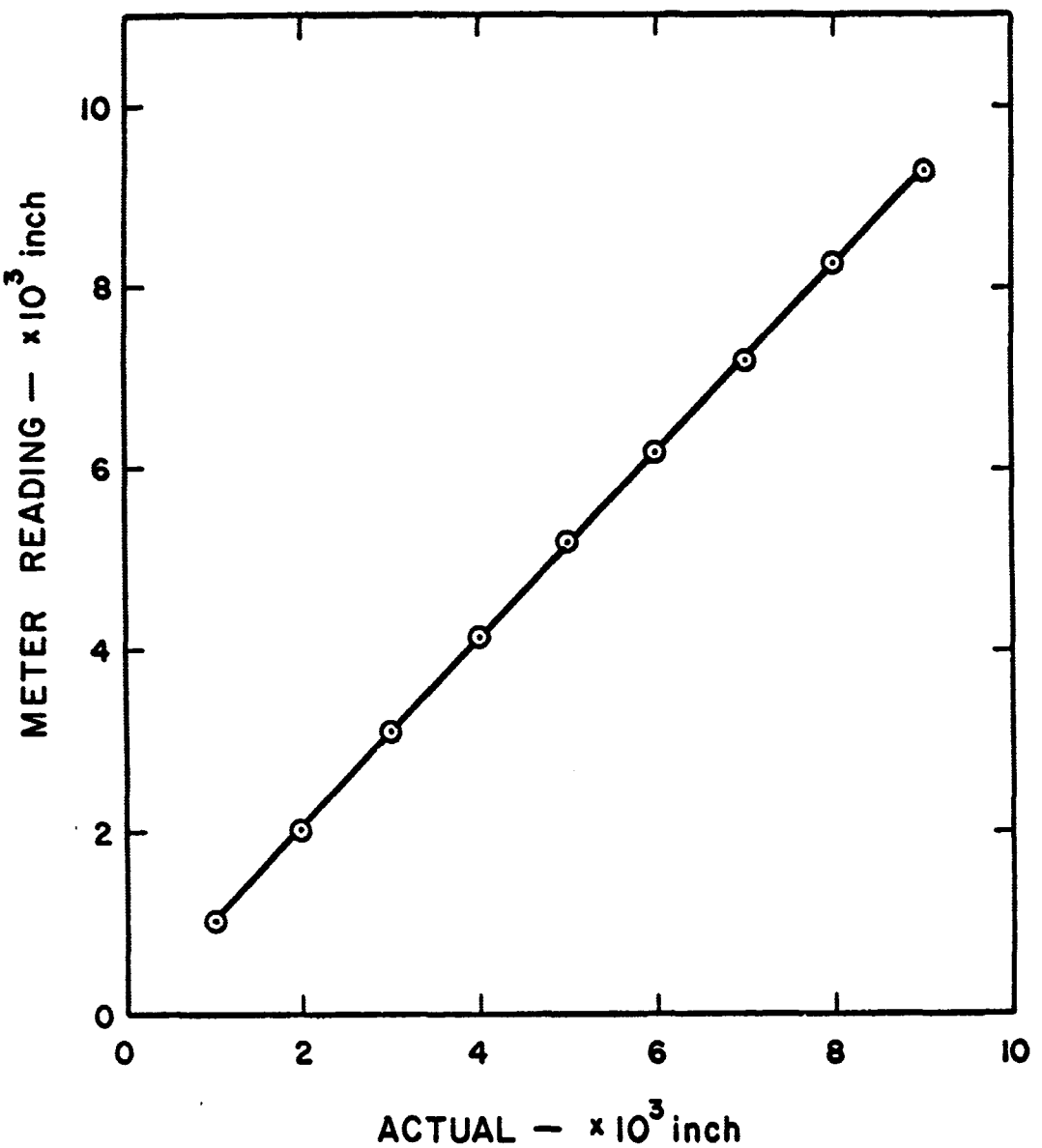

FIGURE 27

Calibration Curve of Wayne Kerr Probe "C"

CHAPTER VI

ACCELERATION COUNTERBALANCING

This chapter contains a complete reproduction of a Masters Thesis presented to the School of Engineering and Applied Science by Richard Grant Ashby, August 1968.

THE COUNTERBALANCING OF ACCELERATIONS IN A SKIN FRICTION METER

A Thesis

Presented to

the Faculty of the School of Engineering and Applied Science

University of Virginia

In Partial Fulfillment

of the Requirements for the Degree

Master of Mechanical Engineering

by

Richard Grant Ashby

August 1968

APPROVAL SHEET

This Thesis is Submitted in Partial Fulfillment of

The Requirements For The Degree of

Master of Mechanical Engineering

_____

Author

Approved:

_____

Faculty Advisor

_____

Dean, School of Engineering and
Applied Science

August 1968

ABSTRACT

Design considerations for an acceleration insensitive skin friction meter are described. The meter, which is to be mounted in a free f'ight aircraft, is made insensitive to accelerations by using a counterbalancing technique. The counterbalanced system consists of two components which are free to rotate and are connected by crossed metal bands.

A theoretical and experimental analysis is performed to determine the effects of any existing rotational spring rate of the crossed metal bands.

Finally, recommended band sizes, which are based on a stress analysis, are given.

ACKNOWLEDGMENTS

The author wishes to thank Dr. J. W. Moore for his aid and advice during the investigation and writing of this thesis.

He also wishes to thank his fellow students for their helpful advice and criticisms in the design of the research apparatus. Also, recognition is due to Mr. Frederick Schenkel for his assistance and encouragement in the fabrication of the research apparatus.

Graduate study was made possible by the financial support of a teaching assistantship provided by the Mechanical Engineering Department. Financial assistance for the thesis research was provided by the National Aeronautical and Space Administration under NASA Grant NGR 47-005-026. This support is greatly appreciated.

TABLE OF CONTENTS

TABLE OF CONTENTS (continued)

LIST OF TABLES

PAGE

TABLE

LIST OF FIGURES

LIST OF FIGURES (continued)

LIST OF SYMBOLS

A	Cross-sectional area, $(inch)^2$
C_1, C_2	Symbol used to denote particular cylinder
C_1R_1	Instantaneous center of rotation
e	Eccentricity, inches
E	Modulus of Elasticity, lb/in^2
E_1, E_2	Potential energy, in-lb
F, F_1, F_2	Force, pounds
g	Acceleration due to gravity, 386 in/sec^2
I_A	Area moment of inertia, in^4
I, I_1, I_2	Mass moment of inertia, $lb\text{-}in\text{-}sec^2$
k	Spring rate lb/in
K	Constant of proportionality, in-lb/rad
$\ell, \ell_1, \ell_2, \ell_3, \ell_4$	Length, inches
ℓ_b	Initial length of band, inches
ℓ_s	Initial length in space, inches
L	Length, inches
m_1, m_2, m_3, m_4, m_5	Mass, slugs
M_n	Induced torque, in-lb
M	Bending moment, in-lb
n	Constant, dimensionless
N	Normal force, pounds
O_1, O_2	Center of Rotation
P	Initial band tension, pounds
P_A, P_1, P_2	Induced band tension, pounds

LIST OF SYMBOLS (continued)

R_o	Radius of band curvature, inches
r, r_1, r_2, R	Radius, inches
S_y	Yield Stress, lb/in^2
S_b	Bending Stress, lb/in^2
S_p	Initial tension stress, lb/in^2
S_{PA}	Induced loading stress, lb/in^2
t	Band thickness, inches
T_A	Applied torque, in-lb
T_o	Temperature increase, °f
T_R	Restoring Torque, in-lb
$\ddot{x}$	Linear Acceleration, in/sec^2
W	Weight, pounds or grams
y	Distance from neutral surface, inches
$\ddot{y}$	Linear acceleration, in/sec^2
'	(prime) Denotes value of variable after thermal expansion
$\alpha, \alpha_1, \alpha_2$	Angle of rotation, radians
$\dot{\alpha}, \dot{\alpha}_1, \dot{\alpha}_2$	Angular velocity, rad/sec
$\ddot{\alpha}\ \ddot{\alpha}_1\ \ddot{\alpha}_2$	Angular acceleration, rad/sec^2
$\beta_{1,2}$	String angle, degrees
Δ	Change in value of variable, dimensionless
γ	Coefficient of thermal expansion, in/in °F
$\phi_{1,2}$	String angle, degrees

LIST OF SYMBOLS (continued)

$\psi_{1,2}$	String angle, degrees
θ_o	Vibration amplitude, radians
$\theta, \theta_1, \theta_2, \theta_3$	Angular displacement, radians or minutes
$\dot{\theta}_1, \dot{\theta}_2$	Angular velocity, rad/sec
$\ddot{\theta}, \ddot{\theta}_1, \ddot{\theta}_2$	Angular acceleration, rad/sec^2
ω	Resonace or natural frequency, cps or Hertz
μ	Coefficient of friction, dimensionless

CHAPTER I

INTRODUCTION

This thesis deals with the development and analysis of a technique to counterbalance a skin friction meter so that it will be insensitive to the vibrations and accelerations of a high speed aircraft during flight conditions.

Background

Currently, much research work is being done to find the correlation between the theoretical parameters and the actual aerodynamic skin friction drag of an aircraft. Also, work is being done to determine the in-flight thrust of a rocket or jet engine. To solve the above problems, the direct measurement of aerodynamic skin friction drag is necessary.

Research work dealing with the development of a system for the direct measurement of skin friction drag is presently being conducted as a joint effort between the Electrical and Mechanical Engineering Departments at the University of Virginia. The research is being sponsored by the Force Measurement Group of NASA at Langley, Virginia.

The skin friction meter is to be used to make thrust measurements of a ramjet engine mounted below a high speed experimental aircraft at altitudes up to 123,000 feet and at speeds up to Mach 8. The specifications used to guide the development of the skin friction meter (1) will be listed here since they will be referred to several times in this thesis.

1) Force measurement range: The meter is to be capable of measuring a force in the range of 0.7 to 7 millipounds.
2) The meter must withstand sustained ambient temperatures of 2000°F.
3) Vibration: The meter is to be capable of operating in environmental levels of 0.06 inch double amplitude at 10-55 cps and 10 g vibration from 55 cps to 2000 cps.
4) Acceleration: The maximum translational acceleration attained in the direction of flight is 3.5 g.
5) Space requirements: The limiting dimension is the height (distance from skin to jet nozzle) which is 2 inches. The other two dimensions may be somewhat larger.
6) Available power: The power supplies available in the X-15A-2 airplane are as follows:
   a.c.: 3 phase, 115V(± 1V), 400 cps (± 4 cps)
   d.c.: 28 volts nominal, varies from 24 to 31 volts, ripple is ± 0.5V at 2400 Hz, maximum of 10 amps available from each source.
7) The maximum deflection of the "target" must not exceed 0.0005 inch. The target is a small area of the aircraft skin which is free to move a small amount when acted upon by a friction drag force.

A schematic diagram of the system being developed is shown in Figure 1(1). The system utilizes the floating element technique in which a small portion of the aircraft skin is suspended so that it will move when a drag force is present. The floating element (or target) is

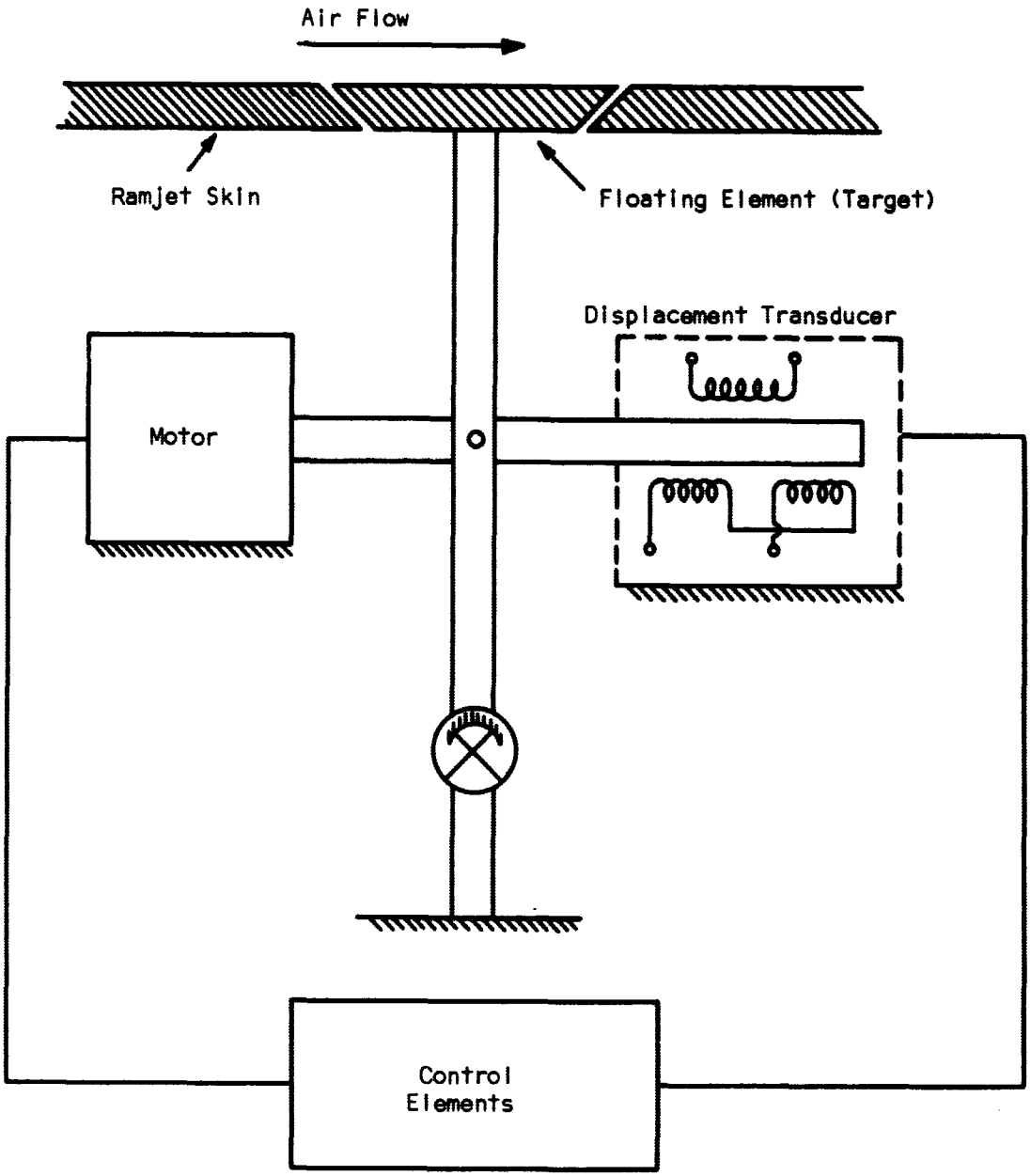

FIGURE 1. Schematic Diagram of Closed Loop System for Measuring Skin Friction

supported by a flexure which provides a frictionless support and which has a linear constraining force. A friction drag force will displace the arm of the meter. The displacement transducer produces an electrical signal proportional to the displacement. The electrical signal is amplified and used to drive a motor which returns the arm to the null position. The closed loop system is used to minimize the effects of variations in the flexure spring constant and displacement transducer constant caused by temperature changes. Force measurements are obtained by monitoring the armature current of the motor.

Research is presently being conducted to develop a gas bearing which will replace the flexure described above. The gas bearing will provide a nearly frictionless support without adding a constraining force to the system. Some of the analysis presented later will be based on the assumption that the flexure is to be replaced by a gas bearing.

Since the meter described above must operate while mounted in an in-flight aircraft, the accelerations and vibrations of the aircraft will cause force readouts due to the inertias of the floating element and support arm. These extraneous readouts may mask the readouts of the drag force to be measured. Thus, the meter must be made insensitive to both linear and angular accelerations of the vehicle. This can be achieved by using counterbalancing techniques.

Literature Survey

Figure 2 shows a technique developed by Weiler (2) for counterbalancing a skin friction meter similar to the one described above.

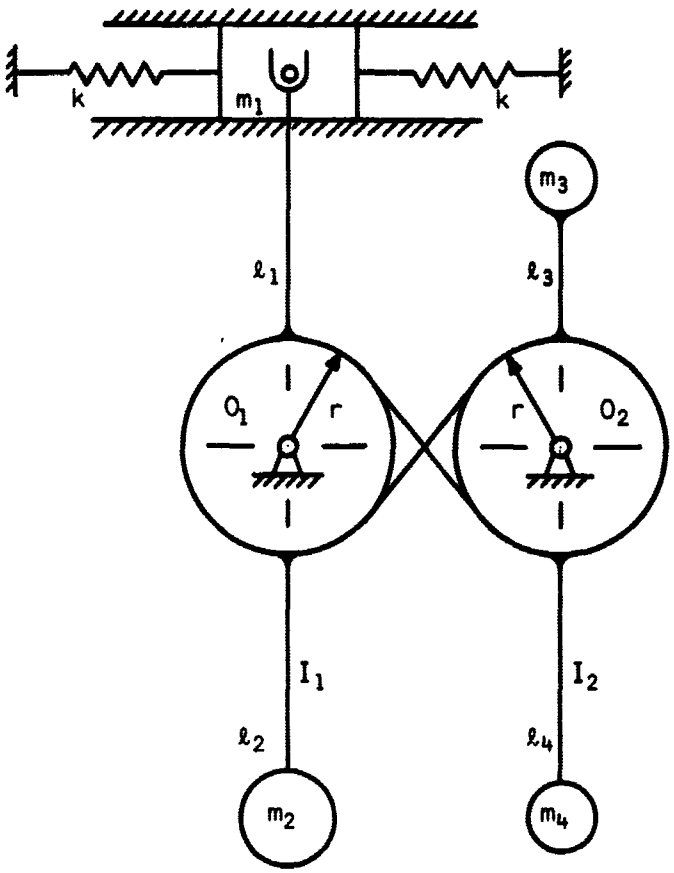

FIGURE 2. Schematic Diagram of the Principle Elements of the Acceleration Insensitive Skin Friction Meter Developed by Weller

The system is an open loop one in which force measurements are obtained by measuring the deflections of the springs, k. The mass, m_1, corresponds to a floating element which is constrained to linear motion by leaf springs (k in Figure 2). The masses; m_2, m_3, and m_4; are counterweights used to complete the counterbalancing technique.

The two component assemblies, m_1m_2 and m_3m_4, rotate about the pivots O_1 and O_2 respectively and are coupled together by thin metal bands wrapped around cylindrical surfaces fastened to each of the two arms connecting the counterweights. The bands are crossed in the middle so that rotation of one is accompanied by rotation of the other in the opposite direction. By proper proportioning of the masses, the system was found to be highly insensitive to accelerations and capable of withstanding the vibrations of an in-flight aircraft (2).

However, no design analysis or procedure was used when designing the bands. The bands were made thin enough so that they would not be overstressed as they were wrapped around the circular surfaces, but no force or stress analysis was performed to determine the band sizes. Band sizes that were considered large enough were used. Also, the possibility that there might be a rotational spring rate associated with the metal bands was not investigated. In other words, there may be a relationship which relates the torque which must be applied for rotation and angular displacement due to the action of the metal bands.

From the design specifications for the skin friction meter being developed, the force range to be measured is 0.7 to 7 millipounds, and the maximum height of the meter is to be two inches. Assuming the pivot point to be in the center of the meter, the moment arm of the

drag force will be one inch. The torque input to the meter due to the drag force will range from 0.7 to 7 x 10^{-3} in-lb. Also, the maximum displacement of the target is to be 0.0005 inch. For a turning radius of one inch, the linear displacement of the target corresponds to an angular displacement of 0.0005 radians for the pivot arm. For a linear measuring system, this means that the output of the torque motor will be 14 in-lb/radian. Thus, any rotational spring rate of the connecting bands will have to be small or at least known when designing the control elements of the closed loop system.

Scope

This thesis will cover the development of a system configuration which will counterbalance the skin friction meter against the effects of accelerations. An analysis of the crossed metal bands used in the counterbalancing scheme will be performed to investigate the existence of a rotational spring rate. An experimental verification of the analysis will be given. Also, other criteria which will influence the design of the control elements will be considered. Recommendations will be given for the band sizes based on a stress analysis so that the design specifications can be realized. A preliminary evaluation of the proposed system configuration and band design is also included.

CHAPTER II

SYSTEM CONFIGURATION

The system used to counterbalance the skin friction meter is shown schematically in Figure 3. The mass, m_1, represents the floating element. Directly coupled to mass, m_1, is an arm, $\ell_1\ell_2$, pivoted at O_1 to which mass, m_2, is fastened. The mass center of the complete component; including the masses of the counterweights, arm $\ell_1\ell_2$, and the circular sectors; is at the pivot O_1. I_1 is the total mass moment of inertia of the m_1m_2 component about O_1 (including moment of inertias of counterweights about O_1). The m_1m_2 component as described will be insensitive to linear accelerations if the component is perfectly balanced.

To render the meter insensitive to angular accelerations, the member m_3m_4 is added. It is pivoted at its mass center, O_2, and has a mass moment of inertia I_2. The construction of the m_3m_4 component has the same features as described for the m_1m_2 component. As in Weiler's system, the two component assemblies are coupled together by crossed thin metal bands wrapped around cylindrical surfaces fastened to each of the two arms to which the counterweights are fastened.

In the analysis to follow, the weights of the metal bands will be neglected and any friction in the pivots is assumed to be negligible.

Figure 4 shows the m_1m_2 component set in a two-dimensional frame of reference. The pivot, O_1, restrains the component so that it has linear motion in two directions only. The masses, m_1 and m_2,

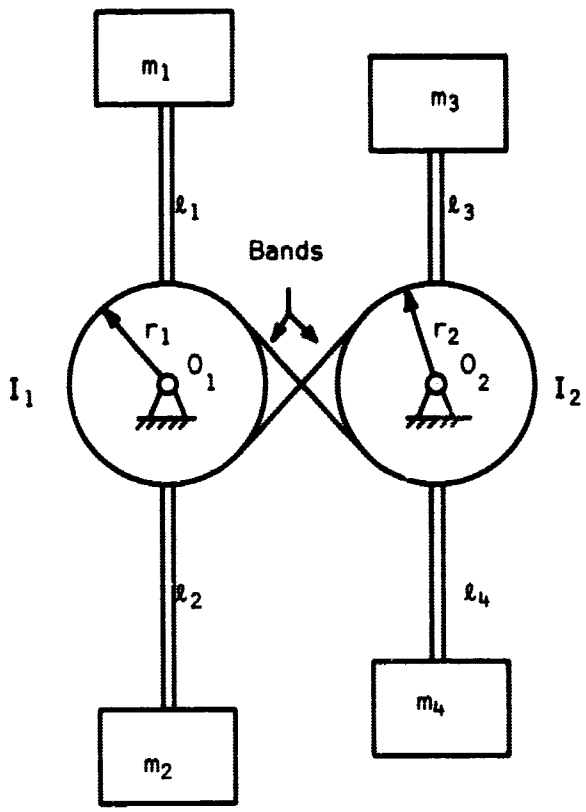

FIGURE 3. Schematic Diagram of System Configuration for Acceleration Insensitive Skin Friction Meter

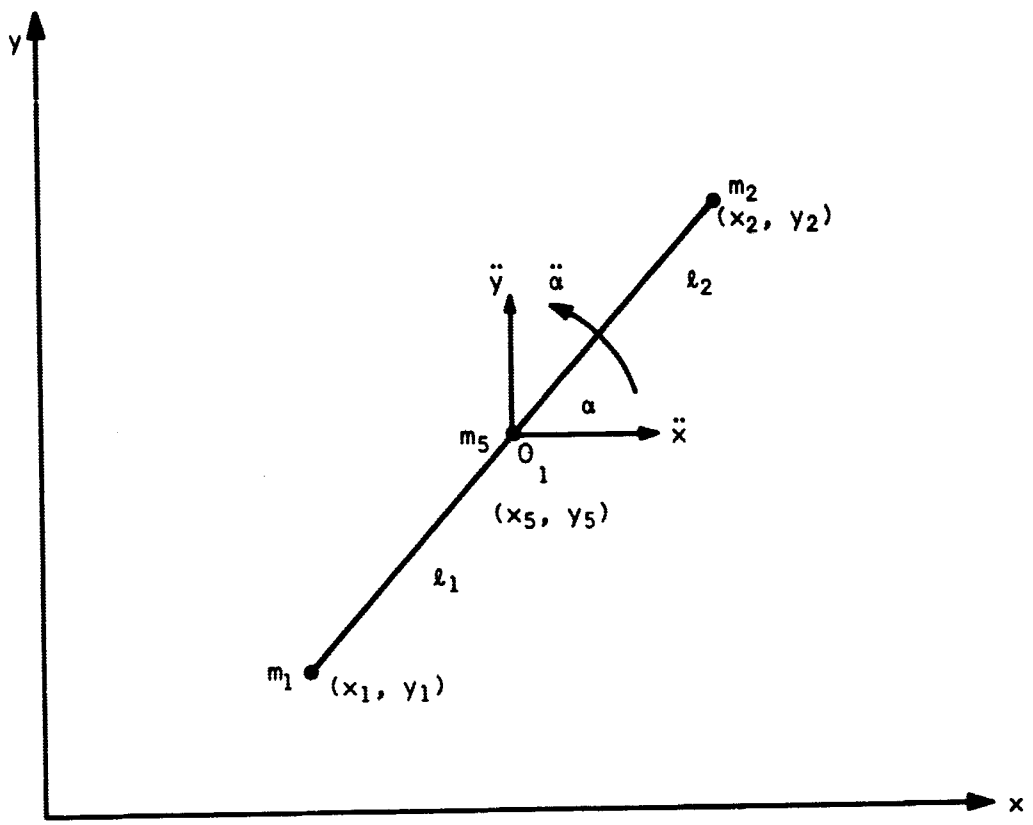

FIGURE 4. Component m_1m_2 Set in a Two-Dimensional Frame of Reference

are shown as point masses located at the extremities of the arm, $\ell_1\ell_2$. The mass, m_5, represents the combined masses of the circular sectors and connecting arms and is located at the pivot, O_1. The accelerations, $\ddot{X}$ and $\ddot{y}$, are the accelerations of the pivot center in the two-dimensional reference frame. $\ddot{\alpha}$ represents the angular acceleration about an axis through O_1 and perpendicular to the xy plane. The accelerations are consequences of changes in the vector velocities of the masses due to forces transmitted through the pivot, O_1.

If the mass center of the m_1m_2 component is to be located at the pivot, O_1, the following relation between m_1 and m_2 must be satisfied

$$m_1\ell_1 = m_2\ell_2. \qquad (2\text{-}1)$$

For a rigid body in plane motion and constrained to rotate about its center of mass, the linear and angular accelerations of the body can be treated separately (3). The equation governing rotation is of the form

$$\Sigma M_{c.g.} = I\ddot{\alpha}. \qquad (2\text{-}2)$$

The top diagram of Figure 5 shows the free body diagram of the m_1m_2 component with the angular acceleration and the force, F_1, of the metal band restraining the arm from rotating. The equation for the rotation of the m_1m_2 component is

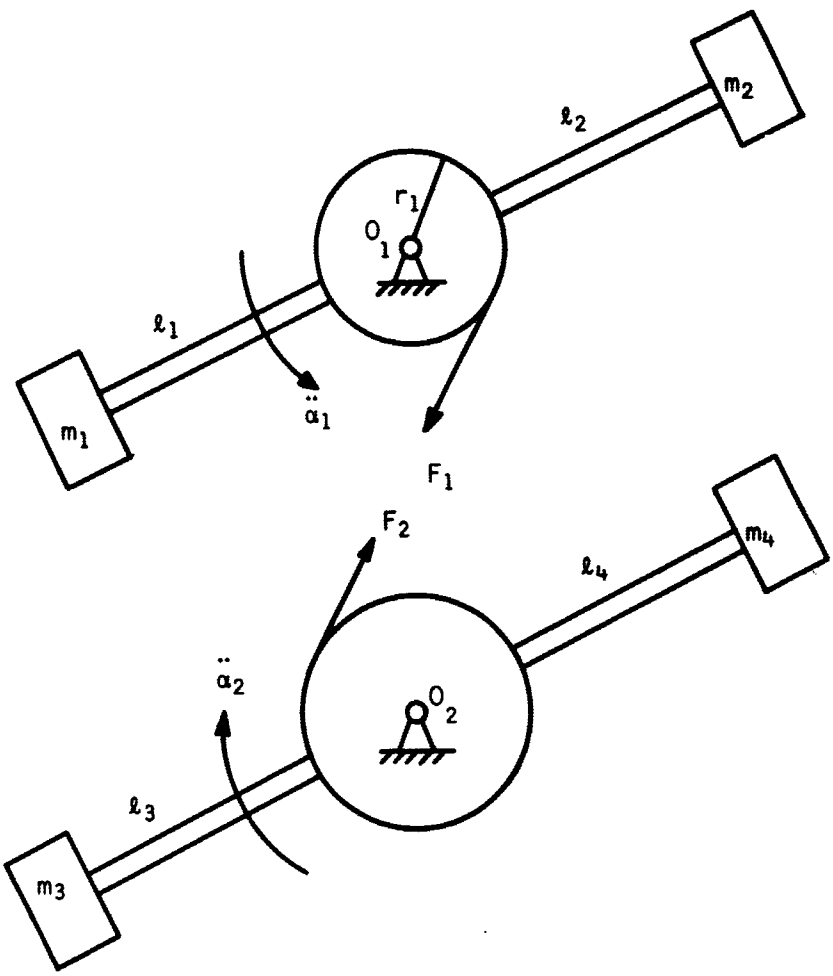

FIGURE 5. Free Body Diagrams of the m_1m_2 and m_3m_4 Components

$$-F_1 r_1 = I_1 \ddot{\alpha}_1. \tag{2-3}$$

The bottom diagram of Figure 5 shows the free body diagram of the m_3m_4 component. The center of mass of the m_3m_4 component is to be located at its pivot, O_2. Thus,

$$m_3 \ell_3 = m_4 \ell_4. \tag{2-4}$$

The equation for the rotation of the m_3m_4 component is

$$F_2 r_2 = I_2 \ddot{\alpha}_2. \tag{2-5}$$

The forces, F_1 and F_2, of Figure 5 are equal in magnitude but have opposite directions, thus

$$-F_1 = F_2 = F. \tag{2-6}$$

Equations (2-3) and (2-5) become

$$Fr_1 = I_1 \ddot{\alpha}_1 \tag{2-7}$$

$$Fr_2 = I_2 \ddot{\alpha}_2. \tag{2-8}$$

Equations (2-7) and (2-8) can be solved to give

$$\frac{I_1 \ddot{\alpha}_1}{r_1} = \frac{I_2 \ddot{\alpha}_2}{r_2}$$

or

$$I_1 = \left(\frac{r_1}{r_2}\right)\left(\frac{\ddot{\alpha}_2}{\ddot{\alpha}_1}\right)I_2. \tag{2-9}$$

For positive connection between the cylinders, the angular displacements are related by the expression

$$r_1\alpha_1 = r_2\alpha_2. \tag{2-10}$$

Differentiating equation (2-10) twice with respect to time, the equation becomes

$$r_1\ddot{\alpha}_1 = r_2\ddot{\alpha}_2$$

or

$$\ddot{\alpha}_2 = \left(\frac{r_1}{r_2}\right)\ddot{\alpha}_1. \tag{2-11}$$

Substituting equation (2-11) into equation (2-9), the equation becomes

$$I_1 = \left(\frac{r_1}{r_2}\right)^2 I_2. \tag{2-12}$$

For insensitivity to both linear and angular accelerations, the system must be designed so that

$$m_1\ell_1 = m_2\ell_2$$

$$m_3\ell_3 = m_4\ell_4$$

$$I_2 = \left(\frac{r_2}{r_1}\right)^2 I_1.$$

Equation (2-12) shows that the mass moment of inertia of the m_3m_4 component can be smaller than the moment of inertia of the m_1m_2 component if the radii of the cylindrical surfaces are properly chosen. Thus, the weight of the system can be reduced if desired.

CHAPTER III

ANALYSIS OF METAL BANDS TO DETERMINE THE ROTATIONAL SPRING RATE

As described in Chapter II, the two main components, m_1m_2 and m_3m_4, of the acceleration insensitive skin friction meter are connected by crossed metal bands (Figure 3). Figure 6 shows the proposed band configuration. The bands are made from material which is initially straight and wrapped around the cylinders as shown in Figure 6. Screws are used to fasten each of the bands to the cylinders. During assembly, the bands are put in tension to insure "positive" motion between the cylinders. The two outside bands have a combined width equal to the width of the "inside" band, and all bands have the same thickness to give the system symmetry. As angular displacement is induced, the angle of wrap of each band is increased on one cylinder while the angle of wrap on the other cylinder is decreased.

Due to the wrapping and unwrapping of the bands on the cylinders during rotation, there may be a rotational spring rate associated with the bands which may be either positive, negative, or zero. This rotational spring rate will affect the readouts of the meter which measures the applied drag force. A positive spring rate will resist the rotation of the cylinders, and the drag force will have to overcome this effect. Thus, for a positive spring rate, the resulting force readouts will be too low. A negative spring rate will make the system open loop unstable, and a zero spring rate for the bands will have no effect on the system.

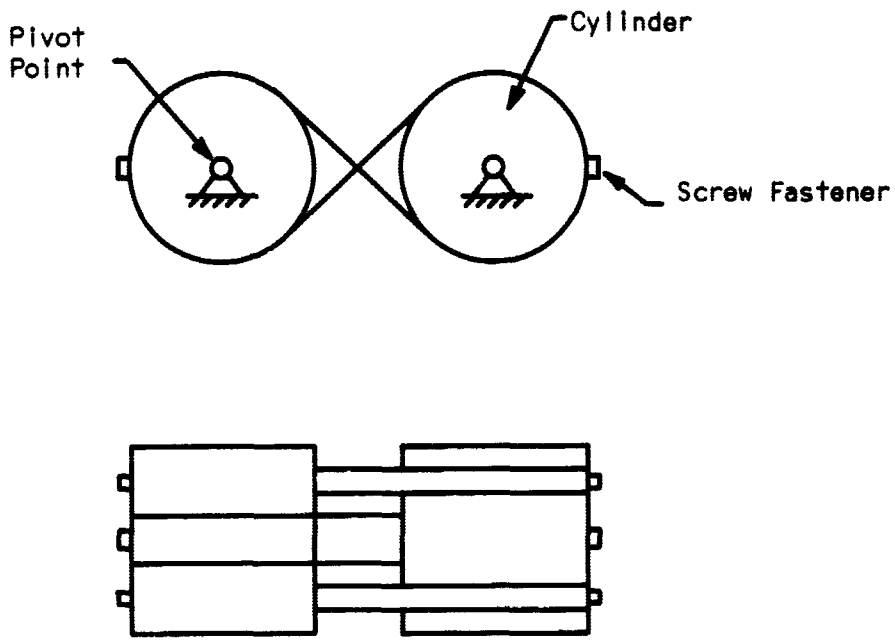

FIGURE 6. Proposed Band Configuration

To investigate the rotational spring rate, the two cylinders are isolated as free bodies as shown in Figure 7. In the free body diagrams, the reactions at the pivots have been neglected. M_n represents an applied torque which will rotate C_1 in a counterclockwise direction; thus, C_2 must rotate in a clockwise direction. P_1 and P_2 are the tensions in the crossed metal bands which act toward the node or line of intersection of the bands. With no external torques applied to C_2, P_1 must be greater than P_2 for C_2 to rotate.

Next, consider the top band from cylinder C_1. The upper diagram of Figure 8 shows the orientation of the band when the system is in its initial position. This diagram shows the length of the center band from the point of attachment to the line of intersection of the bands. P represents the initial tension in the band, while ℓ represents the transition length between the curved portion and the straight portion of the band. Since the thickness of the band will be very small compared to the radius of the cylinder, the length, ℓ, will be small and will depend on the tension in the band. However, if the bands are designed so that any changes in the initial band tension due to applied and inertial loads are small, then, the effect of varying ℓ can be neglected. The angle, θ_1, represents the angle of wrap of the band, and L is the length of band contacting the cylinder.

The middle diagram of Figure 8 shows the strip after the cylinder has rotated through an angle $\Delta\alpha_1$. The tension, P_1, is the tension in the band due to the loading which produces rotation. $L + \Delta L$ is the length of band contacting the cylinder after rotation through the angle $\Delta\alpha_1$.

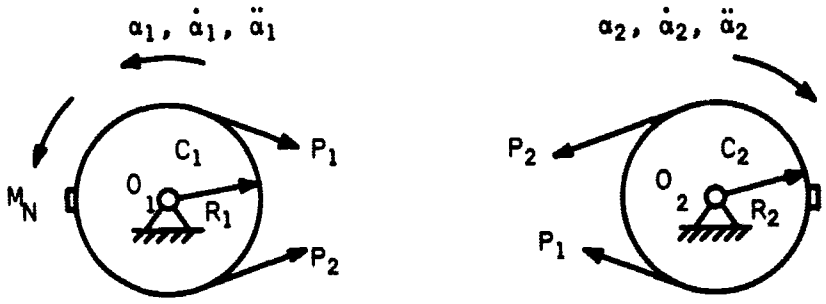

Free Body Diagram of Cylinder C_1

Free Body Diagram of Cylinder C_2

FIGURE 7. Free Body Diagrams of Cylinders

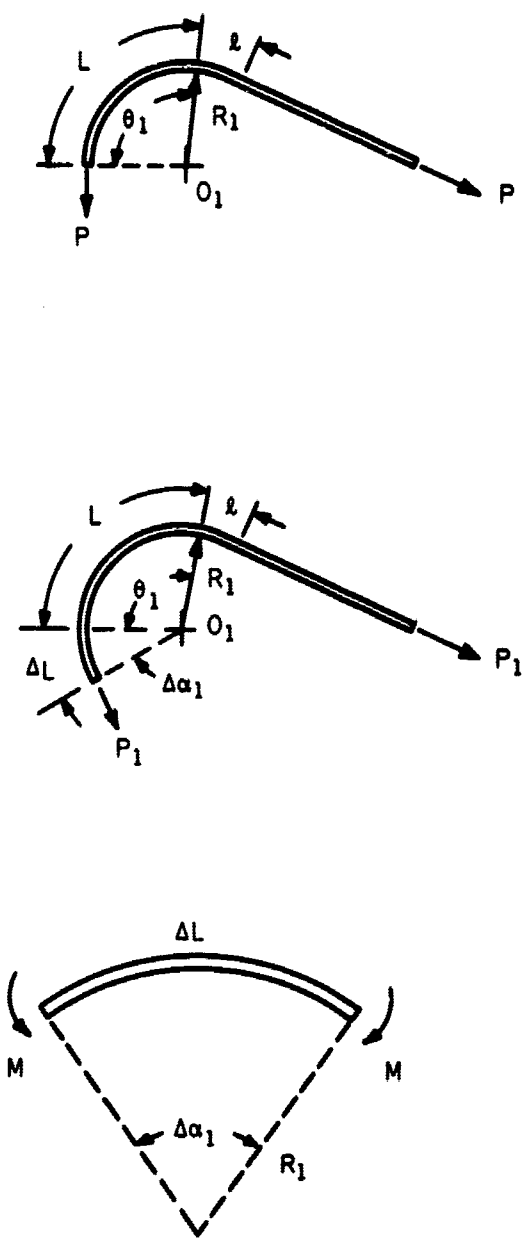

FIGURE 8. Orientations of the Top Band of Cylinder C_1

Since the bands are made of material which is initially straight, a moment must be applied to the band to bend it to the shape of the cylinder. As the cylinder is rotated, the net effect on the band is to transform material from the straight portion to the curved portion. The length of band curved during the angular displacement, $\Delta\alpha_1$, is

$$\Delta L = (R_1)(\Delta\alpha_1) \tag{3-1}$$

The lower diagram of Figure 8 shows the section of the band which is curved during rotation.

The applied torque, or torque of the force to be measured, must supply the moment to bend the band. Using elastic theory for beams (4) and referring to Figure 8, the moment required to bend a length, ΔL, of the band through an angle $\Delta\alpha_1$ is

$$M = \frac{\Delta\alpha_1 E I_A}{\Delta L} \tag{3-2}$$

Since $\Delta L/\Delta\alpha_1 = R_1$ from equation (3-1), the required moment is

$$M = \frac{E I_A}{R_1} \tag{3-3}$$

Equation (3-3) shows that a constant moment will be required to bend the band around the cylinder. The moment is not a function of angular displacement but a function of the constant parameters; E, I_A and R_1.

However, energy is stored in the band as it is curved to the radius of the cylinder, and the energy is increased as the angle of

wrap in increased. The increase in band energy, which is absorbed from the applied drag moment, is

$$\Delta E_1 = M\Delta\alpha_1. \tag{3-4}$$

Next, the lower band of cylinder C_1 (see Figure 7) must be considered. The two bottom bands acting together will have an area moment of inertia equal to the top band, and the two bands can be treated as one band in the analysis to follow.

The upper diagram of Figure 9 shows the initial orientation of the bottom band while the lower diagram shows the band after the cylinder has rotated through the angle $\Delta\alpha_1$. The same notation has been used in Figure 9 as was used in Figure 8.

During rotation, the decrease of the angle of wrap of the bottom band will equal the increase in the angle of wrap of the top band on C_1. Energy will be released from the curved portion of the bottom band as the band straightens and is equal to

$$\Delta E_2 = M\Delta\alpha_1. \tag{3-5}$$

The net change in the energy of the system as a result of the motion of cylinder C_1 is then

$$\Delta E_1 - \Delta E_2 = 0. \tag{3-6}$$

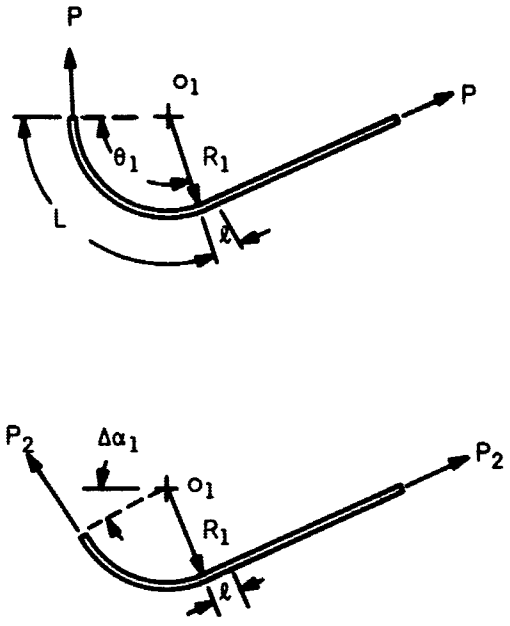

FIGURE 9. Orientations of the Bottom Band of Cylinder C_1

Thus, the motion of the cylinder, C_1, will have no effect on the system.

An analysis of the bands wrapped around cylinder C_2 will yield the same result as reached above. As discussed in Chapter II, it may be desirable to have different radii for the cylinders, C_1 and C_2. The above analysis shows that different radii for the two cylinders will not affect the system. Thus, the operation of the skin friction meter is not dependent on any rotational spring rate of the bands used to connect the principal components.

In the above analysis, the band was treated as a beam subjected to pure bending only. However the bands of the actual system will also be subjected to tension forces. But as long as the elastic limit of the band material is not exceeded, the effects of tension and bending can be treated separately and superimposed (5). The tension forces have no influence on any existing rotational spring rate, and they were neglected. The effects of the tension forces will be considered in the actual design of the bands in Chapter V.

CHAPTER IV

EXPERIMENTAL INVESTIGATION OF ROTATIONAL SPRING RATE

To check the analysis presented in the last Chapter, a model of the proposed band configuration was built and tested.

Apparatus.

A schematic diagram of the experimental system is shown in Figure 10. A band configuration, similar to the one to be used in the counterbalanced skin friction meter and discussed in Chapter III, was mounted on cylinders so that torques could be applied and resulting angular displacements measured. Using this information, the analysis presented in Chapter III can be verified. As discussed in Chapter III, the rotational spring rate of the bands should be zero. Thus, friction in the experimental system was kept to a minimum so that any existing rotational spring rate could be distinguished.

Since the skin friction meter will have a maximum height of two inches, it was decided to test a system which will be comparable to the one used in the final design. To leave space for the mounting of other necessary components, the maximum diameter of the cylinders can be about one inch. The bands will have to be thin enough so that they will not be overstressed as they are wrapped around the cylinders, and yet, strong enough to insure positive motion between the cylinders. In the experiment to be described, only static tests are made to test the rotational spring rate of the bands. Thus, the governing criteria for the band design is to avoid overstressing the bands.

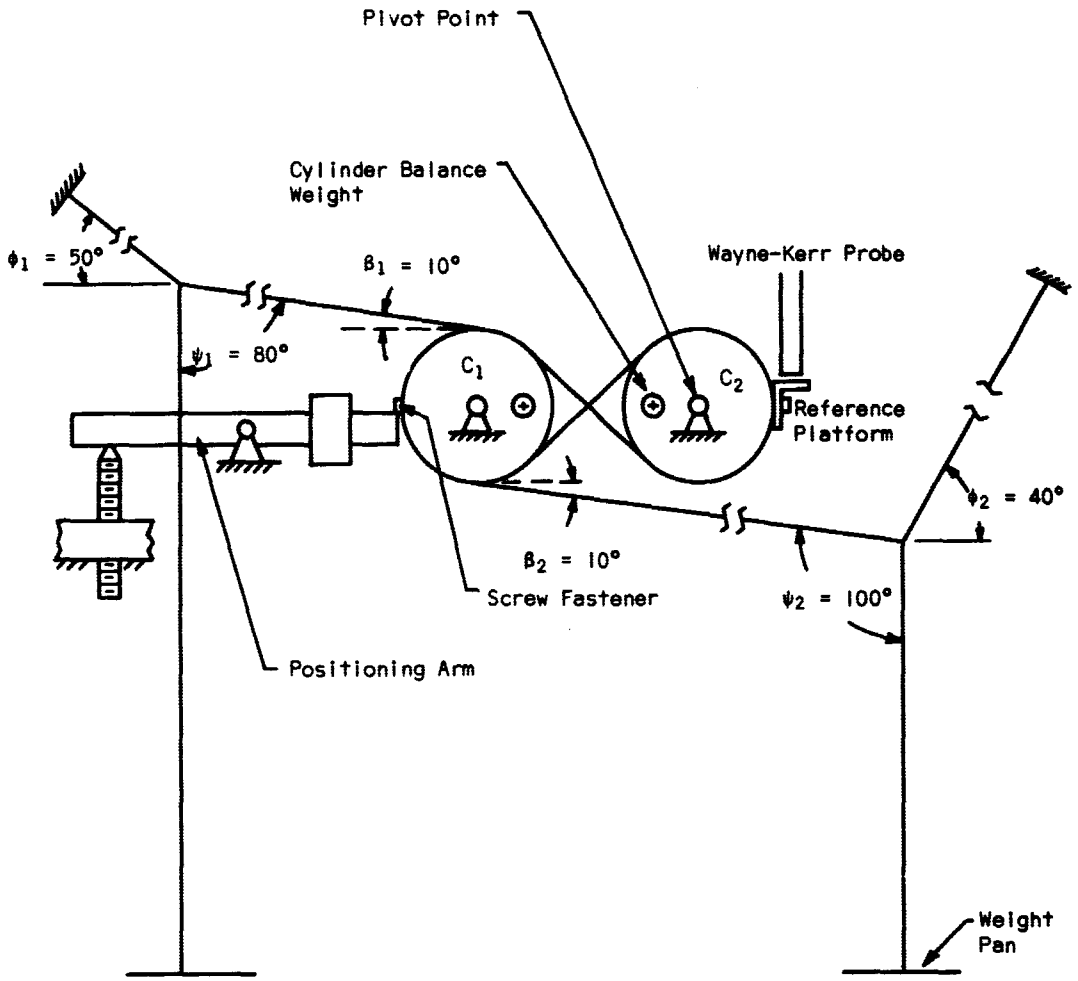

FIGURE 10. Schematic Diagram of Test Apparatus

An equation relating radius of curvature and the physical properties of the band material to maximum thickness for bending without overstressing (6) is

$$t = \frac{2R_o S_y}{E - S_y} \qquad (4\text{-}1)$$

It was decided to use 0.001 stainless steel shim stock for the band material. Using the following values for stainless steel (7) in equation (4-1):

$t = 0.001$ inch
$E = 27.6 \times 10^6$ psi
$S_y = 32.5 \times 10^3$ psi

The minumum value for the radius of each cylinder was found to be 0.425 inch. Using a small factor of safety, the diameter of each cylinder was made 0.9 inch. The cylinders were made of aluminum because it was readily available and easily machined.

The center band was made 0.25 inch wide while the width of each "outside" band is 0.125 inch. Screws were used to fasten the bands to the cylinders at the positions shown in Figure 10, and Figure 11 shows the relative positions of the bands on the cylinders. Since the screws will create an unbalanced moment about the pivot, the cylinders were statically balanced by inserting steel plugs opposite to the screws (see Figure 10).

The cylinders were mounted on small conical pivot bearings to

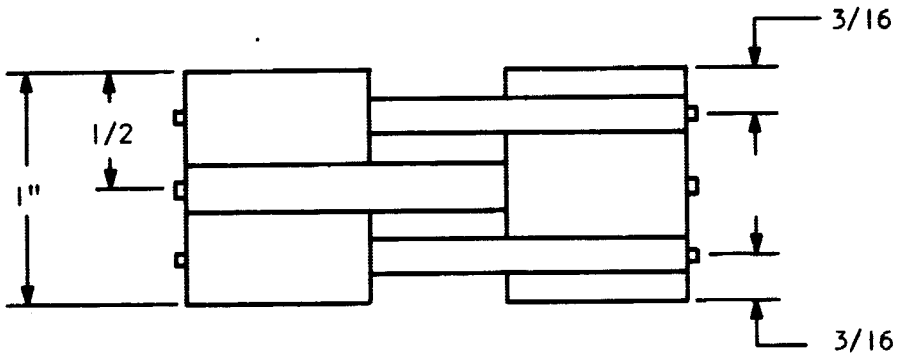

FIGURE 11. Positions of Bands on Cylinders

give the system rigidity while keeping the frictional torques exerted on the system to a minimum. The pivots and the pivot seats of the bearings were made of tool steel, and the pivot seats were inserted into each end of the cylinders. Molybdenum disulphide was used to lubricate the bearings to reduce friction. A more detailed discussion of the pivot bearings will be given later in this Chapter.

To reduce the reaction forces at the pivots, the cylinders were mounted so that the clearance between them was 0.045 inch. The pivot reaction forces due to the tensions in the connecting bands is decreased as the clearance is decreased. The clearance chosen allowed enough space for accurate adjustments during assembly of the apparatus.

Torques were applied by using the string network shown in Figure 10. The strings were attached to cylinder C_1, by looping their ends over the screw fasteners. The angles of the support strings, ϕ_1 and ϕ_2, were set up so that the angles Ψ_1 and Ψ_2 were bisected respectively. With the angles set up as shown, the forces transmitted to the cylinder through the strings will be equal to the weights placed in the weight pans. When equal weights are placed in the weight pans, the forces acting on the cylinder by the top and bottom strings will be equal. Thus, a pure torque will be applied to the system without adding a resultant force which would increase the reaction forces at the pivot. Any increase in the reaction forces will increase the friction of the pivot bearing, and this result should be avoided. Since the effects of contact friction and string bending stiffness of a thin, static, hanging string are negligible, the method of applying torques described above will not induce any frictional forces on the system. An analysis of the errors

in the applied torque due to improper string angles will be discussed in Appendix A.

A capacitance type vibration meter was used to measure the linear displacements of a reference platform attached to cylinder C_2. The meter is discussed in detail in Appendix B. The angular displacement of the cylinders can then be calculated knowing the linear displacement and the radius at which the linear displacement was obtained.

One requirement for using the capacitance type meter is that the probe and test surface must be parallel. However, for an angle of inclination between the surfaces of five degrees, the reading of distances will be affected by less than 0.4 per cent (8). During assembly of the apparatus, the angle of inclination between the surfaces can be adjusted so that it is much less than one degree. This means that the rotational spring rate can be studied for angular displacements through the range of four to five degrees without sacrificing the accuracy of the linear measurements. Also, as discussed in Chapter I, the maximum angular displacement of the skin friction meter will be 0.0005 radians or about 1.75 minutes. Thus, a study of the rotational spring rate through a range of four to five degrees should also well define the rotational spring rate, if it exists, for the range of interest.

The positioning arm, shown in Figure 10, provides a means to adjust the initial distance between the probe and reference platform, and also, to "hold" the system while making weight changes on the weight pans. The arm is pivoted at its center on a ball bearing and one side is weighted. Before each trial, the positioning arm was secured. Then weight changes were made and initial deflections noted. The arm was

released and the weighted half dropped clear to allow rotation.

Figure 12 shows the experimental system used to study the band.

Experimental Results

First, cylinder C_1 was rotated in a counterclockwise direction. A plot of Applied Torque versus Angular Displacement is shown in Figure 13. The data points for this curve are designated by circled points. As seen from the plot, the curve is nonlinear and approaches an asymptote. When a torque corresponding to the asymptote line is applied to the system, the system will rotate until the limit of rotation is reached (approximately 90 degrees).

To check for nonlinearities in the system, a torque was applied which would rotate cylinder C_1 in a clockwise direction. The data points for the Applied Torque versus Angular Displacement curve are designated by squares in Figure 13. As seen from the plot, there is very close agreement between the two curves. Also, the curves approach the same asymptotic line.

At this stage of the testing, no definite conclusions could be reached regarding a rotational spring rate of the bands. As will be explained later in this Chapter, the shape of the curves presented appeared to be governed by the friction of the pivot bearings.

To reduce the effects of friction in the pivot bearings, the system was excited with sonic vibrations of low amplitude and high frequency. This method is discussed in detail in a paper by Fridman and Levesque (9). Their results show that static friction can be greatly reduced and will approach kinetic friction.

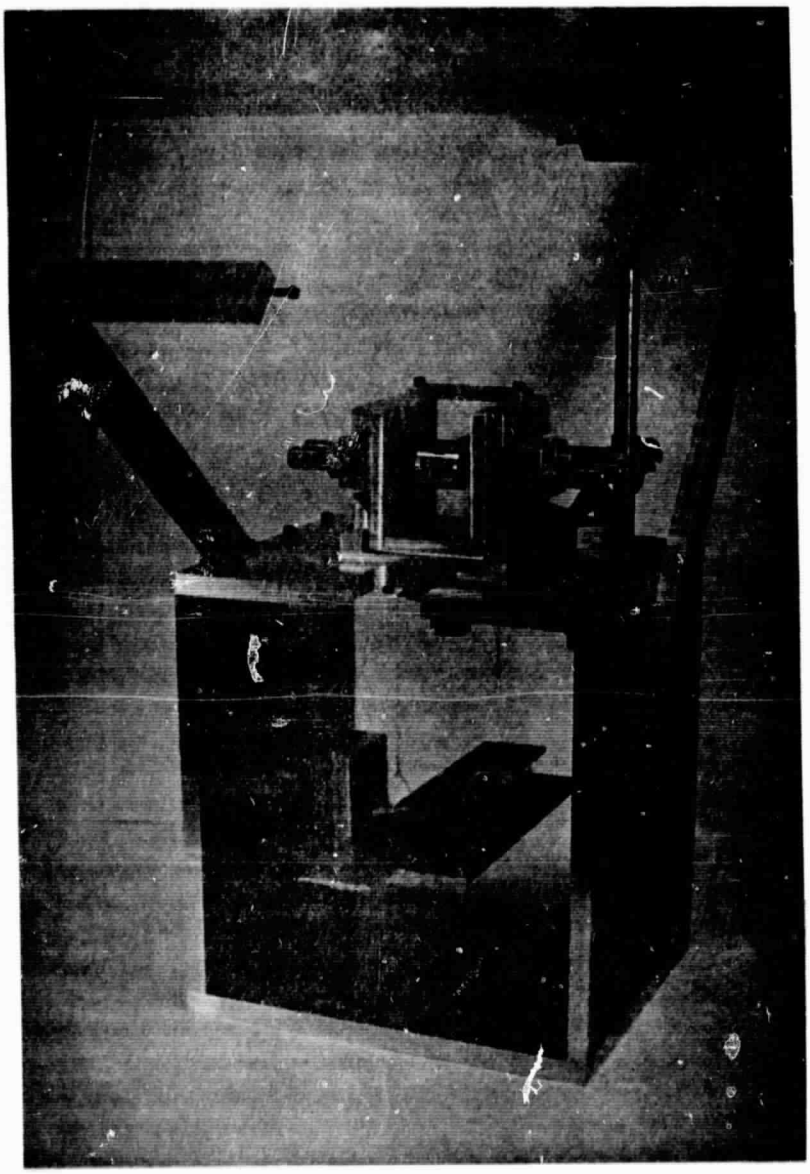

FIGURE 12. Experimental Apparatus

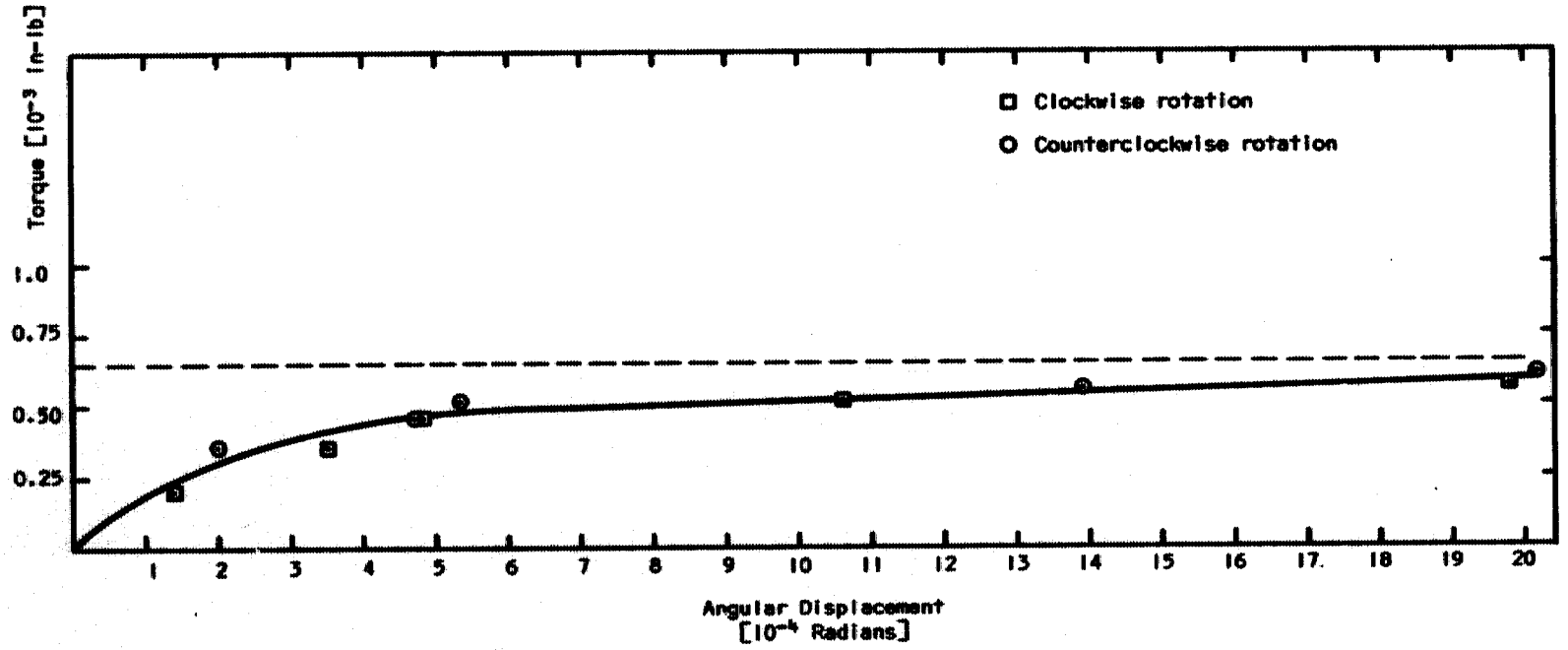

FIGURE 13. Torque vs. Angular Displacement for Cylinders in Horizontal Position

To utilize this method, a regular audio speaker was mounted under the base plate of the system as shown in Figure 14. The speaker was driven by a power amplifier in series with a signal generator. After trial and error testing, it was found that the best results were obtained when the base was excited at a frequency of 300 Hz. For any given weight in the weight pans, the maximum angular displacement was obtained at an excitation frequency of 300 Hz. The amplitude was limited by the power output of the speaker and also the dynamics of the system. The cylinders were statically balanced but not dynamically balanced. Thus, if the amplitude of the exciting vibrations was too large, the system would tend to become unstable due to the dynamic unbalance. No data was recorded for the angular rotation due to the dynamic unbalance.

Curves For Applied Torque versus Angular Displacement using the "dither" effect are shown in Figure 15. The same notation has been used here as for Figure 13. It can be seen from the curves that the friction has been reduced as the asymptotic line has been slightly lowered. However, the greatest difference produced by the "shaking" was to "flatten" the curves near the origin.

The discrepancy between the curves using "dither" and without dither is not nearly as large as discrepancies noted in prior testing. In previous tests, it was noted that the frictional torque asymptote was lowered by approximately 50 per cent. However, the system seemed to be "sticking" at some positions. The system was dismantled and the pivot bearing cleaned. After reassembly, the curves were obtained which were discussed above. The frictional torque asymptote for the system excited by the dither effect remained the same, but the frictional

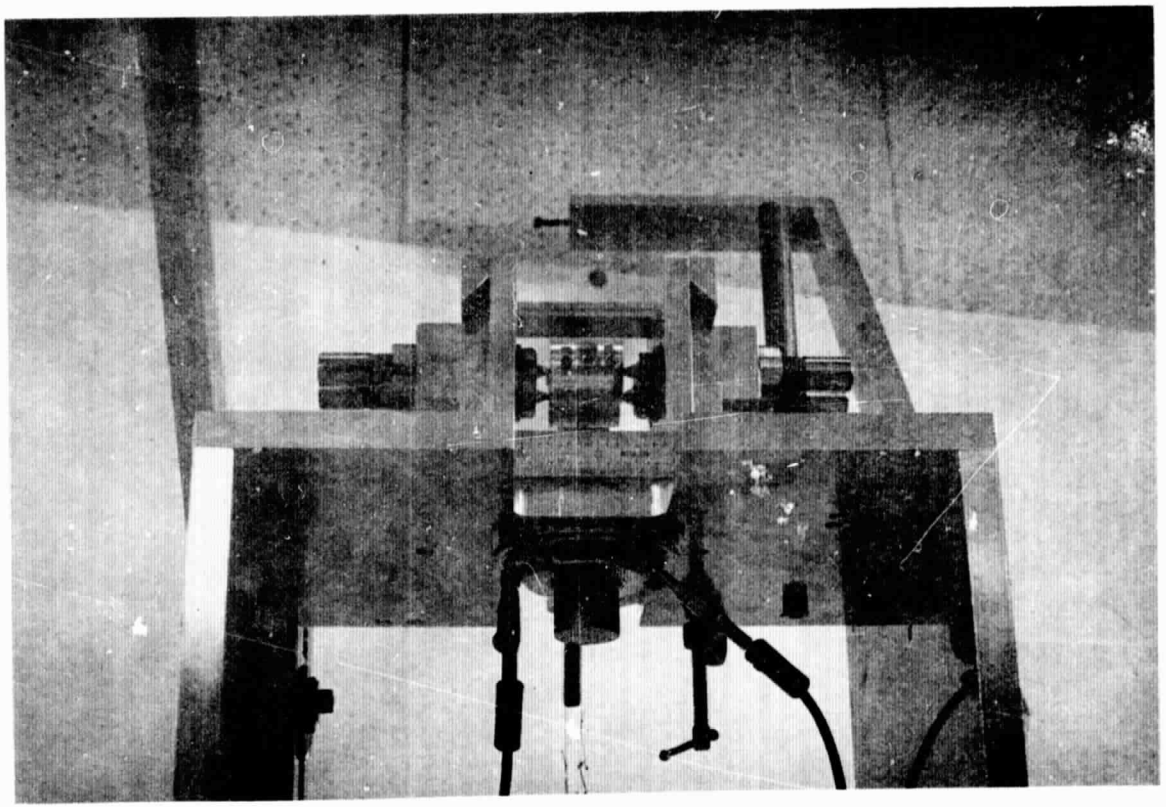

FIGURE 14. Speaker Used in the Dither Method

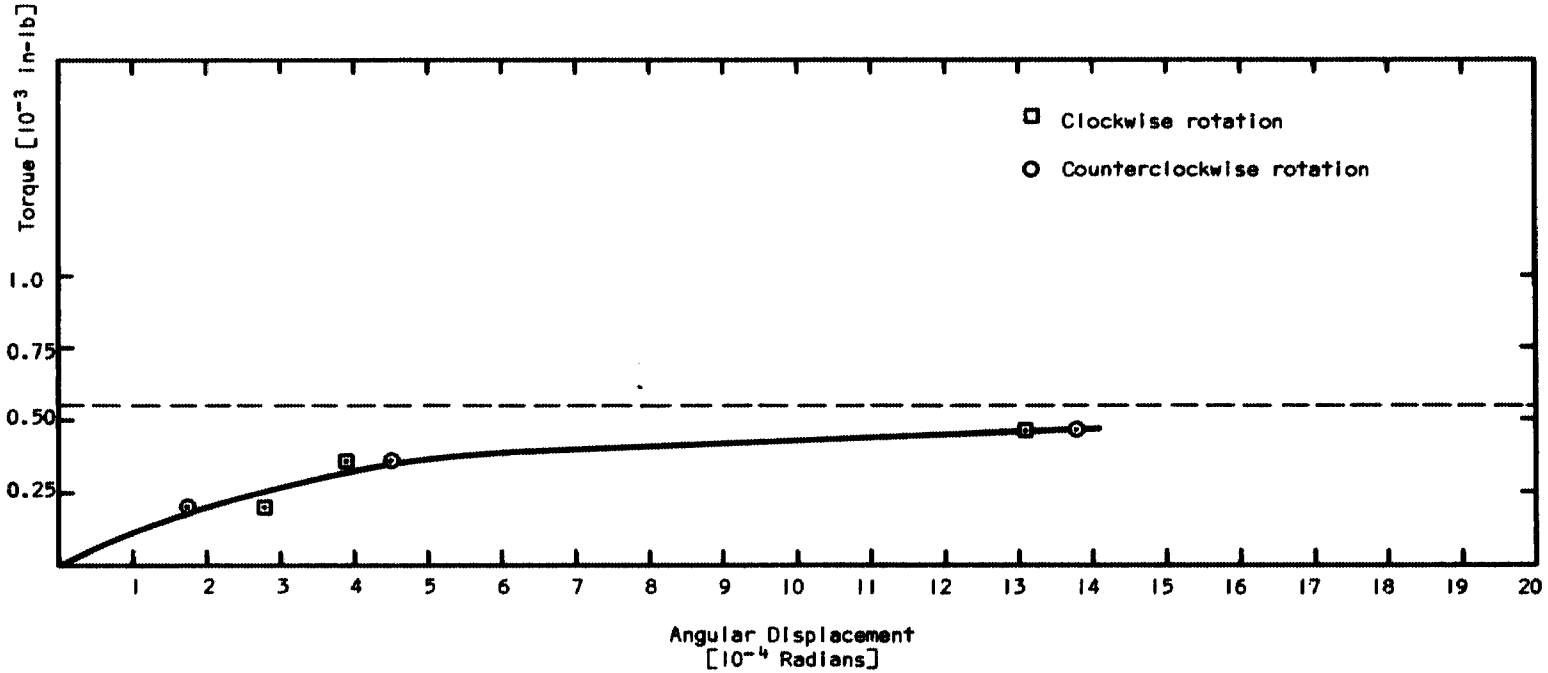

FIGURE 15. Applied Torque vs. Angular Displacement Using Dither Effect

torque asymptote for the system without using dither was greatly reduced. As seen by Figures 13 and 15, the asymptotes approached the same value. This would suggest that the system had been lubricated and aligned in such a manner that optimum conditions were approached.

Discussion

To facilitate the design of the system control elements, a linear relationship between applied torque and angular displacement of the form

$$T_A = K\theta_A \qquad (4\text{-}2)$$

would be desirable. Figures 13 and 15 show that the curves for Applied Torque versus Angular Displacement are not described by equation (4-2).

At first, it was thought that the nonlinearity of the curves could be caused by the pivot bearings. Figure 16 shows a cross-section of the pivot bearings used. The pivot and pivot seat are eccentric, and the pivot does not contact the entire pivot seat. For the system being investigated the pivot is stationary while the pivot seat is rotated.

When a torque is applied to the pivot seat, it will tend to roll around the pivot. As the seat rolls, the point of contact moves around the pivot as shown in Figure 17. The eccentricity, e, is greatly exaggerated in Figures 16 and 17. The normal force varies as

$$N = W\cos\theta_A. \qquad (4\text{-}3)$$

Since the friction force is proportional to normal force, a point will

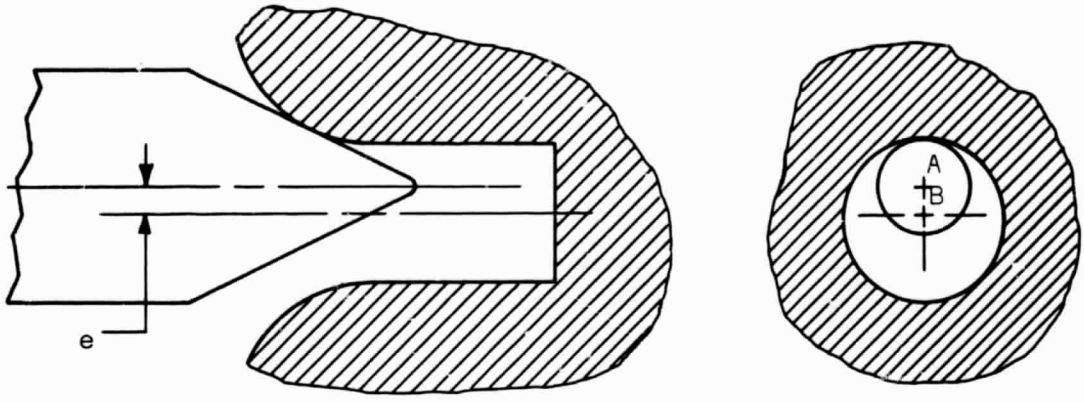

FIGURE 16. Cross Section of Pivot Bearing

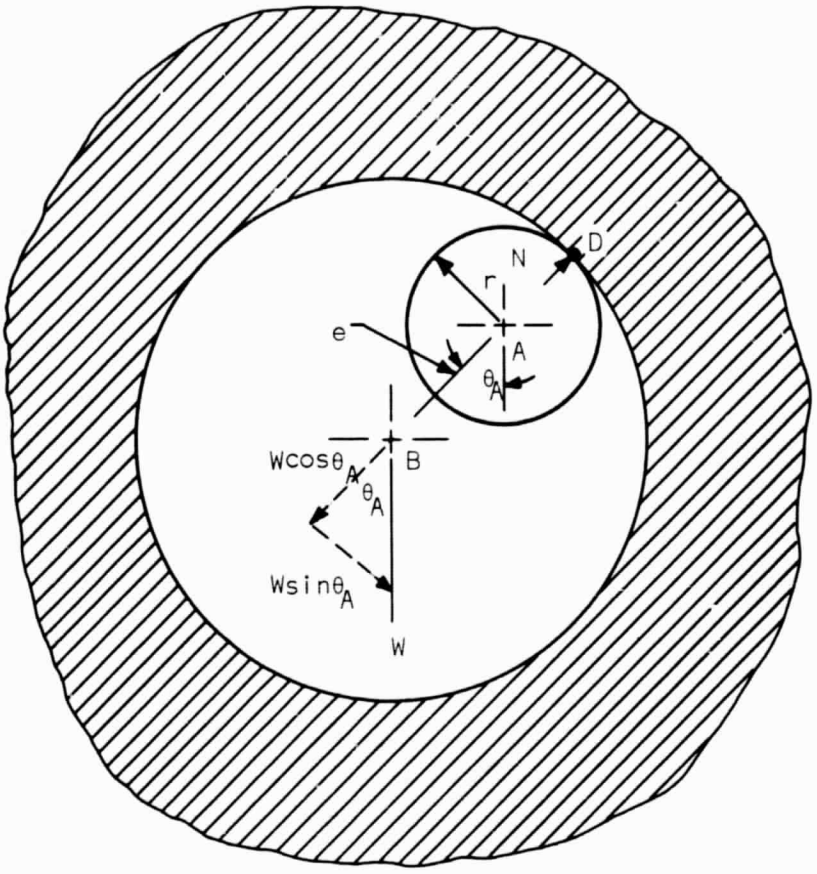

FIGURE 17. Relative Positions of Pivot and Pivot Seat After Rotation

be reached where the friction force will not be large enough to sustain rolling, and sliding will occur.

As the pivot seat rolls around the pivot, the restoring torque which must be overcome for each cylinder is

$$T_R = W(r + e)\sin\theta_A. \tag{4-4}$$

For small angular displacements, the equation becomes

$$T_R = W(r + e)\theta_A. \tag{4-5}$$

For the system investigated, the following values were found to be applicable:

W = 0.0302 lb.
r = .018 in.
e = .001 in. (maximum).

The largest angle of rotation for which a restoring torque was detectable was 0.000175 radians. Using the above values, the maximum restoring torque for one cylinder was found to be 4.43×10^{-6} in-lb. For the two cylinder system, the maximum restoring torque is 8.86×10^{-6} in-lb. Since the maximum restoring torque is small compared to the torques actually applied to the system, the applied torques only had to overcome the sliding friction of the pivots plus any existing spring rate.

To obtain a better understanding of the effects of the friction in the system, the cylinders were mounted in a vertical position as shown in Figure 18. In this position, the weights of the cylinders are supported by the bottom pivots only. The pivots and pivot seats are concentric and make mutual contact. Thus, the relative motion between the two can not be rolling but must always be sliding motion.

A plot of Applied Torque versus Angular Displacement is given for the vertical configuration in Figure 19. As seen from the Figure, the curve has the same general shape as the curves given in Figure 13 and 15. This would suggest that the motion between the pivots and their seats in the horizonal position is also sliding motion. The friction asymptote of Figure 19 is much higher than for Figures 13 and 15.

The reason for the higher friction asymptote can be explained by considering the pivot bearings. A 00 centerdrill was used to shape the pivot seat. Figure 16 shows that the seat surface has a radius of curvature and is not conical. Line contact is desirable between the pivot and its seat. However, line contact is impossible to obtain and the pivot bearing in the vertical position can be considered to behave as the bearing shown in Figure 20. In Figure 20, W is the applied load and ϕ is half of the pivot bearing angle. The friction torque for a bearing like the one in Figure 20 is (15)

$$M_v = \left(\frac{1}{2}\right) \frac{\mu W}{\sin\phi} (R_o + R_i). \qquad (4\text{-}6)$$

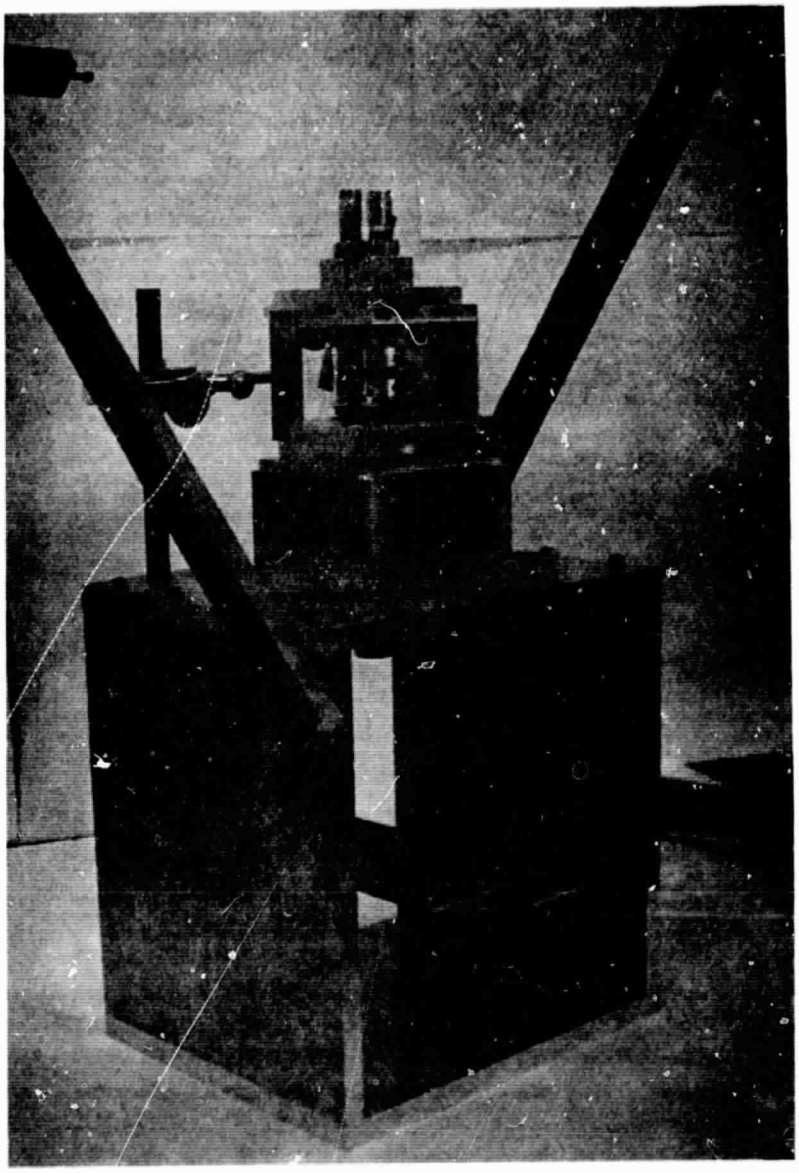

FIGURE 18. Experimental Apparatus with Cylinders in Vertical Position

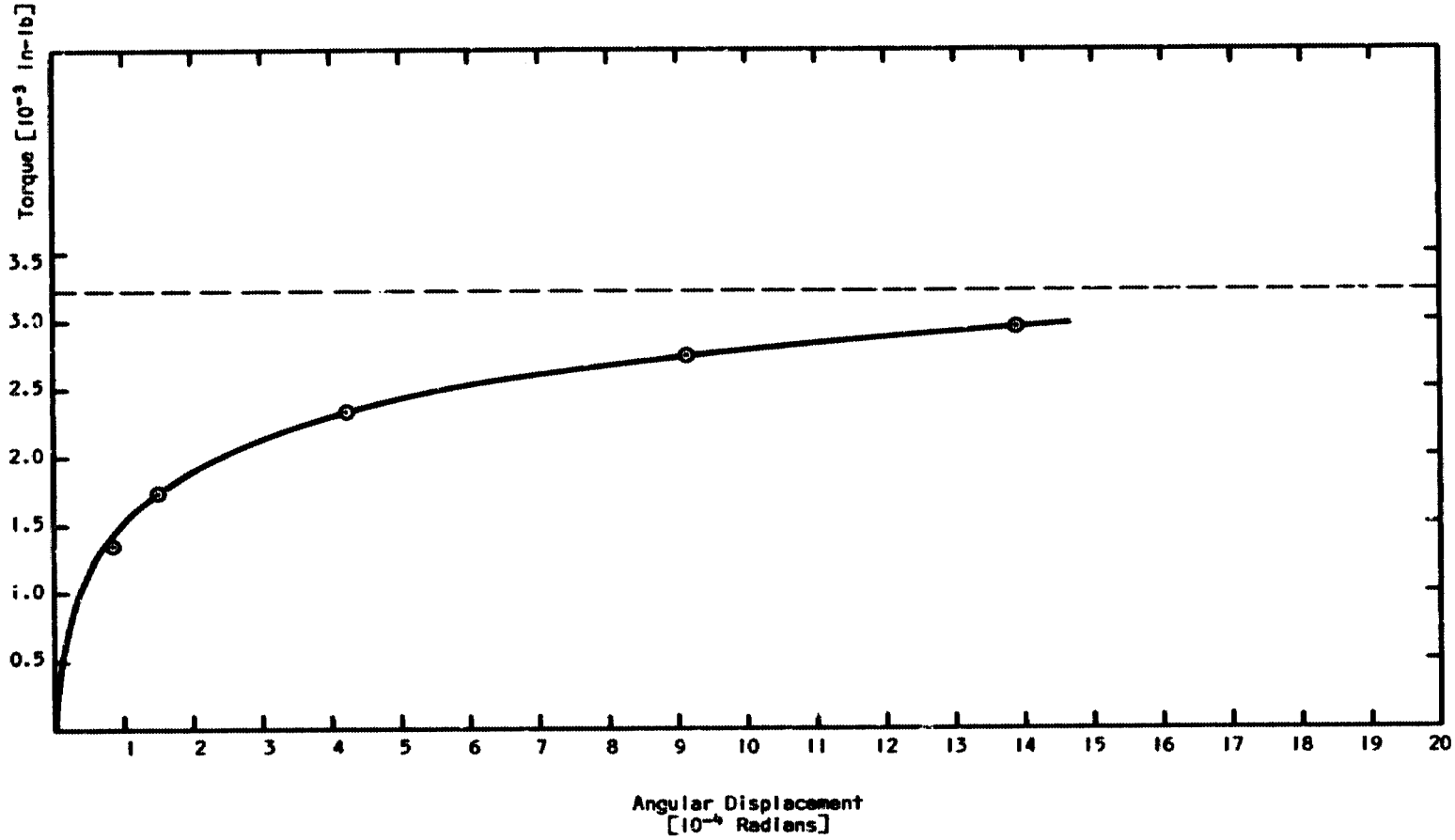

FIGURE 19. Applied Torque vs. Angular Displacement for Cylinders in Vertical Position

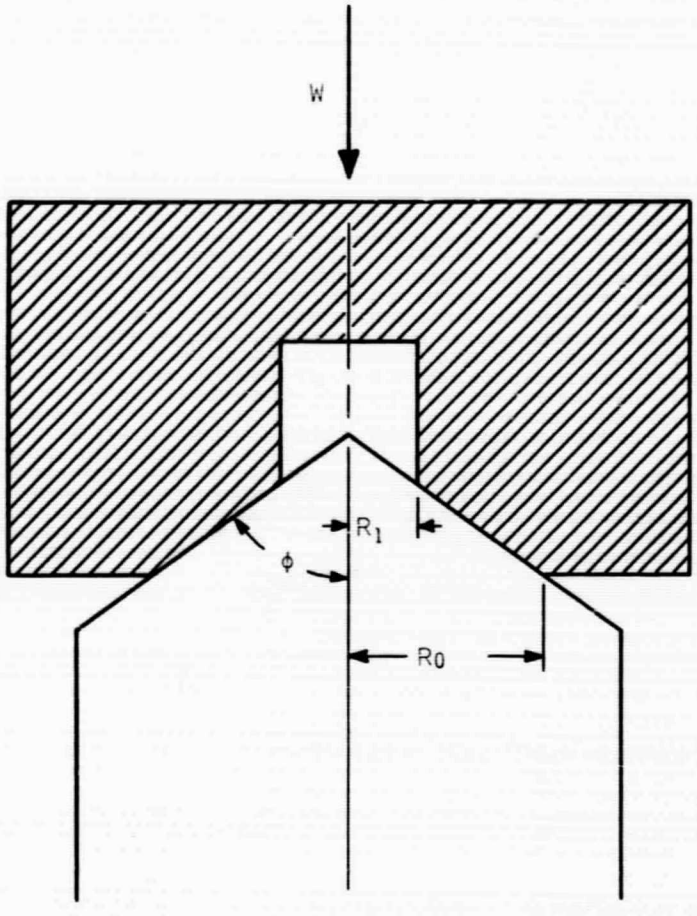

FIGURE 20. Equivalent Vertical Pivot Bearing

It can be shown that the friction torque for two horizonal pivot bearings supporting a load W is

$$M_h = \frac{1}{2} \frac{\mu W}{\cos\phi} (R_o + R_i) \ . \qquad (4\text{-}7)$$

The relationship between M_v and M_h is

$$\frac{M_v}{M_h} = \cot\phi \ . \qquad (4\text{-}8)$$

For the pivot bearings used, ϕ is 22.5 degrees and equation (4-8) gives $M_v/M_h = 2.41$.

By comparing Figures 19 and 13, the actual ratio between the friction asymptotes is 4.96. The value from equation (4-8) and the actual value of M_v/M_h differ by a factor of about 2. The difference between the theoretical and experimental friction torque ratios is probably due to misalignment in the experimental system. If the centerlines of the pivots for each cylinder do not coincide, the pivot seats will be "cocked" with respect to the pivots. Thus, the top pivot for the vertical system will exert a frictional torque on the system which is not considered in the theoretical analysis.

It has been shown that the coefficient of friction for a stationary system being set into motion varies with displacement as shown in Figure 21. The coefficient of friction decreases as displacement increases until the value of kinetic friction is reached. The displacement necessary for the transition from static to kinetic friction is on the order of 10^{-3} centimeter (10).

The reason for this transition displacement can be shown by considering Figure 22. This Figure shows a microscopic view of the area of contact between two bodies under a normal load. Due to surface roughnesses, the two bodies only make contact at a few points where asperities form a junction.

For motion to begin, a tangential force must be applied to break the junctions formed by the asperities, and plastic deformation of the materials takes place. On a microscopic scale, the surfaces sink together, increasing the area of contact, and at the same time a minute tangential displacement occurs. As the tangential force is increased, this process continues until a stage is reached at which the applied shear stress is greater than the strength of the interface. Junction growth comes to an end and gross sliding occurs (11).

For the systems shown in Figures 12 and 18, a relative displacement of 10^{-3} centimeter between the pivots and seats corresponds to an angular displacement of about 209×10^{-4} radians. The plots of torque versus angular displacement show that kinetic conditions should be realized before an angular displacement of 209×10^{-4} radians is reached. This is probably due to the fact that the pivots have been lubricated with M_oS_2 which decreases the strength of the junctions between the pivots and their seats.

Based on the above discussion, the friction of the pivot bearings appears to govern the behavior of the system investigated.

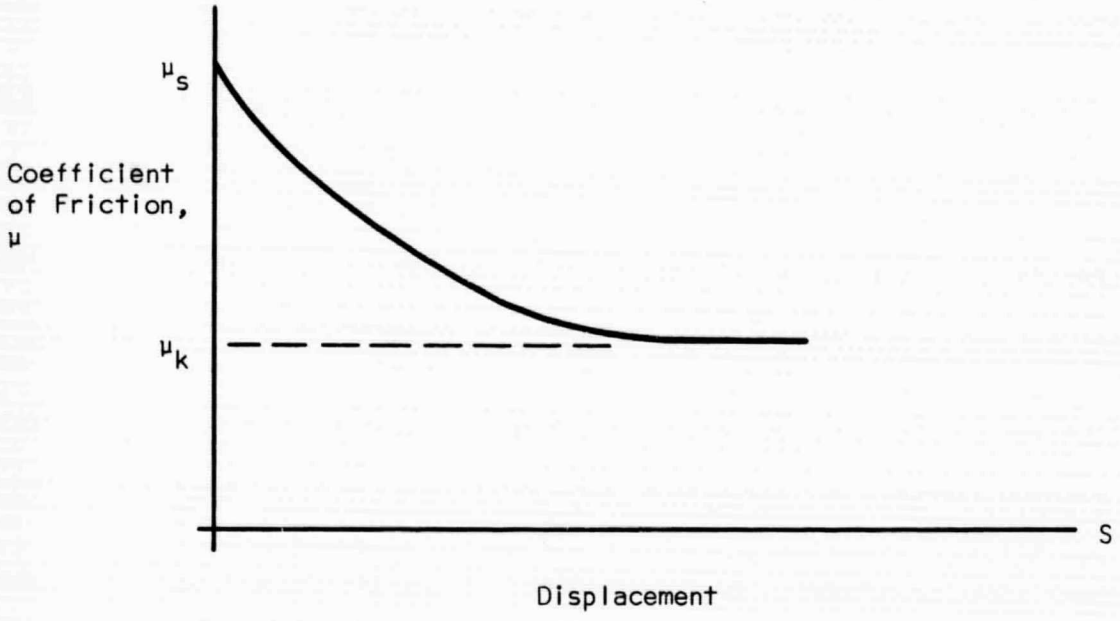

FIGURE 21. Coefficient of Friction vs. Linear Displacement

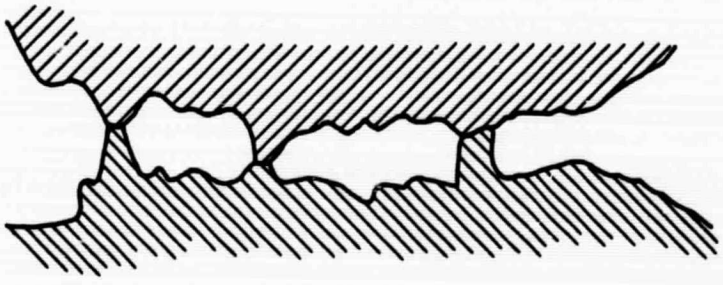

FIGURE 22. Microscopic View of Real Area of Contact

Conclusions

As explained previously, a torque applied to the system which corresponds to the asymptote of the given curves will cause the system to rotate until the limit of rotation is reached. For the system with the cylinders in the horizonal position and using the "dither" effect, an applied torque of 0.56×10^{-3} in-lb will cause full rotation. Because of the friction in the system, it is impossible to determine exactly what is happening near the origin of the curves. Although the theory does not indicate a rotational spring rate, it is possible that such a spring rate could exist due to irregularities in the bands, misalignment, etc. If such a spring rate does exist, the maximum torque it can exert is 0.56×10^{-3} in-lb at an angular rotation of 1.57 radians. This corresponds to a spring rate of 3.57×10^{-4} in-lb/rad assuming any existing spring rate is linear. The minimum torque rate of the control system will have to be 14 in-lb/rad. Thus, any rotational spring rate of the crossed metal bands can be neglected.

CHAPTER V

CONNECTING BAND DESIGN AND ANALYSIS

Band Design

To insure fully elastic behavior for the connecting bands, the maximum stress induced by the combined effects; bending to conform to the cylinders, initial tensioning, and induced loadings; will have to be kept below the yield stress of the band material or

$$S_y > S_B + S_P + S_{PA}. \tag{5-1}$$

In terms of the system parameters; S_B, S_P, and S_{PA} are

$$S_B = \frac{yE}{R_o} \tag{5-2}$$

P_t = initial band tension at 2000°F

$$S_P = \frac{P_t}{A} \tag{5-3}$$

$$S_{PA} = \frac{P_A}{A}. \tag{5-4}$$

Substituting equations (5-2), (5-3), and (5-4) into equation (5-1), the equation becomes

$$S_y > \frac{yE}{R_o} + \frac{\left(P_t + P_A\right)}{A}. \tag{5-5}$$

It was decided to make the bands of one mil Haynes Alloy No. 25 since it can withstand ambient temperatures of 2000°F. For the temperature range of interest, the following values were obtained:

$$E = 21.18 \times 10^6 \text{ psi}$$

$$S_y = 23{,}100 \text{ psi} .$$

Using equation (4-1), the minimum radius of curvature for one mil Haynes Alloy No. 25 was found to be 0.46 inch. To allow for initial tensioning and induced loading, the radius of curvature for the bands should be two inches. Using equation (5-2), the bending stress was found to be 5300 psi.

By rearranging equation (5-5)

$$\frac{P_t + P_A}{A} < S_y - \frac{yE}{R_o} \qquad (5\text{-}6)$$

equation (5-6) can be used to determine a satisfactory initial band tension once P_A has been determined and a value for A has been chosen.

Induced loading is dependent on the angular accelerations of the aircraft. At the present time, it is planned to mount the meter under an experimental airplane, such as the X - 15A - 2. The maximum pitch rate of the X - 15 due to flight characteristics is 3 rad/sec^2 at a speed of mach 3.4 (12). The maximum vibration level recorded has a resonance frequency of 13 Hz with an amplitude of one degree peak to peak at mach 4 (13). For a harmonic vibration of the form

$$\theta = \theta_o \sin\omega t \qquad (5\text{-}7)$$

and differentiating twice with respect to time, the maximum angular accelerations due to vibrations is

$$\ddot{\theta} = \theta_o \omega^2 \ . \qquad (5\text{-}8)$$

At a frequency of 13 Hz and with an amplitude of one degree peak to peak, equation (5-8) gives about 61 rad/sec^2. The total angular acceleration of the aircraft is then 64 rad/sec^2. This anguiar acceleration is the total maximum acceleration recorded through speeds of Mach 6. No angular acceleration information is available for a speed of Mach 8 which is the desired aircraft speed. However, the bands will be designed using 100 rad/sec^2 to allow for a possible increase in accelerations due to the increase in aircraft speed. Also, a band design based on an angular acceleration of 100 rad/sec^2 should be satisfactory if it is decided to mount the meter below another high speed aircraft.

Figure 23 shows the floating element component of the skin friction meter with the forces which cause rotation due to angular accelerations. Point C.R. is an arbitrary point about which the angular acceleration acts. The forces causing rotation will be a maximum if the point C.R. lies on the centerline of the component. The forces are

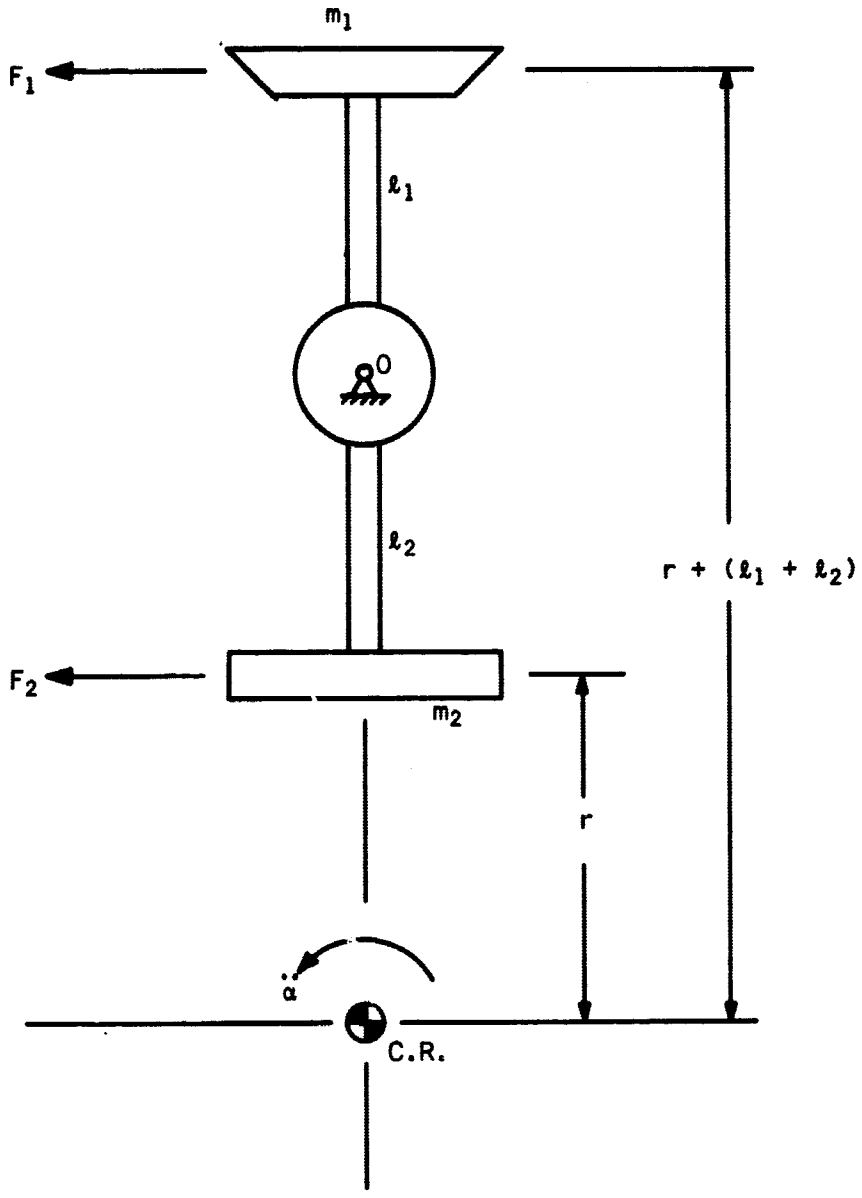

FIGURE 23. mm_1 Component with Forces Due to Angular Accelerations

$$F_1 = m_1[r + (\ell_1 + \ell_2)]\ddot{\alpha} \qquad (5\text{-}9a)$$

$$F_2 = m_2 r\ddot{\alpha} \ . \qquad (5\text{-}9b)$$

The moments, M_1 and M_2, of the forces about 0 respectively are

$$M_1 = m_1\ell_1[r + (\ell_1 + \ell_2)]\ddot{\alpha} \quad \text{c.c.w.} \qquad (5\text{-}10a)$$

$$M_2 = m_2\ell_2 r\ddot{\alpha} \quad \text{c.w.} \qquad (5\text{-}10b)$$

The net moment in the counterclockwise direction is

$$M_n = m_1\ell_1[r + (\ell_1 + \ell_2)]\ddot{\alpha} - m_2\ell_2 r\ddot{\alpha} \ . \qquad (5\text{-}11a)$$

Since $m_1\ell_1 = m_2\ell_2$, equation (5-11a) becomes

$$M_n = m_1\ell_1(\ell_1 + \ell_2)\ddot{\alpha} \ . \qquad (5\text{-}11b)$$

The floating element is to be made of Haynes Alloy No. 25 and will have a mass of 1.005×10^{-2} slugs (maximum). The maximum length of $(\ell_1 + \ell_2)$ will be 2 inches. The length, ℓ_1, will be about one inch. Using $\ddot{\alpha} = 100$ rad/sec^2, the maximum M_n is 0.168 in-lb from equation (5-11b).

Referring to Figure 7, the equations of motion for the components rotating about points 0_1 and 0_2 respectively are

$$M_n - P_1R + P_2R = I_1\ddot{\alpha}_1 \qquad (5\text{-}12a)$$

$$P_1R - P_2R = I_2\ddot{\alpha}_2 \ . \qquad (5\text{-}12b)$$

In equation (5-12), it is assumed that the radii of the cylinders are the same.

Substracting equation (5-12b) from equation (5-12a),

$$M_n - 2R(P_1 - P_2) = I_1\ddot{\alpha}_1 - I_2\ddot{\alpha}_2 \ . \qquad (5\text{-}13)$$

If the radii of the cylinders are the same, then $I_1 = I_2$ and $\ddot{\alpha}_1 = \ddot{\alpha}_2$ from equations (2-12) and (2-11) respectively. Equation (5-13) becomes

$$M_n - 2R(P_1 - P_2) = 0$$

Since the bands are thin, they cannot transmit forces in compression. Thus, P_2 can be considered as the initial tension in the bottom band while P_1 is the tension in the top band required for the rotation of the counterbalancing component about O_2. The quantity, $(P_1 - P_2)$, can be considered as the maximum change in tension of the top band and the equation becomes

$$M_n - 2R\Delta P = 0. \qquad (5\text{-}15)$$

For rotation in the opposite direction, the same analysis will hold for the bottom band.

Rearranging equation (5-15), ΔP becomes

$$\Delta P = \frac{M_n}{2R} \qquad (5\text{-}16)$$

For the final system, R will be about 0.625 inch and the resulting band tension change is 0.134 lb.

When the radius of curvature of the bands has been specified, the induced loading of the bands determined, and a value for the band cross-sectional area is assumed, equation (5-6) can be used to determine the maximum initial tension in the band for elastic loading. If the width of each band is assumed to be 0.5 inch, then P_t must be less than 8.766 lbs. Using a small factor of safety, the tension in the bands should be 8 lb. when the ambient temperature is 2000°F. The change in band tension due to induced loading is 1.68 per cent. Thus, the requirement specified in Chapter III, which states that changes in band tensions must be small, is satisfied.

Next, the effects of ambient temperature changes must be considered. During construction, the system will be assembled at room temperature. The same system must operate in an ambient temperature of about 2000°F. Figure 24 shows the final system with the support frame.

In the analysis to follow, the following assumptions are made:

1) The bands bend to the radius of the cylinders.
2) The ambient temperature for the entire system is 2000°F.
3) Linear exparsions in all directions are assumed to be equal.
4) The same material is to be used to make the bands, cylinders, and support frame.

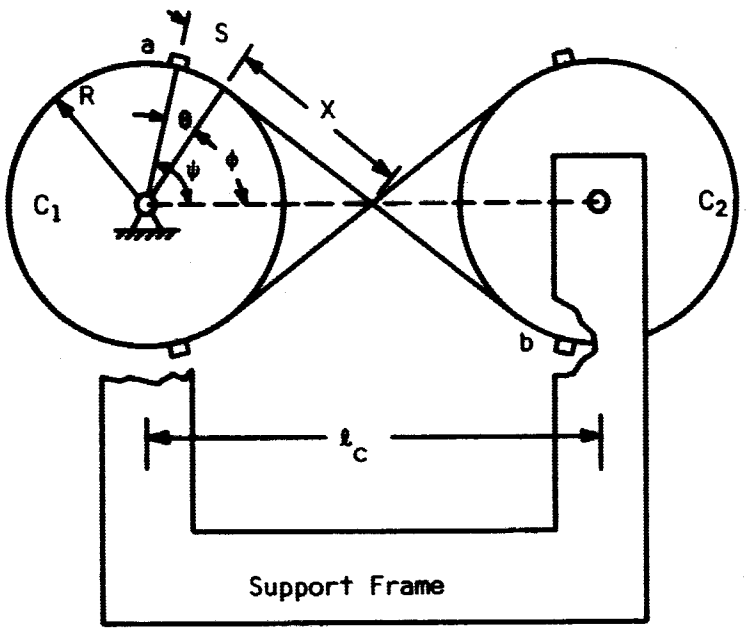

FIGURE 24. Final System with Support Frame

Consider the band connected to cylinders C_1 and C_2 at points a and b respectively. Let ℓ_b be the initial length of the band with an initial tension between points a and b. Let ℓ_s be the initial length in space between a and b following the path of the band. At the time of assembly,

$$\ell_b = \ell_s \tag{5-17}$$

After thermal expansion, let ℓ_b' be the length of the band and ℓ_s' be the length in space between a and b following the path of the band. A relationship between ℓ_b' and ℓ_s' of the form

$$\ell_b' = \ell_s' \tag{5-18}$$

is desired. The length, ℓ_b', is to be the same as the length, ℓ_s'. The initial band tension would then be the same as the tension after thermal expansion. By varying the system parameters; Ψ, R, and ℓ_c; the proper relation between them can be found to satisfy equation (5-18).

If equation (5-18) cannot be satisfied, then the relationship between ℓ_s' and ℓ_b' would be

$$\ell_s' - \ell_b' = d \ . \tag{5-20}$$

The change in band tension for the case of equation (5-20) is proportional to d and can be determined.

To study the behavior of the system, first consider the length ℓ_b'. From the laws of thermal expansion,

$$\ell_b' = \ell_b(1 + \gamma T_o). \tag{5-21}$$

Using equation (5-17), equation (5-21) becomes

$$\ell_b' = \ell_s(1 + \gamma T_o). \tag{5-22}$$

Let $(1 + \gamma T_o) = n$ which is a constant. Equation (5-18) becomes

$$\ell_b' = n\ell_s . \tag{5-23}$$

Next, ℓ_s and ℓ_s' must be written in terms of the system parameters; ψ, R, and ℓ_c. For the symmetrical system shown in Figure 23,

$$\ell_s = 2s + 2x. \tag{5-24}$$

The following relations can also be written:

$$s = R\theta \tag{5-25}$$

$$x = \left[\left(\frac{\ell_c}{2}\right)^2 - (R)^2\right]^{1/2} \tag{5-26}$$

$$\theta = \psi - \tan^{-1}\left(\frac{x}{R}\right). \tag{5-27}$$

Substituting equation (5-26) into equation (5-27),

$$\theta = \psi - \tan^{-1}\left(\frac{\left[\left(\frac{\ell_c}{2}\right)^2 - (R)^2\right]^{1/2}}{R}\right) \tag{5-28}$$

Substituting equations (5-28) and (5-26) into equation (5-24), the equation becomes

$$\ell_s = 2R\left[\psi - \tan^{-1}\left(\frac{\left[\left(\frac{\ell_c}{2}\right)^2 - (R)^2\right]^{1/2}}{R}\right)\right] + 2\left[\left(\frac{\ell_c}{2}\right)^2 - (R)^2\right]^{1/2}. \quad (5\text{-}29)$$

After thermal expansion, the parameters; R, ℓ_c, θ, and x; change to R', ℓ_c', θ', and x' respectively. Also

$$R' = R(1 + \gamma T_o) = nR \quad (5\text{-}30a)$$

$$\ell_c' = \ell_c(1 + \gamma T_o) = n\ell_c \quad (5\text{-}30b)$$

and

$$\ell_s = 2s' + 2x' \quad (5\text{-}31)$$

Using the procedure followed above, the following equation for ℓ_s' can be obtained:

$$\ell_s' = 2nR\left[\psi - \tan^{-1}\left(\frac{\left[\left(\frac{n\ell_c}{2}\right)^2 - (nR)^2\right]^{1/2}}{nR}\right)\right] + 2\left[\left(\frac{n\ell_c}{2}\right)^2 - (nR)^2\right]^{1/2}. \quad (5\text{-}32)$$

Simplifying, equation (5-32) becomes

$$\ell_s' = 2nR\left[\psi - \tan^{-1}\left(\frac{\left[\left(\frac{\ell_c}{2}\right)^2 - (R)^2\right]^{1/2}}{R}\right)\right]$$

$$+ 2n\left[\left(\frac{\ell_c}{2}\right)^2 - (R)^2\right]^{1/2}. \qquad (5\text{-}33)$$

By comparing equations (5-33) and (5-29), it can be seen that equation (5-23) is satisfied. Thus, if the bands, cylinders, and support frame are all made of the same material, the effects of thermal expansion can be eliminated.

The above analysis assumed that the ambient temperature was constant throughout the system. However, this will not be the true situation. The skin friction meter must be capable of surviving an extremely cold environment prior to launch. The low temperature is due to the liquid hydrogen fuel. The meter will be in close proximity to the tubes carrying the fuel. To limit the temperature requirements, the meter will be heated during the time it is soaking in the cold environment (1). In addition to controlling the environment, the heater can also be used to control temperature gradients and insure a constant ambient temperature.

The requirement that the construction be entirely of Haynes Alloy No. 25 is practical since the entire meter must withstand high temperatures. The properties of this material make it very good for high temperature applications.

The results obtained here will be summarized for future reference:

1) The bands are to be 1 mil thick and made of Haynes Alloy No. 25.

2) The width of the bands for each direction of wrap should be 0.5 inch.

3) The radius of curvature of the bands contacting the cylindrical pivots should be 2 inches.

4) The initial band tension should be 8 lb.

5) The cylinders and support frame should be constructed from Haynes Alloy No. 25.

No attempt will be made here to develop a final system design. Research dealing with the development of the control system and other aspects of the system design is still being conducted. No final decisions along these lines have yet been made.

Natural Frequency

Figure 25 shows an equivalent system for the counterbalanced skin friction meter. Depending on the direction of rotation, the connecting band acts as a stiff spring connecting two cylinders. Figure 26 shows a connecting band between the two cylinders. The band length for the configuration shown is 1.60 inches. The band length for the final design should not change appreciably from this length.

The spring constant of the band can be found by using Hooke's Law or

$$K = \frac{EA}{\ell} . \qquad (5\text{-}34)$$

For the Haynes Alloy band, K is 6620 lb/in for the temperature range of interest.

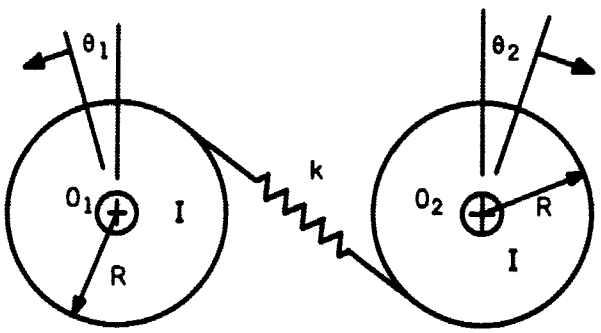

FIGURE 25. Equivalent System for Counterbalanced Skin Friction Meter

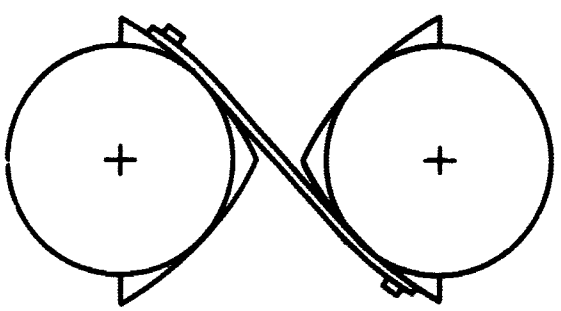

FIGURE 26. Connecting Band Between Rotating Cylinders

For cylinders with equal radii, the equations of motion for the two components about O_1 and O_2 respectively are

$$I\ddot{\alpha}_1 + kR^2[\alpha_1 - \alpha_2] = 0 \qquad (5\text{-}35a)$$

$$I\ddot{\alpha}_2 + kR^2[\alpha_2 - \alpha_1] = 0. \qquad (5\text{-}35b)$$

Assuming the solutions for α_1 and α_2 to be

$$\alpha_1 = A(\sin\omega t + \phi) \qquad (5\text{-}36a)$$

$$\alpha_2 = B(\sin\omega t + \phi) \qquad (5\text{-}36b)$$

and differentiating twice with respect to time, equation (5-36) becomes

$$\ddot{\alpha}_1 = -A\omega^2(\sin\omega t + \phi) \qquad (5\text{-}37a)$$

$$\ddot{\alpha}_2 = -B\omega^2(\sin\omega t + \phi). \qquad (5\text{-}37b)$$

By substituting equations (5-36) and (5-37) into equation (5-35) and simplifying, the equations of motion become

$$(kR^2 - I\omega^2)A + (kR^2)B = 0 \qquad (5\text{-}38a)$$

$$-(kR^2)A + (kR^2 - I\omega^2)B = 0. \qquad (5\text{-}38b)$$

The characteristic equation is the determinant of the coefficients and is

$$\omega^2(I^2\omega^2 - 2kR^2I) = 0. \qquad (5\text{-}39)$$

From equation (5-39), the natural frequencies of the system are

$$\omega = o, R\left(\frac{2k}{I}\right)^{1/2} . \qquad (5\text{-}40)$$

The maximum mass moment of inertia for the rotating components will be 2.77×10^{-4} lb-in-sec^2. This is the mass moment of inertia of the torque motor armature being developed. As discussed above, R for the cylinders will be 0.625 inch. Using these values in equation (5-40), the natural frequences are 0 and 688 cps.

Transfer Function

The equations of motion for the system with a torque applied to cylinder C_1 are

$$I\ddot{\alpha}_1 + kR^2[\alpha_1 - \alpha_2] = T_A \qquad (5\text{-}41a)$$

$$I\ddot{\alpha}_2 + kR^2[\alpha_2 - \alpha_1] = 0. \qquad (5\text{-}41b)$$

Writing the equations in Laplace transform notation

$$(IS^2 + kR^2)\bar{\alpha}_1 - (kR^2)\bar{\alpha}_2 = T_A$$

$$-(kR^2)\bar{\alpha}_1 + [IS^2 + kR^2]\bar{\alpha}_2 = 0$$

Solving the two equations for $\bar{\alpha}_1$

$$\bar{\alpha}_1 = \frac{\begin{vmatrix} T_A & -kR^2 \\ 0^A & (IS^2 + kR^2) \end{vmatrix}}{\begin{vmatrix} (IS^2 + kR^2) & -kR^2 \\ -kR^2 & (IS^2 + kR^2) \end{vmatrix}} \qquad (5\text{-}42)$$

Simplifying equation (5-42), the transfer function becomes

$$\frac{\bar{\alpha}_1}{T_A} = \frac{(S^2 + kR^2/I)}{IS^2(S^2 + 2kR^2/I)} \qquad (5\text{-}43)$$

For the proposed system, the value of kR^2/I is 9.34×10^6 rad/sec^2. The bandwidth of the torque motor and its control system will be about 10 H_z. Thus, for the operating range of interest, the transfer function can be reduced to

$$\frac{\bar{\alpha}_1}{T_A} = \frac{1}{2IS^2} \; . \qquad (5\text{-}44)$$

CHAPTER VI

CONCLUSIONS

Theoretically, the counterbalancing system will eliminate the effects of linear accelerations of the transport vehicle. Also, the system will be insensitive to angular accelerations through 100 rad/sec^2.

The experimental results of Chapter IV show that any rotational spring rate of the crossed metal bands will not influence the operation of the system. In Chapter III, the assumption was made that small changes in the band tension would have no effect on the system. Since a system has not been assembled at this writing, this assumption has not been verified. Also, the analyses in this thesis neglected any influence of the pivots on the system. The pivots should not affect the system if satisfactory gas bearings are developed.

A lack of homogeneity throughout the material, and variations in the distribution of mass due to tolerances allowed on all machined surfaces will cause the rotating members to be unbalanced. The components will be both statically and dynamically unbalanced. It is possible to statically and dynamically balance a component so that the displacement between the center of mass and axis of rotation is 20×10^{-6} inch. The Gisholt Machine Company manufactures a balancing machine (Model 1S) with a working accuracy of 20×10^{-6} inch (14). The weight of the target component is 0.863 lb. The maximum torque about the pivot axis due to the mass unbalance when the meter is stationary is 1.73×10^{-5} in-lb. The maximum linear acceleration of

the meter due to the aircraft will be 3.5g. At this acceleration, the maximum torque about the pivot axis will be 6.06×10^{-5} in-lb. The only effect of the dynamic unbalance will be to increase the reaction forces at the pivot. The gas bearings should be stiff enough to handle this increase in loading. Thus, the errors due to unbalance can be neglected.

The thickness of the band material is critical. When bending the bands to the proper radius of curvature, a deviation from the specified thickness can cause the bands to be overstressed. The deviation from the 1 mil thickness should not exceed 0.0001 inch.

The width of the bands and the radius of curvature are not as critical as the band thickness. The band thickness and radius of curvature should not deviate over 0.010 inch. Using the "worst" combination of the above tolerances, the allowable initial tension is 8.47 lb. Thus, the specified initial tension of 8 lb would still be satisfactory.

Since one of the natural frequences of the counterbalanced system is zero, the system is a semi-definite system. The other natural frequency lies well beyond the bandwidth frequency of the torque motor and control system. Thus, the effects of the resonant frequences of the system can be neglected.

The transfer function given in Chapter V can be used in the design of the system control system.

Since the system must operate in ambient temperatures of 2000°F, creep of the bands will present a problem. A tension of 8 pounds in the bands will produce a band stress of 16,000 psi. No creep information is available for Haynes Alloy No. 25 at a temperature of 2000°F with a

working stress of 16,000 psi. However, the creep rate at 1500°F with a working stress of 19,000 psi is 0.025 per cent elongation per hour. The creep rate at 2000°F will be larger than the creep rate at 1500°F for a given working stress.

The initial tension of 8 pounds will disappear if the elongation of the band is 0.0012 in. Using the creep rate given above for 1500°F, the band tension will disappear after 3 hours. Thus, the life of the system will depend on the bands and will be less than 3 hours.

To reduce the problems of creep, the width of the bands can be increased to decrease the working stress. After completion of tests on a bread board model, a knowledge of the effects of changes in the band tension due to induced loading can be obtained. If the effects of induced loading is sufficiently small, it may be possible to reduce the initial tension.

Using the above methods, it will be possible to reduce the effects of creep. The life of the meter will still be relatively short. Thus, it will be necessary to replace the bands often.

The design specifications listed above and in Chapter V should provide a good starting point for the final design of the system.

LIST OF REFERENCES

1. Seemuller, William W., "The Design of a Skin Friction Meter for Use in Extreme Environmental Conditions," Master's Thesis, The University of Virginia, Charlottesville, August 1966, pp. 1-7.

2. Weiler, John Eugene Sr., "Design of an Acceleration Insensitive Skin Friction Balance for Flight Testing," Master's Thesis, The University of Texas, Austin, June 1954.

3. Pietta, Dan H. and Frederick, Daniel, Engineering Mechanics, Fourth Printing, New York, The Ronald Press Company, 1964, pp. 529-534.

4. Timoshenko, S. and Young, D. H., Elements of Strength of Materials, Fourth Edition, Toronto, D. Van Nostrand Company, 1962, pp. 111-114.

5. Seely, Fred B. and Smith, James O., Advanced Mechanics of Materials, Second Edition, New York, John Wiley and Sons, 1966, p. 551.

6. Lyons, Willis Carson Jr., "The Design of An Acceleration Insensitive Skin Friction Balance for Use in Free Flight Vehicles at Supersonic Speeds," Master's Thesis, The University of Texas, Austin, June 1957.

7. Baumister, Theordore (ed.), Mark's Standard Handbook For Mechanical Engineers, Seventh Edition, New York, McGraw-Hill Book Company, 1967, pp. 5.1-5.6.

8. The Wayne Kerr Laboratories, Ltd., Vibration Meter B731A, Distance Meter DM100, Instruction Manual, The Wayne Kerr Laboratories, Ltd., Chessington, England.

9. Fridman, Hans D. and Levesque, Pascal, "Reduction of Static Friction by Sonic Vibrations," Journal of Applied Physics, Vol. 30, No. 10, Oct. 1959, pp. 1572-1575.

10. Rabinowicz, Ernest, Friction and Wear of Materials, New York, John Wiley and Sons, 1965, p. 99.

11. Rothbart, Harold A. (ed.), Mechanical Design and Systems Handbook, New York, McGraw-Hill Book Company, 1964, pp. 11.3-11.4.

12. Redless, Herman A., Robinson, Glenn H., and Yancey, Roxanah B., "Aerodynamic-Derivative Characteristic of the X-15 Research Airplane as Determined from Flight Tests for Mach Numbers from 0.6 to 3.4," National Aeronautics and Space Administration, NASA TN D-1060, Jan. 1962.

13. Smith, John W. and Taylor, Lawrence W., "An Analysis of the Limit-Cycle and Structural-Resonance Characteristics of the X-15 Stability Augmentation System," National Aeronautics and Space Administration, NASA TN D-4287, Dec. 1967.

14. Ott, Robert D., Personal Correspondence of the Author, Letter dated May 13, 1968.

15. Kauzlarich, J. J., Bhatia, K. G., and Streitman, H. W., "Effect of Wear on Pivot Thrust Bearings," ASLE Transactions, Vol. 9, No. 3, July 1966, pp. 257-263.

UNCITED REFERENCES

1. Beezhold, W. F. and Wild, D. H., "Determination of the Coefficient of Kinetic Friction in the Case of Extremely Small Displacements," Journal of Applied Physics, Vol. 35, No. 4, April 1964, pp. 1169-1175.

2. Boyd, J. and Kaufman H. N., "Pivot Bearings," Lubrication Eng., Aug. 1965, pp. 348-351.

3. Herzl, G., "Conical Pivot Bearings," Machine Design, Vol. 37, No. 28, Dec. 9, 1965, pp. 146-152.

4. Rabinowicz, Earnest, "The Nature of the Static and Kinetic Coefficients of Friction," Journal of Applied Physics, Vol. 22, No. 11, November 1951, pp. 1373-1379.

5. Wilkes, D. F., "Rolamite, A New Mechanism," Mechanical Engineering, Vol. 90, No. 4, April 1968, pp. 11-29.

APPENDIX A

ERROR ANALYSIS OF STRING ANGLES

The ideal string angles are shown in Figure 11. The torque applied to the cylinders in terms of the applied weights is

$$T_A = 1.98 \times 10^{-3} W[\text{in-lb}]. \qquad \text{(A-1)}$$

A machinist's protractor was used to adjust the angles. Using the protractor, the angles could be adjusted so that the maximum deviation was ± 1 degree. Figure 27 shows the maximum deviations from the ideal angles due to improper adjustment at the time of assembly. The torque applied to the cylinders for the string angles shown is

$$T_A = 1.96 \times 10^{-3} W[\text{in-lb}]. \qquad \text{(A-2)}$$

The maximum deviation from the calculated torque for the ideal angles is then about one per cent.

Since the strings are attached to the cylinders, the angles will change as the cylinders rotate. Using the machinist protractor, the changes in the string angles as a function of cylinder rotation was determined. Figure 28 shows the change in applied torque versus angular displacement of the cylinders. The slope of the curve as it crosses the vertical axis is $W(1.2 \times 10^{-5})$ in-lb/degree. Thus, for the small angular displacements measured, the changes in applied torque because of rotation were neglected.

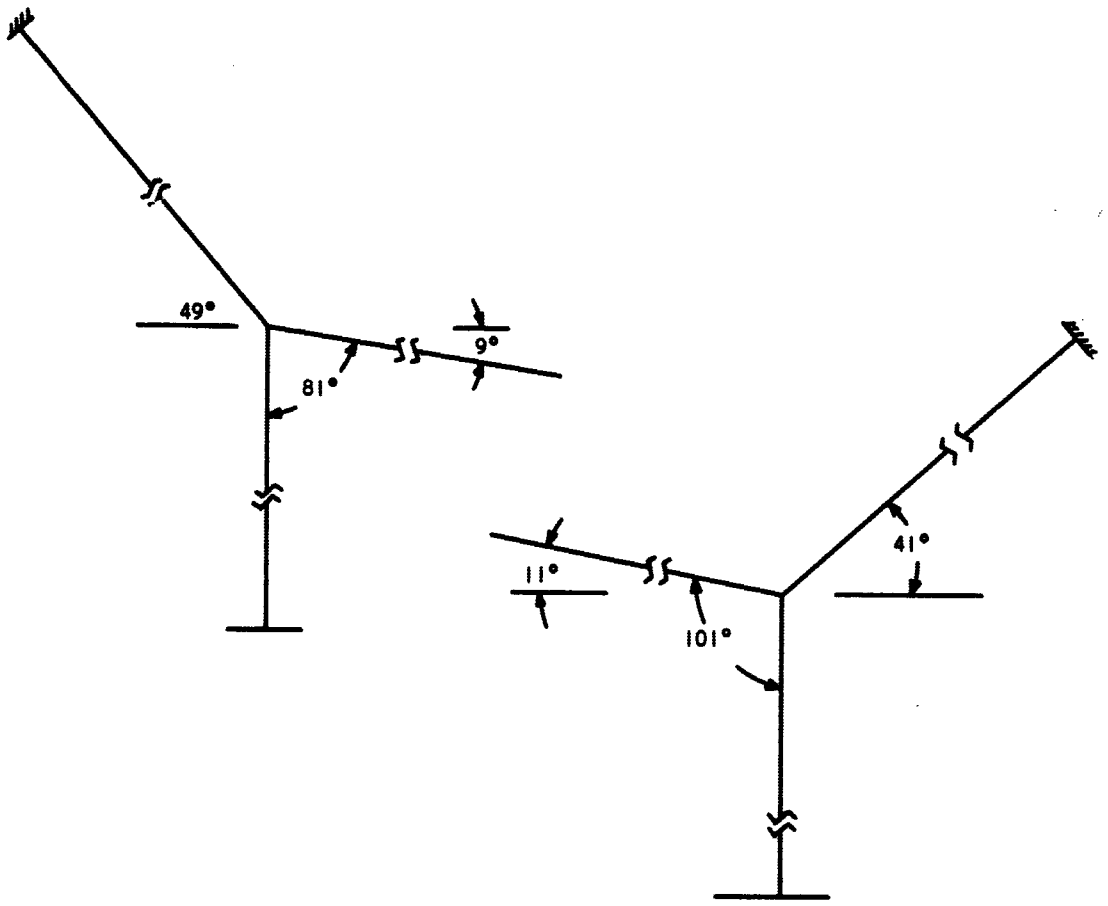

FIGURE 27. Maximum Deviations from Ideal String Angles

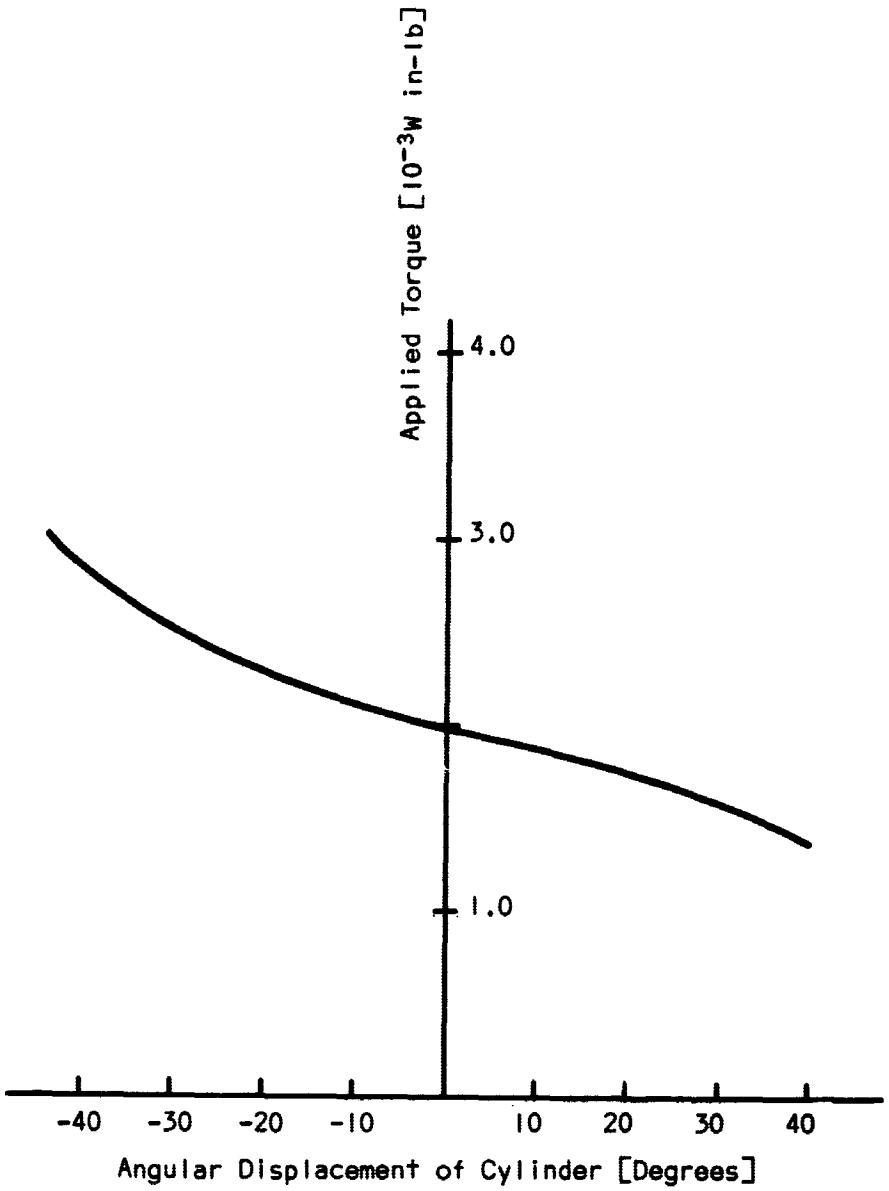

FIGURE 28. Applied Torque vs Angular Displacement of Cylinder

APPENDIX B

VIBRATION METER

The Wayne Kerr model B731A vibration meter is a portable instrument for accurate measurement of distance and vibration amplitude from 50 micro inches to 0.5 inches over the frequency range 1 Hz to 10 KHz. The probe is brought into proximity with the metallic or metallised surface of the object under test and the capacitance so formed is displayed in terms of distance and peak to peak vibration amplitude on the two meters on the instrument front panel. Sockets and terminals are available on the instrument for connection to recorders and oscilloscopes.

Various probes are available for use with the instrument and its range is determined by the range of the probe being used. The range and the accuracy of the various standard probes are tabulated in Table 1.

TABLE 1

PROBE PERFORMANCE

Probe	Range	Accuracy	
	Inches	1 Hz to 10 Hz	10 Hz to 10 KHz
A	0.001	± 0.00006	± 0.00003
C	0.01	± 0.0005	± 0.0002
E	0.1	± 0.005	± 0.002
F	0.5	± 0.025	± 0.01

The discrimination of the distance and vibrations meters is better than 0.5 per cent of full scale deflection.

The "C" probe was used in the experiments described in Chapter IV. The probe was calibrated using grade B Gage Blocks. A calibration curve is shown in Figure 29.

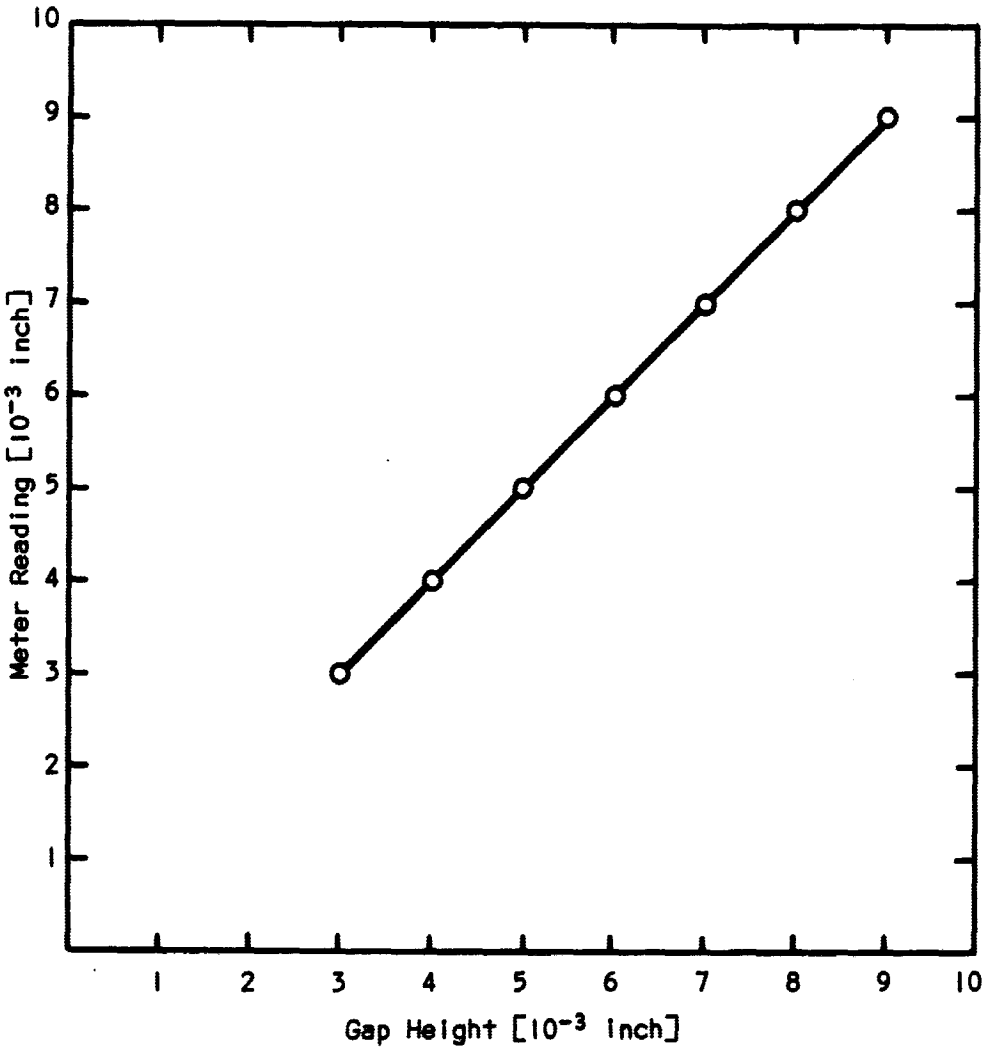

FIGURE 29. Calibration Curve for Wayne Kerr "C" Probe